

¹ Observation of the Higgs boson in the WW^*
² channel and search for Higgs boson pair
³ production in the $b\bar{b}b\bar{b}$ channel with the
⁴ ATLAS detector

⁵ A DISSERTATION PRESENTED
⁶ BY
⁷ TOMO LAZOVICH
⁸ TO
⁹ THE DEPARTMENT OF PHYSICS

¹⁰ IN PARTIAL FULFILLMENT OF THE REQUIREMENTS
¹¹ FOR THE DEGREE OF
¹² DOCTOR OF PHILOSOPHY
¹³ IN THE SUBJECT OF
¹⁴ PHYSICS

¹⁵ HARVARD UNIVERSITY
¹⁶ CAMBRIDGE, MASSACHUSETTS
¹⁷ MAY 2016

¹⁸ ©2016 – TOMO LAZOVICH

¹⁹ ALL RIGHTS RESERVED.

²⁰ **Observation of the Higgs boson in the WW^* channel and search
²¹ for Higgs boson pair production in the $b\bar{b}b\bar{b}$ channel with the
²² ATLAS detector**

²³ ABSTRACT

²⁴ This dissertation presents the observation and measurement of the Higgs boson in the $H \rightarrow WW^* \rightarrow$
²⁵ $\ell\nu\ell\nu$ channel at $\sqrt{s} = 7$ TeV and $\sqrt{s} = 8$ TeV and a search for Higgs pair production in the $HH \rightarrow$
²⁶ $b\bar{b}b\bar{b}$ channel at $\sqrt{s} = 13$ TeV with the ATLAS detector in pp collisions at the Large Hadron Collider.

²⁷ First, the discovery of a particle consistent with the Higgs boson in 4.8 fb^{-1} at $\sqrt{s} = 7$ TeV and
²⁸ 5.8 fb^{-1} at $\sqrt{s} = 8$ TeV is discussed. Then, the measurement of the Higgs boson signal strength
²⁹ and cross section in both the gluon fusion and vector boson fusion (VBF) production modes using
³⁰ 20.3 fb^{-1} of $\sqrt{s} = 8$ TeV data combined with 4.8 fb^{-1} of 7 TeV data is shown. The combined signal
³¹ strength is measured to be $\mu = 1.09^{+0.23}_{-0.21}$. The total observed significance of the $H \rightarrow WW^*$ process
³² is observed to be 6.1σ (with 5.8σ expected). Advanced methods for background reduction and estima-
³³ tion, particularly in same-flavor lepton final states, are shown. The VBF signal strength is measured to
³⁴ be $\mu_{\text{VBF}} = 1.27^{+0.53}_{-0.45}$ with an observed significance of 3.2σ (with 2.7σ expected). In the VBF chan-
³⁵ nel, a selection requirement based method, the precursor to the final multivariate technique used for the
³⁶ result, is detailed.

³⁷ Finally, a search for Higgs pair production in the $b\bar{b}b\bar{b}$ final state with 3.2 fb^{-1} at $\sqrt{s} = 13$ TeV is
³⁸ presented. A particular focus is placed on a tailored signal region for resonant production of Higgs pairs
³⁹ at high masses. No significant excesses are observed, and upper limits on cross sections are placed for
⁴⁰ spin-2 Randall Sundrum gravitons (RSG) and narrow spin-0 resonances. The cross section of $\sigma(pp \rightarrow$
⁴¹ $G_{\text{KK}}^* \rightarrow hh \rightarrow b\bar{b}b\bar{b})$ with $k/\bar{M}_{\text{Pl}} = 1$ is constrained to be less than 70 fb for masses in the range
⁴² $600 < m_{G_{\text{KK}}^*} < 3000 \text{ GeV}$. The cross section upper limits for $\sigma(pp \rightarrow H \rightarrow hh \rightarrow b\bar{b}b\bar{b})$ ranges
⁴³ from 30 to 300 fb in the mass range of $500 < m_H < 3000 \text{ GeV}$.

Contents

44

45	o INTRODUCTION	I
46	I Theoretical and Experimental Background	5
47	I THE PHYSICS OF THE HIGGS BOSON	6
48	1.1 The Standard Model of Particle Physics	6
49	1.2 Electroweak Symmetry Breaking and the Higgs	8
50	1.3 Higgs Boson Production and Decay	II
51	1.4 Higgs Pair Production in the Standard Model	16
52	1.5 Higgs Pair Production in Theories Beyond the Standard Model	17
53	1.6 Conclusion	22
54	2 THE ATLAS DETECTOR AND THE LARGE HADRON COLLIDER	23
55	2.1 The Large Hadron Collider	24
56	2.2 The ATLAS Detector	26
57	2.3 The ATLAS Muon New Small Wheel Upgrade	37
58	2.4 Object Reconstruction in ATLAS	42
59	II Observation and measurement of Higgs boson decays to WW^* in LHC	
60	Run 1 at $\sqrt{s} = 7$ and 8 TeV	52
61	3 $H \rightarrow WW^* \rightarrow \ell\nu\ell\nu$ ANALYSIS STRATEGY	53
62	3.1 Introduction	53
63	3.2 The $H \rightarrow WW^* \rightarrow \ell\nu\ell\nu$ signal in ATLAS	54
64	3.3 Background processes	55
65	3.4 Shared signal region selection requirements	59
66	3.5 Background reduction in same-flavor final states	61
67	3.6 Parameters of interest and statistical treatment	66
68	4 THE DISCOVERY OF THE HIGGS BOSON AND THE ROLE OF THE $H \rightarrow WW^* \rightarrow \ell\nu\ell\nu$ CHANNEL	
69	4.1 Introduction	72

71	4.2	Data and simulation samples	73
72	4.3	$H \rightarrow WW \rightarrow e\nu\mu\nu$ search	73
73	4.4	$H \rightarrow \gamma\gamma$ search	78
74	4.5	$H \rightarrow ZZ \rightarrow 4\ell$ search	79
75	4.6	Combined results	81
76	4.7	Conclusion	83
77	5	EVIDENCE FOR VECTOR BOSON FUSION PRODUCTION OF $H \rightarrow WW^* \rightarrow \ell\nu\ell\nu$	85
78	5.1	Introduction	85
79	5.2	Data and simulation samples	86
80	5.3	Object selection	90
81	5.4	Analysis selection	94
82	5.5	Background estimation	101
83	5.6	Systematic uncertainties	112
84	5.7	Results	116
85	6	COMBINED RUN I $H \rightarrow WW^* \rightarrow \ell\nu\ell\nu$ RESULTS	120
86	6.1	Introduction	120
87	6.2	Results of dedicated gluon fusion $H \rightarrow WW^* \rightarrow \ell\nu\ell\nu$ analysis	121
88	6.3	Signal strength measurements in ggF and VBF production	123
89	6.4	Measurement of Higgs couplings to vector bosons and fermions	128
90	6.5	Higgs production cross section measurement	128
91	6.6	Conclusion	130
92	III	Search for Higgs pair production in the $HH \rightarrow b\bar{b}b\bar{b}$ channel in LHC	
93		Run 2 at $\sqrt{s} = 13$ TeV	132
94	7	SEARCH FOR HIGGS PAIR PRODUCTION IN BOOSTED $b\bar{b}b\bar{b}$ FINAL STATES	133
95	7.1	Introduction	133
96	7.2	Motivation	134
97	7.3	Data and simulation samples	136
98	7.4	Event reconstruction and object selection	138
99	7.5	Event selection	141
100	7.6	Data-driven background estimation	146
101	7.7	Systematic uncertainties	152
102	7.8	Results	155

103	8 COMBINED LIMITS FROM BOOSTED AND RESOLVED SEARCHES	157
104	8.1 Introduction	157
105	8.2 Resolved results	158
106	8.3 Search technique and results	158
107	8.4 Limit setting	159
108	IV Looking ahead	163
109	9 CONCLUSION	164
110	APPENDIX A <i>b</i>-TAGGING PERFORMANCE AT HIGH p_T	168
111	A.1 Changes in MV2 score at high p_T	168
112	A.2 Effect of multiple <i>b</i> -quarks inside one jet	170
113	A.3 Changes in track quality at high p_T	172
114	REFERENCES	175

Listing of figures

116	1.1	The particles of the Standard Model and their properties [6].	7
117	1.2	The four most common Higgs boson production modes at the LHC: (a) gluon-gluon fusion, (b) vector boson fusion, (c) $W/Z + H$ production, (d) $t\bar{t}H$ production	11
118	1.3	Higgs production cross sections as a function of center of mass energy (\sqrt{s}) at a pp collider [18].	12
119	1.4	Higgs boson branching ratios as a function of m_H [18].	15
120	1.5	The two leading diagrams for Standard Model di-Higgs production at the LHC: (a) box diagram, (b) Higgs self coupling.	16
121	1.6	Diagrams with new vertices for non-resonant Higgs pair production arising in composite Higgs models.	18
122	1.7	Generic Feynman diagram for resonant Higgs pair production in BSM theories.	18
123	1.8	Branching ratios for a spin-2 Randall-Sundrum graviton as a function of mass computed in MadGraph with the CP3-Origins implementation [34, 40, 41].	19
124	1.9	$\sigma \times \text{BR}(HH)$ for Randall-Sundrum gravitons as a function of mass computed in MadGraph with the CP3-Origins implementation [34, 40, 41].	20
125	1.10	Randall-Sundrum graviton width as a function of mass computed in MadGraph with the CP3-Origins implementation [34, 40, 41]	21
126	1.11	Branching ratios for heavy Higgs H in Type I (left) and Type II (right) 2HDM models with $\tan \beta = 1.5$ and $\cos(\beta - \alpha) = 0.1(0.01)$ for Type I (Type II) [38].	22
135	2.1	A schematic view of the LHC ring [48]. Four main experiments are located at interaction points along the ring. ATLAS and CMS are general purpose experiments, while ALICE is dedicated to heavy ion collisions and LHCb is dedicated to studying B physics.	24
136	2.2	A full diagram of the ATLAS detector [44].	27
137	2.3	The ATLAS coordinate system. The z direction corresponds to the beam axis, while x and y define the transverse plane. θ is the angle relative to the beam axis and ϕ is the azimuthal angle. η , the pseudorapidity, approaches infinity at small angles relative to the beam axis. .	28
138	2.4	Layout of the ATLAS Inner Detector system [52].	29
139	2.5	Layout of the ATLAS calorimeter system [44].	31
140	2.6	Layout of the ATLAS muon system [44].	33
141	2.7	Predicted field integral as a function of $ \eta $ for the ATLAS magnet system [44].	35

146	2.8	ATLAS trigger rates for Level-1 triggers as a function of instantaneous luminosity in 2012 and 2015 operation. These are single object triggers for electromagnetic clusters (EM), muons (MU), jets (J), missing energy (XE), and τ leptons (TAU). The threshold of the trigger is given in the name in GeV [54].	36
150	2.9	Instantaneous luminosity as a function of time for data recorded by ATLAS at different center of mass energies [55, 56].	38
152	2.10	MDT tube hit (solid) and segment (dashed) efficiency as a function of hit rate per tube [57].	39
153	2.11	Trigger rate as a function of p_T threshold with and without the NSW upgrade [57].	40
154	2.12	Illustrations of the geometry (left) and operating principle (right) of the micromegas de- tector [57].	41
156	2.13	Geometry of the sTGC detector [57].	41
157	2.14	Illustration of particle interactions in ATLAS [60].	43
158	2.15	Electron performance: (a) reconstruction efficiency as a function of electron E_T [62] (b) energy resolution in simulation as a function of $ \eta $ for different energy electrons [63].	44
160	2.16	Muon performance in $\sqrt{s} = 8$ TeV data: (a) reconstruction efficiency as a function of muon p_T (b) dimuon mass resolution as a function of average p_T [64].	46
162	2.17	Jet energy response after calibration as a function of true p_T in simulation [69].	47
163	2.18	Summary of the inputs to the MV2 b -tagging algorithm.	48
164	2.19	Light jet rejection (1/efficiency) vs. b -jet efficiency for MV1 and its input algorithms (a) [70] and MV2 (b) [71] in simulated $t\bar{t}$ events. The numbers in the algorithm names in (b) refer to the fraction of charm events used in the MV2 training.	49
166	2.20	Resolution of E_T^{miss} components as a function of $\sum E_T$ before pileup suppression with different pileup techniques [73].	51
169	3.1	Branching ratios for a WW system. q refers to quarks. ℓ can be either an electron or muon, and the leptonic branching ratios of the τ are included. For example, the $\ell\nu qq$ final state includes one W decaying to $e\nu$, $\mu\nu$, or $\tau\nu$. τ_h refer to hadronic decays of the τ	55
171	3.2	An illustration of the unique analysis signal regions [74]. The most sensitive regions for both gluon fusion and vector boson fusion production	56
174	3.3	Feynman diagram for Standard Model WW production	56
175	3.4	Feynman diagrams for top pair production (left) and Wt production (right)	57
176	3.5	An example Feynman diagram of W +jets production	58
177	3.6	An example Feynman diagram of Z +jets production	58
178	3.7	A graphical illustration of the $E_{T,\text{rel}}^{\text{miss}}$ calculation.	60
179	3.8	Predicted backgrounds (compared with data) as a function of the number of jets, n_j (a and b), and the number of b -tagged jets, n_b (c), after pre-selection requirements. Panel a shows n_j in the same flavor sample, while panels b and c show the n_j and n_b distributions in the different flavor sample.	61

183	3.9	An event display of a Z/γ^* + jets event illustrating the effect of pileup interactions	63
184	3.10	The RMS of different missing transverse momentum definitions as a function of the average number of interactions per bunch crossing	63
185	3.11	The difference between the true and reconstructed values of the missing transverse momentum (a) and m_T (b) in a gluon fusion signal sample using both track-based (p_T^{miss}) and calorimeter-based E_T^{miss} definitions.	65
186	3.12	Comparison of f_{recoil} distributions for $Z/\gamma^* + \text{jets}$, $H \rightarrow WW^*$, and other backgrounds with real neutrinos.	66
187	3.13	Signal significance as a function of required value for f_{recoil} and $p_{T,\text{rel}}^{\text{miss}(\text{trk})}$ in the ggF $H \rightarrow WW^*$ with $n_j = 0$	67
193	4.1	Jet multiplicity distribution in data and MC after applying lepton, jet, and $E_{T,\text{rel}}^{\text{miss}}$ selections. The WW and top backgrounds have been normalized using control samples, and the hashed band indicates the total uncertainty on the prediction [1].	74
194	4.2	Comparison of m_T between data and simulation in the $n_j = 0$ WW (a) and $n_j = 1$ top (b) control samples [1].	76
195	4.3	m_T distribution in the $H \rightarrow WW \rightarrow e\nu\mu\nu$ $n_j \leq 1$ channels for 8 TeV data [1].	78
196	4.4	Diphoton mass spectrum in 7 and 8 TeV data. Panel a) shows the unweighted data distribution superimposed on the background fit, while panel c) shows the data where each event category is weighted by its signal to background ratio. Panels b) and d) show the respective distributions with background subtracted [1].	79
203	4.5	Four lepton invariant mass spectrum ($m_{4\ell}$) in 7 and 8 TeV data compared to background estimate. A 125 GeV SM Higgs signal is shown in blue [1].	80
204	4.6	Local p_0 distribution as a function of hypothesized Higgs mass for the $H \rightarrow ZZ^* \rightarrow 4\ell$ (a), $H \rightarrow \gamma\gamma$ (b), and $H \rightarrow WW^* \rightarrow \ell\nu\ell\nu$ (c) channels. Dashed curves show expected results, while solid curves show observed. Red curves are from 7 TeV data, blue curves from 8 TeV, and black curved combined [1].	82
209	4.7	Combined 95% CL limits (a), local p_0 values (b), and signal strength measurement (c) as a function of Higgs mass [1].	83
211	4.8	Comparison of measured signal strength μ for a 126 GeV Higgs in the 7 and 8 TeV datasets [1].	84
212	4.9	Two dimensional likelihood as a function of signal strength μ and Higgs mass m_H [1]. . .	84
213	5.1	A comparison of the subleading lepton p_T spectrum between VBF $H \rightarrow WW^*$ production and $t\bar{t}$ background.	87
215	5.2	Leading jet η in VBF $H \rightarrow WW^*$ (red) and $t\bar{t}$ (black)	96
216	5.3	Distributions of (a) m_{jj} , (b) Δy_{jj} , (c) $C_{\ell 1}$, and (d) $\Sigma m_{\ell j}$, for the cut-based VBF analysis. The top panels compare simulation and data, while the bottom panels show normalized distributions for all background processes and signal for shape comparisons [74].	97

219	5.4	A cartoon of the WW final state. Momenta are represented with thin arrows, spins with thick arrows [74].	98
220	5.5	Event display of a VBF candidate event [74].	100
221	5.6	Higgs topology variables - $m_{\ell\ell}$ (top left), $\Delta\phi_{\ell\ell}$ (top right), and m_T (bottom) - used in the selection requirements of the cut-based signal region and as inputs to the BDT result. These are plotted after all of the BDT pre-training selection cuts [74]. The VBF Higgs signal cross section is multiplied by a factor of 50 to allow for shape comparisons.	102
222	5.7	VBF topology variables - m_{jj} (top left), Δy_{jj} (top right), $\sum C_\ell$ (bottom) - used in the selection requirements of the cut-based signal region and as inputs to the BDT result. These are plotted after all of the BDT pre-training selection cuts [74]. The VBF Higgs signal cross section is multiplied by a factor of 50 to allow for shape comparisons.	103
223	5.8	Distributions of m_{jj} (a) and O_{BDT} (b) in the VBF $n_b = 1$ top CR [74].	105
224	5.9	Comparison of m_{jj} shape in a same flavor $Z \rightarrow \ell\ell$ control region and the VBF cut-based signal region.	106
225	5.10	General illustration of the ABCD region definitions for $Z/\gamma^* \rightarrow \ell\ell$ background estimation.	107
226	5.11	Distribution of m_{T2} in the WW validation region of the VBF analysis [74].	109
227	5.12	Extrapolation factors for the $W + \text{jets}$ estimate derived for muons (a) and electrons (b) as a function of lepton p_T [74].	III
228	5.13	Background composition in final VBF signal region [74].	112
229	5.14	Variations in the top background extrapolation factor in the cut-based analysis due to PDF uncertainties. The uncertainties are shown in the three bins of m_T used in the final cut-based statistical fit. Variations from the eigenvector of the nominal PDF, CT10, as well as the result from an alternate PDF (NNPDF10), are compared.	114
230	5.15	Variations in the top background extrapolation factor in the cut-based analysis due to QCD scale uncertainties. The uncertainties are shown in the three bins of m_T used in the final cut-based statistical fit. Q_F is the QCD factorization scale, while Q_R is the QCD renormalization scale.	115
231	5.16	Post-fit distributions in the cut-based VBF analysis. Panel (a) shows the one-dimensional m_T distribution, while (b) shows the data candidates split into the bins of m_T and m_{jj} used in the final fit [74].	118
232	5.17	Postfit distributions in the BDT VBF analysis [74].	119
233	5.18	Overlap between cut-based and BDT VBF signal region candidates in the m_{jj} - m_T plane. .	119
234	6.1	Post-fit m_T distribution in the $n_j \leq 1$ regions for the same flavor ($ee/\mu\mu$) final states [74].	122
235	6.2	Post-fit m_T distribution in the $n_j \leq 1$ regions [74].	124
236	6.3	Best fit signal strength $\hat{\mu}$ as a function of hypothesized m_H [74].	125
237	6.4	Local p_0 as a function of m_H [74].	126
238	6.5	Likelihood as a function of $\mu_{\text{VBF}}/\mu_{\text{ggF}}$ [74].	126

256	6.6	Two dimensional likelihood scan as a function of μ_{VBF} and μ_{ggF} [74].	127
257	6.7	Likelihood scan as a function of κ_F and κ_V , the Higgs coupling scale factors [74].	129
258	6.8	Comparison of signal strength measurements in different Higgs decay channels on ATLAS [108].	131
259	7.1	Parton luminosity ratios as a function of resonance mass M_X for 13/8 TeV and 7/8 TeV [109].	134
260	7.2	Summary of HH branching ratios [110].	135
261	7.3	Minimum ΔR between B decay vertices for different RSG masses in a $G_{\text{KK}}^* \rightarrow HH \rightarrow 4b$ sample with $c = 1$	136
262	7.4	Trigger efficiency for events passing all signal region selections as a function of mass in $G_{\text{KK}}^* \rightarrow HH \rightarrow 4b$ samples with $c = 1$ [119]. In the trigger names, “j” refers to a jet or jets. “ht” refers to H_T , the scalar sum of transverse momenta in the event. “bloose” refers to a loose b -tagging requirement applied to the jet. “aor” refers to anti- k_T jets with $R = 1.0$. The numbers at the end of each trigger name are the thresholds on the given quantity in GeV.	138
263	7.5	Comparison of untrimmed and trimmed jet masses for large radius jets in a RSG sample with $m_{G_{\text{KK}}^*} = 1$ TeV. JES (JMS) refers to the standard jet energy (mass) scale calibration for ATLAS [69].	139
264	7.6	Efficiency of finding two b -jets from each Higgs in an RSG event using calorimeter jets with $R = 0.3$ and track jet radii of $R = [0.2, 0.3, 0.4]$ [123].	140
265	7.7	Illustration of the boosted selection requirements on Higgs candidates. Each large-radius calorimeter jet (Higgs candidate) must contain two track jets.	142
266	7.8	Estimated significance as a function of signal mass for RSG $c = 1$ models in the 3 b (a) and 4 b (b) regions for different b -tagging efficiency working points	143
267	7.9	Acceptance \times efficiency as a function of mass for (a) RSG and (b) narrow heavy scalar signal models [126].	144
268	7.10	Efficiency of requiring 3 or 4 b -tagged track jets vs. RSG mass. The efficiency quoted is relative to the previous selection requirements (rather than an absolute efficiency).	145
269	7.11	MV2c20 b -tagging efficiency for each of the four track jets in the boosted 4 b selection as a function of RSG mass for $c = 1$ models.	146
270	7.12	M_J^{sublead} vs. M_J^{lead} in a 2 b -tag data sample. The signal region is defined by the inner black contour ($X_{hh} < 1.6$) and the sideband region is defined by the outer contour ($R_{hh} > 35.8$ GeV). The region between the black contours is the control region. The mass region which is enriched in $t\bar{t}$ background is also shown for illustration [126].	147
271	7.13	An illustration of the data-driven background estimation technique for the boosted analysis	149
272	7.14	Leading large-R jet mass in the 3 b (a) and 4 b (b) sideband regions. The multijet and $t\bar{t}$ backgrounds are estimated using the data-driven methods described above. Because their normalizations are derived in the sideband region, the total background normalization is constrained by default to match the normalization of the data [126].	150

293	7.15	Di-jet invariant mass (M_{2J}) in the 3b (a) and 4b (b) control regions. The multijet and $t\bar{t}$ backgrounds are estimated using the data-driven methods described above [126].	151
294			
295	7.16	Di-jet invariant mass (M_{2J}) in the 3b (a) and 4b (b) signal regions. The multijet and $t\bar{t}$ backgrounds are estimated using the data-driven methods described above. In the 3b region, a graviton signal with $m_{G_{KK}^*} = 1.8$ TeV and $c = 1$ is overlaid, with the cross section multiplied by a factor of 50 so that the signal is visible. In the 4b region, signals with $m_{G_{KK}^*} = 1.0$ TeV and $m_{G_{KK}^*} = 1.5$ TeV are overlaid, both with $c = 1$ and the yields multiplied by factors of 2 and 5 respectively [126].	156
296			
297			
298			
299			
300			
301	8.1	Di-jet invariant mass (M_{2J}) in the resolved signal region. A graviton signal with $m_{G_{KK}^*} = 800$ GeV and $c = 1$ is overlaid. [126].	159
302			
303	8.2	Expected and observed upper limit as a function of mass for G_{KK}^* in the RSG model with (a) $c = 1$ and (b) $c = 2$, as well as (c) H with fixed $\Gamma_H = 1$ GeV, at the 95% confidence level in the CL_s method [126].	162
304			
305			
306	9.1	Combined ATLAS and CMS measurements in Run 1 for (a) Higgs signal strength in gluon fusion and VBF and (b) Higgs couplings normalized to their SM predictions	166
307			
308	9.2	Discovery significance for RSG models at the HL-LHC in three different budget scenarios [133]. Systematic uncertainties on the background prediction (σ_B) of 2.5% and 5.0% are both tested.	167
309			
310			
311	A.1	p_T of the leading track jet in the leading calorimeter jet for different signal masses in RSG $c = 1$ models	169
312			
313	A.2	MV2c2o score for the leading track jet (a) and subleading track jet (b) of the leading calorimeter jet for different signal masses in RSG $c = 1$ models	169
314			
315	A.3	IP3D log-likelihood ratio ($\log(p_b/p_u)$) of the leading track jet in the leading calorimeter jet for different signal masses in RSG $c = 1$ models	170
316			
317	A.4	Mass (a) and number of tracks (b) for the secondary vertices computed with the SV1 algorithm. When no secondary vertex is found, the quantities are assigned to default negative values.	171
318			
319			
320	A.5	Mass (a) and number of tracks (b) for vertices computed with the JetFitter algorithm. When no vertices are found, the quantities are assigned to default negative values.	171
321			
322	A.6	MV2c2o score (a) and SV1 mass (b) for leading track jets with two truth b quarks ($n_{tb,lead} = 2$) compared to those with only one truth b ($n_{tb,lead} = 1$).	172
323			
324	A.7	Track fit χ^2/n_{DOF} (a) and number of pixel detector hits (b) for the leading track of the leading track jet in different mass RSG $c = 1$ samples	173
325			
326	A.8	MV2c2o score (a) and SV1 mass (b) for leading track jets whose leading track jet has at least four pixel hits ($N_{pix} \geq 4$) compared to those which do not ($N_{pix} < 4$).	174
327			

Listing of tables

328

329	1.1	Production cross sections for a 125 GeV Higgs boson at $\sqrt{s} = 8$ TeV with scale and PDF uncertainties [18].	13
330	1.2	Theoretical branching ratios for a 125 GeV Higgs boson, quoted as a percentage of the total width of the Higgs. Uncertainties shown are relative to the branching ratio value [18].	15
331	1.3	Possible channels for Higgs searches. Checkmarks denote the most sensitive production modes for each decay channel [5].	16
332	1.4	Production cross sections for pair production of a 125 GeV Higgs boson at $\sqrt{s} = 14$ TeV with total uncertainty [29]. The uncertainties include QCD scale and PDF variations as well as uncertainties on α_S	17
333	2.1	Evolution of LHC machine conditions [50, 51].	26
334	2.2	Performance requirements for the ATLAS detector [44].	37
335	2.3	Signal efficiencies for WH production with $H \rightarrow b\bar{b}$ and $H \rightarrow WW^* \rightarrow \mu\nu qq$ under different trigger configurations [57].	42
336	3.1	A summary of backgrounds to the $H \rightarrow WW^* \rightarrow \ell\nu\ell\nu$ signal	59
337	4.1	Monte carlo generators used to model signal and background for the Higgs search [1].	73
338	4.2	Normalization factors (ratio of data and MC yields in a control sample) for the Standard Model WW and top backgrounds in the $H \rightarrow WW^* \rightarrow \ell\nu\ell\nu$ analysis [1]. Only statistical uncertainties are shown.	76
339	4.3	Data and expected yields for signal and background in the final $H \rightarrow WW^* \rightarrow \ell\nu\ell\nu$ signal region. Uncertainties shown are both statistical and systematic [1].	77
340	4.4	Summary of the expected and observed significance and measured signal strengths in the combined 7 and 8 TeV datasets for the Higgs discovery analysis [1].	81
341	5.1	Single lepton triggers used for electrons and muons in the $H \rightarrow WW^* \rightarrow \ell\nu\ell\nu$ analysis. A logical “or” of the triggers listed for each lepton type is taken. Units are in GeV, and the i denotes an isolation requirement in the trigger.	88
342	5.2	Di-lepton triggers used for different flavor combinations in the $H \rightarrow WW^* \rightarrow \ell\nu\ell\nu$ analysis. The two thresholds listed refer to leading and sub-leading leptons, respectively. The di-muon trigger only requires a single lepton at level-1.	88

357	5.3	Trigger efficiency for signal events and relative gain of adding a dilepton trigger on top of the single lepton trigger selection. The first lepton is the leading, while the second is the sub-leading. Efficiencies shown here are for the ggF signal in the $n_j = 0$ category but are comparable for the VBF signal.	88
358			
359			
360	5.4	Monte Carlo samples used to model the signal and background processes [74]. The ta- ble lists the cross section for each process, taking into account the branching ratio for the process producing two leptons.	90
361			
362			
363	5.5	p_T dependent isolation requirements for muons. Muons are required to have their calorime- ter based or track based cone sums be less than this fraction of their p_T	92
364			
365			
366	5.6	p_T dependent requirements for electrons. Electrons are required to have their calorimeter based or track based cone sums be less than this fraction of their E_T	92
367			
368	5.7	Summary of event selection for the $n_j \geq 2$ VBF analysis in the 8 TeV cut-based analy- sis [74].	99
369			
370	5.8	Background composition after each requirement in the $n_j \geq 2$ VBF analysis in the 8 TeV cut-based analysis [74].	100
371			
372	5.9	Top normalization factors computed at each stage of the cut-based selection. Uncertainties are statistical only.	104
373			
374	5.10	Top normalization factors computed for each bin of O_{BDT} . Uncertainties are statistical only.	104
375			
376	5.11	$Z/\gamma^* \rightarrow \tau\tau$ correction factors for the VBF cut-based analysis. Uncertainties are statistical only.	107
377			
378	5.12	$Z/\gamma^* \rightarrow \ell\ell$ normalization factors for cut-based and BDT analyses. Uncertainties are statistical only.	108
379			
380	5.13	Systematic uncertainties for various processes in the cut-based VBF analysis, given in units of % change in yield. Values are given for the low m_{jj} signal region.	113
381			
382	5.14	Composition of the post-fit uncertainties (in %) on the total signal (N_{sig}), total back- ground (N_{bkg}), and individual background yields in the VBF analysis [74].	116
383			
384	5.15	Event selection for the VBF BDT analysis. The event yields in (a) are shown after the pre- selection and the additional requirements applied before the BDT classification (see text). The event yields in (b) are given in bins in O_{BDT} after the classification [74].	117
385			
386			
387	6.1	Post-fit yields in ggF dedicated signal regions for the $ee/\mu\mu$ final states [74].	121
388	6.2	All signal regions definitions input into final statistical fit [74].	123
389	6.3	Post-fit yields in the both ggF and VBF dedicated signal regions with all lepton flavor final states combined [74].	123
390			
391	7.1	Summary of requirements on objects used in the $X \rightarrow HH \rightarrow b\bar{b}b\bar{b}$ search	141

392	7.2 Effect of boosted selection on data, RSG signal models, $t\bar{t}$, and $Z+jets$. The numbers from simulation are normalized with the MC generator cross section and do not take into account the data driven estimates described in section 7.6 [127].	146
393		
394		
395	7.3 Mass region definitions used for background estimation.	148
396		
397	7.4 Parameters derived for exponential fit to background M_{2J} shape in the $3b$ and $4b$ signal regions [127].	150
398		
399	7.5 The number of events in data and predicted background events in the boosted 3-tag and 4-tag sideband and control regions [126]. The uncertainties shown are statistical only.	151
400		
401	7.6 Summary of systematic uncertainties in the total background and signal event yields (ex- pressed in %) in the boosted 3-tag and 4-tag signal regions. Systematic uncertainties on the signal normalization are shown for models with $m_{G_{KK}^*} = 1.5$ TeV and both $c = 1$ and $c = 2$ as well as a narrow width heavy scalar.	153
402		
403		
404	7.7 Alternate fit functions used to model the M_{2J} distribution in the QCD multijet back- ground. In the equations, $x = M_{2J}/\sqrt{s}$	154
405		
406	7.8 Observed yields in the 3-tag and 4-tag signal regions for the boosted analysis compared to the predicted number of background events Errors correspond to the total uncertainties in the predicted event yields. The yields for a graviton with $m_{G_{KK}^*} = 1$ TeV and $c = 1$ are also shown [126].	155
407		
408		
409		
410	8.1 Observed yields in the resolved selection 4-tag signal region compared to the predicted number of background events Errors correspond to the total uncertainties in the pre- dicted event yields. The yields for a graviton with $m_{G_{KK}^*} = 800$ GeV and $c = 1$ are also shown [126].	158
411		
412		
413		

Acknowledgments

416 I have been a member of the Harvard ATLAS group for many years now, first as an undergraduate and
 417 then as a graduate student. As a result, I have had the privilege of interacting with many amazing people
 418 there over the years and have accumulated a large list of folks to thank.

419 First and foremost, I must thank the two people who have effectively been my academic parents since I
 420 started in the Harvard group: João Guimarães da Costa and Melissa Franklin. Melissa Franklin and João
 421 Guimarães da Costa. They have both been so important to both my academic and personal development
 422 that I can't even put one before the other. João has been an excellent PhD advisor, showing me how to
 423 look at the big picture and helping me navigate the sometimes complicated politics of ATLAS. He got me
 424 started on my first projects with ATLAS as a young college sophomore before there was even beam in the
 425 LHC (go cosmic ray muons!). He has also been a constant source of advice and support, even when we
 426 have been on different continents. Melissa gave me my start in HEP as a summer student on CDF and
 427 has been an unbelievable mentor throughout my time at Harvard. I still remember our weekly chalkboard
 428 particle physics lessons after that first summer. She also graciously took me on as a co-advisee after João
 429 moved on to his new position at IHEP. I am incredibly lucky to have had both of them as advisors.

430 Another mentor who was essential to my development as a graduate student is Paolo Giromini. His un-
 431 canny knowledge and intuition about detectors is unmatched and I am very grateful to have had the chance
 432 to work with him on the micromegas for the ATLAS New Small Wheel upgrade project. I owe essentially
 433 all my practical knowledge about detectors (and building things in general) to him. I also appreciated his
 434 unique sense of humor which made sometimes difficult tasks much easier to get through.

435 I am grateful to John Huth and Masahiro Morii for their helpful advice as the other professors in the
 436 Harvard ATLAS group as well. I especially thank John for helping me get started on the micromegas
 437 trigger project and being a great professor to TF particle physics for. Additionally I thank Howard Georgi
 438 for serving as my third committee member and offering me feedback throughout my graduate career.

439 I also owe enormous thanks to Hugh Skottowe, the postdoc that I worked most closely with in my early
440 years as a graduate student. He was always able to help me through complicated tasks in everything from
441 writing code to understanding difficult physics concepts. I particularly enjoyed walking down to his office
442 in Palfrey at random times and talking through whatever problem I was tackling on that day.

443 Alex Tuna, the second postdoc that I worked closely with at Harvard, deserves great thanks as well. He
444 helped me push through to the end of my graduate career and offered great advice along the way.

445 Being at Harvard, I have seen an incredible array of graduate students graduate before me: Ben Smith,
446 Verena Martinez Outschoorn, Srivas Prasad, Michael Kagan, Giovanni Zevi Della Porta, Laura Jeanty,
447 Kevin Mercurio, William Spearman, and Andy Yen. I want to thank them all for showing me what a good
448 physicist looks like and for patiently answering my questions and offering insightful advice about physics
449 and life.

450 Getting through graduate school would not have been possible without the support and friendship of
451 the other students in our group. Thanks to Emma Tolley for geeking out with me about cool comput-
452 ing stuff, going to taste delicious beers with me, and helping start the Palfrey tradition of Taco Tuesdays.
453 Thanks to Brian Clark for being a great friend and housing companion both in Kirkland House and in our
454 tiny summer apartment in Geneva (and thanks to his partner Allison Goff for the same reasons!). Thanks
455 to Siyuan Sun for giving me my first aikido lesson and always being there for great conversations, big and
456 small. Tony (Baojia) Tong deserves special recognition for working with me on the $4b$ analysis and putting
457 up with my sometimes strange requests (and giving me rides to the Val Thoiry Migros so I wouldn't have
458 to pay exorbitant Geneva grocery prices!). Stephen Chan is probably the only student in the group who
459 both understands my references to the Sopranos and makes some of his own. To the younger graduate
460 students - Karri Di Petrillo, Jennifer Roloff, Julia Gonski, and Ann Wang - I want to say thank you for
461 making the group a fun and lively place to be and giving all of us energy that the older graduate students
462 like myself can sometimes lack.

463 I'd like to thank Annie Wei and Gray Putnam, the two undergraduates I have worked with as a graduate
464 student. Their unbelievable intuition and quickness in picking up difficult particle physics concepts is
465 inspiring.

466 I would also like to thank all of the postdocs that I have interacted with in my time in the Harvard group:
467 Kevin Black, Alberto Belloni (who would always ask me “Do you have it?”...I can now say that I do!),
468 Shulamit Moed, Corrinne Mills, Geraldine Conti, David Lopez Mateos, Chris Rogan, Valerio Ippolito,
469 and Stefano Zambito.

470 There are many people on ATLAS who have helped me get to this point as well. In the *WW* group, I
471 have to thank Jonathan Long, Joana Machado Miguens, Ben Cerio, Philip Chang, Bonnie Chow, Richard
472 Polifka, Heberth Torres, Tae Min Hong, and Jennifer Hsu for being wonderful colleagues and making the
473 entire analysis run smoothly. In the *4b* group, I have to thank Qi Zeng, Tony Tong, Alex Tuna, Michael
474 Kagan, Max Bellomo, John Alison, and Patrick Bryant.

475 Kirkland House was my home for the last three years of graduate school and was an wonderful envi-
476 ronment and support system. I want to thank my fellow tutors, especially Brian Clark and Allison Goff
477 (again), Zach Abel, Kelly Bodwin, Alex Lupsasca, John and Pam Park, Luke and Erin Walczewski, and
478 Philip Gant for their friendship and support. I also want to thank Kate Drizos Cavell, Bob Butler, and the
479 Faculty Deans Tom and Verena Conley.

480 There are still a few friends that haven’t been covered yet and deserve great thanks. Jake Connors and
481 Meredith MacGregor have been absolutely wonderful friends and I thank them in particular for the many
482 home-cooked meals and great conversations we’ve had in their apartment. Nihar Shah has been my friend
483 and confidant since we were both wee freshmen in Harvard Yard. Gareth Kafka, though he sits on the
484 “neutrino” side of Palfrey House, has made days there more fun and has also been an enthusiastic partici-
485 pant in the Palfrey Taco Tuesdays.

486 Being at Harvard necessarily means having to navigate through bureaucracy at some point or another.
487 I thank Lisa Cacciabuado, Carol Davis, Jacob Barandes, Korin Watras, and Angela Allen for always having
488 open doors and being the most kind, helpful people in the Physics department.

489 I thank Venky Narayananuriti for putting on a great SPU course that I was proud to be a part of and
490 TF for. I’d also like to thank Jim Waldo for offering me much advice about working in Computer Science
491 and giving me a fun data project to be a part of in my free time.

492 I grew up in a very tight knit Serbian community on the south side of Chicago which helped make me

493 the person I am today. I would like to thank all of the people at St. Simeon Mirotochivi Serbian Orthodox
494 Church who have always been sources of enthusiasm and support in my life.

495 I would not be here without the unconditional love and constant support and encouragement of my
496 family. To my pokojni Deda Branko and Miloje, my pokojni Baba Milka, and my Baba Desa, I want to
497 say thank you for instilling in me at an early age the love of curiosity and storytelling that I have carried
498 throughout my life. To my sister Angelina, I want to say thank you for always loving me and being my
499 partner in crime throughout our childhoods. To my parents, Miroljub and Nada, Tata and Mama, I really
500 cannot express how grateful I am to you and how much I owe you. As I look back now I see how I am
501 a combination of both of your best qualities. Every day I am in situations where I better understand the
502 lessons you taught me and the sacrifices you made to make sure I got the best possible education. I love
503 you all.

504 Finally, I have to thank my soul mate, the one person in my life who understands me more than anyone
505 else, my fiancée Kelly Brock. You are my sounding board, my support system, my cheerleader (figuratively
506 and literally!), my best friend, my role model, and my everything. I would not have gotten through grad-
507 uate school without you and my life would not be the same without you. I cannot wait to start our new
508 lives together as the married doctors, tackling whatever comes our way with the same zeal with which we
509 tackled graduate school. I love you with all my heart and soul.

0

510

511

Introduction

512 The Higgs boson is often described as one of the cornerstones of particle physics. When the Standard
513 Model was first developed as a theory to describe the fundamental particles and forces of nature, physicists
514 were faced with a dilemma. The electroweak theory beautifully characterized both electromagnetism and
515 the weak force with a single underlying framework. However, the mass of the weak W and Z bosons
516 was puzzling given the fact that their electromagnetic counterpart, the photon, is massless. The Higgs
517 mechanism was developed as the leading theory for the origin of this electroweak symmetry breaking. It
518 predicted the existence of an additional spin-0 boson in the Standard Model, the Higgs boson. Generations
519 of collider experiments searched for this elusive particle. This dissertation presents research work on the
520 Higgs boson from its discovery to its use as a tool in the search for physics beyond the Standard Model
521 with the ATLAS detector at the Large Hadron Collider (LHC).

522 One of the first priorities for the LHC when it began colliding proton beams in 2010 was the search
523 for the Higgs boson. This search was initially tackled in the $H \rightarrow WW^* \rightarrow \ell\nu\ell\nu$ channel, followed by

524 the $H \rightarrow \gamma\gamma$ and $H \rightarrow ZZ^* \rightarrow 4\ell$ channels. Each channel has its own merits, but the WW^* mode is
525 particularly suited to searching over a wide range of masses. The $H \rightarrow WW^*$ branching ratio is large and it
526 is the primary decay channel above the $2m_W$ mass threshold. Despite the fact that the full Higgs invariant
527 mass cannot be reconstructed in the $H \rightarrow WW^* \rightarrow \ell\nu\ell\nu$ channel, its signal to background ratio makes
528 it ideal for measurement of Higgs properties such as the production cross section and couplings.

529 In 2012, the ATLAS and CMS experiments announced the discovery of a new particle consistent with
530 the Higgs boson [1, 2]. In ATLAS, this discovery was made with 4.8 fb^{-1} collected at $\sqrt{s} = 7 \text{ TeV}$
531 and 5.8 fb^{-1} at $\sqrt{s} = 8 \text{ TeV}$. This dissertation first presents the search for gluon fusion production
532 of the Higgs in the $H \rightarrow WW^* \rightarrow \ell\nu\ell\nu$ channel, which played an important role in this discovery.
533 Selection requirements which were optimized to maximize the discovery significance in this channel, as
534 well as background estimation procedures, are discussed.

535 After its discovery, interest in the Higgs shifted to focus on the measurement of its properties. As a result,
536 extensions of the initial discovery analysis in larger datasets had two main goals. Improvement of signal
537 to background ratio was important to allow for precision measurements. Also, searches for production
538 modes of the Higgs with lower cross sections than gluon fusion were a priority. The first such extension
539 presented in this dissertation is a tailored selection for $\ell\nu\ell\nu$ final states with same flavor leptons. Novel
540 variables for the reduction of the $Z+\text{jets}$ background that could remain robust under increasing LHC
541 instantaneous luminosities are shown. The second post-discovery result shown is the first evidence of
542 Vector Boson Fusion (VBF) production of the Higgs boson.

543 VBF production of the Higgs boson is particularly interesting in the $H \rightarrow WW^* \rightarrow \ell\nu\ell\nu$ final state.
544 In this combination of production and decay modes, the Higgs boson couples exclusively to vector bosons,
545 allowing for precise measurement of the Higgs- W coupling constant. However, it is challenging to observe
546 VBF Higgs production because its cross section at the LHC is an order of magnitude lower than gluon
547 fusion production. The large $H \rightarrow WW^*$ branching ratio thus presents another advantage over other
548 final states. Additionally, VBF production of the Higgs boson creates two forward jets in addition to the
549 Higgs, and these jets can be used to isolate VBF Higgs events from other production modes. The VBF
550 $H \rightarrow WW^* \rightarrow \ell\nu\ell\nu$ analysis first created a selection requirement based signal region using variables

constructed specifically for the VBF Higgs production topology. This “cut-based” analysis is presented in detail in this dissertation. These VBF topology variables, once validated in the cut-based analysis, were then input into a multivariate boosted decision tree discriminant to achieve the first evidence of VBF Higgs production with the full 20.3 fb^{-1} of $\sqrt{s} = 8 \text{ TeV}$ data in ATLAS. Additionally, combining these results with the dedicated gluon fusion Higgs production analysis allowed for precise measurement of the Higgs couplings.

After a two year shutdown, the LHC restarted in 2015 with a center of mass energy of $\sqrt{s} = 13 \text{ TeV}$. This increase improved the LHC’s ability to probe for physics beyond the Standard Model, and the Higgs sector remained one of the largest regions of unprobed phase space where such new physics could be discovered. Production of high mass resonances benefit most from the center of mass energy increase. In particular, the cross section for a generic gluon-initiated 2 TeV resonance increased tenfold with the increase from 8 to 13 TeV . Therefore, a natural next step in studies of the Higgs was a search for a new heavy resonance which decays into a pair of Higgs bosons. The final result shown in this dissertation is a search for resonant di-Higgs production in the $X \rightarrow HH \rightarrow b\bar{b}b\bar{b}$ final state with 3.2 fb^{-1} recorded by ATLAS at $\sqrt{s} = 13 \text{ TeV}$. This search has the unique advantage that it can both probe new physics and gain further understanding of the Higgs potential through constraints on SM pair production of the Higgs. It also extends the previous ATLAS results at $\sqrt{s} = 8 \text{ TeV}$ and probes higher mass resonances that were not previously accessible. Additionally, it is an informative precursor to di-Higgs analyses at the future High Luminosity LHC (HL-LHC), where a projected dataset of 3000 fb^{-1} at $\sqrt{s} = 14 \text{ TeV}$ will begin to become sensitive to the SM Higgs self coupling.

As mentioned above, this dissertation begins by discussing the discovery of the Higgs and the role of the $H \rightarrow WW^* \rightarrow \ell\nu\ell\nu$ channel. It then presents the first evidence for the VBF production mode using the $H \rightarrow WW^* \rightarrow \ell\nu\ell\nu$ channel with the full ATLAS Run 1 dataset. It also shows the final combined Run 1 measurements of gluon fusion Higgs production from this channel. Finally, it presents a search for Higgs pair production in the $HH \rightarrow b\bar{b}b\bar{b}$ channel. It is organized into four parts.

Part 1 presents the theoretical and experimental background required for the subsequent parts. Chapter 1 gives an overview of Higgs physics, particularly single and double Higgs production in the Standard

578 Model and beyond. Chapter 2 presents details regarding the Large Hadron Collider and the ATLAS exper-
579 iment. The evolution of machine conditions, descriptions of the ATLAS sub-detectors, and an overview of
580 object reconstruction in ATLAS are all shown. A brief interlude on the ATLAS Muon New Small Wheel
581 upgrade is also given, as this upgrade has been a focus of my graduate work and will have an important
582 impact on ATLAS' ability to study the Higgs at the High Luminosity LHC.

583 Part 2 discusses the observation and measurement of the Higgs in the $H \rightarrow WW^* \rightarrow \ell\nu\ell\nu$ channel
584 in the ATLAS Run 1 dataset at $\sqrt{s} = 7$ and 8 TeV. Because I worked in this channel from before the
585 discovery through to the final analysis of the Run 1 dataset, Part 2 is organized in such a way to allow
586 easy presentation of multiple analyses on different subsets of the full Run 1 dataset. Chapter 3 presents
587 a general overview of the $H \rightarrow WW^*$ analysis strategy and defines many of the variables and common
588 elements used in the rest of Part 2. Chapter 4 presents the discovery and subsequent measurements of
589 the Higgs boson, focusing on the role of the WW^* channel in this discovery. Chapter 5 presents the
590 first evidence for the VBF production mode of the Higgs, a result from the WW^* channel in the full
591 Run 1 ATLAS dataset. In this chapter, the focus is mainly on the cut-based VBF analysis. The cut-based
592 analysis was an important first step to the final VBF result which used a boosted decision tree. Where
593 appropriate, connections between the cut-based and BDT analyses are shown and their compatibility is
594 discussed. Finally, the VBF analysis was an important input into the combined Run 1 $H \rightarrow WW^* \rightarrow$
595 $\ell\nu\ell\nu$ result, which used both the gluon fusion and VBF channels in a combined fit to infer properties of
596 the Higgs, including its couplings to the gauge bosons and its production cross section. This is the topic
597 of Chapter 6.

598 Part 3 presents a search for Higgs pair production in the $HH \rightarrow b\bar{b}b\bar{b}$ channel. Chapter 7 presents
599 an overview of this search in the boosted regime, where the Higgs pairs are the result of the decay of a
600 heavy resonance. Chapter 8 shows the combined results between the boosted regime and the resolved
601 regime, which is sensitive to lower mass resonances and non-resonant Higgs pair production. Finally, Part
602 4 presents a conclusion and brief outlook of future Higgs physics with ATLAS.

603

Part I

604

Theoretical and Experimental Background

In modern physics, there is no such thing as “nothing.”

Richard Morris

1

605

606

The Physics of the Higgs Boson

607 This chapter presents an overview of the Standard Model of Particle Physics and in particular the physics
608 of the Higgs boson. First, a brief overview of the Standard Model is presented. Then, a description of
609 the Higgs mechanism of electroweak symmetry breaking is given. Next, the physics of single Higgs boson
610 production and decay is described. The Standard Model also allows for production of two Higgs bosons
611 and this is detailed as well. Finally, di-Higgs production in two beyond the Standard Model (BSM) theories
612 - Randall-Sundrum gravitons (RSG) and Two Higgs Doublet Models (2HDM) - is shown.

613 **I.I THE STANDARD MODEL OF PARTICLE PHYSICS**

614 The Standard Model (SM) of Particle Physics is a quantum field theory describing the fundamental parti-
615 cles of nature and the forces that govern their interactions. Several comprehensive pedagogical treatments
616 of the SM already exist in the literature [3–8] and this section will not rehash those. Rather, this section
617 presents a brief overview of the SM particles and forces in order to define them for subsequent discussions.

618 The Standard Model consists of two primary categories of fundamental particles: fermions (spin 1/2
 619 particles) and bosons (integer spin particles). The SM also describes three forces: electromagnetism, the
 620 weak nuclear force, and the strong nuclear force. Gravity is not included in the theory and is largely irrel-
 621 evant at the scales currently probed by collider experiments. Within the fermions, there are both quarks
 622 (which interact via all three forces) and leptons. The charged leptons interact via electromagnetic and weak
 623 interactions, while neutrinos (neutral leptons) interact only via the weak force. Within the bosons, there
 624 are the W^\pm and Z bosons (the mediators of the weak force), the gluon (g , the mediator of the strong
 625 force), and the photon (γ , the mediator of the electromagnetic force). Finally, there is the Higgs boson,
 626 a fundamental spin zero particle resulting from the Higgs mechanism of electroweak symmetry breaking.

627 Figure 1.1 summarizes the fermions and bosons of the SM.

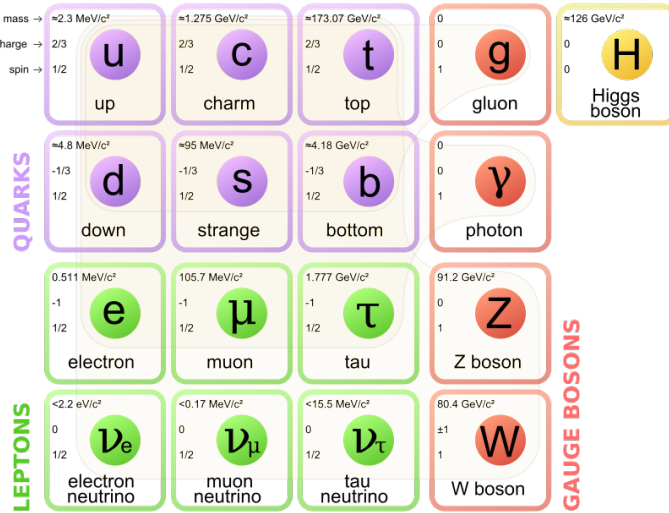


Figure 1.1: The particles of the Standard Model and their properties [6].

628 The Standard Model coalesced into a unified theoretical framework in the 1960s through the work
 629 of Glashow, Weinberg, Salam, and others on the theory of electroweak interactions [9–12]. This theory
 630 characterized both the electromagnetic and weak interactions as unified under a single gauge symmetry
 631 group, namely $SU(2) \times U(1)$. At low enough energy scales (on the order of the W and Z masses), the
 632 electroweak symmetry is broken, as evidenced by the fact that the weak bosons have mass while the photon
 633 does not. The discovery of the Higgs boson in 2012 confirmed the Higgs mechanism as the most likely
 634 candidate for this electroweak symmetry breaking [1, 2]. The complete SM consists of this electroweak

635 theory combined with the theory of quantum chromodynamics (which models the strong sector as a non-
 636 Abelian $SU(3)$ gauge group)¹.

637 1.2 ELECTROWEAK SYMMETRY BREAKING AND THE HIGGS

638 In the Standard Model Lagrangian, it is difficult to include mass terms for the W and Z bosons without
 639 breaking the fundamental gauge symmetry of the Lagrangian. A traditional mass term does not preserve
 640 the $SU(2) \times U(1)$ symmetry. Additionally, scattering of massive W and Z bosons violate unitarity and
 641 these diagrams diverge at high energy scales. In the 1960s, Higgs, Brout, Englert, Guralnik, Kibble, and
 642 Hagen developed a mechanism for spontaneous symmetry breaking via the addition of a complex scalar
 643 doublet to the SM. Three of the four real degrees of freedom of this complex field would go to the lon-
 644 gitudinal modes of the W^\pm and Z , thus allowing them to have mass [14–17]. The remaining degree of
 645 freedom would manifest as an additional scalar, known now as the Higgs boson.

646 The mechanism works by introducing a Lagrangian for the newly introduced field that still respects the
 647 symmetry of the Standard Model inherently, but with a minimum at a non-zero vacuum expectation value
 648 for the field. In this minimum of the potential, the electroweak symmetry is broken. Specifically, consider
 649 a complex scalar doublet Φ with four degrees of freedom, as shown in equation 1.1.

$$\Phi = \begin{pmatrix} \phi^+ \\ \phi^0 \end{pmatrix} = \frac{1}{\sqrt{2}} \begin{pmatrix} \phi_1^+ + i\phi_2^+ \\ \phi_1^0 + i\phi_2^0 \end{pmatrix} \quad (1.1)$$

650 The simplest potential of a self-interacting Higgs that still respects the SM symmetry is given in equa-
 651 tion 1.2.

$$V(\Phi) = \mu^2 \Phi^\dagger \Phi + \lambda (\Phi^\dagger \Phi)^2 \quad (1.2)$$

652 If the μ^2 term of this potential is positive, then the potential has a minimum at $\Phi = 0$ and the electroweak

¹For a pedagogical treatment of the physics of quantum chromodynamics, see reference [13].

653 symmetry is preserved. However, if instead $\mu^2 < 0$, then the minimum is at a finite value of Φ , namely

$$\Phi_{\min} = \frac{1}{\sqrt{2}} \begin{pmatrix} 0 \\ v \end{pmatrix} \quad (1.3)$$

654 where $v = \sqrt{\mu^2/\lambda}$. Because this is the location of the minimum, it corresponds to the vacuum expecta-
655 tion value for the field ($\langle \Phi \rangle = \Phi_{\min}$). The excitations of the Higgs can then be parameterized as

$$\Phi = \frac{1}{\sqrt{2}} \begin{pmatrix} 0 \\ v + H \end{pmatrix} \quad (1.4)$$

656 The full scalar Lagrangian, including the kinetic term, is then given as

$$\mathcal{L}_s = (D^\mu \Phi)^\dagger (D_\mu \Phi) - V(\Phi) \quad (1.5)$$

657 where the covariant derivative is defined as

$$D_\mu = \partial_\mu + \frac{ig}{2} \tau^a W_\mu^a + ig' Y B_\mu \quad (1.6)$$

658 and W^1, W^2, W^3 and B are the $SU(2)$ and $U(1)$ gauge fields of the electroweak theory, respectively. g
659 and g' are the corresponding coupling constants. The Pauli matrices are represented with τ . With the
660 scalar Lagrangian in place, the physical gauge fields can then be written as

$$W_\mu^\pm = \frac{1}{\sqrt{2}} (W_\mu^1 \mp i W_\mu^2) \quad (1.7)$$

661

$$Z_\mu = \frac{-g' B_\mu + g W_\mu^3}{\sqrt{g^2 + g'^2}} \quad (1.8)$$

662

$$A_\mu = \frac{g B_\mu + g' W_\mu^3}{\sqrt{g^2 + g'^2}} \quad (1.9)$$

663 Equation 1.7 corresponds to the charged W^+ and W^- bosons, equation 1.8 corresponds to the neutral Z
 664 boson, and equation 1.9 corresponds to the neutral photon. The masses of the particles also arise from the
 665 Lagrangian. The photon has zero mass, while the masses of the W and Z bosons are given in equation 1.10.

666

$$M_W^2 = \frac{1}{4}g^2 v^2 \quad (1.10)$$

$$M_Z^2 = \frac{1}{4}(g^2 + g'^2)v^2$$

667 The fermion masses also arise through a coupling with the Higgs via the Yukawa interaction (for a detailed
 668 description, see [8]). In this case the coupling between the Higgs and the fermions goes as

$$g_{h f \bar{f}} = \frac{m_f}{v} \quad (1.11)$$

669 The full Lagrangian of Higgs interactions can be written as

$$\mathcal{L}_{\text{Higgs}} = -g_{h f \bar{f}} \bar{f} f h + \frac{g_{hhh}}{6} h^3 + \frac{g_{hhhh}}{24} h^4 + \delta_V V_\mu V^\mu \left(g_{hVV} H + \frac{g_{hhVV}}{2} h^2 \right) \quad (1.12)$$

670 with

$$g_{hVV} = \frac{2m_V^2}{v} \quad g_{hhVV} = \frac{2m_V^2}{v^2}$$

$$g_{hhh} = \frac{3m_h^2}{v} \quad g_{hhHH} = \frac{3m_h^2}{v^2} \quad (1.13)$$

671 The last term of the Lagrangian appears twice, once for W bosons and once for Z bosons. V refers to
 672 the W^\pm and Z , and $\delta_W = 1$ while $\delta_Z = 1/2$. Phenomenologically, there are a few features of this
 673 Lagrangian that are useful to note. First, note that the Higgs mass is a free parameter of the theory that
 674 must be determined experimentally. Second, note that the coupling of the Higgs to the vector bosons and
 675 fermions scales as a function of the masses of these particles, a fact that is important when considering
 676 both the production and decays of the Higgs. Finally, note the presence of the cubic and quartic Higgs self
 677 interaction terms, which can lead to final states with multiple Higgs bosons produced.

678 1.3 HIGGS BOSON PRODUCTION AND DECAY

679 This section discusses the properties of Higgs production and decay mechanisms. The details presented
680 here will focus on the properties of a 125 GeV Higgs boson, as this is the mass closest to that of the newly
681 discovered Higgs.

682 1.3.1 HIGGS PRODUCTION

683 The Higgs is produced by four main production modes at the Large Hadron Collider - gluon-gluon fusion
684 (ggF), vector boson fusion (VBF), associated production with a W or Z boson, or associated production
685 with top quarks ($t\bar{t}H$). Figure 1.2 shows the Feynman diagrams for these four modes.

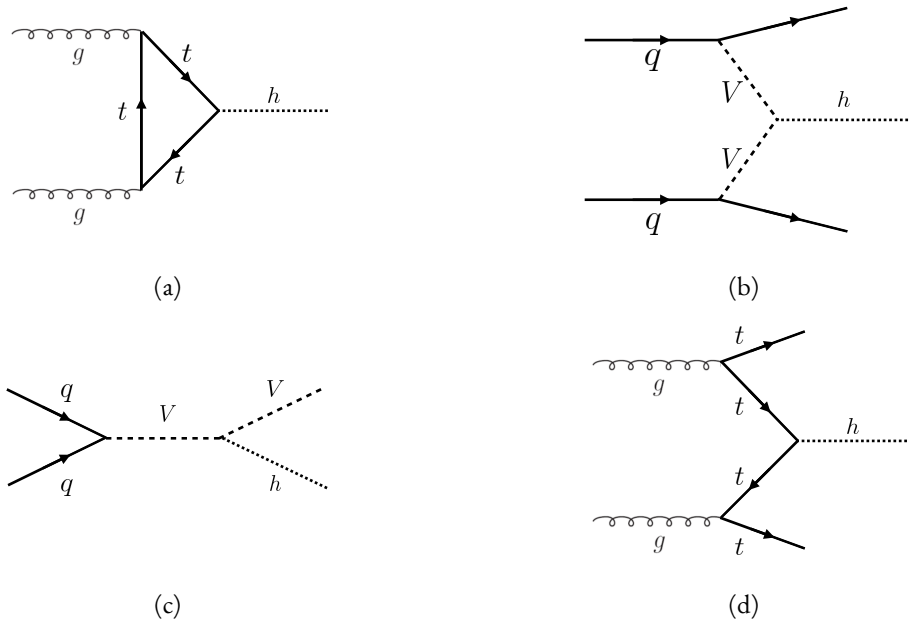


Figure 1.2: The four most common Higgs boson production modes at the LHC: (a) gluon-gluon fusion, (b) vector boson fusion, (c) $W/Z + H$ production, (d) $t\bar{t}H$ production

686 In gluon-gluon fusion, gluons from the incoming protons fuse via a top-quark loop to produce a Higgs.
687 The top quark is the dominant contribution in the loop due to its heavy mass and the fact that the Higgs-
688 fermion coupling constant scales with fermion mass. In vector boson fusion, the incoming quarks each
689 radiate a W or Z boson which fuse to produce the Higgs. This production mode results in a final state
690 with a Higgs boson and two additional jets which tend to be forward because they carry the longitudinal

691 momentum of the incoming partons. The Higgs can also be produced in association with a W or Z boson.
 692 The W/Z is produced normally and then radiates a Higgs². Finally, the Higgs can be produced in associa-
 693 tion with two top quarks. Each incoming gluon splits into a $t\bar{t}$ pair, and one of the top pairs combines to
 694 create a Higgs. Figure 1.3 shows the production cross section for a 125 GeV Higgs boson in each of these
 modes at a pp collider as a function of center of mass energy. In figure 1.3, note that gluon fusion has the

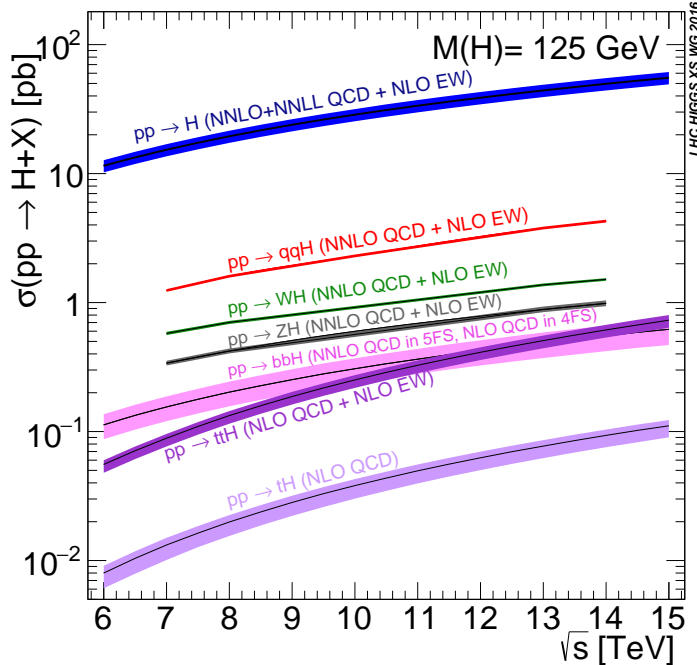


Figure 1.3: Higgs production cross sections as a function of center of mass energy (\sqrt{s}) at a pp collider [18].

695
 696 largest cross section, while VBF is the second largest at approximately a factor of 10 smaller. The figure also
 697 includes the less commonly studied $b\bar{b}H$ and tH modes. While the $b\bar{b}H$ mode has a larger cross section
 698 than $t\bar{t}H$, it also has larger backgrounds and is thus less sensitive. The tH mode is not as sensitive as $t\bar{t}H$
 699 due to its lower cross section. At $\sqrt{s} = 8$ TeV, ggF production of a 125 GeV Higgs has a cross section
 700 of $19.47^{+1.54}_{-1.67}$ pb, while VBF has a cross section of $1.601^{+0.036}_{-0.035}$ pb [18]. Both the gluon fusion and vector
 701 boson fusion cross sections have been computed to next-to-next-to-leading order (NNLO) in the QCD
 702 couplings and next-to-leading order in the electroweak couplings [19–26]. The gluon fusion cross section
 703 also includes next-to-next-to-leading logarithm (NNLL) resummation [27]. The cross sections of all of

²This mode is also sometimes known as “Higgs-strahlung”.

704 the main Higgs production modes at this center of mass energy, as well as their uncertainties from varying
 705 the QCD renormalization and factorization scales and PDFs, are summarized in table 1.1 for a 125 GeV
 706 Higgs. The relative uncertainty of the gluon fusion mode is larger than the relative uncertainty in the
 707 vector boson fusion mode due to the fact that gluon fusion production happens through a loop.

Production mode	σ (pb)	QCD scale uncert. (%)	PDF + α_s uncert. (%)
Gluon fusion	19.47	+7.3 / - 8.0	3.1
Vector boson fusion	1.601	+0.3 / - 0.2	2.2
WH	0.7026	+0.6 / - 0.9	2.0
ZH	0.4208	+2.9 / - 2.4	1.7
$b\bar{b}H$	0.2021	+20.7 / - 22.3	
$t\bar{t}H$	0.1330	+4.1 / - 9.2	4.3
tH (t -channel)	0.01869	+7.3 / - 16.5	4.6
tH (s -channel)	1.214×10^{-3}	+2.8 / - 2.4	2.8

Table 1.1: Production cross sections for a 125 GeV Higgs boson at $\sqrt{s} = 8$ TeV with scale and PDF uncertainties [18].

708 1.3.2 HIGGS BRANCHING RATIOS

709 The fact that the Higgs couples more strongly to more massive particles is crucial for understanding its
 710 branching ratios. The width for Higgs decays to fermions is given by equation 1.14 [5].

$$\Gamma(H \rightarrow f\bar{f}) = \frac{N_c \sqrt{2} G_F m_f^2 m_H}{8\pi} \quad (1.14)$$

711 In this case, N_c is the number of colors, G_F is the Fermi constant, m_f is the mass of the fermion, and
 712 m_H is the mass of the Higgs. Note that the width scales with the square of the fermion mass. (This also
 713 assumes that the Higgs mass is large enough to decay with both the fermions on shell.)

714 The decay width to WW , in the case where both W bosons are produced on shell ($m_H \geq 2m_W$), is
 715 given in equation 1.15 [5].

$$\Gamma(H \rightarrow W^+ W^-) = \frac{\sqrt{2} G_F M_W^2 m_H}{16\pi} \frac{\sqrt{1-x_W}}{x_W} (3x_W^2 - 4x_W + 4) \quad (1.15)$$

⁷¹⁶ where m_W is the mass of the W and $x_W = 4M_W^2/m_H^2$. To get the branching ratio to ZZ (in the regime
⁷¹⁷ where $m_H \geq 2m_Z$), the equation is divided by 2 to account for identical particles in the final state, and
⁷¹⁸ x_W is replaced with $x_Z = 4M_Z^2/m_H^2$. This is shown in equation 1.16 [5].

$$\Gamma(H \rightarrow ZZ) = \frac{\sqrt{2}G_F M_Z^2 m_H}{32\pi} \frac{\sqrt{1-x_Z}}{x_Z} (3x_Z^2 - 4x_Z + 4) \quad (1.16)$$

⁷¹⁹ The more general formula for Higgs branching into WW or ZZ , taking into account the case where one
⁷²⁰ or both vector bosons is off-shell, is shown in equation 1.17 [28].

$$\Gamma(H \rightarrow V^*V^*) = \frac{1}{\pi^2} \int_0^{M_H^2} \frac{dq_1^2 M_V \Gamma_V}{(q_1^2 - M_V^2)^2 + M_V^2 \Gamma_V^2} \int_0^{(M_H - q_1)^2} \frac{dq_2^2 M_V \Gamma_V}{(q_2^2 - M_V^2)^2 + M_V^2 \Gamma_V^2} \Gamma_0 \quad (1.17)$$

⁷²¹ Here, q_1^2 and q_2^2 are the invariant masses of the virtual gauge bosons, M_V is the W or Z mass, and Γ_V is
⁷²² the W or Z width. Γ_0 is the squared matrix element, which is given in equation 1.18 [28].

$$\Gamma_0 = \frac{G_F M_H^3}{8\sqrt{2}\pi} \delta_V \sqrt{\lambda(q_1^2, q_2^2, M_H^2)} \left[\lambda(q_1^2, q_2^2, M_H^2) + \frac{12q_1^2 q_2^2}{M_H^4} \right] \quad (1.18)$$

⁷²³ The function λ is defined as $\lambda(x, y, z) = (1 - x/z - y/z)^2 - 4xy/z^2$. The integral in the general
⁷²⁴ off-shell boson case is much more difficult to interpret than the simpler on-shell branching ratios, but it
⁷²⁵ can be evaluated numerically. These branching ratio formulas can also be visualized as a function of Higgs
⁷²⁶ mass, as shown in figure 1.4. There are a few interesting features to note in this figure. First, note that at
⁷²⁷ high Higgs masses, once on-shell production of both W and Z bosons is possible, these two decays are
⁷²⁸ dominant due to the large masses of the W/Z . Also note that the branching ratio to W s is twice that of
⁷²⁹ Z s at these large masses due to the fact that there are two charged W bosons (W^\pm) and only one Z boson³.
⁷³⁰ At 125 GeV, the Higgs is accessible through many different decay modes. The largest branching ratio is
⁷³¹ the decay $H \rightarrow b\bar{b}$ at 58.24% [18]. This branching is larger than the WW/ZZ decays because one of
⁷³² the two bosons must be produced off-shell for $m_h = 125$ GeV. The second largest branching ratio is
⁷³³ to WW^* at 21.37 % (before taking into account the branching ratios of the W). Table 1.2 summarizes

³In the Higgs Lagrangian, this extra symmetry factor is quantified by the δ_V noted in equation 1.12.

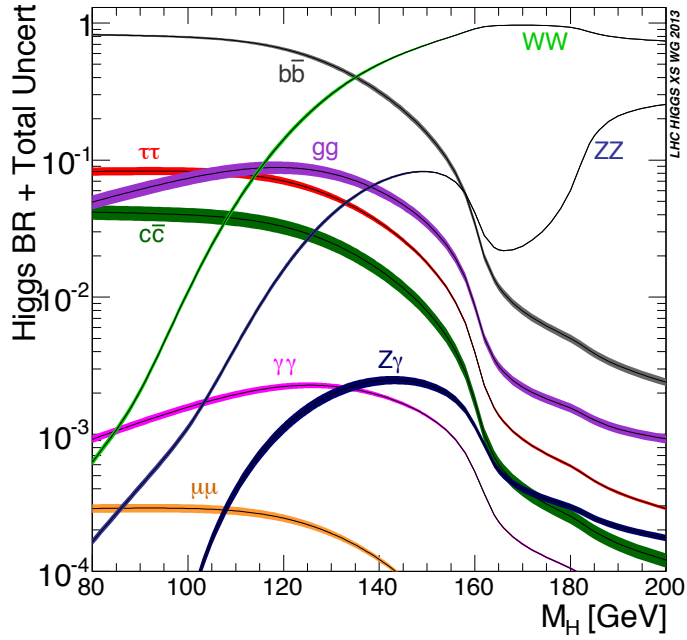


Figure 1.4: Higgs boson branching ratios as a function of m_H [18].

⁷³⁴ the theoretical branching ratios for a Higgs with a mass of 125 GeV. Note that there is a Higgs branching
⁷³⁵ ratio to $\gamma\gamma$ even though photons are massless. This decay happens through a loop, which suppresses the
⁷³⁶ branching ratio⁴.

Decay	Branching ratio (%)	Relative uncertainty (%)
bb	58.24	+0.25 / -0.25
WW^*	21.37	+0.99 / -0.99
gg	8.187	+3.40 / -3.41
$\tau\tau$	6.272	+1.17 / -1.16
cc	2.891	+1.20 / -1.20
ZZ^*	2.619	+0.99 / -0.99
$\gamma\gamma$	0.2270	+1.73 / -1.72
$Z\gamma$	0.1533	+5.71 / -5.71
$\mu\mu$	0.02176	+1.23 / -1.23

Table 1.2: Theoretical branching ratios for a 125 GeV Higgs boson, quoted as a percentage of the total width of the Higgs. Uncertainties shown are relative to the branching ratio value [18].

⁷³⁷ Note that the branching ratios alone do not tell the full story of which Higgs channels are the most

⁴The largest contributions to the loop are the top quark and W boson.

738 sensitive. For example, the $H \rightarrow b\bar{b}$ channel in gluon fusion production is incredibly difficult to observe
 739 due to the large QCD dijet background at the LHC. However, in associated production of the Higgs,
 740 where a W or Z gives additional final state particles that can be used to reduce background, a search for
 741 $H \rightarrow b\bar{b}$ can be sensitive. The combinations of production and decay modes that are most commonly
 742 studied at the LHC are summarized in table 1.3 [5].

Decay	Inclusive (incl. ggF)	VBF	WH/ZH	$t\bar{t}H$
$H \rightarrow \gamma\gamma$	✓	✓	✓	✓
$H \rightarrow b\bar{b}$			✓	✓
$H \rightarrow \tau^+\tau^-$		✓		
$H \rightarrow WW^* \rightarrow \ell\nu\ell\nu$	✓	✓	✓	
$H \rightarrow ZZ \rightarrow 4\ell$	✓			
$H \rightarrow Z\gamma \rightarrow \ell\ell\gamma$	very low			

Table 1.3: Possible channels for Higgs searches. Checkmarks denote the most sensitive production modes for each decay channel [5].

743 1.4 HIGGS PAIR PRODUCTION IN THE STANDARD MODEL

744 The Standard Model also allows for processes that produce two Higgs bosons in the final state, known
 745 as Higgs pair production or di-Higgs production. The two main production mechanisms are shown in
 figure 1.5. The two diagrams in figure 1.5 interfere destructively with one another, resulting in a low overall

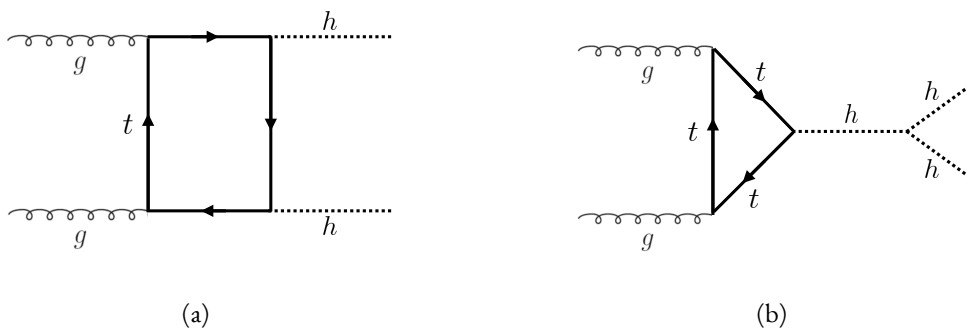


Figure 1.5: The two leading diagrams for Standard Model di-Higgs production at the LHC: (a) box diagram, (b) Higgs self coupling.

746
 747 cross section for di-Higgs production at the LHC. Nevertheless, Higgs pair production is quite interesting

748 to study because it gives direct access to the λ parameter of the Higgs potential, also known as the Higgs
749 self coupling. The diagram in figure 1.5(b) is sensitive to this coupling through the triple Higgs vertex.

750 One can substitute the gluon fusion production of diagram 1.5(b) with any of the other production
751 modes previously discussed. These other modes do not suffer from interference with the box diagram in
752 figure 1.5(a) due to the presence of additional particles in the final state. They still have a lower cross section
753 than the gluon fusion mode, however. The cross sections for di-Higgs production in the different modes,
754 as well as their uncertainties, are shown in table 1.4 [29]. These are shown for $\sqrt{s} = 14$ TeV as this is the
755 expected center of mass energy for the High Luminosity LHC and this energy is more sensitive to di-Higgs
production. Note that the scale of cross section quoted is now in fb rather than pb.

Production mode	σ (fb)	Total uncert. (%)
Gluon fusion	33.89	+37.2 / - 27.8
Vector boson fusion	2.01	+7.6 / - 5.1
$W H H$	0.57	+3.7 / - 3.3
$Z H H$	0.42	+7.0 / - 5.5
$t \bar{t} H$	1.02	-

Table 1.4: Production cross sections for pair production of a 125 GeV Higgs boson at $\sqrt{s} = 14$ TeV with total uncertainty [29]. The uncertainties include QCD scale and PDF variations as well as uncertainties on α_S .

756

757 1.5 HIGGS PAIR PRODUCTION IN THEORIES BEYOND THE STANDARD MODEL

758 The Higgs pair production cross section in the Standard Model is rather small, and datasets on the scale of
759 the full 3000 fb^{-1} expected from the High Luminosity LHC will be required to obtain sensitive measure-
760 ments of the Higgs self-coupling [29]. However, the discovery of the Higgs also gives particle physicists
761 a new tool that can be exploited in the search for new physics beyond the Standard Model. In particular,
762 Higgs pair production is a promising channel in the search for new physics. The cross section for di-Higgs
763 production can be altered through both resonant and non-resonant production of Higgs pairs. In non-
764 resonant production, di-Higgs production vertices can arise from the presence of a new strong sector and
765 additional colored particles [30–32]. Figure 1.6 shows examples of the types of vertices that can arise. In
766 the resonant case, new heavy particle can decay to Higgs pairs. Such new particles can include heavy Higgs

767 bosons arising in two Higgs doublet models (2HDM) or Higgs portal models as well as heavy gravitons in
 768 Randall-Sundrum theories [30, 33–39]. Figure 1.7 shows a generic diagram for a heavy resonance decaying
 769 to two Higgs bosons. In the 2HDM, X corresponds to the heavy CP-even scalar H . In the Randall-
 Sundrum model, X corresponds to a heavy spin-2 graviton G_{KK}^* . The next sections provide more detail

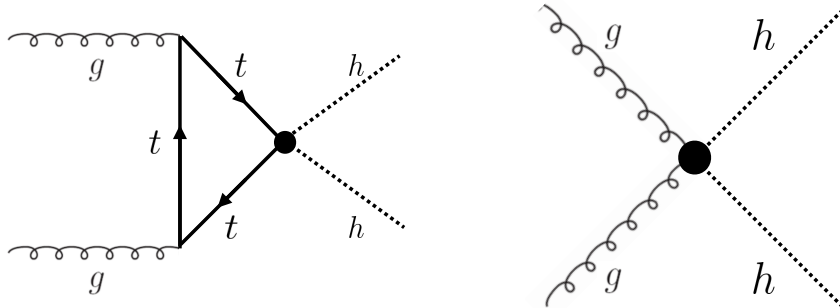


Figure 1.6: Diagrams with new vertices for non-resonant Higgs pair production arising in composite Higgs models.

770
 771 on the phenomenology of resonant Higgs production in Randall-Sundrum and 2HDM models, as these
 models will later be tested in a dedicated search for resonant production of boosted Higgs pairs.

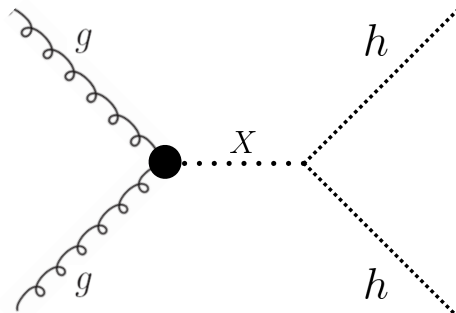


Figure 1.7: Generic Feynman diagram for resonant Higgs pair production in BSM theories.

772

773 1.5.1 RANDALL-SUNDRUM GRAVITONS

774 The Randall-Sundrum model is a proposed solution to the hierarchy problem that posits a five-dimensional
 775 warped spacetime that contains two branes: one where the force of gravity is very strong and a second brane
 776 at the TeV scale corresponding to the known Standard Model sector [33]. In the theory, the branes are

777 weakly coupled and the graviton probability function drops exponentially going from the gravity brane
 778 to the SM brane, rendering gravity weak on the SM brane. The experimental consequence of this theory
 779 is a tower of widely spaced (in mass) Kaluza-Klein graviton resonances. In theories where the fermions
 780 are localized to the SM brane, production of gravitons from fermion pairs is suppressed and the primary
 781 mode of production is gluon fusion [34]. These gravitons have a substantial branching fraction to Higgs
 782 pairs, ranging from 6.43% for gravitons with a mass of 500 GeV to 7.66% at 3 TeV. Figure 1.8 shows the
 783 branching ratios of the spin-2 Randall Sundrum graviton (RSG) as a function of its mass. The predomi-
 784 nant decays are to $t\bar{t}$ above the mass threshold for that channel.

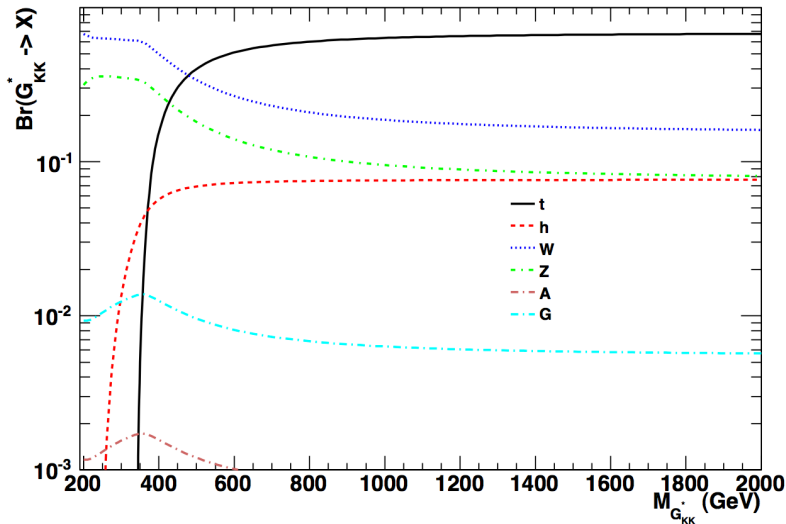


Figure 1.8: Branching ratios for a spin-2 Randall-Sundrum graviton as a function of mass computed in MadGraph with the CP3-Origins implementation [34, 40, 41].

785 Randall-Sundrum models have two free parameters - the mass of the graviton and a curvature parameter
 786 k . Typically, rather than k , the theory is parameterized using $c \equiv k/\bar{M}_{\text{pl}}$, where \bar{M}_{pl} is the reduced
 787 Planck mass. The cross section for production of the RSG decreases as a function of mass and is strongly
 788 dependent on the gluon PDF. The increase in center of mass energy from 8 to 13 TeV in LHC Run 2
 789 greatly increases the cross section at higher mass. Figure 1.9 shows the cross section as a function of graviton
 790 mass at $\sqrt{s} = 13$ TeV for RSG models with $c = 1.0$ and $c = 2.0$.

791 Another interesting feature of the theory is that the width of the graviton increases with both c and
 792 $m_{G_{\text{KK}}^*}$. Figure 1.10 shows the graviton width for both $c = 1.0$ and $c = 2.0$ as a function of mass. In

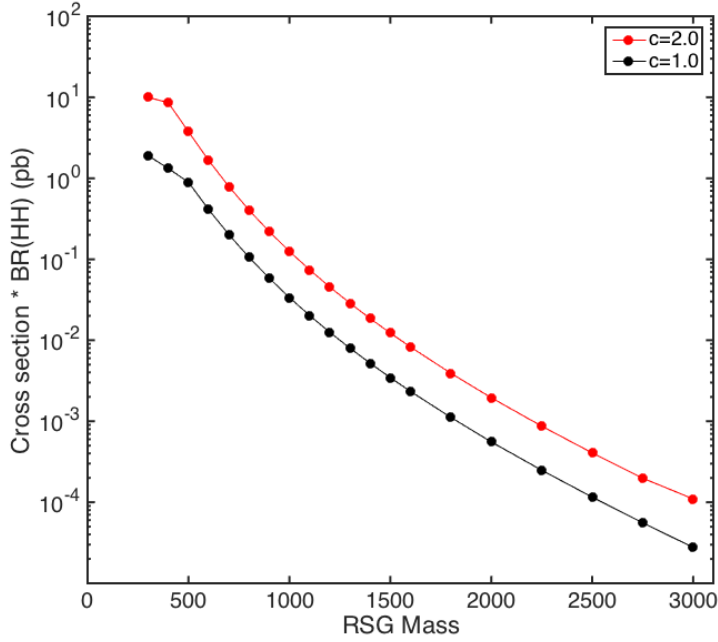


Figure 1.9: $\sigma \times \text{BR}(HH)$ for Randall-Sundrum gravitons as a function of mass computed in MadGraph with the CP3-Origins implementation [34, 40, 41].

793 $c = 1.0$, the width starts at 8.365 GeV for a mass of 300 GeV and increases to 187.2 GeV at a mass of
 794 3 TeV. Similarly, with $c = 2.0$, the width starts at 33.46 GeV for $m_G = 300$ GeV and increases to
 795 748.8 GeV at a mass of 3 TeV.

796 1.5.2 TWO HIGGS DOUBLET MODELS

797 In Two Higgs Doublet Models (2HDM), a second complex scalar doublet is added to the Standard Model [36–
 798 38]. In this case, all four degrees of freedom in the second doublet correspond to new particles, meaning
 799 that there are five total scalars from the two Higgs doublets - h (light CP-even Higgs), H (heavy CP-even
 800 Higgs), A (heavy CP-odd Higgs), and H^\pm (charged Higgs). The model is parameterized by two main pa-
 801 rameters. The first, $\tan \beta \equiv \frac{v_2}{v_1}$, is the ratio of the vacuum expectation values of the two Higgs doublets
 802 (where v_1 corresponds to the v in the SM Higgs model described above). The second parameter is α , a mix-
 803 ing angle between the heavy and light Higgs fields. Models are also often parameterized with $\cos(\beta - \alpha)$
 804 rather than α directly. The limit where $\cos(\beta - \alpha) = 0$ is called the alignment limit, and in this limit the

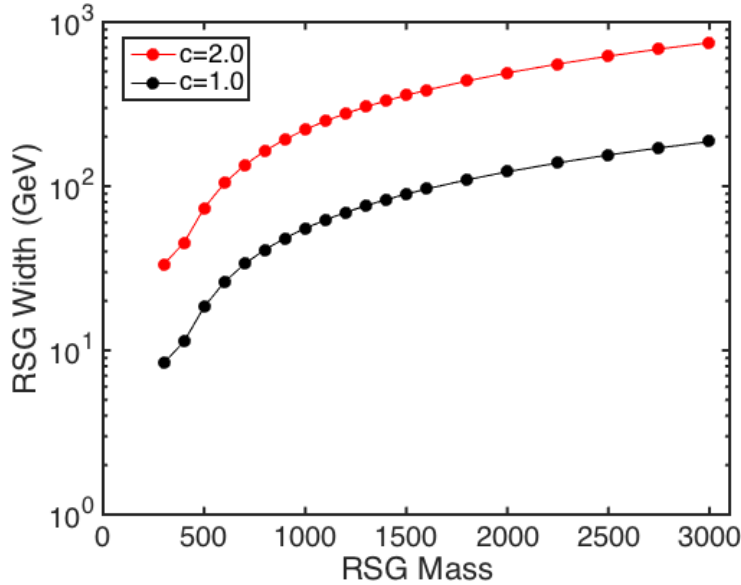


Figure 1.10: Randall-Sundrum graviton width as a function of mass computed in MadGraph with the CP3-Origins implementation [34, 40, 41]

805 light Higgs h has the same couplings as a Standard Model Higgs. Measurements of the Higgs boson have
 806 put constraints on these two parameters, but near the alignment limit there is still much unprobed phase
 807 space depending on the exact models and values of $\tan \beta$ being considered [42].

808 2HDM models are usually separated into two main types - Type I and Type II. In Type I models, the
 809 charged fermions only couple to the second Higgs doublet, leading to a fermiophobic light Higgs. In
 810 Type II models, up-type quarks couple to the first doublet while down-type quarks couple to the second
 811 doublet. One specific realization of a Type II 2HDM is the Minimal Supersymmetric Standard Model
 812 (MSSM).

813 Resonant di-Higgs production in 2HDM models can proceed through decays of the heavy CP-even
 814 Higgs $H \rightarrow hh$. The branching ratio for $H \rightarrow hh$ depends on the model type as well as the values of
 815 $\tan \beta$ and $\cos \beta - \alpha$. Figure 1.11 shows the branching ratios as a function of the mass of the heavy scalar
 816 H for both Type I and Type II models. Depending on the type of model hh can be a substantial fraction
 817 of the decays of H .

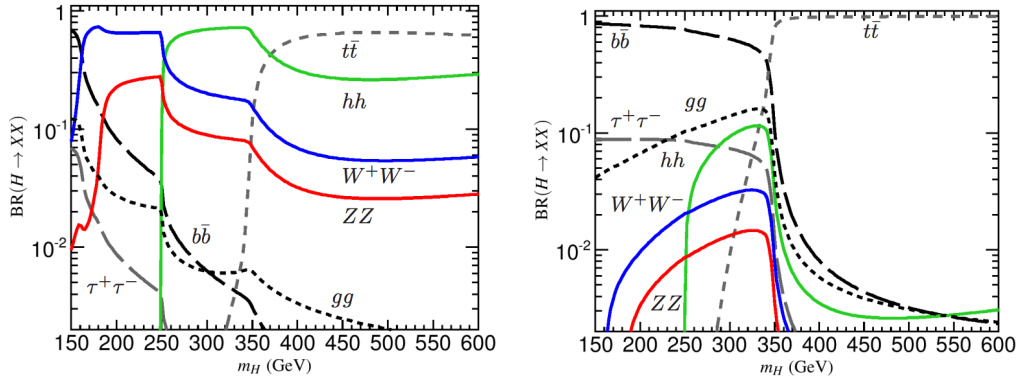


Figure 1.II: Branching ratios for heavy Higgs H in Type I (left) and Type II (right) 2HDM models with $\tan \beta = 1.5$ and $\cos(\beta - \alpha) = 0.1$ (0.01) for Type I (Type II) [38].

818 1.6 CONCLUSION

819 Studying the Higgs sector is essential for understanding the details of how mass arises in the Standard
 820 Model and how the electroweak symmetry is broken. The discovery of the Higgs boson also opens the
 821 door for its use as a tool to search for new physics, and Higgs pair production is an ideal candidate for
 822 this study. Even if no BSM physics is found in Higgs pair production, searches for Higgs pairs will put
 823 constraints on the Higgs self coupling and thus improve knowledge of the Standard Model and the details
 824 of the Higgs potential.

*The enthusiasm and motivation to explore particle physics
at the high-energy frontier knows no borders between the
nations and regions of the planet.*

Peter Jenni

2

825

826

827

The ATLAS detector and the Large Hadron Collider

828 This chapter presents an overview of the experimental systems used to conduct the measurements in this
829 thesis. First, a brief overview of the accelerator, the Large Hadron Collider, will be given. In this section,
830 the accelerator conditions relevant to data-taking are presented as well. Next, an overview of the ATLAS
831 experiment is given. The basics of each sub-detector's role are summarized, as well as the details of the
832 datasets accumulated. Then, a brief interlude on the ATLAS Muon New Small Wheel upgrade is pre-
833 sented. While this new detector does not have a direct impact on any of the datasets recorded so far, it will
834 have an impact on future analyses and the work done on it is briefly summarized here. Finally, an overview
835 of object reconstruction in ATLAS is given. While the details of all of the algorithms will not be presented
836 in detail, aspects of the reconstruction performance are shown as these are relevant to the results presented
837 later in this thesis.

838 2.1 THE LARGE HADRON COLLIDER

839 The Large Hadron Collider (LHC) is a proton-proton collider at the CERN laboratory in Geneva, Switzer-
840 land [43]. It was designed for a maximum collision center of mass energy of $\sqrt{s} = 14 \text{ TeV}$ and has a
841 circumference of 26.7 kilometers. Four main experiments are located at the interaction points (IP) of
842 the accelerator: ATLAS (A Toroidal LHC ApparatuS), CMS (the Compact Muon Solenoid), ALICE (A
843 Large Ion Collider Experiment), and LHCb [44–47]. Figure 2.1 shows a schematic of the LHC ring and
844 its experiments.

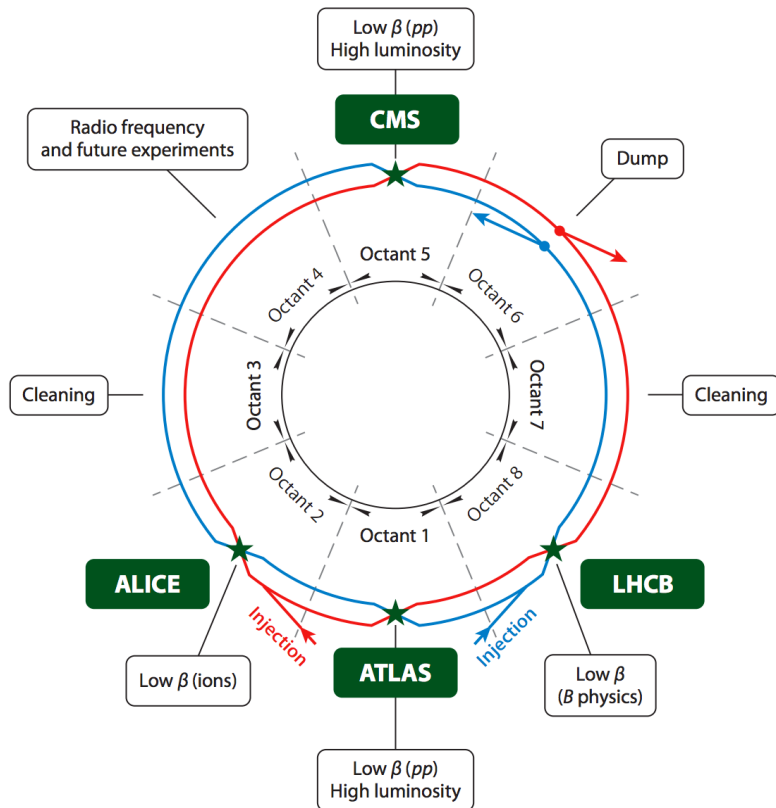


Figure 2.1: A schematic view of the LHC ring [48]. Four main experiments are located at interaction points along the ring. ATLAS and CMS are general purpose experiments, while ALICE is dedicated to heavy ion collisions and LHCb is dedicated to studying B physics.

845 One of the most interesting features of the LHC is its magnet design. Because the tunnel does not have
846 room for separate superconducting magnets for each of the beam pipes, the LHC employs a twin-bore
847 magnet design. Each magnet must hold an 8.3 Tesla magnetic field in order to bend the proton beams at

848 $\sqrt{s} = 14 \text{ TeV}$. The superconducting magnets are cooled to a temperature of 1.9 Kelvin with superfluid
849 helium.

850 2.1.1 INSTANTANEOUS LUMINOSITY

851 The rate of physics events expected from the accelerator is dependent on the instantaneous luminosity
852 of the machine and the cross section of the physics process, $R_{\text{events}} = L\sigma$. Here, R_{events} is the num-
853 ber of events per second, L is the instantaneous luminosity of the machine, and σ is the cross section for
854 the physics process being measured. The instantaneous luminosity of the LHC is determined by numer-
855 ous factors related to beam conditions. Equation 2.1 gives the equation for instantaneous luminosity of a
856 Gaussian beam profile [48].

$$L = \frac{N_b^2 n_b f_{\text{rev}} \gamma_r}{4\pi \epsilon_n \beta^*} F \quad (2.1)$$

857 The LHC collides protons in bunches, and in the above equation N_b is the number of protons per bunch
858 while n_b is the number of bunches per beam. Nominally, the LHC can hold up to 2808 proton bunches.
859 f_{rev} is the revolution frequency. ϵ_n is the normalized transverse beam emittance, a measurement of the
860 average spread of the particles in position-momentum space which has the dimension of length. β^* is the
861 value of the β function for the beam at the interaction point. It relates the emittance to the Gaussian
862 width of the beam with $\sigma_{\text{beam}} = \sqrt{\epsilon \cdot \beta}$. F is a reduction factor that corrects for the fact that the beams
863 are colliding at an angle at the IP.

864 Another way of writing the instantaneous luminosity is shown in equation 2.2. In this case, the instan-
865 taneous luminosity is written as the ratio of the rate of inelastic collisions to the inelastic cross section [49].

866

$$L = \frac{R_{\text{inel}}}{\sigma_{\text{inel}}} = \frac{\mu n_b f_{\text{rev}}}{\sigma_{\text{inel}}} \quad (2.2)$$

867 In this case, μ is the average number of interactions per bunch crossing in the accelerator. μ is a useful
868 parameter for characterizing the amount of activity recorded in an experiment. As the instantaneous lu-
869 minosity and thus μ increase, there are more interactions per bunch crossing and more activity is present
870 in the detector. The level of activity is often characterized with $\langle \mu \rangle$, the measured per bunch crossing μ

871 value averaged over all bunch crossings. The interactions inside each bunch crossing that are not the main
 872 physics process of interest are often referred to as “pileup” interactions, and $\langle \mu \rangle$ is a measurement of the
 873 level of pileup in the detector.

874 **2.1.2 EVOLUTION OF MACHINE CONDITIONS**

875 This thesis uses datasets taken at three different center of mass energies: $\sqrt{s} = 7$ TeV data taken in the
 876 year 2011, $\sqrt{s} = 8$ TeV data taken in the year 2012, and $\sqrt{s} = 13$ TeV data taken in the year 2015. In
 877 addition to increasing center of mass energy, the instantaneous luminosity and parameters that determine
 878 it were evolving. Table 2.1 summarizes that machine conditions in each of these datasets.

	2011	2012	2015	Design
\sqrt{s} [TeV]	7	8	13	14
Number of bunches	1380	1380	1825	2808
Max. protons per bunch	1.45×10^{11}	1.7×10^{11}	1.2×10^{11}	1.15×10^{11}
Bunch spacing [ns]	50	50	25	25
Max. instantaneous luminosity [$\text{cm}^{-2}\text{s}^{-1}$]	3.7×10^{33}	7.7×10^{33}	5×10^{33}	10^{34}
β^* [m]	1.0	0.6	0.8	0.55
$\langle \mu \rangle$	11.6	20.7	13.7	-

Table 2.1: Evolution of LHC machine conditions [50, 51].

879 **2.2 THE ATLAS DETECTOR**

880 The ATLAS detector is the multi-purpose particle detector experiment located at the LHC’s Point 1 [44].
 881 It has nearly 4π coverage in solid angle around the interaction point. It consists of an inner detector for
 882 measuring charged particles, electromagnetic and hadronic calorimeters, and a muon spectrometer. Fig-
 883 ure 2.2 gives an overview of the detector.

884 **2.2.1 COORDINATE SYSTEM**

885 Before defining the properties of the individual detectors, it is important to establish the coordinate system
 886 used. Figure 2.3 shows a schematic of the coordinate system. The azimuthal plane (perpendicular to the



Figure 2.2: A full diagram of the ATLAS detector [44].

beam line) is defined as the x - y plane. The angle in this plane is referred to as ϕ . The angle relative to the beam axis is referred to as θ . Rather than using θ directly as a coordinate, the experiment often uses the pseudorapidity η , defined in equation 2.3.

$$\eta = -\ln \left(\tan \left(\frac{\theta}{2} \right) \right) \quad (2.3)$$

Pseudorapidity is the massless approximation of rapidity, the angle used to parameterize boosts in special relativity. This coordinate is useful in particle physics for two reasons. First, it means that differences in η are Lorentz invariant. Second, particle production is roughly constant in pseudorapidity. Particles with η close to zero are referred to as “central”, while those at high $|\eta|$ are called “forward”. In general, two main detector configurations can be seen in figure 2.2. There are “barrel” elements, which surround the beam line cylindrically and are in the central region of the detector. In the forward region, there are “endcap” regions which are arranged as disks perpendicular to the beam line.

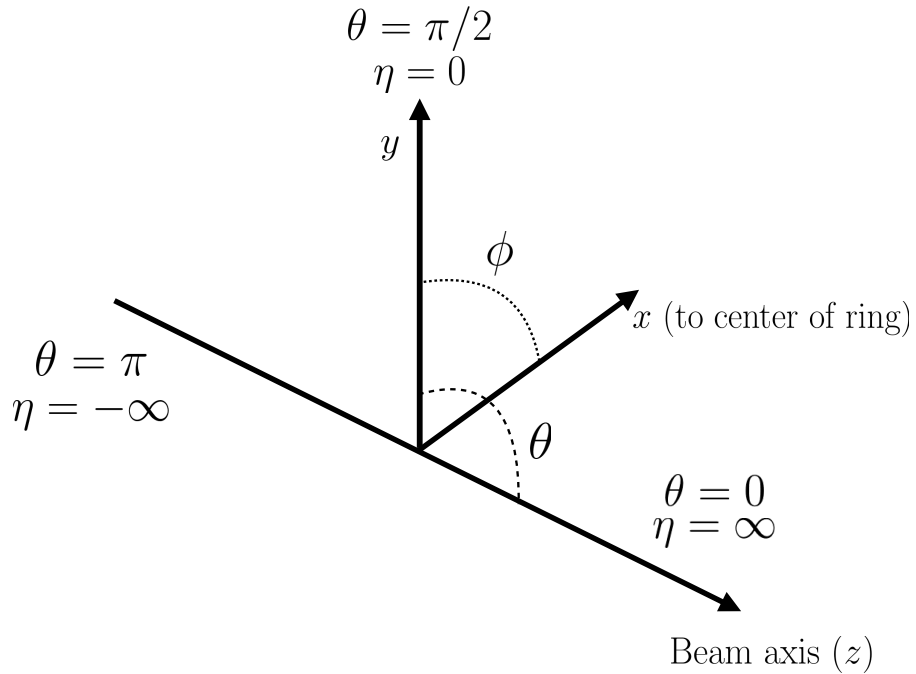


Figure 2.3: The ATLAS coordinate system. The z direction corresponds to the beam axis, while x and y define the transverse plane. θ is the angle relative to the beam axis and ϕ is the azimuthal angle. η , the pseudorapidity, approaches infinity at small angles relative to the beam axis.

897 2.2.2 INNER DETECTOR

898 The ATLAS Inner Detector (ID) system is built for precision tracking of charged particles. It covers the
 899 range $|\eta| < 2.5$. In this range, approximately 1000 particles are generated every bunch crossing in the de-
 900 tector [44]. This requires having fine granularity to achieve the resolutions required for good momentum
 901 measurement and vertex reconstruction.

902 The ID consists of three sub-components: the pixel detector, semiconductor tracker (SCT), and trans-
 903 sition radiation tracker (TRT). It is surrounded by a solenoid providing a 2 T axial magnetic field which
 904 bends particles in the transverse plane to allow for momentum measurement. Figure 2.4 shows the layout
 905 of each of these components.



Figure 2.4: Layout of the ATLAS Inner Detector system [52].

906 PIXEL DETECTOR

907 The pixel detector is the first detector particles traverse after being generated in proton collisions and is
 908 the most granular detector. Its operation is crucial for precision tracking and vertex reconstruction as well
 909 as higher level object reconstruction like tagging of jets from b -quarks. The basic sensing element in this
 910 subdetector is a silicon pixel detector. The operating principle for the silicon pixels is that of a $p-n$ junction.
 911 When a charged particle passes through, it creates electron-hole pairs that are then separated by the electric
 912 field. The sensors are $250 \mu\text{m}$ thick and use oxygenated n -type wafers with readout pixels on the n^+ side
 913 of the detector [44]. Overall, the pixel detector has 1744 sensors and 80.4 million readout channels.

914 In the barrel region, the pixel detector has three concentric layers of sensors surrounding the beamline.
 915 In the endcap region, it consists of disks perpendicular to the beam axis. The detector is segmented in
 916 the $R-\phi$ plane and in z . Usually, three pixel layers are crossed by a charged particle track. The intrinsic
 917 accuracies of the sensors are $10 \mu\text{m}$ in $R-\phi$ and $115 \mu\text{m}$ in z (or R for the endcap).

918 **INSERTABLE B-LAYER**

919 In Run 2, a new innermost pixel layer, known as the insertable B-layer (IBL), was added to the Inner
920 Detector [53]. This layer was added to cope with the higher luminosities planned in LHC Run 2 and at the
921 high luminosity HL-LHC. Additionally it improves tracking position resolution which in turn improves
922 the vertexing and *b*-tagging capabilities in ATLAS. The detector sits directly on a new beam pipe, only
923 33.25 mm away from the collision points in the azimuthal plane.

924 **SEMICONDUCTOR TRACKER (SCT)**

925 The semiconductor tracker (SCT) consists of silicon microstrips and comprises the next four layers of
926 the ID. This sub-detector has 6.4 cm long sensors that are daisy-chained into strips with a strip pitch of
927 80 μm [44]. Some of the strips have a small stereo angle to allow for measurement of both angular co-
928 ordinates. In total there are 6.3 million readout channels. The intrinsic accuracies are 17 μm in $R\text{-}\phi$ and
929 580 μm in z (or R in the endcap).

930 **TRANSITION RADIATION TRACKER (TRT)**

931 The transition radiation tracker (TRT) serves two purposes. First, it consists of 4 mm diameter straw tubes
932 filled with a 70/27/3% gas mixture of xenon, carbon dioxide, and oxygen to provide tracking of charged
933 particles. Particles typically have 36 TRT straw tube hits per track. The material in between the straws
934 is designed to induce transition radiation which can be useful for particle identification. As particles pass
935 between media with different dielectric constants, they emit transition radiation that can cause additional
936 showers in the TRT. In particular it is useful for discrimination between electrons and pions or other
937 charged hadrons, as the amount of transition radiation is proportional to the Lorentz factor of the particle.

938 **2.2.3 CALORIMETERS**

939 The calorimeter system consists of two main sub-components: a fine granularity electromagnetic calorime-
940 ter tailored for the measurement of photons and electrons and multiple coarser hadronic calorimeters ded-
941 icated to the measurement of hadronic showers [44]. The calorimeter system has broader coverage than

942 the inner detector, covering the region out to $|\eta| < 4.9$. It is also designed to deliver good containment of
943 showers so as to limit leakage into the muon system. Figure 2.5 shows the layout of the calorimeter system.

944 Both the electromagnetic and hadronic calorimeters are sampling calorimeters. They alternate active
945 material for energy measurement with passive material for energy absorption. The materials used for each
946 purpose vary based on the type of calorimeter and its location in the detector.

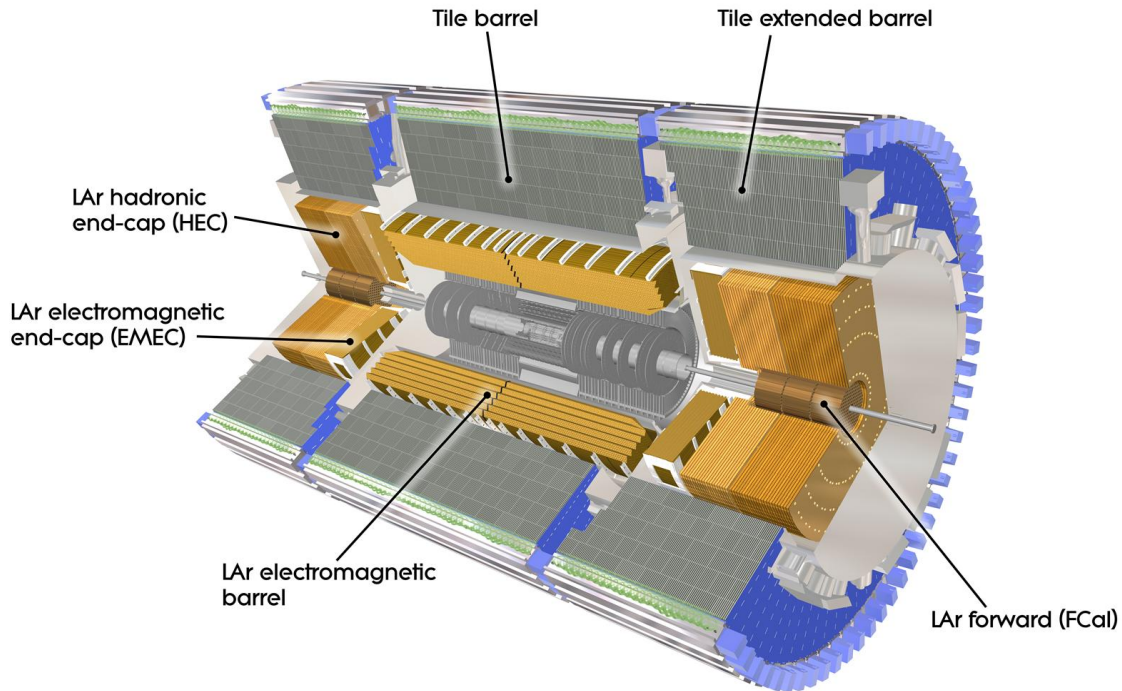


Figure 2.5: Layout of the ATLAS calorimeter system [44].

947 ELECTROMAGNETIC CALORIMETER

948 The electromagnetic calorimeter (EM calorimeter) use liquid Argon (LAr) as its active material and lead
949 as its passive material. It is arranged in an accordion geometry to increase the absorption area while still
950 allowing it to have no azimuthal cracks (complete symmetry in ϕ). The EM calorimeter is divided into a
951 barrel portion that extends to $|\eta| < 1.475$ and an endcap portion going from $1.375 < |\eta| < 3.2$. The
952 region where these two units overlap is called the “transition region”.

953 In order to provide good containment the calorimeter depth must be optimized. Typically, for elec-
954 tricalmagnetic calorimeters the depth is measured in radiation lengths. In general, the intensity of a particle
955 beam attenuates exponentially in distance with an attenuation constant equal to the radiation length. That
956 is, $I(x) = I_0 e^{-x/X_0}$, where I is the intensity, x is the distance traveled, and X_0 is the radiation length.
957 The ATLAS EM calorimeter is designed to have > 22 radiation lengths in the barrel and > 24 in the
958 endcap [44].

959 **HADRONIC CALORIMETERS**

960 There are three types of hadronic calorimeters present in ATLAS: the tile calorimeter (TileCal), hadronic
961 endcap (HEC), and forward calorimeter (FCal). Each one is optimized for stopping of hadronic showers
962 and the materials chosen are specific to their placement in the detector.

963 The TileCal is a scintillating tile calorimeter placed directly outside the EM calorimeter. It uses steel as
964 the absorber and plastic scintillator tiles as the active material. It has coverage in the barrel at $|\eta| < 1.0$
965 and in the “extended barrel” region of $0.8 < |\eta| < 1.7$.

966 The HEC had two wheels perpendicular to the beam line per endcap and is located directly behind the
967 EM calorimeter endcap modules. The HEC covers the region from $1.5 < |\eta| < 3.2$, overlapping slightly
968 with both the tile calorimeter and the forward calorimeter. Like the EM calorimeter, it uses liquid Argon
969 as the active material, but it uses copper as the absorber.

970 The FCal covers the most forward regions of the calorimeter system, extending to the region of $3.1 <$
971 $|\eta| < 4.9$. It again uses liquid argon as its active material. For absorber, it consists of an innermost module
972 made of copper followed by a module made of tungsten.

973 The hadronic equivalent of radiation length is called the interaction length and is denoted as λ . In the
974 barrel, the hadronic calorimeter depth is approximately 9.7λ , while in the endcap is is 10λ . The outer
975 supports contribute an additional 1.3λ . This is been shown to be sufficient to limit punch-through of
976 showers to the muon system [44].

977 2.2.4 MUON SPECTROMETER

978 The muon spectrometer is dedicated to measuring the momentum and position of muons. It consists
979 of tracking and trigger chambers which are unique in the barrel and endcap regions. The magnetic field
980 for bending of muons is provided by a system of three large air-core toroid magnets (from which ATLAS
981 derives its name.) These magnets provide 1.5 to 5.5 Tm of bending power at $0 < |\eta| < 1.4$ and approx-
982 imately 1 to 7.5 Tm in the endcap region of $1.6 < |\eta| < 2.7$. The entire muon system covers the range
983 $0 < |\eta| < 2.7$. Monitored drift tubes (MDTs) are used for tracking in the barrel and the two outer layers
984 of the endcap, while cathode strip chambers (CSCs) are used to provide tracking in the innermost endcap
985 wheel. In the barrel, resistive plate chambers (RPCs) are used as trigger chambers while thin gap chambers
986 (TGCs) are used in the endcap. Figure 2.6 shows the layout of the ATLAS muon system. The entire muon
987 system is designed with the specification of providing a 10% momentum resolution for a 1 TeV muon.

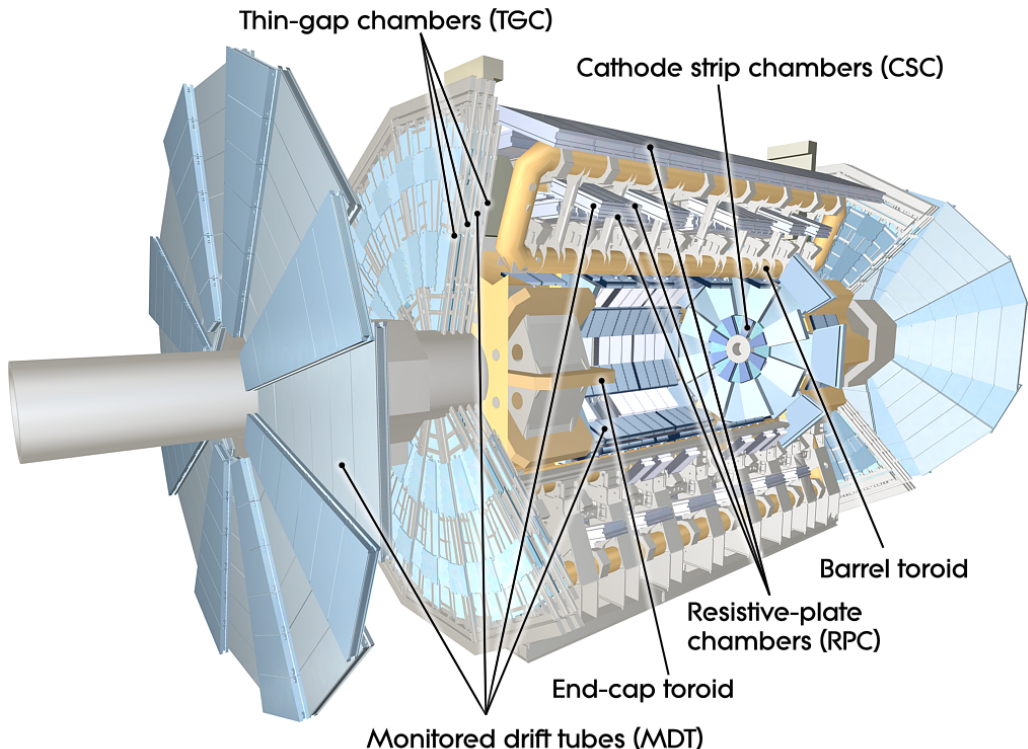


Figure 2.6: Layout of the ATLAS muon system [44].

988 MONITORED DRIFT TUBES (MDTs)

989 The monitored drift tubes (MDTs) are aluminum 3 cm diameter tubes filled with a 93/7 % mixture of
990 Argon and CO₂, with trace amounts of water. As a charged particle traverses the tube, it ionizes the gas
991 and the ions drift to a wire at the center of the tube. The radial distance of traversal of the particle in the
992 tube is determined by the drift time of the electrons, allowing for fine position resolution. The tubes have
993 an average resolution of 80 μm per tube and a maximum drift time of approximately 700 ns. The tubes
994 are oriented so that they give precision measurement in η and run along ϕ . They cover $|\eta| < 2.7$, except
995 in the innermost layer of the endcap where they only go to $|\eta| < 2.0$ [44].

996 CATHODE STRIP CHAMBERS (CSCs)

997 The cathode strip chambers cover a narrow window of the innermost endcap region at $2.0 < |\eta| <$
998 2.7. In this region the background rates in the cavern are particularly high and the CSCs are designed to
999 handle these higher rates. The CSCs are multiwire proportional chambers with wires pointing in the radial
1000 direction (away from the beam pipe). The wire serves as an anode and there are two types of segmented
1001 cathode strip, one perpendicular to the wires which gives the precision measurement and one parallel which
1002 provides the transverse coordinate. It has an 80/20% gas mixture of Argon and CO₂ [44].

1003 RESISTIVE PLATE CHAMBERS (RPCs)

1004 The resistive plate chambers (RPCs) are gaseous electrode-plate detectors covering the region $|\eta| < 1.05$.
1005 They consist of two resistive plates separated by a distance of 2 mm. The gas mixture used is a 94.7/5/0.3%
1006 mixture of C₂H₂F₄, Iso-C₄H₁₀, and SF₆. It has readout strips with a pitch of 23-35 mm for both η and
1007 ϕ measurement and thus provides measurement of the azimuthal coordinate in the barrel. The thin gas
1008 gap allows for a quick response time which makes it ideal for use in the trigger. Signals in the RPC have
1009 a width of approximately 5 ns. There are three layers of RPCs which are referred to as the three trigger
1010 stations. They allow for programmable thresholds in both a low p_T and high p_T trigger. The coincidence
1011 of hits in the innermost chambers allows for setting muon trigger thresholds between 6 and 9 GeV, while
1012 the outermost layer allows the trigger to set trigger thresholds in the range of 9 to 40 GeV [44].

1013 THIN GAP CHAMBERS (TGCs)

1014 The thin gap chambers (TGCs) are multiwire proportional chambers where the wire to cathode distance
1015 (1.4mm) is smaller than the wire-to-wire distance (1.8 mm). They contain a gas mixture of CO₂ and *n*-
1016 pentane and use a high electric field to gain good time resolution. They serve two functions in the end-cap
1017 system. First, they serve as the trigger chambers. Second, they also provide azimuthal coordinate measure-
1018 ment. They sit on the inner and middle layers of the endcap. The outermost layer's azimuthal coordinate
1019 is determined by extrapolation [44]. As with the RPCs, the TGCs also are capable of triggering with pro-
1020 grammable thresholds in the same p_T range specified for the RPCs above.

1021 2.2.5 MAGNET SYSTEM

1022 As mentioned previously, there are two independent magnet systems in ATLAS. The first is a 2 T solenoid
1023 field in the inner detector which provides bending in the azimuthal plane. The second is an approximately
1024 0.5 T toroidal field in the muon system which provides bending in η . Figure 2.7 shows the predicted field
1025 integral as a function of $|\eta|$ [44].

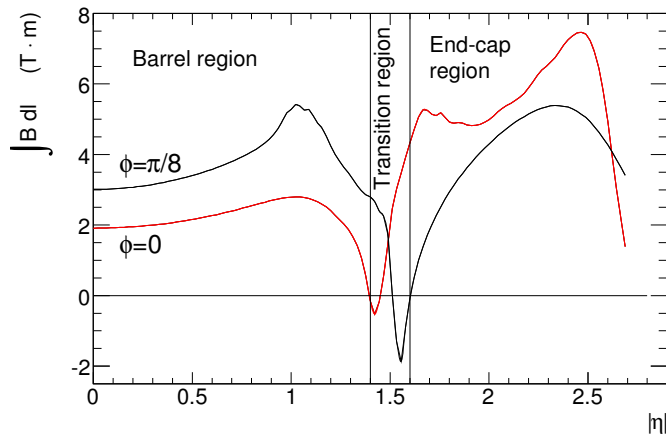


Figure 2.7: Predicted field integral as a function of $|\eta|$ for the ATLAS magnet system [44].

1026 2.2.6 TRIGGER SYSTEM

1027 The ATLAS trigger system searches for signatures of muons, electrons, photons, hadronically decaying τ
 1028 leptons, and jets in order to save these events for further analysis. The trigger system in ATLAS is designed
 1029 to reduce the maximum LHC event rate of 40 MHz to a more reasonable rate that can be recorded. The
 1030 trigger first consists of a fast, hardware based system called the Level-1 (L1) trigger. The L1 trigger consists
 1031 of independent dedicated detector sub-components that can seed regions of interest (RoIs) for further
 1032 analysis downstream. For muons, the RPCs and TGCs are used, while in the calorimeter coarsely grained
 1033 sections of calorimeter cells called towers are used. Once regions of interest are seeded, a software based
 1034 system called the High Level Trigger (HLT) is used to reconstruct objects and integrate information from
 1035 different parts of the detector. In Run 1 of ATLAS, the HLT consisted of two separate stages: the level 2
 1036 (L2) trigger and the event filter (EF).

1037 The maximum trigger rate that the L1 trigger can handle is 75 kHz. In the HLT, the rate of events
 1038 written to disk is approximately 400 Hz. Figure 2.8 shows the trigger rates for different L1 triggers in 2012
 1039 and 2015 for ATLAS [54].

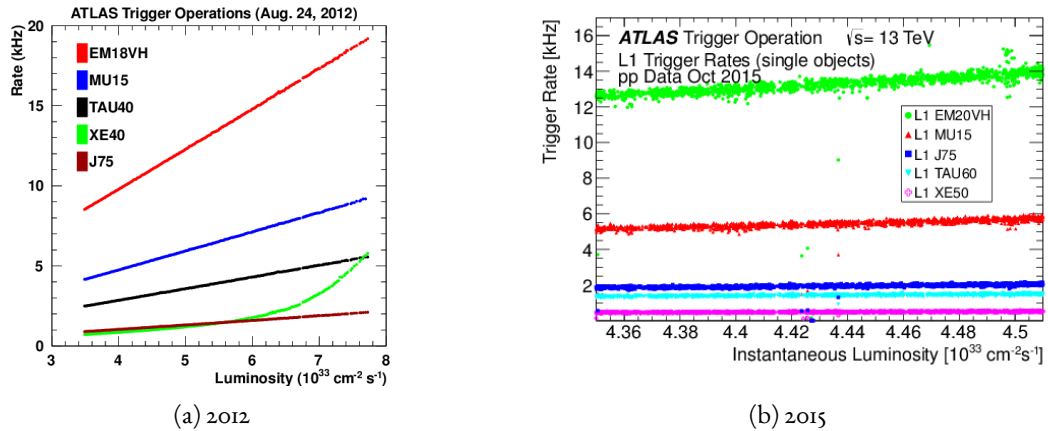


Figure 2.8: ATLAS trigger rates for Level-1 triggers as a function of instantaneous luminosity in 2012 and 2015 operation. These are single object triggers for electromagnetic clusters (EM), muons (MU), jets (J), missing energy (XE), and τ leptons (TAU). The threshold of the trigger is given in the name in GeV [54].

1040 2.2.7 ATLAS DATASETS

1041 ATLAS has collected data at center of mass energies of 7, 8, and 13 TeV. Figure 2.9 shows the integrated
1042 luminosity as a function of time for each of the three datasets. In the 2011 dataset with $\sqrt{s} = 7$ TeV,
1043 ATLAS recorded 5.08 fb^{-1} . Increased instantaneous luminosity in 2012 led to a larger dataset of 21.3 fb^{-1}
1044 recorded at $\sqrt{s} = 8$ TeV. After Long Shutdown 1 (LS1) of the LHC and a restart in 2015, ATLAS
1045 recorded 3.9 fb^{-1} of data at $\sqrt{s} = 13$ TeV [55, 56]. The data recorded by ATLAS can only be used for
1046 analysis if the required sub-detectors were in a stable state when the data was being taken. The fraction
1047 of recorded ATLAS data that was labeled as being good for physics analysis was 90%, 95%, and 82% in
1048 the 7, 8, and 13 TeV data respectively. Thus, the Run 1 results presented in this thesis use 4.6 fb^{-1} at
1049 $\sqrt{s} = 7$ TeV and 20.3 fb^{-1} at $\sqrt{s} = 8$ TeV¹. The Run 2 results use 3.2 fb^{-1} at $\sqrt{s} = 13$ TeV.

1050 2.2.8 DETECTOR PERFORMANCE

1051 Table 2.2 summarizes the design requirements for each of the different sub-detectors. This table shows the
1052 energy and momentum resolution of tracking, calorimetry, and muon measurements.

	Required resolution
Tracking	$\sigma_{p_T}/p_T = 0.05\% p_T \oplus 1\%$
EM calorimetry	$\sigma_E/E = 10\%/\sqrt{E} \oplus 0.7\%$
Hadronic calorimetry	
Barrel and end-cap	$\sigma_E/E = 50\%/\sqrt{E} \oplus 3\%$
Forward	$\sigma_E/E = 100\%/\sqrt{E} \oplus 10\%$
Muon spectrometer	σ_{p_T}/p_T at $p_T = 1$ TeV

Table 2.2: Performance requirements for the ATLAS detector [44].

1053 2.3 THE ATLAS MUON NEW SMALL WHEEL UPGRADE

1054 As the LHC continues operation, it is scheduled to be upgraded in several phases to allow it to reach higher
1055 instantaneous luminosities and thus collect larger datasets. These conditions will open new doors for study

¹The analyses combined in the Higgs discovery (presented in chapter 4) use between 4.6 and 4.8 fb^{-1} at 7 TeV depending on which detectors are required to be in a stable state. The discovery also only uses the 5.8 fb^{-1} of 8 TeV data that was available at the time of the analysis.

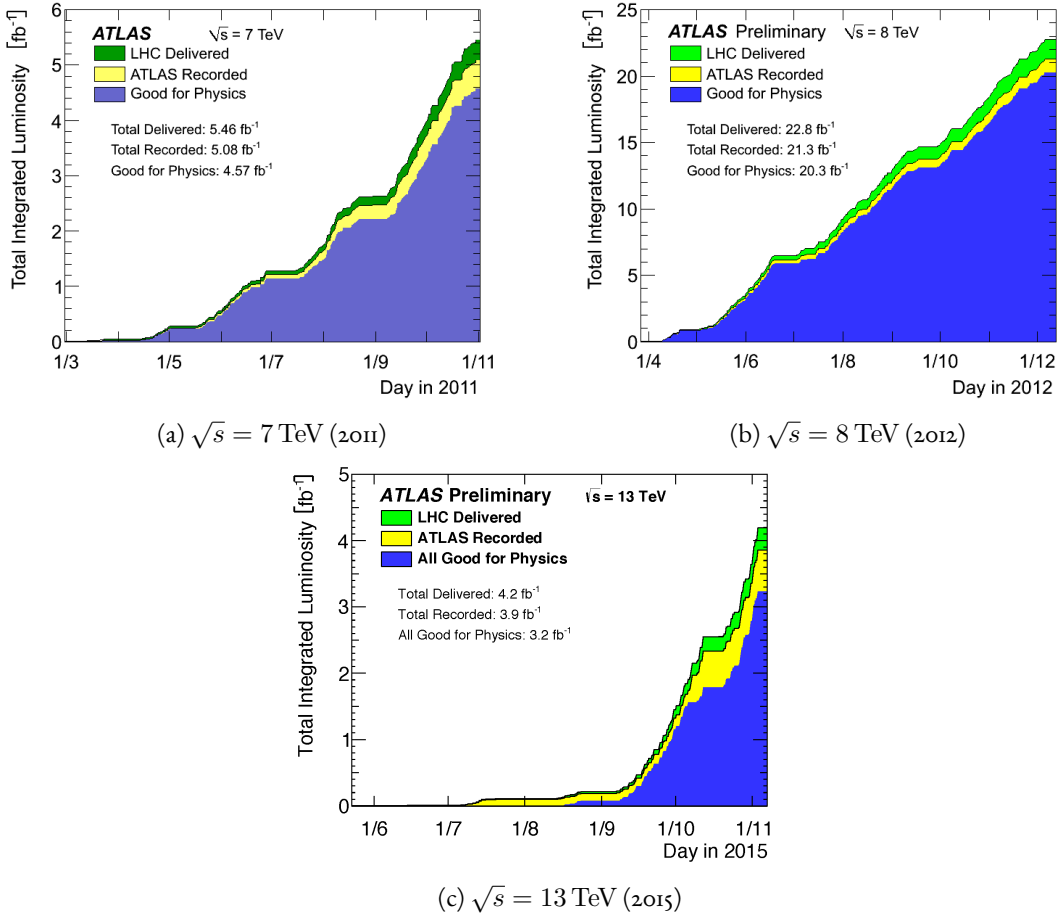


Figure 2.9: Instantaneous luminosity as a function of time for data recorded by ATLAS at different center of mass energies [55, 56].

of rare physics processes but will also present interesting challenges that must be faced. ATLAS will require new detector technologies to cope with the increased background rates in the cavern in these high luminosity conditions. One such upgrade, scheduled to be installed during Long Shutdown 2 (LS2) of the LHC in 2018, is the ATLAS Muon New Small Wheel (NSW) [57]. The NSW will replace the innermost end-cap wheel of the muon system with new technologies. This is the part of the muon detector closest to the beam line and thus experiences the highest rates of particle flux in the muon system.

1062 2.3.1 MOTIVATION

1063 The motivation of the NSW is two-fold. The first objective is to alleviate the decreased tracking efficiency
1064 that comes in a high rate environment. As shown in figure 2.10, at the LHC design luminosity both the
1065 efficiency of recording hits and reconstructing track segments in the MDTs decreases. While the MDTs
1066 were designed to cope with the hit rates at the LHC design luminosity, the High Luminosity LHC will
1067 exceed these design specifications and the MDTs will have to be replaced.

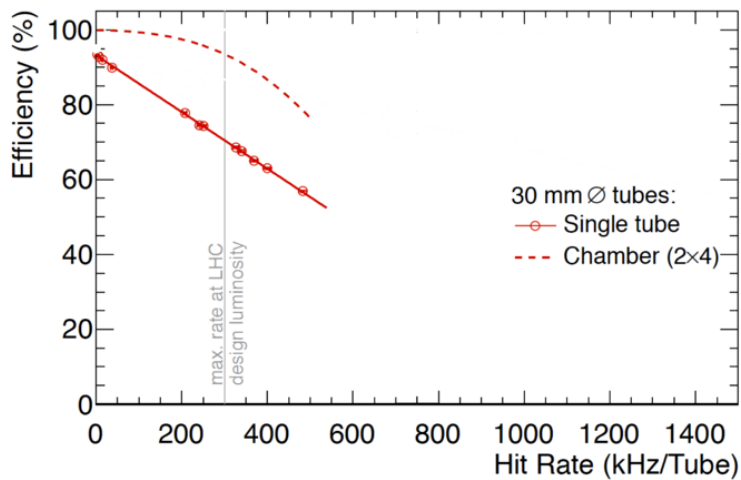


Figure 2.10: MDT tube hit (solid) and segment (dashed) efficiency as a function of hit rate per tube [57].

1068 The NSW will also work to alleviate the rate of fake triggers arising in the endcap. Figure 2.11 shows the
1069 extrapolated trigger rates as a function of the p_T threshold with and without the NSW upgrade. As the
1070 figure shows, the NSW upgrade will reduce the trigger rate considerably compared to the current endcap
1071 trigger system. At a p_T threshold of 20 GeV, the level-1 trigger rate drops from 20 kHz to 7 kHz. This
1072 reduction allows the p_T thresholds on muons to remain low, increasing the phase space of possible physics
1073 studies and in particular maintaining good acceptance for Higgs physics.

1074 2.3.2 NSW DETECTOR TECHNOLOGIES

1075 The NSW will use two new detector technologies - micromesh gaseous structure detectors (micromegas)
1076 and small-strip thin gap chambers (sTGCs) [57, 58]. The micromegas is more suited to tracking because

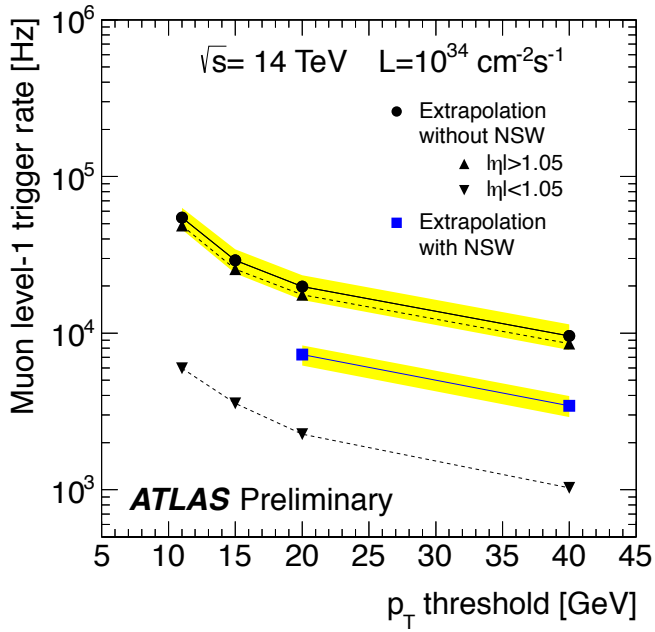


Figure 2.11: Trigger rate as a function of p_T threshold with and without the NSW upgrade [57].

of its good spatial resolution, while the sTGCs have better time resolution and are more suited for the trigger. However, both systems are capable of providing tracking and trigger information. To maintain full redundancy in cases of detector failure, both technologies will be used for tracking and trigger in the NSW.

1081 MICROMEGAS

1082 Micromegas detectors operate using a thin metallic mesh that sits approximately $100\ \mu\text{m}$ away from the
 1083 readout electrodes to create the amplification region. Above this mesh, there is a drift region on the order
 1084 of a few mm in length capped by a drift electrode. As a charged particle traverses the detector, it ionizes gas
 1085 and the electrons drift down towards readout strips. The timing of the drift can be used to reconstruct the
 1086 angle of traversal of the particle. This is illustrated in figure 2.12. The micromegas used in ATLAS will be
 1087 resistive micromegas, where the readout electrodes are topped with resistive strips [59]. This alleviates the
 1088 risk of sparking in the large area detectors that ATLAS will use.

1089 In ATLAS, the micromegas drift gap will be 5 mm and the amplification gap will be $128\ \mu\text{m}$. They are

1090 filled with the same gas mixture as the MDTs. They will be stacked in an octuplet in an XXUV-UVXX
 1091 geometry, where X refers to nominal strips and U and V refer to stereo strips at an angle of $\pm 1.5^\circ$. This
 1092 arrangement allows for measurement of the azimuthal coordinate and gives a large lever arm between the
 1093 straight strips for triggering purposes. Figure 2.12 shows the geometry of a single micromegas detector as
 1094 well as its operating principle [57].

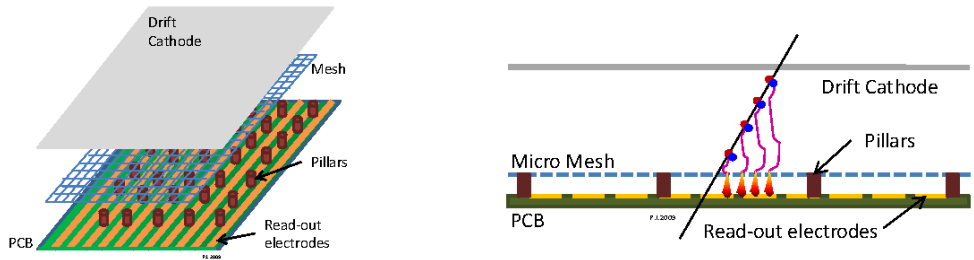


Figure 2.12: Illustrations of the geometry (left) and operating principle (right) of the micromegas detector [57].

1095 sTGCs

1096 The sTGCs are similar to the TGCs currently in the ATLAS endcap muon system [44]. They consist
 1097 of gold-plated tungsten wires (with a 1.8 mm pitch) between two cathode planes 1.4 mm away from the
 1098 wire plane. One cathode plane consists of strips with a 3.2 mm pitch (much smaller pitch than the TGCs),
 1099 while the other consists of coarser pads that are used for defining regions of interest in the sTGC trigger
 1100 algorithm. Figure 2.13 shows the basic detector geometry.

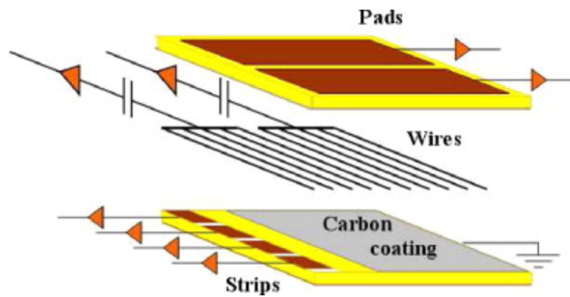


Figure 2.13: Geometry of the sTGC detector [57].

1101 2.3.3 PHYSICS IMPACT

1102 Maintaining low p_T thresholds for muons while still staying within the trigger rate budget at Level 1 for the
1103 muon system (20 kHz) is crucial for physics analyses to be successful in high luminosity conditions. One
1104 realm where the lepton trigger threshold is especially important is in Higgs physics. In the $H \rightarrow WW^*$
1105 analysis, one of the W bosons is off shell and tends to decay to soft leptons. In associated production of a
1106 Higgs with a W , the lepton is also important because it provides the main handle which allows the event
1107 to be triggered. Without the NSW, analyses would be required to either raise the muon p_T threshold or
1108 only use muons triggered from the barrel muon system. Table 2.3 shows that both of these alternatives
1109 significantly reduce the Higgs signal efficiency. With the NSW, the signal efficiency is largely maintained
1110 and the triggers can remain unprescaled at lower p_T thresholds.

Threshold	$H \rightarrow b\bar{b}$ (%)	$H \rightarrow WW^*$ (%)
$p_T > 20 \text{ GeV}$	93	94
$p_T > 40 \text{ GeV}$	61	75
$p_T > 20 \text{ GeV} (\text{barrel only})$	43	72
$p_T > 20 \text{ GeV} (\text{with NSW})$	90	92

Table 2.3: Signal efficiencies for WH production with $H \rightarrow b\bar{b}$ and $H \rightarrow WW^* \rightarrow \mu\nu qq$ under different trigger configurations [57].

1111 2.4 OBJECT RECONSTRUCTION IN ATLAS

1112 ATLAS analyses first start by requiring the presence of certain reconstructed physics objects in the event.
1113 This section will present a brief overview of the algorithms used to reconstruct electrons, muons, jets (in-
1114 cluding b -jets), and missing energy². The performance of physics object reconstruction and identification
1115 will also be discussed as these are relevant to the analyses presented later. Figure 2.14 gives an overview of
1116 the different sub-detectors that each type of particle will interact with in ATLAS.

²Reconstruction algorithms for other objects, such as photons and hadronically decaying τ leptons, are not detailed here as these objects are not used in the results presented in this dissertation.

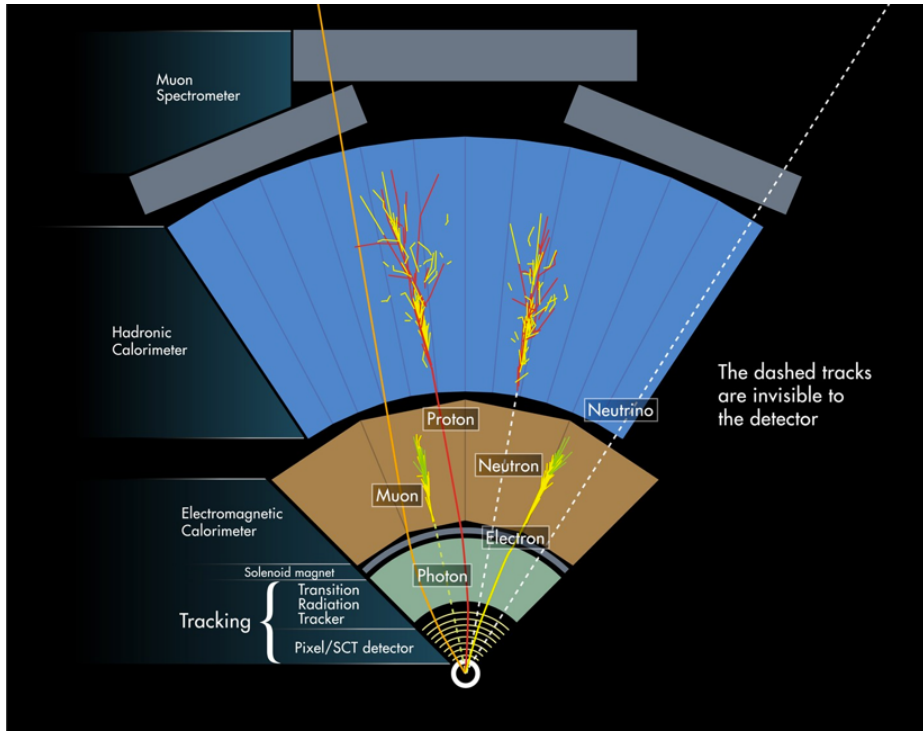


Figure 2.14: Illustration of particle interactions in ATLAS [60]

1117 2.4.I ELECTRONS

1118 Electrons in ATLAS will leave tracks in the inner detector and energy deposits in the electromagnetic
1119 calorimeter. The algorithm for recognizing the signature of electrons proceeds in two steps: reconstruction
1120 and identification.

1121 In reconstruction, an electron candidate is formed by matching EM calorimeter deposits with ID tracks.
1122 The algorithm first chooses seed clusters in the EM calorimeter by using a sliding window algorithm that
1123 searches for towers with transverse energy larger than 2.5 GeV. In addition to seed clusters, track candi-
1124 dates must be identified in the ID. The algorithm selects seed tracks with $p_T > 1$ GeV that do not fit well
1125 with a pion hypothesis. Once candidate tracks are selected, they are re-fit with a Gaussian Sum Filter (GSF)
1126 algorithm to estimate electron parameters [61]. Finally, an electron candidate is formed if at least one track
1127 matches to a seed cluster in the calorimeter. The full details of the reconstruction algorithm can be found
1128 in reference [62].

1129 Once an electron candidate is present, identification criteria must be applied in order to reject fake elec-

trons from background. Many different variables are used for this identification. They include information about the shower shape in the EM calorimeter and the amount of leakage into the hadronic calorimeter, as well as information from the ID and in particular the TRT. There are both selection requirement based and likelihood-based criteria that range from “loose” to “very tight”. For details, see reference [62]. In the $H \rightarrow WW^*$ analysis, both medium and very tight likelihood electrons are used depending on the electron p_T .

Figure 2.15 shows the algorithm’s reconstruction efficiency for true electrons with different identification criteria as well as the electron energy resolution in simulation [62, 63]. The reconstruction efficiency is measured using both the Z and J/ψ with 8 TeV data.

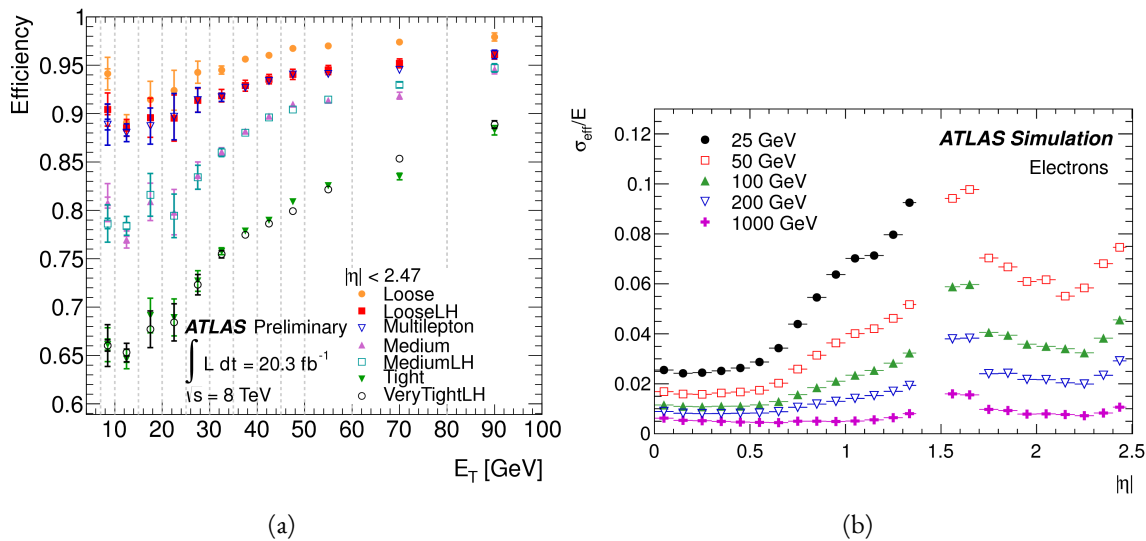


Figure 2.15: Electron performance: (a) reconstruction efficiency as a function of electron E_T [62] (b) energy resolution in simulation as a function of $|\eta|$ for different energy electrons [63].

2.4.2 MUONS

The ATLAS detector is designed to stop most particles before they reach the muon spectrometer. Muons, however, are minimum ionizing particles, meaning that they will not lose a significant amount of energy through interactions with the detector and will thus pass through. Therefore, the muon reconstruction works to match tracks in the muon spectrometer with tracks in the inner detector.

1144 The first step of reconstruction is to reconstruct local straight line tracks, called segments, in each muon
1145 chamber. Segments are then fit to larger tracks that traverse the entire muon spectrometer. Such muon
1146 tracks are referred to as “standalone” tracks (SA) as they only use information from the muon spectrometer.
1147 The standalone tracks are then matched to tracks in the inner detector to form “combined” (CB) muons,
1148 and both tracks are used to determine the momentum and direction of the muon. To improve acceptance,
1149 segment-tagged and calorimeter-tagged muons are also reconstructed. In these cases, ID tracks are matched
1150 to segments in the MS and calorimeter deposits consistent with a minimum ionizing particle, respectively.
1151 The details of the reconstruction can be found in reference [64].

1152 As with electrons, once muon candidates are reconstructed they have identification criteria applied to
1153 reduce background. These criteria include the χ^2 match between the ID and MS tracks, the number of
1154 hits in the ID, overall ID and MS track fit quality, and additional variables. In Run 1, the muons used are
1155 simply referred to as combined muons [64]. In Run 2, an improved reconstruction algorithm is used and
1156 criteria ranging from “loose” to “tight” are defined (similar to what is done with electrons) [65]. Figure 2.16
1157 shows the muon reconstruction efficiency (measured with the Z and J/ψ) and invariant mass resolution
1158 in $\sqrt{s} = 8$ TeV data.

1159 2.4.3 JETS

1160 When a quark or gluon is produced in collisions, it is not measured directly in ATLAS. Rather, due to
1161 QCD effects, it produces a collimated spray of hadrons in the direction of the original parton, which is
1162 known as a jet. Jets are reconstructed in ATLAS using energy deposits in the hadronic calorimeter. The
1163 first step is build “topological clusters” out of energy deposits in calorimeter cells [66, 67]. This is done
1164 using strategy where seed cells are chosen by picking cells whose energy measurements are four times the
1165 amount of noise expected for that cell. Adjacent cells with at least 2σ energy measurements are added to
1166 the cluster, then a final layer of clusters with energy above 0σ are added. Once calorimeter clusters are
1167 formed, they are clustered further into jet candidates. The analyses presented in this thesis use the anti- k_T
1168 jet clustering algorithm [68]. This algorithm defines a parameter R that appears in the denominator of
1169 the clustering distance metric and defines the radial size of the jet in η - ϕ space.

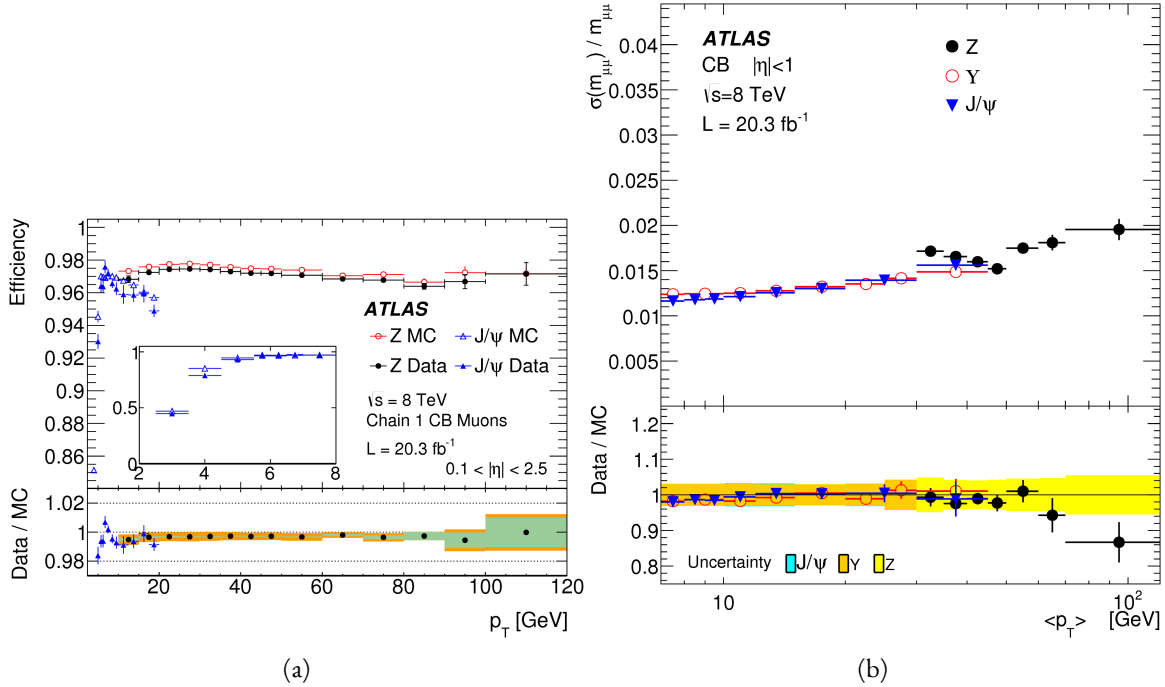


Figure 2.16: Muon performance in $\sqrt{s} = 8$ TeV data: (a) reconstruction efficiency as a function of muon p_T (b) dimuon mass resolution as a function of average p_T [64].

The energy response of the calorimeter must be properly characterized in order to reconstruct the true jet energy. Calorimeter clusters can be calibrated either with the EM calibration, where each cluster is assumed to have come from the energy deposit of an electron or photon, or the LCW calibration, where local cluster weights are computed to allow for local calibration of clusters as hadronic or electromagnetic. The details of the jet energy calibration are not discussed here and are presented in reference [69]. Figure 2.17 shows the jet energy response after calibration in Monte Carlo as a function of the true p_T of the jet [69]. Analyses often need to know how consistent a particular jet is with the primary vertex of the event in order to avoid contamination from pileup interactions. One measure of this consistency is known as the jet vertex fraction (JVF). The JVF is the ratio of tracks associated with a primary vertex to the total number of tracks inside a jet. Jets from the primary interaction in the event should have a large fraction of tracks consistent with the primary vertex and therefore have a large JVF value.

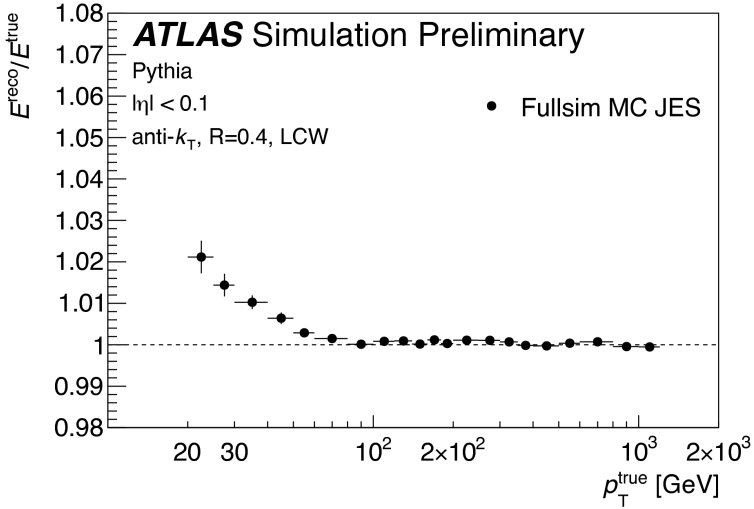


Figure 2.17: Jet energy response after calibration as a function of true p_T in simulation [69].

1181 2.4.4 b -TAGGING

1182 One important aspect of jet physics is the task of identifying the flavor of parton that produced the mea-
 1183 sured jet. While in general this is very difficult, jets from b -quarks offer an interesting case where such
 1184 identification is possible. B mesons have a lifetime on the order of 10^{-12} seconds, which makes a $c\tau$ of
 1185 0.5 mm [6]. This type of displaced decay vertex can be identified in detectors like ATLAS and allows b -jets
 1186 to be distinguished from other flavors of jets³. With boosts, B mesons can travel for several millimeters
 1187 before decaying.

1188 ATLAS uses several algorithms, including a multivariate machine learning technique, to identify jets
 1189 from b -quarks. The inputs to the multivariate algorithm are determined from lower level reconstruction
 1190 algorithms. There are three distinct algorithms that reconstruct variables which are used as input to the
 1191 multivariate technique.

1192 The first family of algorithms is referred to as IPx D (where the x can either be 2 or 3). These algorithms
 1193 use the transverse and longitudinal impact parameters d_0 and z_0 of the tracks inside a jet to determine their
 1194 consistency with the primary vertex. They use two or three dimensional (hence the x) templates for light

³Jets from charm quarks can also be detected in this way but they do not live quite as long so the displacement of the vertex is harder to distinguish

1195 flavor, charm, and bottom jets and then evaluate the likelihood of the jet coming from each of these types.

1196 The likelihood ratios are used as inputs to the multivariate algorithm.

1197 The next two algorithms used as input are referred to as the secondary vertex (SV) and JetFitter (JF)
1198 algorithms. The SV algorithm uses tracks inside the jet to fit for vertices that are displaced from the pri-
1199 mary vertex. The JF algorithm attempts to reconstruct the full flight path of the b by looking for multiple
1200 displaced vertices along the same line (as B decays often result in subsequent charm meson decays).

1201 In Run 1, the multivariate b -tagging algorithm used a neural network and was referred to as MV1. The
1202 details of this algorithm and its inputs are given in reference [70]. This algorithm is used for defining
1203 a veto on b -jets in the $H \rightarrow WW^* \rightarrow \ell\nu\ell\nu$ analysis presented in Part 2. In Run 2, the number of
1204 inputs was simplified and a boosted decision tree with 24 input variables was used, referred to as MV2 [71].
1205 The MV2 algorithm is a boosted decision tree incorporating twenty-four input variables constructed from
1206 three lower level input algorithms described above. This algorithm is used for b -tagging in the $X \rightarrow$
1207 $HH \rightarrow b\bar{b}b\bar{b}$ search presented in Part 3. Figure 2.18 summarizes the inputs to MV2. Figure 2.19 shows the
1208 performance of each of these algorithms in Run 1 and Run 2.

IP2D and IP3D (6 inputs)	SV1 (8 inputs)	JetFitter (8 inputs)
$\log(p_b/p_u)$	Mass	Mass
$\log(p_b/p_c)$	Energy fraction	Energy fraction
$\log(p_c/p_u)$	# tracks at vertex	# vertices
	# 2 track vertices	# tracks at vertex
	Lxy	# 1 track vertices
	L3d	# 2 track vertices
	3D significance	3D significance
	ΔR	ΔR
Kinematics (2 inputs)		
	p_T	
	η	

Figure 2.18: Summary of the inputs to the MV2 b -tagging algorithm.

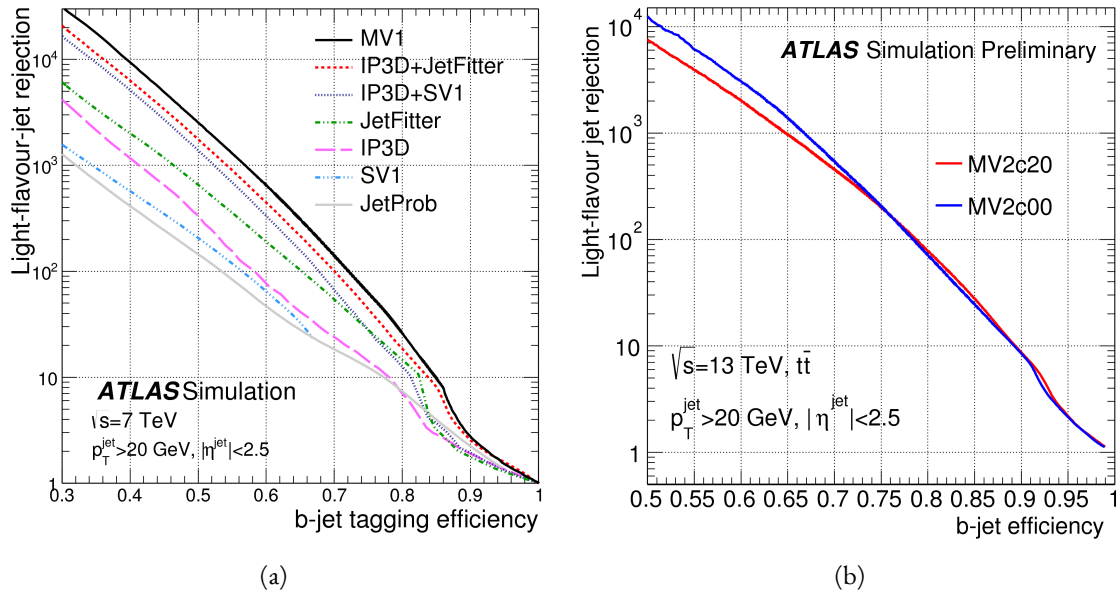


Figure 2.19: Light jet rejection ($1/\text{efficiency}$) vs. b -jet efficiency for MV1 and its input algorithms (a) [70] and MV2 (b) [71] in simulated $t\bar{t}$ events. The numbers in the algorithm names in (b) refer to the fraction of charm events used in the MV2 training.

1209 2.4.5 MISSING TRANSVERSE ENERGY

1210 As noted in figure 2.14, neutrinos produced in ATLAS will pass through the detector without interacting.
 1211 The only way of detecting the presence of weakly interacting particles like neutrinos (or BSM particles
 1212 that are long-lived) is to use missing transverse momentum. The basic principle of missing transverse en-
 1213 ergy is to use the momentum balance of the incoming protons to infer the presence of missing particles.
 1214 The net longitudinal momentum of the incoming partons that collide is not known (since each carries
 1215 an unknown fraction of the proton's momentum). However, the protons (and thus incoming partons)
 1216 have essentially no net momentum in the plane transverse to the beam line (the x - y plane). Therefore, if
 1217 there are no undetected particles in the final state, the transverse momenta of all of the final state particles
 1218 should balance. The magnitude of the imbalance in the transverse plane is known as missing transverse
 1219 momentum (E_T^{miss}).

1220 The basic calculation of missing transverse momentum from calorimeter cells is given in equation 2.4 [72].

1221

$$\begin{aligned} E_x^{\text{miss}} &= -\sum_{i=1}^{N_{\text{cell}}} E_i \sin \theta_i \cos \phi_i \\ E_y^{\text{miss}} &= -\sum_{i=1}^{N_{\text{cell}}} E_i \sin \theta_i \sin \phi_i \end{aligned} \quad (2.4)$$

1222 The E_T^{miss} calculation is separated into different terms based on the objects that the calorimeter clusters
 1223 are associated with. This way, each cell's contribution is calibrated appropriately according to the object.
 1224 This separation of terms used to define the E_T^{miss} in Run 1 is shown in equation 2.5 [72].

$$\begin{aligned} E_{x(y)}^{\text{miss,calo}} &= E_{x(y)}^{\text{miss},e} + E_{x(y)}^{\text{miss},\gamma} + E_{x(y)}^{\text{miss},\tau} + E_{x(y)}^{\text{miss,jets}} \\ &\quad + E_{x(y)}^{\text{miss,softjets}} + E_{x(y)}^{\text{miss},\mu} + E_{x(y)}^{\text{miss,CellOut}} \end{aligned} \quad (2.5)$$

1225 The CellOut term of the above equation corresponds to calorimeter cells with energy deposits that are
 1226 not associated with other objects. The soft jets term comes from cells associated to jets with p_T between
 1227 7 and 20 GeV, while the jets term comes from jets with $p_T > 20$ GeV. Because muons do not deposit
 1228 significant energy in the calorimeter, the muon momentum (after correction for the energy deposited in
 1229 the calorimeter for non-isolated muons) is used for the muon term [72]. The final E_T^{miss} is calculated using
 1230 equation 2.6.

$$E_T^{\text{miss}} = \sqrt{(E_x^{\text{miss}})^2 + (E_y^{\text{miss}})^2} \quad (2.6)$$

1231 Figure 2.20 shows the resolution of the components of the E_T^{miss} with different pileup suppression tech-
 1232 niques [73].

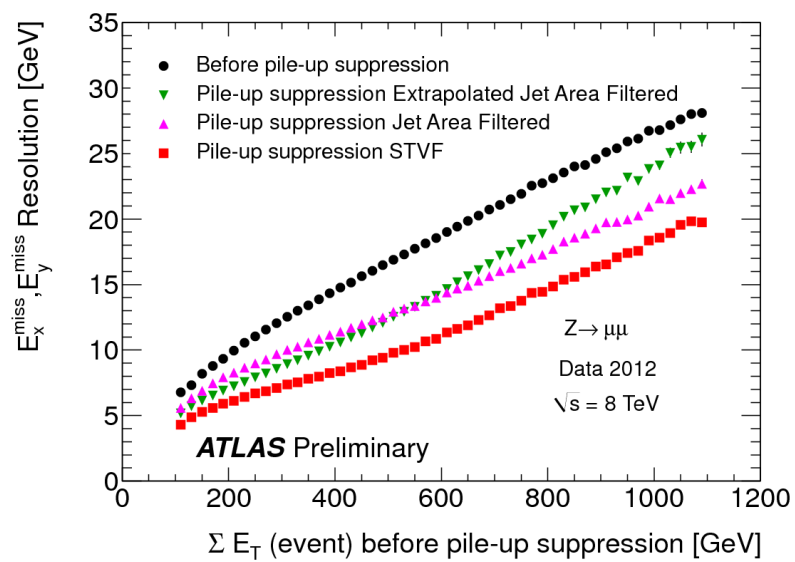


Figure 2.20: Resolution of E_T^{miss} components as a function of $\sum E_T$ before pileup suppression with different pileup techniques [73].

1233

Part II

1234

Observation and measurement of Higgs

1235

boson decays to WW^* in LHC Run I at

1236

$\sqrt{s} = 7$ and 8 TeV

*Basic research is what I am doing when I don't know what
I am doing.*

Wernher von Braun

3

1237

1238

$H \rightarrow WW^* \rightarrow \ell\nu\ell\nu$ Analysis Strategy

1239 3.1 INTRODUCTION

1240 This chapter presents an overview of the strategy for searching for a Higgs boson in the $H \rightarrow WW^* \rightarrow$
1241 $\ell\nu\ell\nu$ decay topology. Its purpose is to define in broad terms how the search and measurement are under-
1242 taken, discussing common aspects of the analysis before going into the details of individual sub-categories.
1243 First, the properties of the Higgs signal are discussed and the associated backgrounds are presented. Next,
1244 the observables used to enhance the signal to background ratio are defined. Finally, the parameters of in-
1245 terest in the search and measurement will be shown, along with a brief overview of the statistical treatment
1246 of the final Higgs candidates.

1247 Following this chapter, three different results from the $H \rightarrow WW^* \rightarrow \ell\nu\ell\nu$ channel are shown.
1248 Chapter 4 presents the discovery and subsequent measurement of Higgs boson production in gluon fusion
1249 mode and the role of the $H \rightarrow WW^*$ channel. Chapter 5 shows the search and first evidence in ATLAS
1250 for the Vector Boson Fusion (VBF) production mode of the Higgs. Finally, chapter 6 shows the combined

1251 Run 1 $H \rightarrow WW^*$ results for the measurement of the Higgs cross section and relative coupling strengths
1252 to other SM particles.

1253 3.2 THE $H \rightarrow WW^* \rightarrow \ell\nu\ell\nu$ SIGNAL IN ATLAS

1254 The signal studied in this and subsequent chapters is the Higgs boson in the WW^* final state, where each
1255 W boson subsequently decays into a charged lepton and a neutrino. In the simplest decay path, the final
1256 state consists of two neutrinos and two charged leptons, each of which can be either an electron or a muon.
1257 If a W decays to a τ lepton, only leptonic decays of the τ are considered. The τ leptons produce additional
1258 neutrinos in the final state but still yield two charged leptons (where each lepton is an electron or muon).
1259 Neutrinos are not detected in ATLAS, so the final state ultimately consists of two reconstructed leptons
1260 and missing transverse momentum. Final states where both of the charged leptons are electrons or muons
1261 are referred to as the “same flavor” ($ee/\mu\mu$) final states, while those with one electron and one muon are
1262 referred to as “different flavor” ($e\mu$ or μe).

1263 There can be additional jets produced in association with the Higgs boson. As described in detail in
1264 Chapter 1, if the Higgs is produced via vector boson fusion production, there will be two additional forward
1265 jets in the event. In gluon fusion, one or more jets can be produced through initial state radiation from
1266 the incoming gluons. Because of the varying background composition as a function of jet multiplicity,
1267 each bin in this variable has its own dedicated requirements applied in the search and measurement. The
1268 $n_j = 0$ and $n_j = 1$ bins are dedicated to gluon fusion production, while the $n_j \geq 2$ bin has separate
1269 dedicated searches for ggF and VBF production.

1270 Figure 3.1 shows the relative branching fractions for the $H \rightarrow WW^*$ process, calculated from the Par-
1271 ticle Data Group values for the W and τ branching ratios [6]. The largest branching ratio corresponds
1272 to both W bosons decaying to quark pairs at 45.44%. The second largest ratio is for one W decaying lep-
1273 tonically and the other decaying to quarks, a branching ratio of 34.18%. In all cases, ℓ denotes either an
1274 electron or muon, and the leptonic branching ratios of the τ are included. For example, the $\ell\nu qq$ final
1275 state includes one W decaying to $e\nu$, $\mu\nu$, or $\tau\nu$. In the case of the $W \rightarrow \tau\nu$ decay, the τ lepton then
1276 decays to an electron or muon via $\tau \rightarrow \nu_\tau \ell \nu_\ell$. Final states with a τ_h refer to hadronic decays of the τ . The

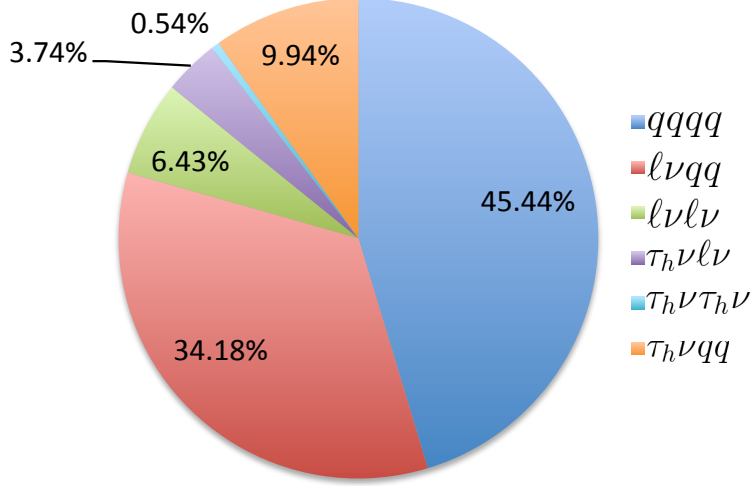


Figure 3.1: Branching ratios for a WW system. q refers to quarks. ℓ can be either an electron or muon, and the leptonic branching ratios of the τ are included. For example, the $\ell\nu qq$ final state includes one W decaying to $e\nu$, $\mu\nu$, or $\tau\nu$. τ_h refer to hadronic decays of the τ .

¹²⁷⁷ branching ratio of the $\ell\nu\ell\nu$ final state is 6.43%.

¹²⁷⁸ While the $\ell\nu\ell\nu$ final state is not a large fraction of the branching ratio, there are significant advantages
¹²⁷⁹ to using this channel in an analysis. First, both the $qqqq$ and $\ell\nu qq$ channels suffer from a large QCD
¹²⁸⁰ multijet background, which is often difficult to model. Second, events in the the $\ell\nu\ell\nu$ channel in data can
¹²⁸¹ be triggered more efficiently due to the presence of two leptons.

¹²⁸² Figure 3.2 delineates the different signal regions used in the gluon fusion and vector boson fusion anal-
¹²⁸³ yses of $H \rightarrow WW^*$. Signal regions are defined using jet multiplicity and the flavor combination of the
¹²⁸⁴ final state leptons.

¹²⁸⁵ 3.3 BACKGROUND PROCESSES

¹²⁸⁶ Many processes from the Standard Model can also produce a final state with two leptons and missing
¹²⁸⁷ transverse momentum. This section describes the dominant backgrounds to Higgs production and further
¹²⁸⁸ explains how they can be reduced. Table 3.1 summarizes the different background processes.

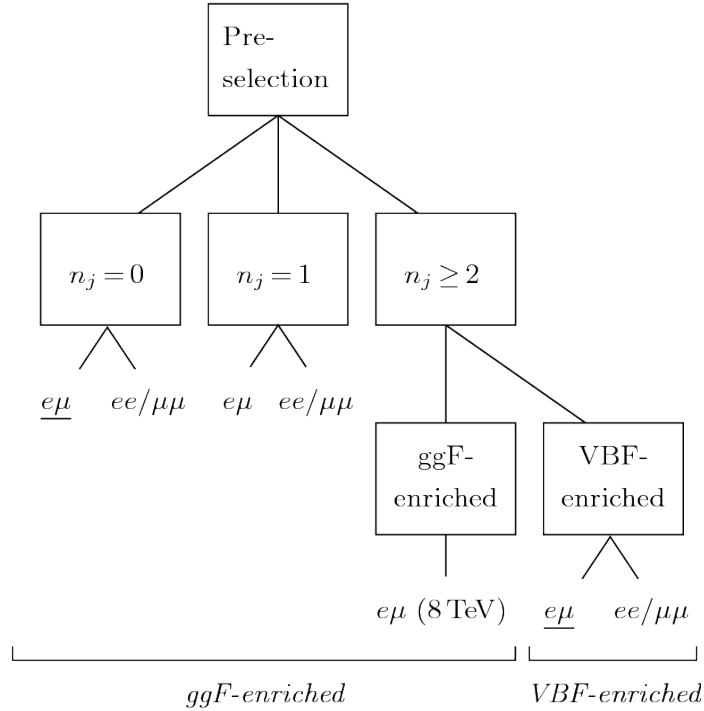


Figure 3.2: An illustration of the unique analysis signal regions [74]. The most sensitive regions for both gluon fusion and vector boson fusion production are underlined.

1289 3.3.1 STANDARD MODEL WW PRODUCTION

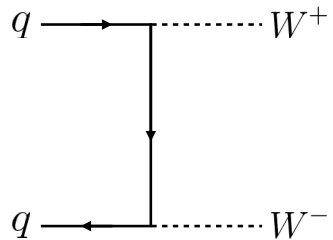


Figure 3.3: Feynman diagram for Standard Model WW production

1290 Non-resonant Standard Model diboson production, as shown in figure 3.3, is an irreducible background
1291 to Higgs boson production in the WW final state. It produces the same exact final state objects, namely
1292 leptonically decaying W bosons. There are no additional objects in the final state that allow for back-
1293 ground reduction. Therefore the analysis solely relies on the correlations between the leptons to reduce
1294 this background.

1295 3.3.2 TOP QUARK PRODUCTION

1296 Top quark production can mimic the Higgs in the WW^* final state as well. Top quarks can be produced
1297 either in pairs ($t\bar{t}$ production) or singly (s -channel, t -channel, or associated production Wt). The domi-
1298 nant top background are $t\bar{t}$ and Wt production.

1299 Because top quarks decay via $t \rightarrow Wb$, top pair production can produce a final state with two W bosons
1300 that then decay leptonically. In Wt production, there are two real W bosons produced, as with $t\bar{t}$. In
1301 both cases, there is at least one b -jet in the final state. By vetoing on the presence of b -jets, these top quark
1302 backgrounds can be reduced. Figure 3.4 shows the Feynman diagrams for $t\bar{t}$ and Wt production.

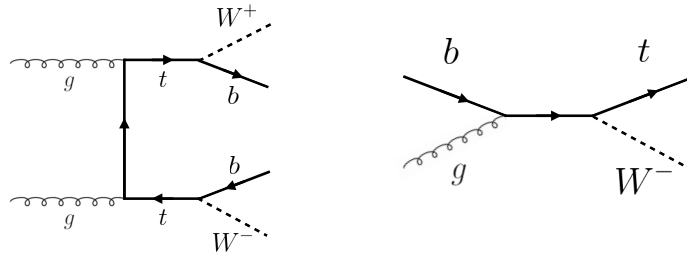


Figure 3.4: Feynman diagrams for top pair production (left) and Wt production (right)

1303 3.3.3 W +JETS BACKGROUND

1304 Single W boson production in association with jets is a unique background to Higgs production. The
1305 other backgrounds considered thus far have all included two prompt leptons, each decaying from a W
1306 boson, in the final state. In W +jets production, however, only one reconstructed lepton originates from
1307 a W . The second reconstructed lepton is either an algorithmic “fake” or the result of non-prompt decays.
1308 In the first case, the lepton is a jet misidentified as a lepton by either the electron or muon reconstruction
1309 algorithms. In the second case, the lepton may be a real lepton but coming from semi-leptonic decays of
1310 particles inside the shower of the jet. This background can be reduced by requiring that the reconstructed
1311 lepton have little activity in the surrounding region of the calorimeter (also known as an “isolation”). Fig-
1312 ure 3.5 shows the Feynman diagram for W +jets production.

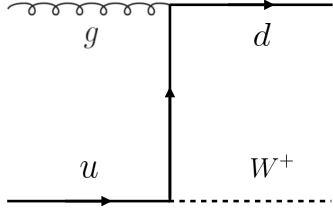


Figure 3.5: An example Feynman diagram of W +jets production

1313 3.3.4 Z/γ^* +JETS BACKGROUND

1314 Production of a Z boson or virtual photon (also known as Drell-Yan and denoted with Z/γ^*) in associa-
1315 tion with jets is also a background to Higgs production. The Z boson decays to two leptons of the same
1316 flavor. However, the background is present in both the same flavor and different flavor samples. When the
1317 Z/γ^* decays directly to electrons or muons, the background enters the same flavor final state sample, and
1318 when it decays to two τ leptons the background can enter the different flavor sample as well. Figure 3.6
1319 shows the production of a Z in association with one jet. Because there are no neutrinos in this final state,
1320 variables like E_T^{miss} can be used to reduce the background¹.

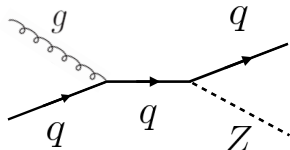


Figure 3.6: An example Feynman diagram of Z +jets production

1321 3.3.5 SUBDOMINANT BACKGROUNDS

1322 There are additional processes which contribute to the background composition. These backgrounds are
1323 subdominant and contribute less to the total background estimate than those discussed previously. The

¹The E_T^{miss} cut is much more effective for the reduction of Z/γ^* production in the same flavor final state. If the background enters the different flavor final state through τ decays, there will be neutrinos present. Other requirements on the lepton invariant mass are made to reduce the $Z/\gamma^* \rightarrow \tau\tau$ background.

1324 first process is referred to as VV or “Other diboson” processes and includes multiple Standard Model
 1325 diboson processes, including WZ , ZZ , $W\gamma$, $W\gamma^*$, and $Z\gamma$ production. Additionally, there is a back-
 1326 ground contribution from QCD multijet production. While the cross section for this process is large, its
 1327 contribution to the WW^* final state is small because two jets must be misidentified as leptons.

Category	Process	Description
SM WW	$WW \rightarrow \ell\nu\ell\nu$	Real leptons and neutrinos
Top quark production	$t\bar{t} \rightarrow WbW\bar{b} \rightarrow \ell\nu b\ell\nu\bar{b}$	Real leptons, untagged b s
	$tW \rightarrow WbW \rightarrow \ell\nu\ell\nu b$	Real leptons, untagged b
	$t\bar{b}, t\bar{q}\bar{b}$	Untagged b , jet misidentified as lepton
Drell-Yan	$Z/\gamma^* \rightarrow ee, \mu\mu$	“Fake” E_T^{miss}
	$Z/\gamma^* \rightarrow \tau\tau \rightarrow \ell\nu\nu\ell\nu\nu$	Real leptons and neutrinos
Other dibosons	$ZZ \rightarrow \ell\ell\nu\nu$	Real leptons and neutrinos
	$W\gamma^*, WZ \rightarrow \ell\nu\ell\ell, ZZ \rightarrow \ell\ell\ell\ell$	Unreconstructed leptons
	$W\gamma, Z\gamma$	γ reconstructed as e , unreconstructed lepton
$W + \text{jets}$	$Wj \rightarrow \ell\nu j$	Jet reconstructed as lepton
QCD multijet	jj	Jets reconstructed as leptons

Table 3.1: A summary of backgrounds to the $H \rightarrow WW^* \rightarrow \ell\nu\ell\nu$ signal

1328 3.4 SHARED SIGNAL REGION SELECTION REQUIREMENTS

1329 As presented in section 3.2, there are many different combinations of physics objects that can define a
 1330 $H \rightarrow WW^* \rightarrow \ell\nu\ell\nu$ final state. The multiplicity of jets and the flavor combinations of the leptons
 1331 both lead to many potential signal regions. Additionally, signal regions can be optimized separately to be
 1332 sensitive to the distinct production modes of the Higgs. Gluon fusion, vector boson fusion, and associated
 1333 production of a Higgs all lead to unique final state topologies. While there are different optimizations
 1334 possible in each signal region, there are also some commonly shared selections that will be described here.

1335 3.4.1 EVENT PRE-SELECTION

1336 Before being sorted into the distinct signal regions, basic requirements are applied to the reconstructed
 1337 objects in the event to select Higgs-like event candidates. First, two oppositely charged leptons are required.
 1338 Once the leptons are selected, the last requirement for event pre-selection is the presence of neutrinos.
 1339 E_T^{miss} is used as a proxy for the combined neutrino momentum in the transverse plane.

1340 In general, the signal tends to have higher values of E_T^{miss} than backgrounds, especially if these back-
 1341 grounds do not contain neutrinos in the final state. It is possible mis-measurements of objects in the detec-
 1342 tor can lead to imbalances in the transverse plane. When such a mis-measurement occurs, the E_T^{miss} vector
 1343 in the transverse plane will often point in the same direction as the mis-measured object. Therefore, a new
 1344 variable, $E_{T,\text{rel}}^{\text{miss}}$, is used in the pre-selection. $E_{T,\text{rel}}^{\text{miss}}$ is defined in equation 3.1.

$$E_{T,\text{rel}}^{\text{miss}} = \begin{cases} E_T^{\text{miss}} \sin \Delta\phi_{\text{near}} & \text{if } \Delta\phi_{\text{near}} < \pi/2 \\ E_T^{\text{miss}} & \text{otherwise,} \end{cases} \quad (3.1)$$

1345 If the closest object to the E_T^{miss} vector is within $\pi/2$ radians in the transverse plane, the E_T^{miss} is projected
 1346 away from this object. Otherwise, the normal E_T^{miss} vector is used. Figure 3.7 shows a graphical illustration
 of this concept.

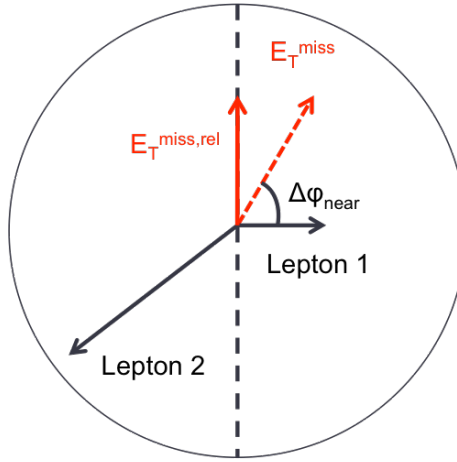


Figure 3.7: A graphical illustration of the $E_{T,\text{rel}}^{\text{miss}}$ calculation.

1347
 1348 Once the lepton and E_T^{miss} pre-selections are made, the analysis is divided into different regions accord-
 1349 ing to jet multiplicity.

1350 3.4.2 JET MULTIPLICITY

1351 Jet multiplicity, denoted as n_j , is used to sub-divide the analysis into distinct signal regions. By creating
 1352 separate signal regions, each bin in jet multiplicity becomes sensitive to different modes of Higgs produc-
 1353 tion and different backgrounds. For example, the $n_j \geq 2$ region is more sensitive to VBF production

1354 because of the two high momentum jets produced at matrix element level. For gluon fusion production
 1355 to enter this bin, two initial state radiation jets must be emitted.

1356 Figure 3.8 shows the jet multiplicity in both the different flavor and same flavor regions after the pre-
 1357 selection. It also shows the background composition in the bins of the number of b -tagged jets, n_b . A
 1358 few trends from this distribution are worth noting. The first is that the Drell-Yan background dominates
 1359 in the same flavor channels for $n_j \leq 1$. Second, the top background becomes a clear contributor to the
 1360 total background for $n_j \geq 1$. Lastly, the SM WW production dominates in the $n_j = 0$ bin, as it is an
 1361 irreducible background to $H \rightarrow WW^*$ production. Because of these distinct features, each jet multiplicity
 1362 bin is treated separately.

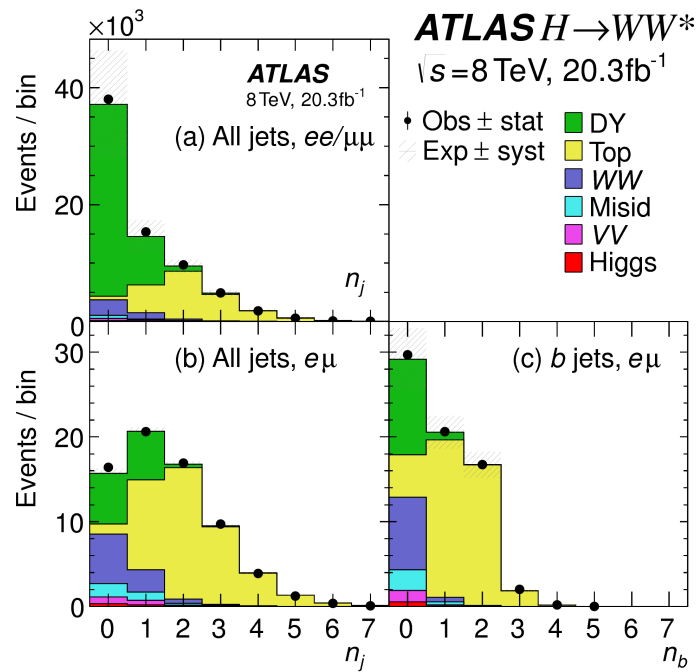


Figure 3.8: Predicted backgrounds (compared with data) as a function of the number of jets, n_j (a and b), and the number of b -tagged jets, n_b (c), after pre-selection requirements. Panel a shows n_j in the same flavor sample, while panels b and c show the n_j and n_b distributions in the different flavor sample.

1363 3.5 BACKGROUND REDUCTION IN SAME-FLAVOR FINAL STATES

1364 As described in section 3.4.2, the background composition of the same flavor final states is different from
 1365 that of the different flavor states. In particular, Drell Yan processes play a much larger role because the

1366 Z/γ^* decays to same flavor leptons. Because real neutrinos are absent in the Z/γ^* decays to ee and $\mu\mu$, a
1367 requirement on E_T^{miss} should largely reduce the background. However, as this section will demonstrate,
1368 with increasing pileup conditions the resolution of the calorimeter-based E_T^{miss} degrades greatly. There-
1369 fore, two new variables for Z/γ^* background reduction are constructed and described in this section.

1370 **3.5.1 PILEUP AND E_T^{miss} RESOLUTION**

1371 Secondary interactions of protons in the colliding bunches of the LHC (known as pileup interactions,
1372 described in detail in Chapter 2) deposit energy into the ATLAS calorimeter in addition to the energy that
1373 comes from the hard scatter process of interest. The calculation of E_T^{miss} is fundamentally like a Poisson
1374 process - summing up all of the energy deposits in individual calorimeter cells or clusters is similar to a
1375 counting experiment. The error on a mean of N in a Poisson distribution is \sqrt{N} , so the energy resolution
1376 scales as \sqrt{E} . As more energy is deposited in the calorimeter, the E_T^{miss} resolution degrades, meaning that
1377 the E_T^{miss} resolution is particularly sensitive to LHC instantaneous luminosity conditions.

1378 Figure 3.9 shows an event display of a $Z/\gamma^* + \text{jets}$ event candidate with the twenty-five reconstructed
1379 primary vertices. This display illustrates that while the interaction of interest only has tracks coming from
1380 the hardest primary vertex, all of the secondary interactions deposit energy in the calorimeter as well.

1381 Figure 3.10 shows the RMS of the E_T^{miss} distribution in $Z \rightarrow \mu\mu$ events (where there are no real neu-
1382 trinos) as a function of the number of the average number of interactions. Under 2011 LHC conditions,
1383 this RMS was approximately 9 GeV, while under 2012 running conditions the resolution worsened to 12
1384 GeV. The increase in pileup dilutes the E_T^{miss} variable's ability to reduce the Z/γ^* background.

1385 **3.5.2 TRACK-BASED DEFINITIONS OF MISSING TRANSVERSE MOMENTUM**

1386 Because the increasing number of secondary proton-proton interactions degrades calorimeter-based E_T^{miss}
1387 resolution, a new variable using only contributions from the primary interaction vertex is necessary to
1388 further reduce the Z/γ^* background. While it is not possible to associate calorimeter energy deposits
1389 with a particular vertex, individual charged particle tracks in the Inner Detector are associated to unique
1390 vertices. Thus, two track-based definitions of missing transverse momentum , using only tracks coming

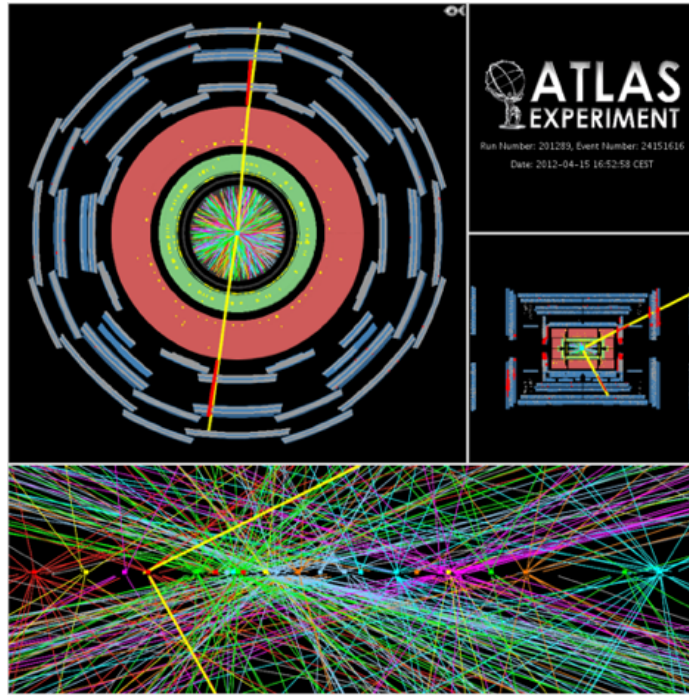


Figure 3.9: An event display of a $Z/\gamma^* + \text{jets}$ event illustrating the effect of pileup interactions

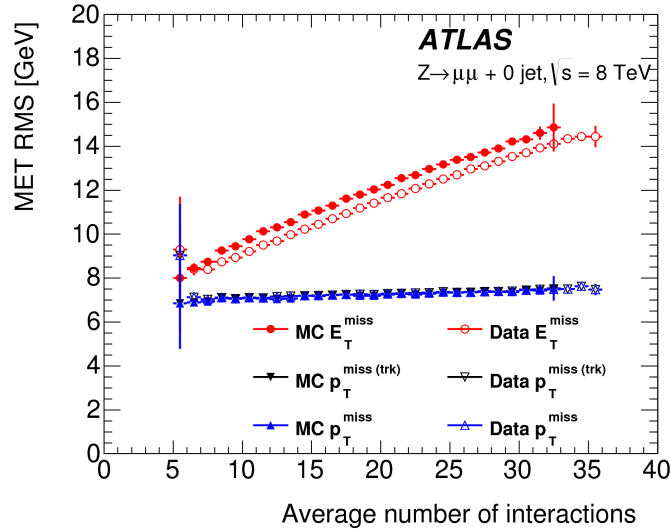


Figure 3.10: The RMS of different missing transverse momentum definitions as a function of the average number of interactions per bunch crossing

1391 from the primary vertex in the event, are used in the analysis. The simplest variable, $p_T^{\text{miss}(\text{trk})}$, is the
 1392 vectorial sum of the p_T of all of the tracks from the primary vertex and the selected leptons (excluding the

¹³⁹³ tracks associated with the selected leptons to avoid double counting). Equation 3.2 defines $p_T^{\text{miss}(\text{trk})}$.

$$p_T^{\text{miss}(\text{trk})} = - \left(\sum_{\text{selected leptons}} p_T + \sum_{\text{other tracks}} p_T \right), \quad (3.2)$$

¹³⁹⁴ To further improve the resolution on the missing transverse momentum, the variable p_T^{miss} is used as de-
¹³⁹⁵ fined in equation 3.3. For selected leptons and jets, the nominal p_T measurements are used. Tracks are used
¹³⁹⁶ to estimate the soft component of the missing transverse momentum instead of calorimeter measurements.

¹³⁹⁷

$$p_T^{\text{miss}} = - \left(\sum_{\text{selected leptons}} p_T + \sum_{\text{selected jets}} p_T + \sum_{\text{other tracks}} p_T \right), \quad (3.3)$$

¹³⁹⁸ Figure 3.10 illustrates that these two new variables accomplish their intended purpose. The resolution as a
¹³⁹⁹ function of mean number of interactions for both $p_T^{\text{miss}(\text{trk})}$ and p_T^{miss} is much flatter than the dependence
¹⁴⁰⁰ for E_T^{miss} . Figure 3.11a shows the difference between the true and reconstructed values of missing transverse
¹⁴⁰¹ momentum using both the track-based p_T^{miss} and calorimeter based E_T^{miss} . The RMS of the distribution
¹⁴⁰² improves by 3.5 GeV when using p_T^{miss} .

¹⁴⁰³ 3.5.3 DISTINGUISHING Z/γ^* +JETS AND $H \rightarrow WW^*$ TOPOLOGIES

¹⁴⁰⁴ In addition to measuring missing transverse momentum, another variable can be constructed to exploit
¹⁴⁰⁵ kinematic and topological differences between the Z/γ^* background and $H \rightarrow WW^*$ signal. Because
¹⁴⁰⁶ there are no real neutrinos in the final state (in the case of $Z/\gamma^* \rightarrow ee, \mu\mu$ decays), the dilepton system will
¹⁴⁰⁷ be balanced with the jets produced in the hard scatter. A new variable, f_{recoil} , is constructed to estimate
¹⁴⁰⁸ the balance between the dilepton system and recoiling jets and is defined in equation 3.4. The transverse
¹⁴⁰⁹ plane is divided into four sections, or quadrants, with one quadrant centered on the dilepton vector. The
¹⁴¹⁰ numerator of f_{recoil} is the magnitude of the vectorial sum of the p_T of jets in the quadrant opposite the
¹⁴¹¹ dilepton system, weighted by each jet's Jet Vertex Fraction (JVF, described in chapter 2). The denominator

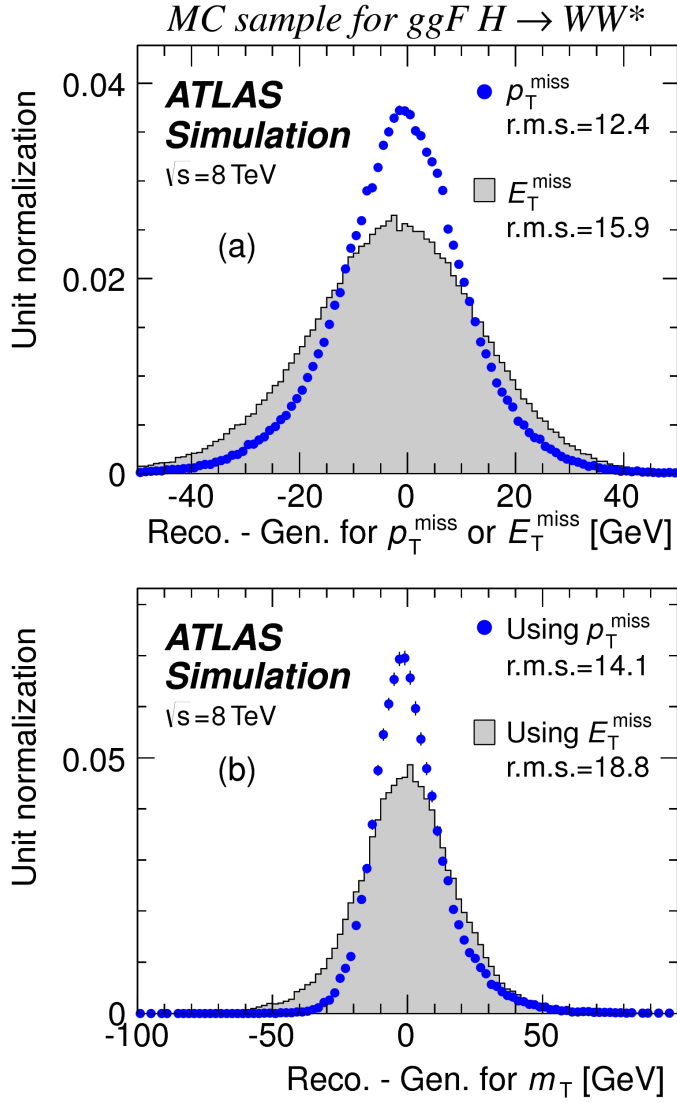


Figure 3.11: The difference between the true and reconstructed values of the missing transverse momentum (a) and m_T (b) in a gluon fusion signal sample using both track-based (p_T^{miss}) and calorimeter-based E_T^{miss} definitions.

¹⁴¹² is the magnitude of the dilepton p_T .

$$f_{\text{recoil}} = \left| \sum_{\text{jets } j \text{ in } \wedge} \text{JVF}_j \cdot \mathbf{p}_T^j \right| / p_T^{\ell\ell}. \quad (3.4)$$

¹⁴¹³ Figure 3.12 shows a shape comparison of the f_{recoil} distribution in a simulated $Z/\gamma^* + \text{jets}$ sample, a
¹⁴¹⁴ $H \rightarrow WW^*$ signal sample, and other backgrounds that contain real neutrinos. The $Z/\gamma^* + \text{jets}$ events

1415 tend to be more balanced between the dilepton system and recoiling jets, while the processes containing
 1416 real neutrinos are less balanced in the transverse plane. Thus, a requirement on f_{recoil} will reduce the Z/γ^*
 1417 + jets background while maintaining a good signal efficiency.

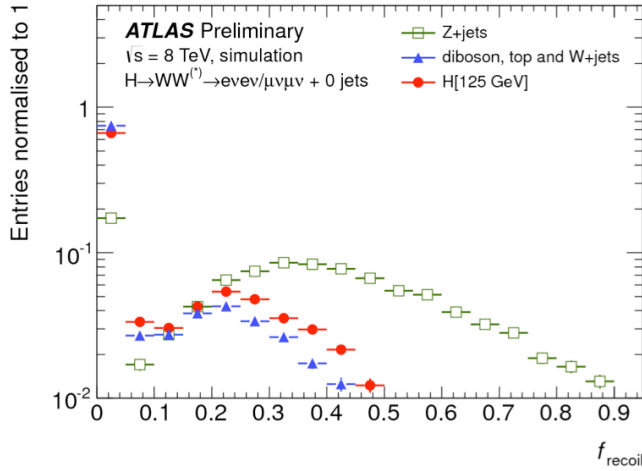


Figure 3.12: Comparison of f_{recoil} distributions for $Z/\gamma^* + \text{jets}$, $H \rightarrow WW^*$, and other backgrounds with real neutrinos.

1418 3.5.4 OPTIMIZING BACKGROUND REDUCTION SELECTION REQUIREMENTS

1419 The requirements on $p_T^{\text{miss}(\text{trk})}$ and f_{recoil} used to reduce the $Z + \text{jets}$ background must be optimized to
 1420 maximize expected signal significance in the same flavor channels. Figure 3.13 shows an optimization of the
 1421 combination of the two requirements in the gluon fusion zero jet bin. Each bin shows the expected signal
 1422 significance if the $p_{T,\text{rel}}^{\text{miss}(\text{trk})}$ (the track-based version of $E_{T,\text{rel}}^{\text{miss}}$) is required to be greater than the left edge
 1423 of the bin and the f_{recoil} is required to be less than the top edge of the bin. The figure shows that the best
 1424 signal significance comes from requiring low values of f_{recoil} (< 0.05) and $p_{T,\text{rel}}^{\text{miss}(\text{trk})}$ values greater than
 1425 45 GeV.

1426 3.6 PARAMETERS OF INTEREST AND STATISTICAL TREATMENT

1427 As with any search or measurement, there are particular parameters of the Higgs that the $H \rightarrow WW^*$
 1428 analysis is interested in measuring. In this case, the parameters of interest are the mass of the Higgs boson

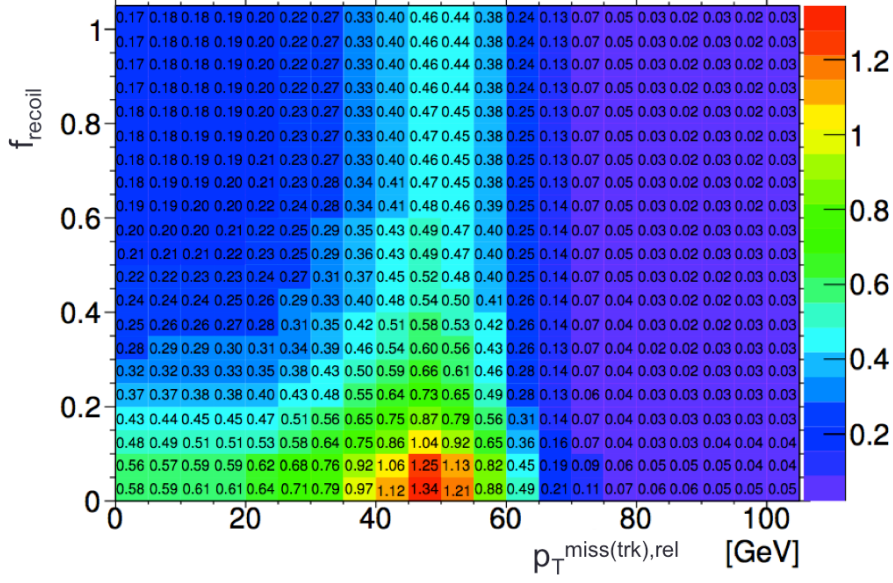


Figure 3.13: Signal significance as a function of required value for f_{recoil} and $p_{T,\text{rel}}^{\text{miss}(\text{trk})}$ in the ggF $H \rightarrow WW^*$ with $n_j = 0$

and its production cross section. In the $H \rightarrow WW^* \rightarrow \ell\nu\ell\nu$ final state, it is not possible to measure the full invariant mass of the Higgs due to the presence of neutrinos. However, a proxy for the invariant mass is defined using transverse plane information and detailed in section 3.6.1. The second parameter of interest is the cross section σ , which in this analysis is measured relative to the theoretical prediction for a Standard Model Higgs. This ratio, μ , is defined in equation 3.5.

$$\mu = \frac{\sigma}{\sigma_{\text{SM}}} \quad (3.5)$$

All of the likelihoods used in the statistical analysis of the final signal region events are parameterized as a function of μ . μ is a natural variable for hypothesis testing, as $\mu = 0$ corresponds to a background only hypothesis and $\mu = 1$ corresponds exactly to a Standard Model Higgs.

3.6.1 TRANSVERSE MASS

The $H \rightarrow WW^* \rightarrow \ell\nu\ell\nu$ analysis cannot reconstruct the full invariant mass of the Higgs because of the neutrinos in the final state. The transverse mass serves as a proxy for the full invariant mass by exploiting

1440 information from the transverse plane. The transverse mass is defined in equation 3.6.

$$m_T = \sqrt{(E_T^{\ell\ell} + p_T^{\text{miss}})^2 - |\vec{p}_T^{\ell\ell} + \vec{p}_T^{\text{miss}}|^2}, \quad (3.6)$$

1441 Here the $E_T^{\ell\ell}$ and $\vec{p}_T^{\ell\ell}$ are the transverse energy and momentum of the dilepton system, while p_T^{miss} is a
1442 proxy for the transverse momentum of the di-neutrino system. The track-based p_T^{miss} is used in the m_T
1443 rather than the calorimeter based E_T^{miss} because it has a better resolution on the true transverse mass.
1444 Figure 3.IIB shows the improvement in the RMS of the difference between the true and reconstructed
1445 transverse mass in a ggF signal sample. The RMS improves by 4.7 GeV using p_T^{miss} in the m_T calculation.

1446 **3.6.2 STATISTICAL TREATMENT**

1447 **LIKELIHOOD FUNCTION**

1448 The statistical analysis² of final event candidates is framed as a hypothesis test, where the null hypothesis is
1449 background-only (no Standard Model Higgs). The first step in the analysis is to form a likelihood function
1450 for the data. In its simplest form, this likelihood is the probability of observing the number of events seen
1451 in the final signal region given knowledge of the signal strength. Because observation of events is funda-
1452 mentally a Poisson counting experiment, this simple likelihood can be expressed as a Poisson probability of
1453 observing N events given a total number of predicted signal and background events. This basic likelihood
1454 is shown in equation 3.7.

$$\mathcal{L}(\mu) = P(N|\mu S + B) \quad (3.7)$$

1455 Here, P is the Poisson probability density function, N is the total number of observed events, μ is the
1456 signal strength, S is the predicted number of signal events, and B is the predicted number of background
1457 events.

1458 Generally, in searches, certain background estimates are commonly normalized in so-called “control” re-
1459 gions and those predictions are scaled by the same normalization factor in the signal region. This method
1460 allows for more precise background estimation by using data as a constraint, reducing the impact of theo-

²Many thanks to Aaron Armbruster, whose thesis [75] inspired parts of this section.

1461 retical uncertainties on the background model. This leads to a slightly more complicated likelihood, which
1462 is a function of both the signal strength and the background normalization. This is shown in equation 3.8.

1463

$$\mathcal{L}(\mu, \theta) = P(N|\mu S + \theta B) P(N_{\text{CR}}|\theta B_{\text{CR}}) \quad (3.8)$$

1464 Here, θ serves as a “nuisance parameter”, or a parameter that is not of primary interest but still enters the
1465 likelihood. The second Poisson term enforces that the background normalization be consistent with the
1466 number of observed events in data in the control region, N_{CR} .

1467 So far, these two formulations of likelihoods have assumed a single signal region and do not take into
1468 account any shape information of potential discriminating variables. The $H \rightarrow WW^*$ analysis is divided
1469 into many different categories, and the counting experiment described above can be performed in each
1470 individual category. As mentioned in section 3.6.1, the transverse mass is used as the primary discriminating
1471 variable in many of the $H \rightarrow WW^*$ signal regions. The same counting experiment can be performed
1472 in each bin of the m_T distribution to incorporate some shape information. Thus, the total likelihood
1473 becomes a product over signal regions and bins of the m_T distribution. Finally, there are usually many
1474 background sources that are normalized in control regions. The new formulation of the likelihood takes
1475 this into account by including a product over control regions in the second Poisson term. All of these
1476 modifications are shown in equation 3.9.

$$\mathcal{L}(\mu, \theta) = \prod_{\substack{\text{SRs } i \\ \text{bins } b}} P\left(N_{ib} \middle| \mu S_{ib} + \sum_{\text{bkg } k} \theta_k B_{kib}\right) \prod_{\text{CRs } l} P\left(N_l \middle| \sum_{\text{bkg } k} \theta_k B_{kl}\right) \quad (3.9)$$

1477 Here, the variable i counts over the different signal regions, b counts over bins of m_T , k counts over the
1478 backgrounds, and l counts over the control regions.

1479 The final step to obtain the full likelihood used in the analysis is to add nuisance parameters for the
1480 systematic uncertainties. In cases where the uncertainty does not affect the shape of m_T bin-by-bin, each
1481 systematic uncertainty ϵ is allowed to affect the expected event yields through a linear response function
1482 of the nuisance parameter, namely $\nu(\theta) = (1 + \epsilon)^{\theta}$. If instead the uncertainty does affect the shape, the
1483 effect is instead parameterized by $\nu_b(\theta) = 1 + \epsilon_b \theta$. The value of the nuisance parameters for the systematic

1484 uncertainty are constrained with a Gaussian term that is added to the likelihood as well. This is of the form
 1485 $g(\delta|\theta) = e^{-(\delta-\theta)^2/2}/\sqrt{2\pi}$, where δ is the central value and θ is a nuisance parameter. Finally, a last term is
 1486 added to account for the statistical uncertainty in the Monte Carlo samples used, which adds an additional
 1487 poisson term. The full likelihood used in the final statistical analysis is defined in equation 3.10.

$$\begin{aligned}
 \mathcal{L}(\mu, \boldsymbol{\theta}) = & \prod_{\substack{\text{SRs i} \\ \text{bins b}}} P \left(N_{ib} \left| \mu S_{ib} \cdot \prod_{\substack{\text{sig.} \\ r}} \nu_{br}(\theta_r) + \sum_{\text{bkg k}} \theta_k B_{kib} \cdot \prod_{\substack{\text{syst.} \\ s}} \nu_{bs}(\theta_s) \right. \right) \\
 & \cdot \prod_{\text{CRs l}} P \left(N_l \left| \sum_{\text{bkg k}} \theta_k B_{kl} \right. \right) \\
 & \cdot \prod_{\substack{\text{syst} \\ t}} g(\delta_t|\theta_t) \cdot \prod_{\text{bkg k}} P(\xi_k|\zeta_k \theta_k)
 \end{aligned} \tag{3.10}$$

1488 Here, $\boldsymbol{\theta}$ represents the full vector of nuisance parameters, r is an index for signal systematics, s is an index
 1489 for background systematics, and t is an index for Monte Carlo samples. The fourth term of the equation
 1490 quantifies the uncertainty due to finite Monte Carlo sample size. Here, ξ represents the central value of the
 1491 background prediction, θ is the associated nuisance parameter, $\zeta = (B/\delta B)^2$, where δB is the statistical
 1492 uncertainty of B .

1493 The best fit value of the signal strength μ is determined by finding the values of μ and $\boldsymbol{\theta}$ that maximize
 1494 the likelihood, while setting $\delta = 0$ and $\xi = \zeta$. Once the likelihood is defined, a test statistic must be built
 1495 for use in hypothesis testing.

1496 TEST STATISTIC

1497 To distinguish whether the data match a background only or background and signal hypothesis, a test
 1498 statistic must be used. The $H \rightarrow WW^*$ analysis uses the profile likelihood technique [76]. The first step
 1499 in formulating this test statistic is to define the profile likelihood ratio, shown in equation 3.11.

$$\lambda(\mu) = \frac{\mathcal{L}(\mu, \hat{\theta}_\mu)}{\mathcal{L}(\hat{\mu}, \hat{\theta})} \tag{3.11}$$

1500 Here $\hat{\theta}_\mu$ is the value of θ that maximizes the likelihood for the choice of μ being tested. Additionally, $\hat{\theta}$
1501 and $\hat{\mu}$ represent the values of θ and μ that gives the overall maximum value of the likelihood.

1502 Once this is defined, a test statistic q_μ is constructed. This is shown in equation 3.12.

$$q_\mu = -2 \ln \lambda(\mu) \quad (3.12)$$

1503 A higher value of q_μ indicates that the data are more incompatible with the hypothesized value of μ , and
1504 q_0 then corresponds to the value of the test statistic for the background only hypothesis. A p_0 value is
1505 then defined to quantify the compatibility between the data and the null hypothesis. The p_0 value is the
1506 probability of obtaining a value of q_0 larger than the observed value, and this is shown in equation 3.13.

$$p_0 = \int_{q_0^{\text{obs}}}^{\infty} f(q_\mu | \mu = 0) dq_\mu \quad (3.13)$$

1507 Here $f(q_\mu)$ is the probability distribution function of the test statistic. Finally, the p_0 value can be con-
1508 verted into a signal significance, using the formula in equation 3.14, or the one-sided tail of the Gaussian
1509 distribution.

$$Z_0 = \sqrt{2} \operatorname{erf}^{-1}(1 - 2p_0) \quad (3.14)$$

1510 The threshold for discovery used in particle physics is $Z_0 \geq 5$, more commonly known as a value of 5σ .

The real voyage of discovery consists not in seeking new landscapes, but in having new eyes.

Marcel Proust

4

1511

1512 The discovery of the Higgs boson and the role 1513 of the $H \rightarrow WW^* \rightarrow \ell\nu\ell\nu$ channel

1514 4.1 INTRODUCTION

1515 This chapter presents the results of the search for the Higgs boson in 4.8 fb^{-1} collected at $\sqrt{s} = 7 \text{ TeV}$
1516 and 5.8 fb^{-1} at $\sqrt{s} = 8 \text{ TeV}$. The results of three searches at $\sqrt{s} = 8 \text{ TeV}$ in the $H \rightarrow WW^* \rightarrow$
1517 $\ell\nu\ell\nu$, $H \rightarrow \gamma\gamma$, and $H \rightarrow ZZ \rightarrow 4\ell$ channels are shown. These results at 8 TeV are combined
1518 with the results of searches at $\sqrt{s} = 7 \text{ TeV}$ in the same channels along with $H \rightarrow \tau\tau$ production and
1519 associated production searches for $H \rightarrow b\bar{b}$. The results of this combination are a 5.9σ detection of a
1520 new particle consistent with a Higgs boson produced via gluon fusion. Rather than going into detail for
1521 all of the different Higgs decay searches, this chapter will discuss the three most sensitive channels and in
1522 particular focus on $H \rightarrow WW^* \rightarrow \ell\nu\ell\nu$. While the focus is on WW^* , some of the ZZ^* and $\gamma\gamma$ results

1523 are shown for completeness. The results not discussed here can be found in the ATLAS Higgs discovery
1524 publication [1].

1525 **4.2 DATA AND SIMULATION SAMPLES**

1526 The data sample used for the following results was taken in 2011 and 2012 at center of mass energies of 7 and
1527 8 TeV, respectively, with 4.8 fb^{-1} collected at 7 TeV and 5.8 fb^{-1} collected at 8 TeV. Higgs production
1528 in the gluon fusion and vector boson fusion modes is modeled with POWHEG for the hard scattering event
1529 and PYTHIA for the showering and hadronization. Associated production of a Higgs with a vector boson
1530 or top quarks is modeled via PYTHIA . Table 4.1 shows the Monte Carlo generators used for modeling the
1531 signal and background processes relevant for the three analyses to be discussed.

Process	Generator
ggF, VBF H	POWHEG + PYTHIA
$WH, ZH, t\bar{t}H$	PYTHIA
$W + \text{jets}, Z/\gamma^* + \text{jets}$	ALPGEN + HERWIG
$t\bar{t}, tW, tb$	MC@NLO + HERWIG
tqb	ACERMC + PYTHIA
$q\bar{q} \rightarrow WW$	MC@NLO + HERWIG
$gg \rightarrow WW$	GG2WW+ HERWIG
$q\bar{q} \rightarrow ZZ$	POWHEG + PYTHIA
$gg \rightarrow ZZ$	GG2ZZ+ HERWIG
WZ	MADGRAPH+ PYTHIA , HERWIG
$W\gamma + \text{jets}$	ALPGEN + HERWIG
$W\gamma^*$	MADGRAPH+ PYTHIA
$q\bar{q}/gg \rightarrow \gamma\gamma$	SHERPA

Table 4.1: Monte carlo generators used to model signal and background for the Higgs search [1].

1532 **4.3 $H \rightarrow WW \rightarrow e\nu\mu\nu$ SEARCH**

1533 The $H \rightarrow WW \rightarrow e\nu\mu\nu$ search is unique compared to the ZZ and $\gamma\gamma$ channels. The Higgs mass
1534 cannot be fully reconstructed due to the presence of neutrinos in the final state, so the transverse mass m_T
1535 is used as the final discriminating variable. This channel also has a wider variety of backgrounds compared
1536 to other channels, as discussed in chapter 3. The same flavor final states are excluded from the 8 TeV dataset

1537 due to high pileup conditions¹. These final states are later included in results with the full Run 1 dataset,
1538 as discussed in chapters 5 and 6.

1539 **4.3.1 EVENT SELECTION**

1540 The analysis requires to opposite charge isolated leptons, with the leading (sub-leading) lepton required to
1541 have $p_T > 25(15)$ GeV. The events are separated into different signal regions depending on which flavor
1542 of lepton is leading ($e\mu$ for leading electron, μe for leading muon). Strict lepton quality cuts are applied
1543 to the sample to reduce backgrounds from mis-reconstructed leptons.

1544 Jets are reconstructed with the anti- k_T algorithm with a radius parameter $R = 0.4$. The jets are re-
1545 quired to have $p_T > 25$ GeV and $|\eta| < 4.5$, with jets in the tracking volume required to have a jet vertex
1546 fraction of 0.5 and jets in the forward region required to have $p_T > 30$ GeV. The analysis is separated
1547 into three different signal regions based on jet multiplicity: $n_j = 0, 1, \geq 2$.

1548 To indicate the presence of neutrinos in the event, a requirement of $E_{T,\text{rel}}^{\text{miss}} > 25$ GeV is made². This
1549 requirement significantly reduces the QCD multijet and Z/γ^* + jets backgrounds. Figure 4.1 shows the
1550 distribution of n_j in data and simulation after applying these “pre-selection” requirements.

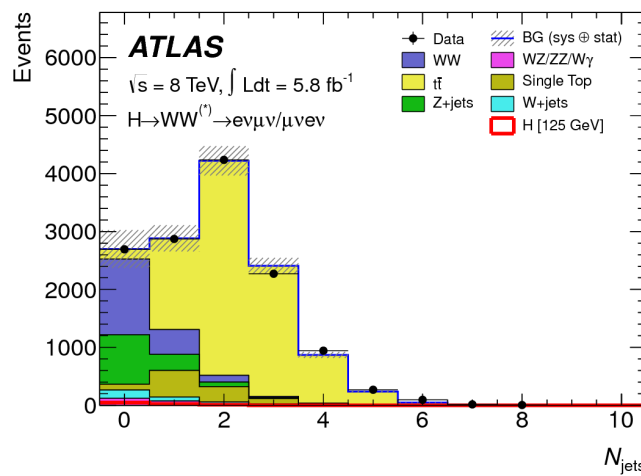


Figure 4.1: Jet multiplicity distribution in data and MC after applying lepton, jet, and $E_{T,\text{rel}}^{\text{miss}}$ selections. The WW and top backgrounds have been normalized using control samples, and the hashed band indicates the total uncertainty on the prediction [1].

¹The less sensitive 7 TeV search result includes both different flavor and same flavor final states.

²For the definition of $E_{T,\text{rel}}^{\text{miss}}$, see section 3.4.1.

1551 Additional selections are applied to require the dilepton topology to correspond to that of a Standard
1552 Model Higgs boson. The requirements are presented here - more detailed discussion on the motivation
1553 for each requirement is saved for Chapter 5. In all of the jet multiplicity channels, the dilepton system
1554 is required to have a small gap in azimuthal angle, $\Delta\phi_{\ell\ell} < 1.8$. Similarly, the dilepton invariant mass,
1555 $m_{\ell\ell}$, is required to be less than 50 GeV in the lower jet multiplicity channels and less than 80 GeV in the
1556 $n_j \geq 2$ channel. In the $n_j = 0$ channel, the magnitude of the dilepton p_T , $p_T^{\ell\ell}$, is required to be greater
1557 than 30 GeV.

1558 In the higher jet multiplicity channels ($n_j \geq 1$), the top background is a larger fraction of the total
1559 background and must be reduced more carefully. The total transverse momentum p_T^{sum} is thus required
1560 to be less than 30 GeV. Additionally, the di- τ invariant mass $m_{\tau\tau}$ (dilepton mass computed under the
1561 assumption that the neutrinos from the τ decay are emitted collinear to the charged leptons [77]) is used
1562 to reject $Z \rightarrow \tau\tau$ events by requiring $|m_{\tau\tau} - m_Z| > 25$ GeV. These variables are also discussed in more
1563 detail in Chapter 5.

1564 In the $n_j \geq 2$ channel, requirements are made to isolate the VBF contribution to Higgs production.
1565 The kinematics of the two leading jets are used to make these requirements. In particular, the event must
1566 have $\Delta y_{jj} > 3.8$ and $m_{jj} > 500$ GeV, along with a veto on having any additional jets with rapidity
1567 between the two leading jets.

1568 4.3.2 BACKGROUND ESTIMATION

1569 The details of the background estimation techniques used in the $H \rightarrow WW^* \rightarrow \ell\nu\ell\nu$ analysis are
1570 discussed in section 5.5. The dominant backgrounds are SM WW production and top (both pair and
1571 single) production, and these backgrounds have their normalizations estimated from dedicated control
1572 regions while their shapes are taken from simulation.

1573 The control sample for the Standard Model WW background is defined by making the same require-
1574 ments as the signal region with the $m_{\ell\ell}$ requirement inverted (now requiring $m_{\ell\ell} > 80$ GeV) and remov-
1575 ing the $\Delta\phi_{\ell\ell}$ requirement. This creates a control sample that is 70% (40%) pure in the 0(1)-jet region. The
1576 correction to the pure MC-based background estimate is quantified by defining a normalization factor β

which is the ratio of the data yield to the MC yield ($N_{\text{data}}/N_{\text{MC}}$) in this control sample. Table 4.2 shows the WW normalization factors in the $n_j = 0$ and $n_j = 1$ bins (the $n_j \geq 2$ estimate is taken directly from MC).

n_j	β_{WW}	β_t
= 0	1.06 ± 0.06	1.11 ± 0.06
= 1	0.99 ± 0.15	1.11 ± 0.05
≥ 2	-	1.01 ± 0.26

Table 4.2: Normalization factors (ratio of data and MC yields in a control sample) for the Standard Model WW and top backgrounds in the $H \rightarrow WW^* \rightarrow \ell\nu\ell\nu$ analysis [1]. Only statistical uncertainties are shown.

The top background estimate is also computed separately in each jet multiplicity bin. In the $n_j = 0$ channel, the background is first normalized using data after pre-selection requirements with no selection on n_j . Then, a dedicated b -tagged control sample is used to evaluate the ratio of one-jet to two-jet events in data. The details of this technique are shown in reference [78]. In the $n_j = 1$ and the $n_j \geq 2$ regions, the top background is normalized in a control sample where the signal region selections are applied, but the b -jet veto is reversed and the Higgs topology requirements on $m_{\ell\ell}$ and $\Delta\phi_{\ell\ell}$ are removed. The resulting normalization factors for these techniques are shown in table 4.2.

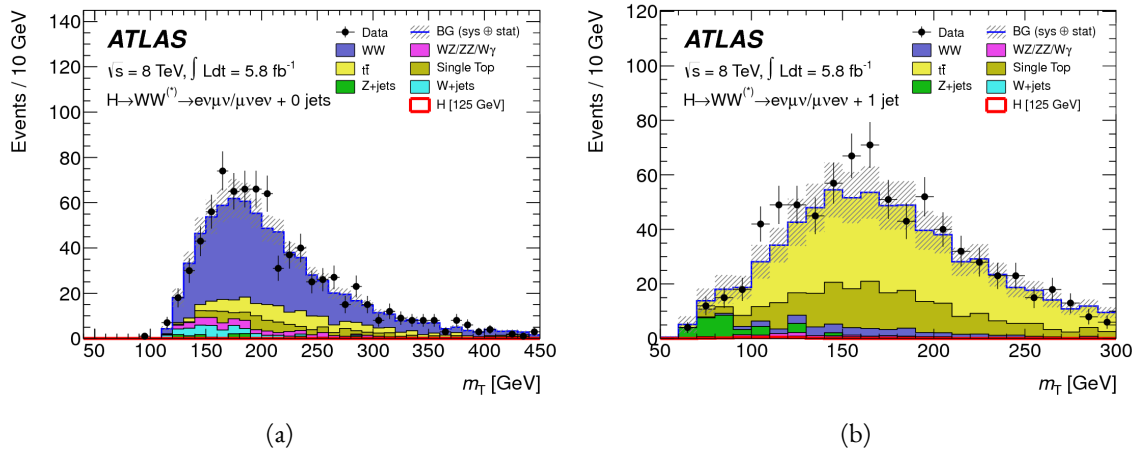


Figure 4.2: Comparison of m_T between data and simulation in the $n_j = 0$ WW (a) and $n_j = 1$ top (b) control samples [1].

The control samples which are used for background normalization can also be used to validate the modeling of the m_T distribution for each background. Figure 4.2 shows the comparison between data and MC

1589 for the m_T distribution after correcting the normalization of the backgrounds in the WW and top control
1590 regions. Good agreement between data and simulation is seen in both cases.

1591 The $W + \text{jets}$ background estimate is taken entirely from data using a control sample with one well recon-
1592 structed lepton and one anti-identified lepton. All other backgrounds are taken purely from simulation.

1593 4.3.3 SYSTEMATIC UNCERTAINTIES

1594 The systematic uncertainties that have the largest impact on the analysis are the theoretical uncertainties
1595 associated with the signal cross section. These are shared with the ZZ^* and $\gamma\gamma$ channels. The uncertainties
1596 resulting from variations of the QCD scale are $+7\% / -8\%$ on the final signal yield. Those coming from
1597 variations of the parton distribution function (PDF) used in the simulation add a $\pm 8\%$ uncertainty on
1598 the yield. The uncertainties on the branching ratios of the Higgs are $\pm 5\%$.

1599 The main experimental uncertainties come from variations of the jet energy scale (JES), jet energy reso-
1600 lution, pile-up, E_T^{miss} , b -tagging efficiency, $W + \text{jets}$ background estimate, and integrated luminosity. For
1601 more details, see reference [1].

1602 4.3.4 RESULTS

1603 Table 4.3 shows the signal and background yields in the final signal region after normalizing the back-
1604 grounds according to the methods described above.

	$n_j = 0$	$n_j = 1$	$n_j \geq 2$
Signal	20 ± 4	5 ± 2	0.34 ± 0.07
WW	101 ± 13	12 ± 5	0.10 ± 0.14
Other dibosons	12 ± 3	1.9 ± 1.1	0.10 ± 0.10
$t\bar{t}$	8 ± 2	6 ± 2	0.15 ± 0.10
Single top	3.4 ± 1.5	3.7 ± 1.6	-
$Z/\gamma^* + \text{jets}$	1.9 ± 1.3	0.10 ± 0.10	-
$W + \text{jets}$	15 ± 7	2 ± 1	-
Total background	142 ± 16	26 ± 6	0.35 ± 0.18
Observed in data	185	38	0

Table 4.3: Data and expected yields for signal and background in the final $H \rightarrow WW^* \rightarrow \ell\nu\ell\nu$ signal region.
Uncertainties shown are both statistical and systematic [1].

1605 Figure 4.3 shows the m_T distribution in the $n_j \leq 1$ channels for 8 TeV data. (No events are observed
 1606 in data in the $n_j \geq 2$ channels in this dataset). The excess shown here relatively flat as a function of
 1607 hypothesized Higgs mass. The combined 7 and 8 TeV data gives an excess with local significance of 2.8σ
 1608 with an expected significance of 2.3σ , corresponding to a μ measurement of 1.3 ± 0.5 .

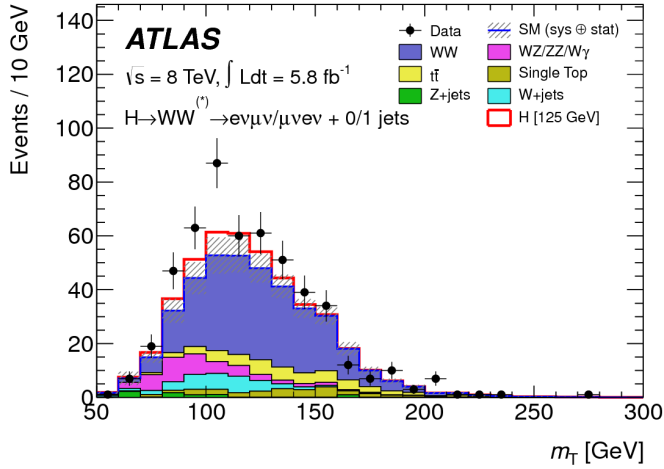


Figure 4.3: m_T distribution in the $H \rightarrow WW \rightarrow e\nu\mu\nu \text{ } n_j \leq 1$ channels for 8 TeV data [1].

1609 4.4 $H \rightarrow \gamma\gamma$ SEARCH

1610 The $H \rightarrow \gamma\gamma$ search is a search for a peaked excess above the falling SM diphoton mass spectrum, with
 1611 $m_{\gamma\gamma}$ as the ultimate discriminating variable. Events are selected by requiring two isolated photons, with
 1612 the leading (sub-leading) photon required to have $E_T > 40(30)$ GeV. In the 8 TeV data, the photons are
 1613 required to pass identification criteria consistent with a photonic shower in the electromagnetic calorimeter
 1614 and little leakage in the hadronic calorimeter.

1615 The main challenges for this analysis are accurate mass reconstruction and background estimation. In
 1616 order to accurately reconstruct the invariant mass of the di-photon system, both the energy and direction
 1617 of the photons must be measured well. Therefore, the identification of the primary vertex of the hard
 1618 interaction is particularly important, and is done using a multivariate likelihood which combines informa-
 1619 tion about the photon direction and vertex position. The background is modeled with a falling spectrum
 1620 in $m_{\gamma\gamma}$ that is parameterized by different functions depending on the category of the event.

1621 4.4.1 RESULTS

1622 The resulting diphoton mass spectrum is shown in figure 4.4. The best fit mass value in the $\gamma\gamma$ channel
 1623 alone in the combined 7 and 8 TeV data is 126.5 GeV. The local significance at this point is 4.5σ , with
 1624 an expected significance of 2.5σ . Therefore, the measured signal strength μ is 1.8 ± 0.5 in this channel.

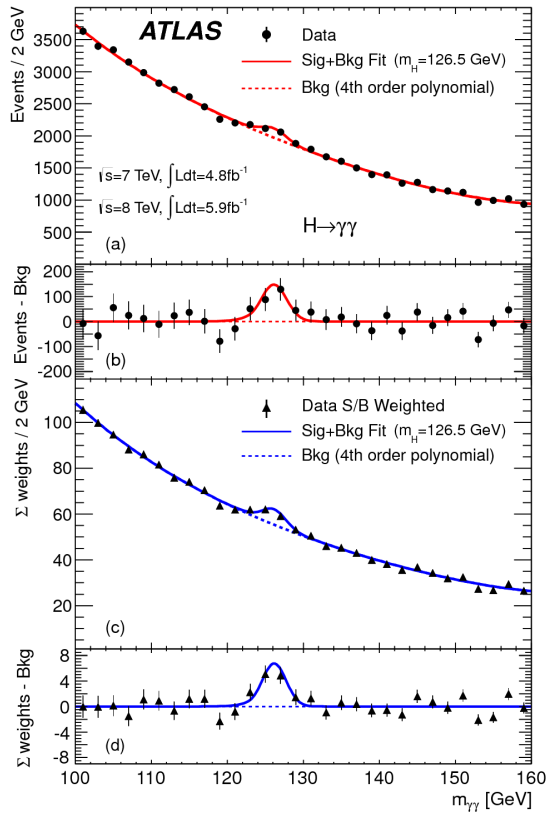


Figure 4.4: Diphoton mass spectrum in 7 and 8 TeV data. Panel a) shows the unweighted data distribution superimposed on the background fit, while panel c) shows the data where each event category is weighted by its signal to background ratio. Panels b) and d) show the respective distributions with background subtracted [1].

1625 4.5 $H \rightarrow ZZ \rightarrow 4\ell$ SEARCH

1626 The $H \rightarrow ZZ \rightarrow 4\ell$ analysis searches for a Standard Model Higgs boson decaying to two Z bosons, each
 1627 of which decays to a pair of same flavor, opposite charge isolated leptons. The ultimate discriminating
 1628 variable is $m_{4\ell}$, or the invariant mass of the four selected leptons. The ℓ denotes an e or μ as with the
 1629 $H \rightarrow WW^* \rightarrow \ell\nu\ell\nu$ analysis.

1630 Four distinct signal regions are constructed depending on the flavors of the final state, additionally sep-
 1631 arated by the flavor of the leading lepton pair. These are referred to as $4e$, $2e2\mu$, $2\mu2e$, 4μ .

1632 The main backgrounds in the $H \rightarrow ZZ \rightarrow 4\ell$ search are continuum ZZ^* production, $Z + \text{jets}$ pro-
 1633 duction, and $t\bar{t}$. The $m_{4\ell}$ distribution for background is estimated from simulation. The normalization
 1634 of the SM ZZ^* background is also taken from MC simulation, while the $Z + \text{jets}$ and $t\bar{t}$ normalizations are
 1635 taken from data-driven methods.

1636 **4.5.1 RESULTS**

1637 Figure 4.5 shows the $m_{4\ell}$ spectrum measured in the 7 and 8 TeV datasets. The total number of events
 1638 observed in the window between 120 and 130 GeV is 13, with 6 events in the 4μ channel, 2 events in
 1639 the $4e$ channel, and 5 events in the $2e2\mu/2\mu2e$. The best fit μ value in the combined 7 and 8 TeV data
 1640 occurs at 125 GeV and is measured to be 1.2 ± 0.6 . The observed significance at this mass is 3.6σ , with
 1641 an expected significance of 2.7σ .

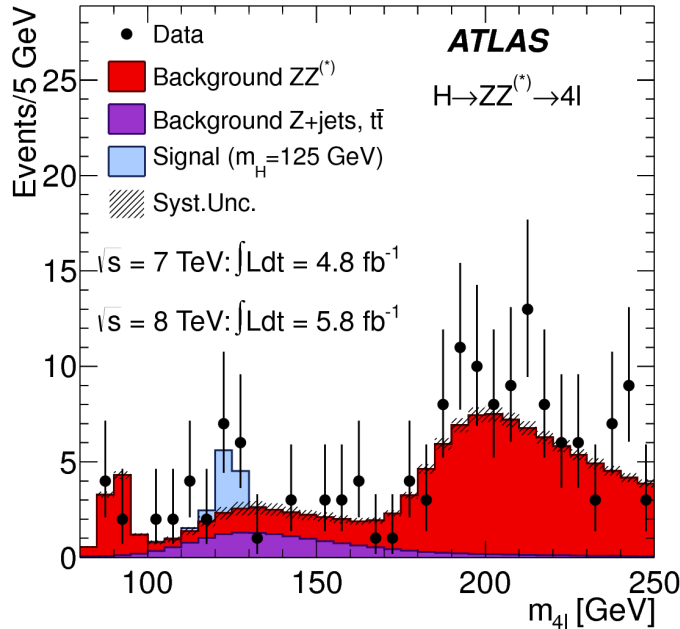


Figure 4.5: Four lepton invariant mass spectrum ($m_{4\ell}$) in 7 and 8 TeV data compared to background estimate. A 125 GeV SM Higgs signal is shown in blue [1].

1642 4.6 COMBINED RESULTS

1643 The statistical interpretation of the combined results is undertaken as described in section 3.6.2, with a hy-
1644 pothesis test based on a likelihood ratio parameterized by the Higgs signal strength μ . The null hypothesis
1645 corresponds to $\mu = 0$, while the SM Higgs corresponds to $\mu = 1$.

1646 Table 4.4 summarizes the properties of the individual channels as well as the significances of the excesses
1647 seen. The most significant observed local excess comes from the $\gamma\gamma$ channel. Figure 4.6 shows a com-
1648 parison of the observed local p_0 values as a function of hypothesized mass for the three different search
1649 channels. Both the ZZ^* and $\gamma\gamma$ channels have very peaked excesses, while the WW^* excess can be seen as
1650 very broad because the m_T distribution does not provide detailed information about the true Higgs mass.
1651 Figure 4.7 shows the combined exclusion limit, p_0 , and signal strength. The highest local excess comes at
1652 a value of 126.5 GeV and corresponds to a 6.0σ observed excess.

Channel	Fit var.	Observed Z_l	Expected Z_l	$\hat{\mu}$
$H \rightarrow ZZ^* \rightarrow 4\ell$	$m_{4\ell}$	3.6	2.7	1.2 ± 0.6
$H \rightarrow \gamma\gamma$	$m_{\gamma\gamma}$	4.5	2.5	1.8 ± 0.5
$H \rightarrow WW^* \rightarrow e\nu\mu\nu$	m_T	2.8	2.3	1.3 ± 0.5
Combined	-	6.0	4.9	1.4 ± 0.3

Table 4.4: Summary of the expected and observed significance and measured signal strengths in the combined 7
and 8 TeV datasets for the Higgs discovery analysis [1].

1653 Figure 4.8 shows a comparison of the measured signal strengths between the different Higgs search
1654 channels. All measured μ are consistent with unity within their uncertainty, and the combined μ mea-
1655 surement is 1.4 ± 0.3 .

1656 The likelihood can also be computed in a two-dimensional plane of m_H and μ , and this is shown in
1657 figure 4.9. The figure shows that while the $\gamma\gamma$ and ZZ^* channels have very good mass resolution, the
1658 excess in WW^* covers a broad mass range. The banana shape of the WW^* result is due to the fact that
1659 the excess in this channel can either be explained by increasing the signal strength or by changing the mass
1660 (and thus the cross section). The two parameters are correlated due to the lack of mass sensitivity in this
1661 channel.

1662 Because multiple Higgs mass points are searched for, the local significance must be corrected for a look-

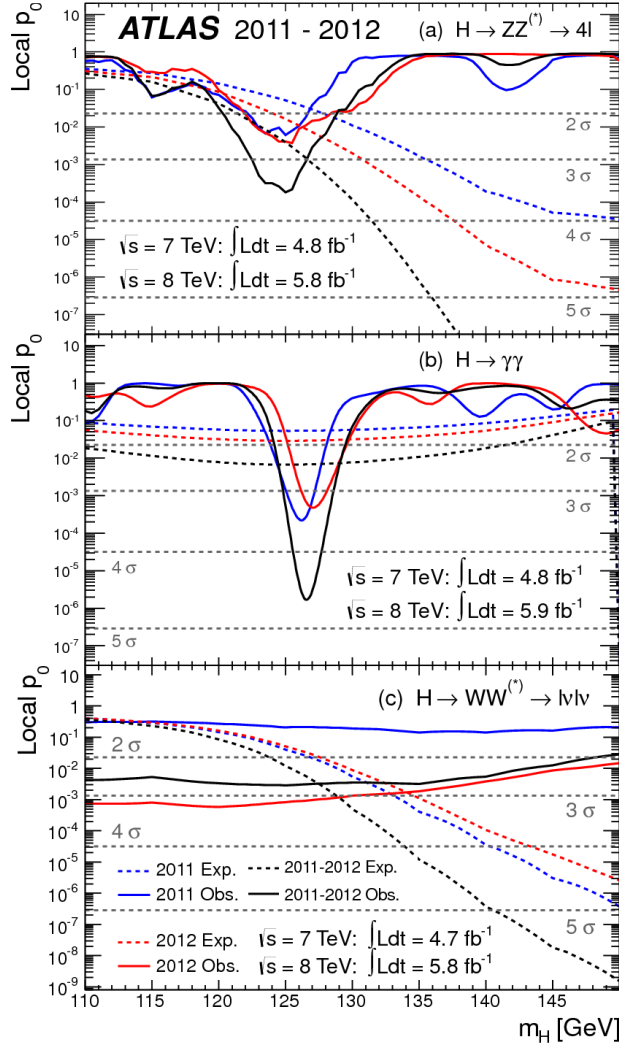


Figure 4.6: Local p_0 distribution as a function of hypothesized Higgs mass for the $H \rightarrow ZZ^* \rightarrow 4\ell$ (a), $H \rightarrow \gamma\gamma$ (b), and $H \rightarrow WW^* \rightarrow \ell\nu\ell\nu$ (c) channels. Dashed curves show expected results, while solid curves show observed. Red curves are from 7 TeV data, blue curves from 8 TeV, and black curved combined [1].

¹⁶⁶³ elsewhere effect to compute a true global significance. The global significance for finding a Higgs anywhere
¹⁶⁶⁴ in the mass range of 110 GeV to 600 GeV is 5.1σ . This increases slightly to 5.3σ if only mass range from
¹⁶⁶⁵ 110 to 150 GeV.

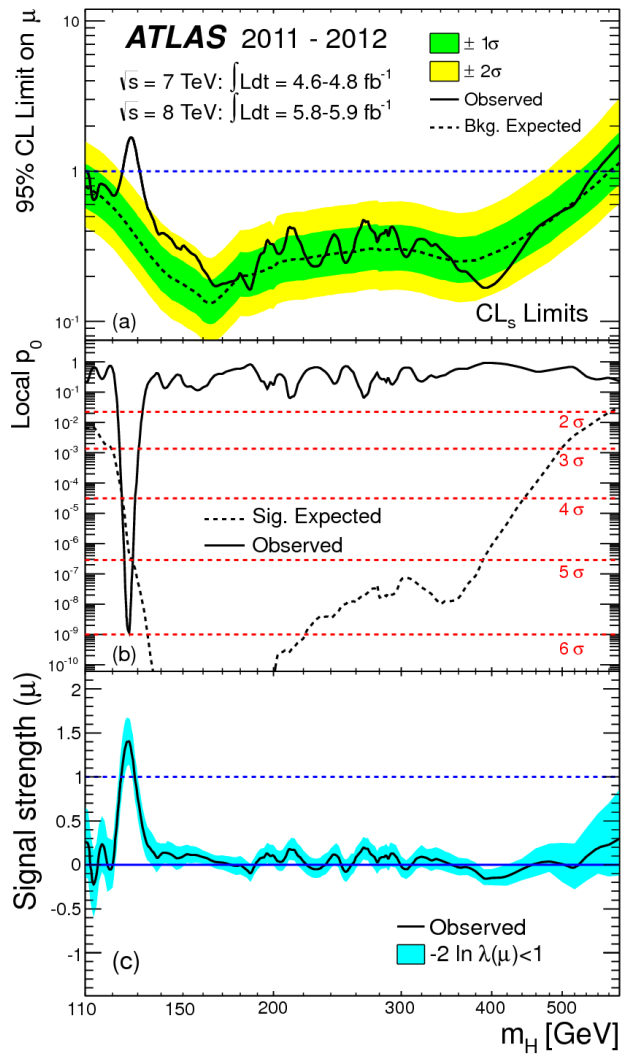


Figure 4.7: Combined 95% CL limits (a), local p_0 values (b), and signal strength measurement (c) as a function of Higgs mass [1].

1666 4.7 CONCLUSION

1667 A search for the production of a Standard Model Higgs boson was conducted in 4.8 fb^{-1} collected at
 1668 $\sqrt{s} = 7 \text{ TeV}$ and 5.8 fb^{-1} at $\sqrt{s} = 8 \text{ TeV}$. A new particle consistent with the Higgs boson was observed,
 1669 with a mass of 126.5 GeV and a global (local) significance of $5.1(6.0)\sigma$. This is the first discovery level
 1670 observation of a particle consistent with the Higgs.

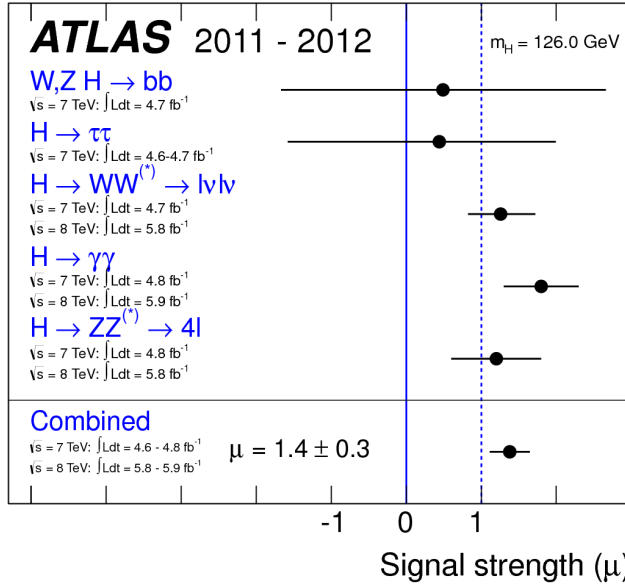


Figure 4.8: Comparison of measured signal strength μ for a 126 GeV Higgs in the 7 and 8 TeV datasets [1].

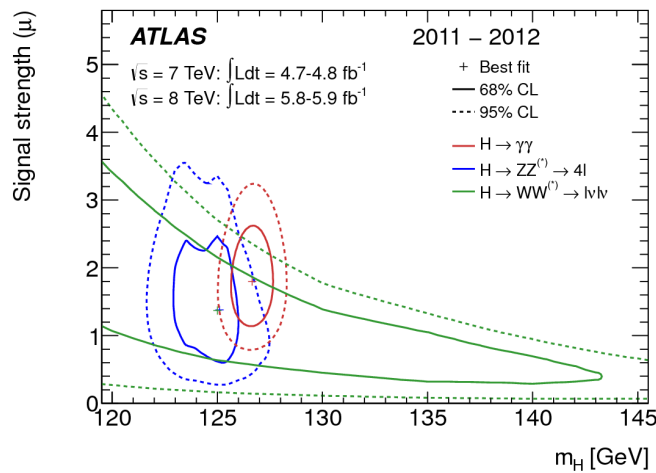


Figure 4.9: Two dimensional likelihood as a function of signal strength μ and Higgs mass m_H [1].

*The imagination of nature is far, far greater than the
imagination of man.*

Richard Feynman

5

1671

1672 Evidence for Vector Boson Fusion production

1673

$$\text{of } H \rightarrow WW^* \rightarrow \ell\nu\ell\nu$$

1674 5.1 INTRODUCTION

1675 After the discovery of the Higgs boson, the $H \rightarrow WW^*$ analysis had two main goals. The first goal was
1676 to increase the sensitivity of the analysis to fully confirm that the $H \rightarrow WW^*$ process did indeed exist.
1677 The second goal was to characterize the particle as much as possible, including searching for the lower
1678 cross-section production modes. This chapter presents a dedicated search for Vector Boson Fusion (VBF)
1679 production of a Higgs boson decaying via the $H \rightarrow WW^* \rightarrow \ell\nu\ell\nu$ mode. First, the data and Monte
1680 Carlo samples are detailed, along with trigger and physics object selections. Then, the details of the analysis
1681 are shown, including signal region definition, background estimation techniques, and systematic uncer-
1682 tainties. Finally, the results of the analysis are presented. As will be shown, this analysis is the first and

1683 most sensitive evidence for VBF production of the Higgs at the LHC.

1684 The VBF $H \rightarrow WW^* \rightarrow \ell\nu\ell\nu$ analysis defines two signal regions. The first is a more standard
1685 selection, referred to as “cut-based”, that applies requirements on VBF topology variables and uses m_T as
1686 the final discriminating variable. The second is a looser selection that uses an algorithm known as a Boosted
1687 Decision Tree (BDT). A BDT is a multivariate technique that uses an ensemble of decision trees to split the
1688 phase space of input variables into signal-like and background-like regions in order to provide separation
1689 power [79–81]. The output score of a BDT trained to distinguish the VBF Higgs signal from background
1690 processes is used as the final discriminating variable in the second signal region. While the BDT-based
1691 signal region is ultimately more sensitive, the cut-based result is an important component of the analysis.
1692 First, the cut-based analysis allows for confirming the modeling and validity of the variables used as input
1693 to the BDT. Second, because this is the first use of a multivariate technique in the $H \rightarrow WW^*$ analysis,
1694 the cut-based selection allows confirmation of the final BDT result with a more traditional analysis. The
1695 cut-based techniques are the focus of this chapter, but connections to the BDT result will be illustrated
1696 when appropriate.

1697 One important note is that because this analysis is dedicated to the measurement of the VBF pro-
1698 duction mode of the Higgs, events coming from gluon fusion production with the Higgs decaying via
1699 $H \rightarrow WW^* \rightarrow \ell\nu\ell\nu$ are treated as background events. This will be seen throughout the background
1700 predictions shown below.

1701 5.2 DATA AND SIMULATION SAMPLES

1702 The results presented here are with 20.3 fb^{-1} taken at $\sqrt{s} = 8 \text{ TeV}$ and 4.5 fb^{-1} taken at $\sqrt{s} = 7 \text{ TeV}$.
1703 The details of the LHC and detector conditions during this period are given in Chapter 2. The trigger
1704 selection defining the dataset is discussed in section 5.2.1. The simulation samples used for signal and back-
1705 ground modeling are given in section 5.2.2.

1706 5.2.1 TRIGGERS

1707 The analysis uses a combination of single lepton and dilepton triggers to allow lowering of the p_T thresh-
1708 olds and increased signal acceptance. The p_T threshold on the leptons is a particularly important con-
1709 sideration for this signal. Because the W^* produced in the decay is off-shell, it tends to produce lower
1710 momentum leptons. Thus, being able to lower the p_T threshold while still maintaining a low background
1711 rate is critical. Figure 5.1 shows an example of the subleading lepton p_T for a VBF $H \rightarrow WW^*$ signal com-
1712 pared to the corresponding $t\bar{t}$ background. Note that the lepton p_T spectrum is considerably softer in the
1713 signal sample. The spectrum shown here is also similar in gluon fusion production of the Higgs as well.

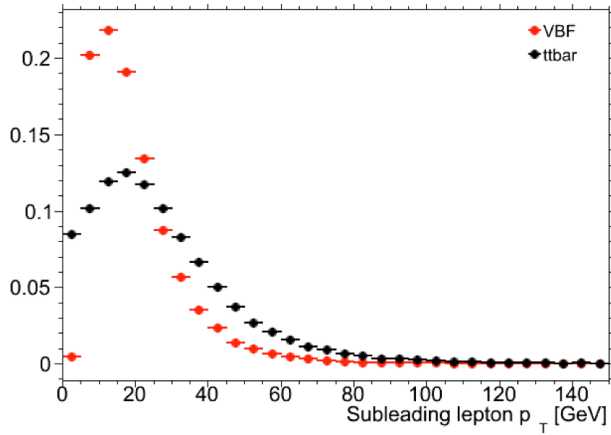


Figure 5.1: A comparison of the subleading lepton p_T spectrum between VBF $H \rightarrow WW^*$ production and $t\bar{t}$ background.

1714 As discussed in Chapter 2, there are multiple levels in the ATLAS trigger system, and there are different
1715 p_T thresholds imposed for the leptons at each level. Additionally, some triggers have a loose selection on
1716 the isolation of the lepton (looser than that applied offline in the analysis object selection). Table 5.1 shows
1717 the p_T thresholds used for single lepton triggers, while table 5.2 shows the p_T thresholds coming from
1718 di-lepton triggers. The single lepton trigger efficiency for muons that pass the analysis object selection is
1719 70% for muons in the barrel region ($|\eta| < 1.05$) and 90% in the endcap region. The electron trigger
1720 efficiency increases with electron p_T but the average is approximately 90%. These efficiencies are measured
1721 by combined performance and trigger signature groups [82, 83].

	Level-1 threshold	High-level threshold
Electron	18	$24i$
	30	60
Muon	15	$24i$
		36

Table 5.1: Single lepton triggers used for electrons and muons in the $H \rightarrow WW^* \rightarrow \ell\nu\ell\nu$ analysis. A logical “or” of the triggers listed for each lepton type is taken. Units are in GeV, and the i denotes an isolation requirement in the trigger.

	Level-1 threshold	High-level threshold
ee	10 and 10	12 and 12
$\mu\mu$	15	18 and 8
$e\mu$	10 and 6	12 and 8

Table 5.2: Di-lepton triggers used for different flavor combinations in the $H \rightarrow WW^* \rightarrow \ell\nu\ell\nu$ analysis. The two thresholds listed refer to leading and sub-leading leptons, respectively. The di-muon trigger only requires a single lepton at level-1.

The combination of all listed triggers gives good efficiency for signal events. This efficiency is summarized in table 5.3. The relative improvement in efficiency by adding the dilepton triggers is also shown in the same table. The largest gain comes in the $\mu\mu$ channel. Overall the trigger selection shows a good efficiency for $H \rightarrow WW^*$ signal events.

Channel	Trigger efficiency	Gain from 2ℓ trigger
ee	97%	9.1%
$\mu\mu$	89%	18.5%
$e\mu$	95%	8.3%
μe	81%	8.2%

Table 5.3: Trigger efficiency for signal events and relative gain of adding a dilepton trigger on top of the single lepton trigger selection. The first lepton is the leading, while the second is the sub-leading. Efficiencies shown here are for the ggF signal in the $n_j = 0$ category but are comparable for the VBF signal.

5.2.2 MONTE CARLO SAMPLES

In both the gluon fusion and vector boson fusion focused analyses, modeling of signal and background processes in the signal region is an important consideration for the final interpretation of the analysis. Therefore, careful consideration must be paid to which Monte Carlo (MC) generators are used for specific

1730 processes. With the exception of the $W + \text{jet}$ and multijet backgrounds, the m_T shape used as the final
1731 discriminant is taken from simulation¹.

1732 Table 5.4 shows the MC generators used for the signal and background processes, as well as the cross
1733 sections of each process. In order to include corrections up to next-to-leading order (NLO) in the QCD
1734 coupling constant α_s , the `POWHEG` [84] generator is often used. In some cases, only leading order gener-
1735 ators like `ACERMC` [85] and `GG2VV` [86] are available for the process in question. If the process requires
1736 good modeling for very high parton multiplicities, the `SHERPA` [87] and `ALPGEN` [88] generators are used
1737 to provide merged calculations for five or fewer additional partons. These matrix element level calculations
1738 must then be additionally matched to models of the underlying event, hadronization, and parton shower.
1739 There are four generators used for this purpose: `SHERPA`, `PYTHIA 6` [89], `PYTHIA 8` [90], or `HERWIG`
1740 [91] + `JIMMY` [92]. The simulation additionally requires an input parton distribution function (PDF).
1741 The `CT10` [93] PDFs are used for `SHERPA` and `POWHEG` simulated samples, while `CTEQ6L1` [94] is used
1742 for `ALPGEN + HERWIG` and `ACERMC` simulations. The Drell-Yan samples are reweighted to the `MRST` [95]
1743 PDFs, as these are found to give the best agreement between data and simulation. The branching ratio
1744 for Higgs to WW^* and ZZ^* is computed with `PROPHECY4f` [96], while the width of all other decays is
1745 computed with `HDECAY`[97].

1746 Once the basic hard scattering process is simulated, it must be passed through a detector simulation and
1747 additional pile-up events must be overlaid. The pile-up events are modeled with `PYTHIA 8`, and the ATLAS
1748 detector is simulated with `GEANT4` [98]. Because of the unique phase space of the $H \rightarrow WW^*$ analysis,
1749 events are sometimes filtered at generator level to allow for more efficient generation of relevant events.
1750 The efficiency of the trigger in MC simulation does not always match the measured efficiency in data, so
1751 trigger scale factors are applied to correct the MC efficiency to the data. The details of these corrections are
1752 given in reference [82] for muons and reference [83] for electrons.

¹Many backgrounds are normalized from data, as described in section 5.5.

Process	MC generator	$\sigma \cdot \mathcal{B}$ (pb)
Signal		
ggF $H \rightarrow WW^*$	POWHEG +PYTHIA 8	0.435
VBF $H \rightarrow WW^*$	POWHEG +PYTHIA 8	0.0356
VH $H \rightarrow WW^*$	PYTHIA 8	0.0253
WW		
$q\bar{q} \rightarrow WW$ and $qg \rightarrow WW$	POWHEG +PYTHIA 6	5.68
$gg \rightarrow WW$	GG2VV +HERWIG	0.196
$(q\bar{q} \rightarrow W) + (q\bar{q} \rightarrow W)$	PYTHIA 8	0.480
$q\bar{q} \rightarrow WW$	SHERPA	5.68
VBS $WW + 2$ jets	SHERPA	0.0397
Top quarks		
$t\bar{t}$	POWHEG +PYTHIA 6	26.6
Wt	POWHEG +PYTHIA 6	2.35
$t\bar{q}\bar{b}$	ACERMC +PYTHIA 6	28.4
$t\bar{b}$	POWHEG +PYTHIA 6	1.82
Other dibosons (VV)		
$W\gamma$ ($p_T^\gamma > 8$ GeV)	ALPGEN +HERWIG	369
$W\gamma^*$ ($m_{\ell\ell} \leq 7$ GeV)	SHERPA	12.2
WZ ($m_{\ell\ell} > 7$ GeV)	POWHEG +PYTHIA 8	12.7
VBS $WZ + 2$ jets	SHERPA	0.0126
($m_{\ell\ell} > 7$ GeV)		
$Z\gamma$ ($p_T^\gamma > 8$ GeV)	SHERPA	163
$Z\gamma^*$ (min. $m_{\ell\ell} \leq 4$ GeV)	SHERPA	7.31
ZZ ($m_{\ell\ell} > 4$ GeV)	POWHEG +PYTHIA 8	0.733
$ZZ \rightarrow \ell\ell\nu\nu$ ($m_{\ell\ell} > 4$ GeV)	POWHEG +PYTHIA 8	0.504
Drell-Yan		
Z ($m_{\ell\ell} > 10$ GeV)	ALPGEN +HERWIG	16500
VBF $Z + 2$ jets	SHERPA	5.36
($m_{\ell\ell} > 7$ GeV)		

Table 5.4: Monte Carlo samples used to model the signal and background processes [74]. The table lists the cross section for each process, taking into account the branching ratio for the process producing two leptons.

1753 5.3 OBJECT SELECTION

1754 In order to define the signal region, the analysis must first select the reconstructed physics objects to be
1755 considered. The details of the object reconstruction algorithms were discussed in Chapter 2, while this

1756 section gives specific selection requirements used in the $H \rightarrow WW^*$ analysis. The first step in this process
1757 is to select a primary vertex candidates. The event's primary vertex is chosen to be the vertex with the largest
1758 sum of p_T^2 for its associated tracks. It is required to have at least three tracks with $p_T > 450$ MeV. Many
1759 of the object selection cuts are then made relative to this chosen primary vertex.

1760 **5.3.1 MUONS**

1761 The analysis uses combined muon candidates, where a track in the Inner Detector has been matched to a
1762 standalone track in the Muon Spectrometer. The track parameters are combined statistically in the muon
1763 reconstruction algorithm [64]. The muons are required to be within $|\eta| < 2.5$ and have a $p_T > 10$ GeV.
1764 To reduce backgrounds coming from mis-reconstructed leptons, there are requirements on the impact
1765 parameter of the muon relative to the primary vertex. The transverse impact parameter d_0 is required to
1766 be small relative to its estimated uncertainty, the exact cut value being $d_0/\sigma_{d_0} < 3$. The longitudinal
1767 impact parameter z_0 must satisfy $|z_0 \sin \theta| < 1$ mm.

1768 As discussed previously, the muons must also be isolated. There are two types of lepton isolations
1769 that are calculated: track-based and calorimeter-based. For muons, the track-based isolation is defined
1770 using the scalar sum $\sum p_T$ for tracks with $p_T > 1$ GeV (excluding the muon track) within a cone of
1771 $\Delta R = 0.3$ (0.4) around the track for muons with $p_T > 15$ GeV ($10 < p_T < 15$ GeV). The final
1772 isolation requirement is made by requiring that this scalar sum be no more than a certain fraction of the
1773 muon p_T . This requirement varies with muon p_T and the exact requirements are defined in table 5.5.

1774 The calorimeter-based muon isolation is defined using the $\sum E_T$ calculated from calorimeter cells with
1775 the same cone size as the track-based isolation but excluding cells within $\Delta R < 0.05$ around the muon.
1776 This isolation is also defined as a requirement on the ratio of the sum to the muon p_T and varies with
1777 muon p_T . The requirement values as a function of p_T are also given in table 5.5.

1778 The isolation requirements loosen as a function of p_T to allow for larger signal acceptance. At low p_T ,
1779 the isolation is tightened to reduce the $W + \text{jets}$ background which arises from a misidentified lepton.

p_T range (GeV)	Calorimeter isolation	Track isolation
10 – 15	0.06	0.06
15 – 20	0.12	0.08
20 – 25	0.18	0.12
> 25	0.30	0.12

Table 5.5: p_T dependent isolation requirements for muons. Muons are required to have their calorimeter based or track based cone sums be less than this fraction of their p_T .

1780 5.3.2 ELECTRONS

1781 Electrons are identified and reconstructed using the methods previously described in chapter 2. The elec-
 1782 trons are required to have $|\eta| < 2.47$, and candidates in the transition region between the barrel and
 1783 endcap ($1.37 < |\eta| < 1.52$) are excluded. As the muons, the electrons are required to have transverse
 1784 impact parameter significance < 3 , while in the longitudinal direction they must have $|z_0 \sin \theta| < 0.4$
 1785 mm. Some electron requirements also vary with electron E_T , and these requirements are summarized in
 1786 table 5.6.

1787 The isolation for electrons is defined similarly to the muons but with unique requirements on the ob-
 1788 jects included. The track-based isolation is constructed using tracks with $p_T > 400$ MeV with cone sizes
 1789 as defined for the muons. The calorimeter-based isolation also uses the same cone size as the muon, but
 1790 here the cells within a 0.125×0.175 area in $\eta \times \phi$ around the electron cluster's barycenter are excluded.
 1791 The other difference with respect to muons is that the denominator of the isolation ratio is the electron
 1792 E_T rather than p_T . The isolation cuts vary with electron E_T and are defined in table 5.6. The electron is
 1793 also required to not be consistent with a vertex coming from a photon conversion.

p_T range (GeV)	Quality cut	Calorimeter isolation	Track isolation
10 – 15	Very tight LH	0.20	0.06
15 – 20	Very tight LH	0.24	0.08
20 – 25	Very tight LH	0.28	0.10
> 25	Medium	0.28	0.10

Table 5.6: p_T dependent requirements for electrons. Electrons are required to have their calorimeter based or track based cone sums be less than this fraction of their E_T .

1794 5.3.3 JETS

1795 Jets are clustered with the anti- k_T reconstruction algorithm using a radius parameter of $R = 0.4$. They
1796 are required to have a jet vertex fraction (JVF) of at least 50%, meaning that half of the tracks associated with
1797 the jet originated from the primary vertex. Jets with no tracks associated (i.e. those outside the acceptance
1798 of the ID) do not have this requirement applied. Jets are required to have $p_T > 25$ GeV if they are within
1799 the tracking acceptance ($|\eta| < 2.4$). Jets with $2.4 < |\eta| < 4.5$ are required to have $p_T > 30$ GeV. This
1800 tighter requirement reduces jets from pileup in the region where JVF requirements cannot be applied. The
1801 two highest p_T jets in the event are referred to as the “VBF” jets and used to compute variables used in the
1802 analysis selection.

1803 Identification of b -jets is done using the MV1 algorithm and is limited to the acceptance of the ID ($|\eta| <$
1804 2.5) [70]. The operating point of MV1 used is 85% efficient for identifying true b -jets. This operating
1805 point has a 10.3% probability of mis-tagging a light quark jet as a b -jet. The analysis vetoes events that
1806 contain b -tagged jets with $p_T > 20$ GeV.

1807 5.3.4 OVERLAP REMOVAL

1808 There are some cases where reconstructed objects will overlap and one will have to be chosen (for example,
1809 an electron and a jet in the calorimeter). First, the case of lepton overlap is dealt with. If an electron
1810 candidate extends into the muon spectrometer, it is removed. If a muon and electron are within $\Delta R < 0.1$
1811 of each other, the electron is removed and the muon is kept. If two electron candidates overlap within the
1812 same radius, then the higher E_T electron is kept. Next, the overlap between leptons and jets is considered.
1813 If an electron and jet are within $\Delta R < 0.3$ of one another, the electron is kept and the jet is removed.
1814 However, if a muon and jet overlap within $\Delta R < 0.3$, the jet is kept (as it is likely that the muon is the
1815 result of a semileptonic decay inside the jet). Once the overlap removal is complete, the final set of objects
1816 used in the analysis is defined.

1817 5.4 ANALYSIS SELECTION

1818 This section discusses the variables used to distinguish VBF production of the Higgs in the $H \rightarrow WW^* \rightarrow$
1819 $\ell\nu\ell\nu$ final state. First, pre-selection requirements are presented. Then, the definitions of analysis variables
1820 and the cut-based signal region are shown. Finally, the BDT signal region is defined and the commonalities
1821 between the two signal regions are discussed.

1822 5.4.1 PRE-SELECTION

1823 Both the cut-based and BDT analyses have a common pre-selection that is applied before the signal region
1824 requirements. The requirements on leptons are common to all n_j bins. The analysis requires two oppo-
1825 sitely charged leptons, with the leading lepton required to have $p_T > 22$ GeV while the subleading lepton
1826 must have $p_T > 10$ GeV. Next, to remove low mass Z/γ^* events, a requirement on the dilepton mass
1827 $m_{\ell\ell} > 10$ (12) GeV is applied in the different (same) flavor channel. In the same flavor channels, there is
1828 an additional veto placed on the region around the Z peak, requiring that $|m_{\ell\ell} - m_Z| > 15$ GeV.

1829 There are also requirements on the amount of missing transverse momentum in the event. These
1830 are only applied in the same flavor channels, where $Z/\gamma^* + \text{jets}$ production is one of the dominant back-
1831 grounds. The BDT analysis requires $p_T^{\text{miss}} > 40$ GeV and $E_T^{\text{miss}} > 45$ GeV. The cut-based analysis
1832 must select more tightly on these variables to have maximal sensitivity and thus requires $p_T^{\text{miss}} > 50$ GeV
1833 and $E_T^{\text{miss}} > 55$ GeV.

1834 Finally, because this analysis is focused on VBF Higgs production, a requirement on the jet multiplicity
1835 is placed, with $n_j \geq 2$. Additionally, the analysis requires that there are no jets identified as b-quarks in
1836 the event, or $n_b = 0$.

1837 5.4.2 ANALYSIS VARIABLE DEFINITIONS AND CUT-BASED SELECTION

1838 The cut-based selection places sequential requirements on variables reconstructed from the VBF jets in
1839 order to increase the signal to background ratio. This section defines the variables that are used in the
1840 cut-based selection and details the requirements that are placed on these variables.

1841 GENERAL BACKGROUND REDUCTION

1842 Top pair production is the primary background in the $n_j \geq 2$ bin. Even though $n_b = 0$ is required, an
1843 additional variable is constructed to further suppress the top background. There is often additional QCD
1844 radiation that accompanies the $t\bar{t}$ system when it is produced. Therefore, a variable which tests for the
1845 presence of this additional radiation, p_T^{sum} , is constructed. It is defined in equation 5.1.

$$p_T^{\text{sum}} = p_T^{\ell\ell} + p_T^{\text{miss}} + \sum p_T^j \quad (5.1)$$

1846 After pre-selection, the cut-based analysis requires the event to have $p_T^{\text{sum}} < 15$ GeV to further suppress
1847 $t\bar{t}$ production.

1848 In the different flavor channels, a requirement is made to reduce the contamination from $Z \rightarrow \tau\tau$
1849 decays. The di- τ invariant mass, $m_{\tau\tau}$, is constructed by assuming that the neutrinos from the τ decays
1850 were collinear with the leptons [77]. The analysis requires that this mass satisfy $m_{\tau\tau} < m_Z - 25$ GeV so
1851 that it is not consistent with the mass of the Z boson.

1852 VBF TOPOLOGICAL CUTS

1853 The characteristic feature of VBF production of the Higgs is the presence of two additional forward jets
1854 coming from the incoming partons which radiate the vector bosons that make the Higgs. These jets are
1855 forward because the outgoing partons still carry the longitudinal momentum of the incoming partons.
1856 Figure 5.2 shows the distribution of the η for the leading jet in a VBF event compared to a background top
1857 pair production event. As can be seen, the VBF jets tend to be more forward in η , while the $t\bar{t}$ jets are more
1858 central. Because the cross section for VBF production is an order of magnitude smaller than gluon fusion
1859 production, these forward jets must be used in order to reduce background and achieve a good signal to
1860 background ratio. The dedicated VBF search selection requirements are constructed to maximally exploit
1861 the features of the unique VBF topology.

1862 Requirements on the VBF jets are collectively referred to as the “VBF topological cuts”. First, a require-
1863 ment on the dijet invariant mass of the VBF jets, m_{jj} , is placed, requiring $m_{jj} > 600$ GeV. Next, the

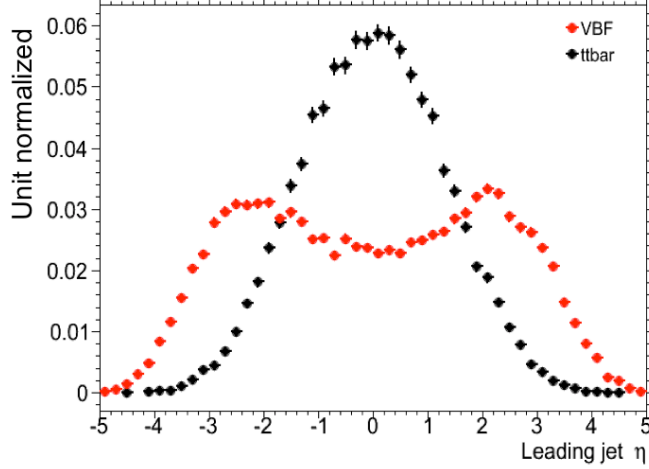


Figure 5.2: Leading jet η in VBF $H \rightarrow WW^*$ (red) and $t\bar{t}$ (black)

event is required to have a large gap in rapidity between the two VBF jets, or $\Delta y_{jj} > 3.6$. Both of these are tight requirements on the presence of two forward, high p_T jets moving in opposite directions in the longitudinal plane.

Beyond requiring the presence of the two forward VBF jets, the analysis also vetoes on the presence of any additional jets that fall between the two VBF jets. This requirement is referred to as the central jet veto, or CJV. Events are vetoed if they have a third jet with $p_T > 20$ GeV whose rapidity is between the region defined by the two VBF jets. This requirement can be expressed in terms of a variable called the jet centrality, defined in equation 5.2.

$$C_{j3} = \left| \eta_{j3} - \frac{\eta_{j1} + \eta_{j2}}{2} \right| / \frac{|\eta_{j1} - \eta_{j2}|}{2}, \quad (5.2)$$

Here, η_{j1} and η_{j2} are the pseudorapidities of the leading and subleading jets, respectively, while η_{j3} is the pseudorapidity of the extra jet in the event (if one exists). Intuitively, C_{j3} is zero when η_{j3} is directly centered between the two jets and unity when η_{j3} is aligned with either of the VBF jets. Thus, the CJV can be expressed as a requirement that $C_{j3} > 1$.

The decay products of the Higgs tend to be central as well. Thus, the analysis also requires that both

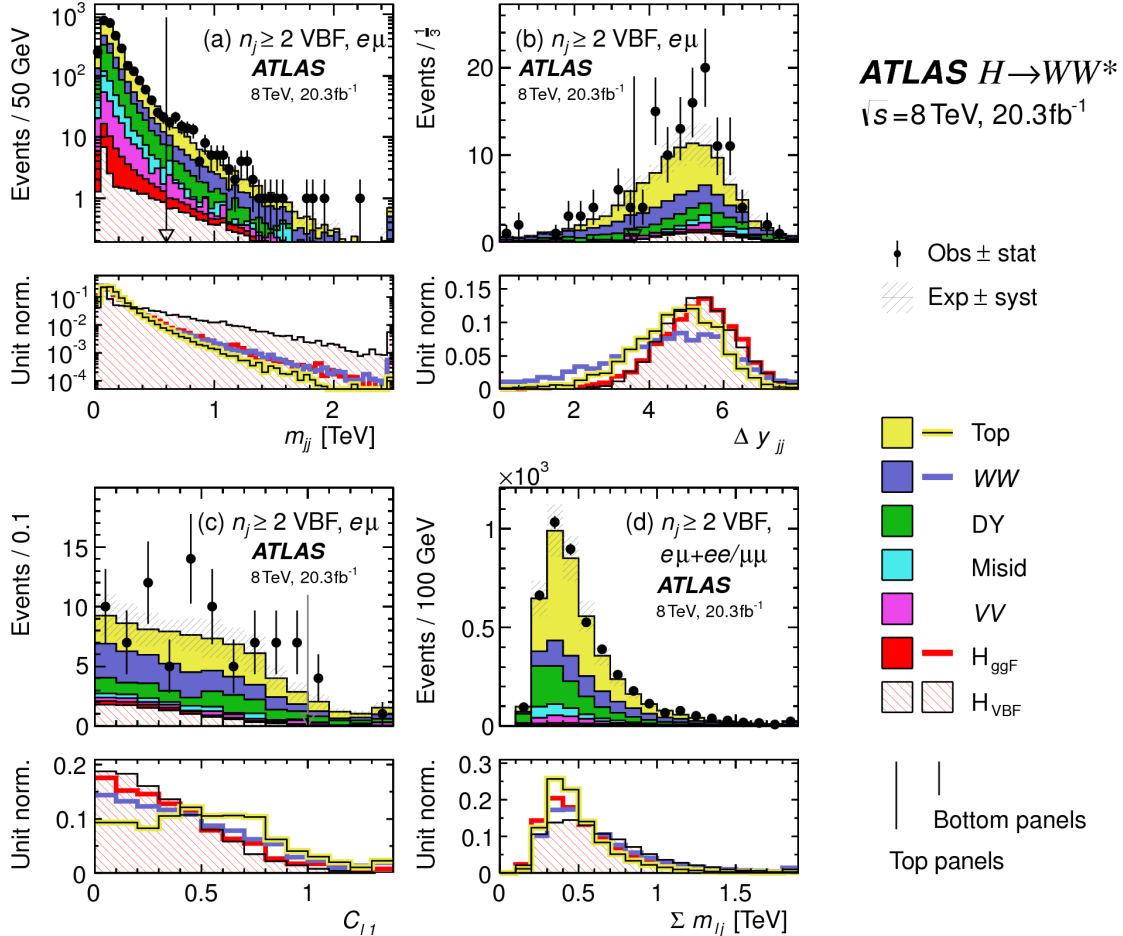


Figure 5.3: Distributions of (a) m_{jj} , (b) Δy_{jj} , (c) $C_{\ell 1}$, and (d) $\Sigma m_{\ell j}$, for the cut-based VBF analysis. The top panels compare simulation and data, while the bottom panels show normalized distributions for all background processes and signal for shape comparisons [74].

leptons in the analysis fall within the rapidity gap defined by the jets. This cut is referred to as the outside lepton veto, or OLV. Stated another way, leptons are required to have a centrality (defined analogously to that of the third jet in equation 5.2) within the jet rapidity gap, or $C_{\ell} < 1$ for both leptons.

Figure 5.3a-c shows the m_{jj} , Δy_{jj} , and $C_{\ell 1}$ variables at the stage where all previous requirements in the sequence have been made. The agreement between data and Monte Carlo is good, and the bottom panels show their power in discriminating the VBF signal from the background processes.

The final signal region is also split into two bins of m_{jj} , with the first bin corresponding to $600 \text{ GeV} < m_{jj} < 1 \text{ TeV}$ and the second bin corresponding to $m_{jj} > 1 \text{ TeV}$. The first bin has more events but also

1885 a larger contribution from background, while the second bin has a lower expected number of events but a
1886 1:1 signal to background ratio.

1887 HIGGS TOPOLOGICAL CUTS

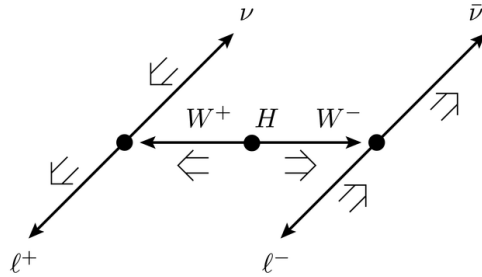


Figure 5.4: A cartoon of the WW final state. Momenta are represented with thin arrows, spins with thick arrows [74].

1888 The final state leptons will exhibit unique correlations due to the fact that they arise from the decay of
1889 a spin zero resonance. These characteristics are present in $H \rightarrow WW^* \rightarrow \ell\nu\ell\nu$ decays regardless of the
1890 production mode being studies. In particular, the spins of the final state leptons and neutrinos must all
1891 cancel, as shown in figure 5.4. Because the neutrino has a left handed chirality and the anti-neutrino has a
1892 right handed chirality (in the massless neutrino approximation), the spin and momentum of the particles
1893 will be anti-aligned and aligned, respectively. In the transverse plane, the momenta of all four final state
1894 objects must cancel as well. With the constraint of having both the momenta and the spin alignments
1895 cancel, the final state kinematics strongly prefer having a small angle between the leptons in the transverse
1896 plane (low $\Delta\phi_{\ell\ell}$). This angular correlation will also lead to low values of the di-lepton invariant mass $m_{\ell\ell}$.
1897 These unique signal final state kinematic correlations are exploited to define the ultimate signal region.

1898 Two requirements on dilepton kinematics are made that are common with lower multiplicity jet bins
1899 as well. The angle between leptons in the transverse plane, $\Delta\phi_{\ell\ell}$, is required to be less than 1.8 radians.
1900 Additionally, the dilepton invariant mass, $m_{\ell\ell}$, is required to be less than 50 GeV.

1901 The cut-based analysis uses m_T as the final discriminating variable as in the ggF focused analysis. The
1902 optimal number of bins in m_T was found to be three bins, with the bin boundaries at 80 and 130 GeV.

1903 Table 5.7 shows a summary of the data and estimated signal and background yields from simulation
 1904 as each requirement described above is made. The table shows how the overall signal to background ra-
 1905 tio grows through the various selection requirements. Table 5.8 shows the background composition after
 1906 each selection requirement, illustrating which backgrounds are reduced most by certain requirements. Fig-
 1907 ure 5.5 shows an ATLAS event display of a candidate event in the final signal region.

Selection	Summary					
	$N_{\text{obs}}/N_{\text{bkg}}$	N_{obs}	N_{bkg}	N_{signal}		
				N_{ggF}	N_{VBF}	N_{VH}
$e\mu$ sample	1.00 ± 0.00	61434	61180	85	32	26
$n_b = 0$	1.02 ± 0.01	7818	7700	63	26	16
$p_T^{\text{sum}} < 15$	1.03 ± 0.01	5787	5630	46	23	13
$m_{\tau\tau} < m_Z - 25$	1.05 ± 0.02	3129	2970	40	20	9.9
$m_{jj} > 600$	1.31 ± 0.12	131	100	2.3	8.2	—
$\Delta y_{jj} > 3.6$	1.33 ± 0.13	107	80	2.1	7.9	—
$C_{j3} > 1$	1.36 ± 0.18	58	43	1.3	6.6	—
$C_{\ell 1} < 1, C_{\ell 2} < 1$	1.42 ± 0.20	51	36	1.2	6.4	—
$m_{\ell\ell}, \Delta\phi_{\ell\ell}, m_T$	2.53 ± 0.71	14	5.5	0.8	4.7	—
<hr/>						
$ee/\mu\mu$ sample	0.99 ± 0.01	26949	27190	31	14	10.1
$n_b, p_T^{\text{sum}}, m_{\tau\tau}$	1.03 ± 0.03	1344	1310	13	8.0	4.0
$m_{jj}, \Delta y_{jj}, C_{j3}, C_\ell$	1.39 ± 0.28	26	19	0.4	2.9	0.0
$m_{\ell\ell}, \Delta\phi_{\ell\ell}, m_T$	1.63 ± 0.69	6	3.7	0.3	2.2	0.0

Table 5.7: Summary of event selection for the $n_j \geq 2$ VBF analysis in the 8 TeV cut-based analysis [74].

1908 5.4.3 BDT-BASED SELECTION

1909 The boosted decision tree based analysis uses many of the variables defined in the cut-based selection as
 1910 inputs to the BDT. The output BDT score (O_{BDT}) is used as the final discriminant rather than m_T ².
 1911 The BDT is trained with the VBF $H \rightarrow WW^*$ simulation as the signal samples and all other processes as
 1912 background, including ggF $H \rightarrow WW^*$ production. While the BDT based analysis is ultimately treated
 1913 as a separate result, it has significant overlap with the cut-based selection.

²For the final discriminant analysis, the O_{BDT} distribution is divided into four bins, with boundaries at $[-1, -0.48, -0.3, 0.78, 1]$.

	Composition of N_{bkg}									
	N_{WW}		$N_{t\bar{t}}$		N_{misid}		N_{VV}		$N_{\text{Drell-Yan}}$	
	N_{WW}^{QCD}	N_{WW}^{EW}	$N_{t\bar{t}}$	N_t	N_{Wj}	N_{jj}	N_{VV}	$N_{ee/\mu\mu}$	$N_{\tau\tau}^{\text{QCD}}$	$N_{\tau\tau}^{\text{EW}}$
$e\mu$ sample	1350	68	51810	2970	847	308	380	51	3260	46
$n_b = 0$	993	43	3000	367	313	193	273	35	2400	29
$p_T^{\text{sum}} < 15$	781	38	1910	270	216	107	201	27	2010	23
$m_{\tau\tau} < m_Z - 25$	484	22	1270	177	141	66	132	7.6	627	5.8
$m_{jj} > 600$	18	8.9	40	5.3	1.8	2.4	5.1	0.1	15	1.0
$\Delta y_{jj} > 3.6$	11.7	6.9	35	5.0	1.6	2.3	3.3	—	11.6	0.8
$C_{j3} > 1$	6.9	5.6	14	3.0	1.3	1.3	2.0	—	6.8	0.6
$C_{\ell 1} < 1, C_{\ell 2} < 1$	5.9	5.2	10.8	2.5	1.3	1.3	1.6	—	5.7	0.6
$m_{\ell\ell}, \Delta\phi_{\ell\ell}, m_T$	1.0	0.5	1.1	0.3	0.3	0.3	0.6	—	0.5	0.2
$ee/\mu\mu$ sample	594	37	23440	1320	230	8.6	137	690	679	16
$n_b, p_T^{\text{sum}}, m_{\tau\tau}$	229	12.0	633	86	26	0.9	45	187	76	1.5
$m_{jj}, \Delta y_{jj}, C_{j3}, C_\ell$	3.1	3.1	5.5	1.0	0.2	0.0	0.7	3.8	0.7	0.1
$m_{\ell\ell}, \Delta\phi_{\ell\ell}, m_T$	0.4	0.2	0.6	0.2	0.2	0.0	0.1	1.5	0.3	0.1

Table 5.8: Background composition after each requirement in the $n_j \geq 2$ VBF analysis in the 8 TeV cut-based analysis [74].

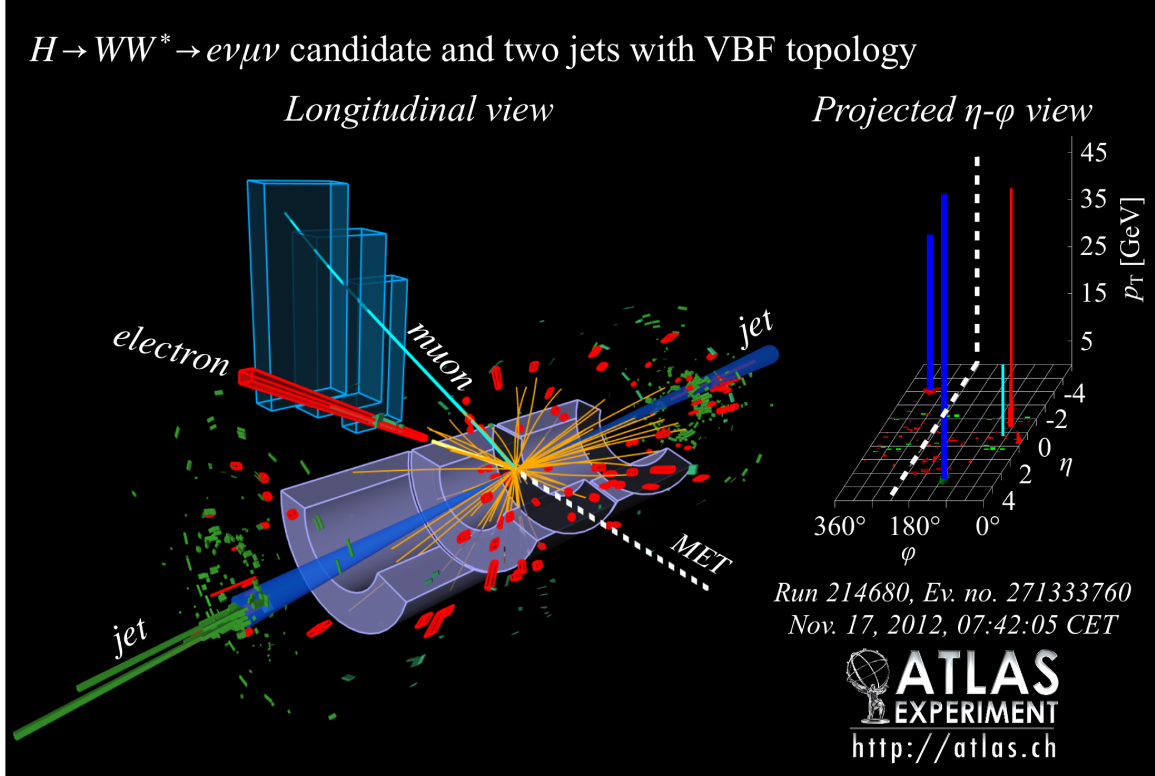


Figure 5.5: Event display of a VBF candidate event [74].

1914 PRE-TRAINING SELECTION AND BDT INPUTS

1915 Before training, the common pre-selection cuts described in section 5.4.1 are applied. Additionally, the
1916 central jet veto and outside lepton veto described in section 5.4.2 are applied. The BDT has eight input
1917 variables, six of which are also variables that are used in the cut-based analysis. The six shared variables
1918 are p_T^{sum} , m_{jj} , Δy_{jj} , $m_{\ell\ell}$, $\Delta\phi_{\ell\ell}$, and m_T . The seventh variable input in the BDT is a combination of
1919 the variables used to define the OLV in the cut-based analysis. The BDT uses as input the sum of lepton
1920 centralities, or $\sum C_\ell = C_{\ell 1} + C_{\ell 2}$. The final BDT input variable, $\Sigma m_{\ell j}$, is constructed to account for
1921 the correlations between the jets and leptons in the event. It is the sum of the invariant masses of all four
1922 possible lepton-jet combinations.

1923 Figure 5.3d shows the agreement between data and simulation for the $\Sigma m_{\ell j}$ variable, as well as showing
1924 its discriminating power. Figure 5.6 shows the distributions of the Higgs topological variables that are
1925 shared between the cut-based and BDT analyses. Figure 5.7 shows the distributions of the VBF topological
1926 variables shared between the cut-based and BDT analyses. In both cases, the VBF yield has been scaled by
1927 a factor of 50 to better show the shape difference compared to the backgrounds.

1928 5.5 BACKGROUND ESTIMATION

1929 This section describes the procedures used to estimate backgrounds for the VBF analysis in both the cut-
1930 based and BDT analyses.

1931 5.5.1 GENERAL STRATEGY

1932 Most of the backgrounds in both the gluon fusion and VBF Higgs analyses have shapes estimated from
1933 Monte Carlo simulation but normalizations derived from control regions in data. In essence, a normaliza-
1934 tion factor (denoted with β or abbreviated as NF) is derived by scaling the MC yield in the control region
1935 to the corresponding yield in data. Once this factor is derived, it can be used to scale the MC estimate of
1936 the background in the signal region. This is illustrated in equation 5.3.

$$B_{\text{SR}}^{\text{est}} = B_{\text{SR}} \times \frac{N_{\text{CR}}}{B_{\text{CR}}} \equiv B_{\text{SR}} \times \beta \quad (5.3)$$

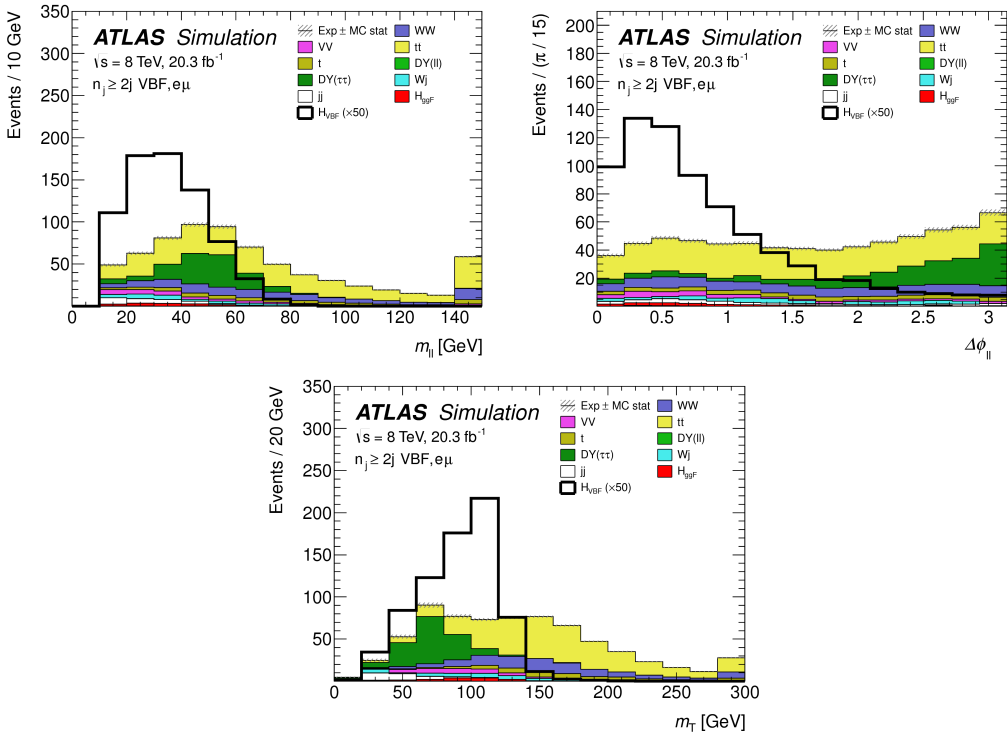


Figure 5.6: Higgs topology variables - $m_{\ell\ell}$ (top left), $\Delta\phi_{\ell\ell}$ (top right), and m_T (bottom) - used in the selection requirements of the cut-based signal region and as inputs to the BDT result. These are plotted after all of the BDT pre-training selection cuts [74]. The VBF Higgs signal cross section is multiplied by a factor of 50 to allow for shape comparisons.

1937 Here, B is the MC yield prediction in the denoted region, while N is the observed number of events in
 1938 data in the denoted region.

1939 There is an alternative way of writing the same equation in terms of an extrapolation factor α rather
 1940 than a normalization factor β . The overall calculation is exactly the same. However, when phrased in
 1941 this way, it shows how the uncertainty on the background estimation can be reduced. This is shown in
 1942 equation 5.4.

$$B_{\text{SR}}^{\text{est}} = N_{\text{CR}} \times \frac{B_{\text{SR}}}{B_{\text{CR}}} \equiv N_{\text{CR}} \times \alpha \quad (5.4)$$

1943 Phrased this way, the equation shows that with enough events in the control region, a large theoretical
 1944 uncertainty on the overall background yield in the signal region can be replaced by a small statistical un-
 1945 certainty coming from the number of data events in the CR and a smaller theoretical uncertainty on the
 1946 extrapolation from the control region to the signal region.

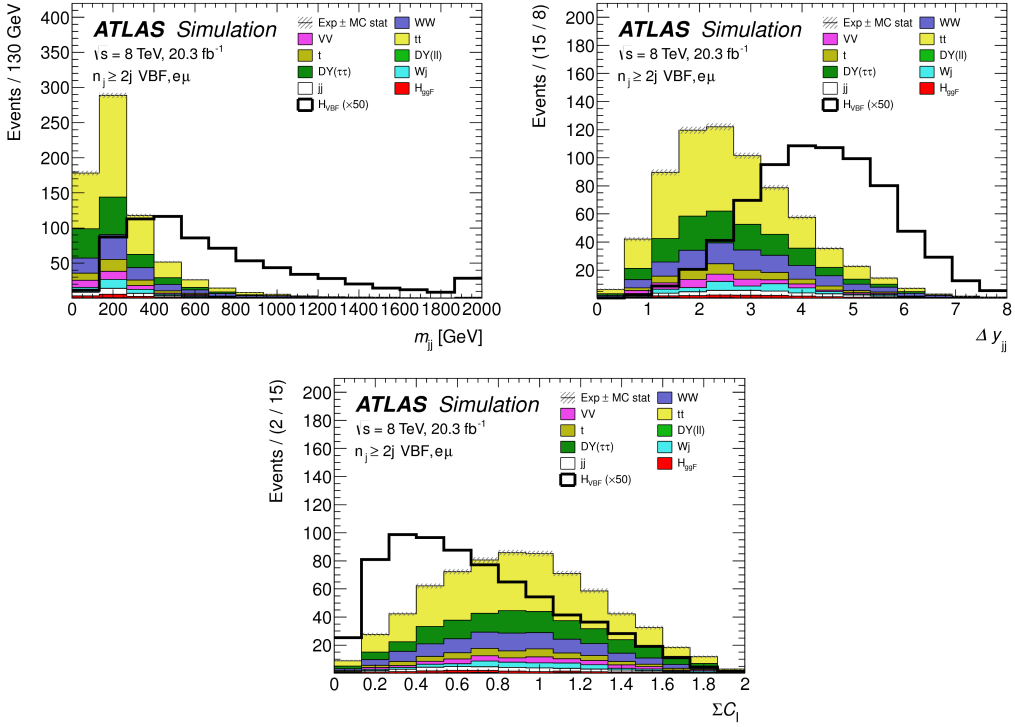


Figure 5.7: VBF topology variables - m_{jj} (top left), Δy_{jj} (top right), $\sum C_\ell$ (bottom) - used in the selection requirements of the cut-based signal region and as inputs to the BDT result. These are plotted after all of the BDT pre-training selection cuts [74]. The VBF Higgs signal cross section is multiplied by a factor of 50 to allow for shape comparisons.

1947 5.5.2 TOP BACKGROUND

1948 The normalization factor β_t for the top background in the VBF analysis is derived in a region required to
 1949 have one b-tagged jet, or $n_b = 1$. In the cut-based analysis, normalization factors are computed after every
 1950 selection requirement by making the same requirements in the CR. These NF are then applied to the $t\bar{t}$ and
 1951 single top event yields in the SR. In the BDT analysis, a single normalization factor is computed for each
 1952 bin of O_{BDT} after applying the BDT pre-training cuts described previously. The computed normaliza-
 1953 tion factors are derived with all flavor combinations combined in order to decrease statistical uncertainty.
 1954 Additionally, in the BDT analysis, BDT bins 2 and 3 are merged for the same reason.

1955 Table 5.9 shows the evolution of the β_t through the cut-based selection. Table 5.10 shows the value of
 1956 the β_t in each bin of O_{BDT} . In all cases, the computed factors are relatively consistent with unity, with
 1957 the largest discrepancy coming in bin 1 of O_{BDT} . The normalization factors in the bins of O_{BDT} are also

¹⁹⁵⁸ consistent with those derived in the cut-based signal region, increasing confidence in the BDT estimation.

Figure 5.8 shows the m_{jj} and O_{BDT} distributions in the top control region. Overall the modeling looks

Cut	β_t
$p_T^{\text{sum}} < 15 \text{ GeV}$	1.03 ± 0.01
$m_{\tau\tau} < m_Z - 25$	1.05 ± 0.01
$m_{jj} > 600 \text{ GeV}$	0.96 ± 0.06
$\Delta y_{jj} > 3.6$	1.02 ± 0.08
CJV	1.13 ± 0.16
OLV	1.01 ± 0.19
$m_{jj} < 1 \text{ TeV}$	0.94 ± 0.19
$m_{jj} > 1 \text{ TeV}$	1.48 ± 0.66

Table 5.9: Top normalization factors computed at each stage of the cut-based selection. Uncertainties are statistical only.

O_{BDT}	β_t
Bin 0	1.09 ± 0.02
Bin 1	1.58 ± 0.15
Bin 2	0.95 ± 0.31
Bin 3	0.95 ± 0.31

Table 5.10: Top normalization factors computed for each bin of O_{BDT} . Uncertainties are statistical only.

¹⁹⁵⁹

¹⁹⁶⁰ consistent with the data. While these normalization factors can be computed and applied to the expected background yields listed in tables like table 5.8, the final normalization of the top background is profiled ¹⁹⁶¹ (meaning there is a dedicated Poisson constraint) and allowed to float in the final statistical fit. ¹⁹⁶²

¹⁹⁶³ 5.5.3 $Z/\gamma^* \rightarrow \tau\tau$ BACKGROUND

¹⁹⁶⁴ In the different flavor channels, the $Z/\gamma^* \rightarrow \tau\tau$ background is an important one. Di-tau production can ¹⁹⁶⁵ produce an $e\mu$ final state if each τ lepton decays to a different flavor lepton.

¹⁹⁶⁶ In the BDT analysis, a single normalization factor for the background is derived. A control region ¹⁹⁶⁷ is defined using the pre-training selection cuts, except requiring that $|m_{\tau\tau} - m_Z| < 25 \text{ GeV}$ so that ¹⁹⁶⁸ the region is enriched in $Z/\gamma^* \rightarrow \tau\tau$ background. Additional requirements of $m_{\ell\ell} < 80(75) \text{ GeV}$ ¹⁹⁶⁹ in the different (same) flavor channel, as well as $O_{\text{BDT}} > -0.48$ are applied to increase the purity of the

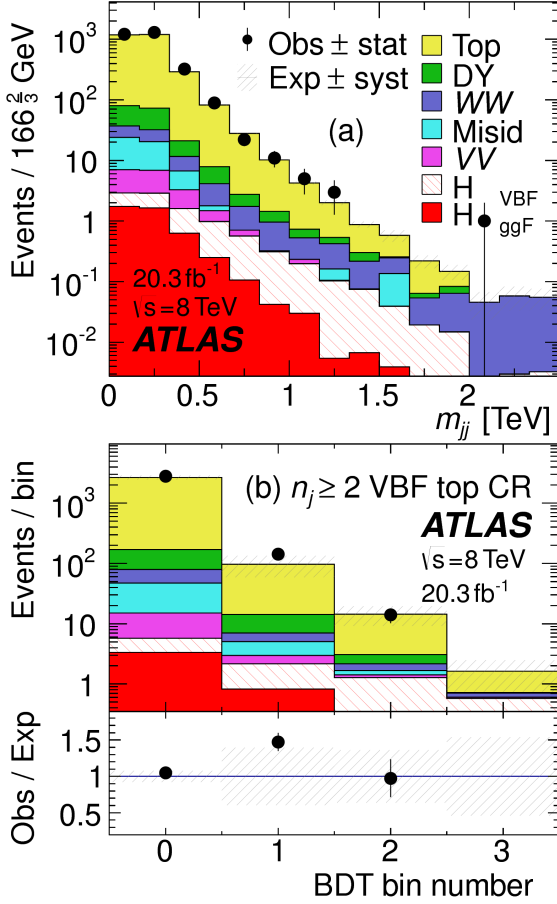


Figure 5.8: Distributions of m_{jj} (a) and O_{BDT} (b) in the VBF $n_b = 1$ top CR [74].

region. The final $\beta_{Z/\gamma^* \rightarrow \tau\tau}$ is calculated to be 0.9 ± 0.3 (statistical uncertainty only). Because of the small contribution of this background in the BDT analysis and the large statistical uncertainty, no additional systematics are calculated. The final SR estimate is scaled by this β and not allowed to float in the fit.

The cut-based corrections are a bit more involved because they need to be applied selection by selection, as well as in the final signal region for the fit. The control region is defined including all SR requirements up to the $Z/\gamma^* \rightarrow \tau\tau$ veto, which is instead turned into a Z mass peak requirement as for the BDT region. The $m_{\ell\ell}$ cut from the BDT region is included as well. The cut-based approach aims to correct the normalization of the $Z/\gamma^* \rightarrow \tau\tau$ background in two ways. First, an overall normalization factor is computed from the control region. However, the VBF topological cuts are not included in this region, and applying them as is done in the top CR is not feasible due to limited statistics. So, instead, correction

1980 factors (CF) to the cut efficiencies of the VBF cuts are derived in a same flavor $Z \rightarrow \ell\ell$ control region,
 1981 which has significantly more statistics. The CF is simply the ratio of the cut efficiencies in data and MC
 1982 derived in this region. In the end, the overall background estimate is given by equation 5.5.

$$N_{Z/\gamma^* \rightarrow \tau\tau}^{\text{est}} = B_{Z/\gamma^* \rightarrow \tau\tau}^{\text{SR}} \times \beta_{\tau\tau} \times \frac{\epsilon_{\text{VBF cuts}}^{\text{data}}}{\epsilon_{\text{VBF cuts}}^{\text{MC}}} \quad (5.5)$$

1983 The hypothesis is that while the normalization correction must be derived in a dedicated region, the effi-
 1984 ciency of the VBF topology requirements should not be sensitive to the type of Z/γ^* process and thus the
 1985 higher number of events can be exploited to derive the CF. Figure 5.9 shows a shape comparison for the
 1986 m_{jj} variable in $Z \rightarrow \tau\tau$ events in the signal region and $Z \rightarrow \ell\ell$ events in the control region. The figure
 1987 shows that the shapes are indeed comparable and thus any CF derived in the same flavor control region
 1988 can reliably be applied in the signal region.

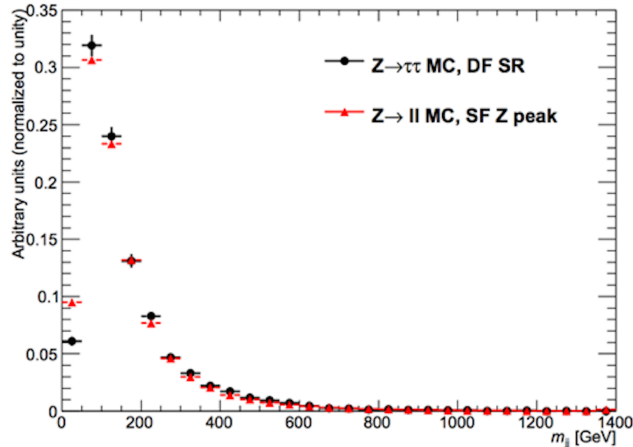


Figure 5.9: Comparison of m_{jj} shape in a same flavor $Z \rightarrow \ell\ell$ control region and the VBF cut-based signal region.

1989 Table 5.11 shows the overall normalization factor $\beta_{\tau\tau}$ and the efficiency correction factors for the various
 1990 VBF topological cuts. In general, the statistical uncertainties on the cut efficiency corrections are quite
 1991 good, and the MC tends to underestimate the efficiency of the VBF cuts for the $Z/\gamma^* \rightarrow \tau\tau$ background.
 1992 The overall normalization factor is also consistent with that calculated for the BDT analysis.

$\beta_{\tau\tau}$	0.97 ± 0.04
Cut	Correction factors
$m_{jj} > 600 \text{ GeV}$	1.09 ± 0.01
$\Delta y_{jj} > 3.6$	1.14 ± 0.02
CJV	1.20 ± 0.02
OLV	1.17 ± 0.03
$m_{jj} < 1 \text{ TeV}$	1.17 ± 0.06
$m_{jj} > 1 \text{ TeV}$	1.18 ± 0.13

Table 5.II: $Z/\gamma^* \rightarrow \tau\tau$ correction factors for the VBF cut-based analysis. Uncertainties are statistical only.

1993 5.5.4 $Z/\gamma^* \rightarrow \ell\ell$ BACKGROUND

1994 In the same flavor channels, the $Z/\gamma^* \rightarrow \ell\ell$ background is dominant and thus must be estimated cor-
 1995 rectly. In both the BDT and cut-based analyses, the background is estimated using the so-called “ABCD”
 1996 method. The ABCD method creates four different regions by defining requirements on two variables.
 1997 One of the regions (A) is the signal region, while the other regions are defined by inverting one of both of
 1998 the requirements. in this case, the two variables used are $m_{\ell\ell}$ and E_T^{miss} , because inverting either of the
 1999 SR cuts on these variables will give regions rich in the $Z/\gamma^* \rightarrow \ell\ell$ background. Figure 5.10 illustrates the
 2000 definitions of each region.

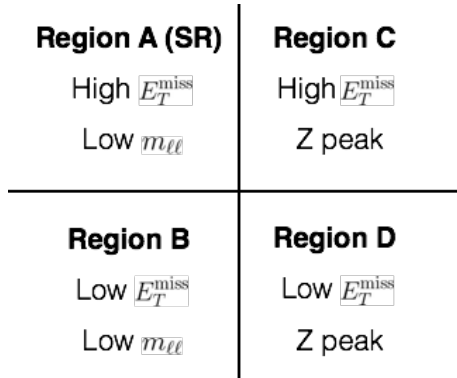


Figure 5.10: General illustration of the ABCD region definitions for $Z/\gamma^* \rightarrow \ell\ell$ background estimation.

2001 In both of the cut-based and BDT analyses, the Z peak region is defined with $|m_{\ell\ell} - m_Z| < 15 \text{ GeV}$.
 2002 In the cut-based analysis, low $m_{\ell\ell}$ corresponds to $m_{\ell\ell} < 50 \text{ GeV}$ (this defines the cut-based SR) while
 2003 in the BDT it is $m_{\ell\ell} < 75 \text{ GeV}$. In the cut-based, high and low E_T^{miss} are defined as opposite ends of

2004 the 55 GeV cut applied for the signal region definition. The BDT low E_T^{miss} region is between 25 and
 2005 45 GeV, while the high E_T^{miss} region is $E_T^{\text{miss}} > 45$ GeV.

2006 Once the regions are defined, the background in the signal region is estimated by extrapolating the
 2007 estimate in region B to region A. This extrapolation is done by multiplying the number of events in region
 2008 B by the ratio of the number of events in regions C and D. Effectively, the Z peak region is used to estimate
 2009 the efficiency of the E_T^{miss} requirement in data, and then this efficiency is applied in the low $m_{\ell\ell}$ region.
 2010 An additional correction is also applied for the non-closure of the method in MC. This is summarized in
 2011 equations 5.6 and 5.7.

$$N_{Z/\gamma^* \rightarrow \ell\ell}^{\text{SR}} = N_{Z/\gamma^* \rightarrow \ell\ell}^B \times \frac{N_{Z/\gamma^* \rightarrow \ell\ell}^C}{N_{Z/\gamma^* \rightarrow \ell\ell}^D} \times f_{\text{corr}} \quad (5.6)$$

2012

$$f_{\text{corr}} = \frac{B_{\text{MC}}^A / B_{\text{MC}}^B}{B_{\text{MC}}^C / B_{\text{MC}}^D} \quad (5.7)$$

2013 Here, the N refer to data yields in each region with the non Z/γ^* backgrounds subtracted, while B refer
 2014 to the Z/γ^* yields in MC in each region.

2015 A normalization factor $\beta_{\ell\ell}$ is computed for each analysis as the ratio of the predicted data yield to the
 2016 MC yield in the SR. The shape of the BDT distribution is taken from data region B, while the shape of
 2017 the m_T distribution in the cut-based analysis is taken from Z/γ^* MC in the SR. The values of $\beta_{\ell\ell}$ in the
 2018 cut-based and BDT analyses from this method are summarized in table 5.12. They are quite consistent with
 2019 one another within the statistical uncertainties. In the cut-based analysis, the same cut efficiency correction
 2020 factors shown in table 5.11 are also applied (in product with the $\beta_{\ell\ell}$) in the same flavor channels to the Z/γ^*
 2021 background.

	β_t
BDT Bin 1	1.01 ± 0.15
BDT Bin 2	0.89 ± 0.28
Cut-based	0.81 ± 0.21

Table 5.12: $Z/\gamma^* \rightarrow \ell\ell$ normalization factors for cut-based and BDT analyses. Uncertainties are statistical only.

2022 **5.5.5 WW AND OTHER DIBOSON BACKGROUNDS**

2023 The Standard Model WW and other diboson backgrounds have both their shape and normalization taken
 2024 from MC simulation. They are validated in dedicated control regions and found to agree with data well.

2025 As SM WW production is the largest of these backgrounds and is irreducible, validating the estimate
 2026 is of particular importance. A validation region is constructed by requiring the pre-selection requirements
 2027 on leptons and $m_{\ell\ell}$, $n_b = 0$, and $m_T > 100$ GeV. The m_{T2} variable [99] is an additional discriminant
 2028 that will isolate the SM WW background, and a requirement of $m_{T2} > 160$ GeV is placed to define
 2029 the WW validation region. This requirement gives a 60% purity for the validation region. The derived
 2030 normalization factor in the region is 1.15 ± 0.19 and is thus consistent with unity. Figure 5.11 shows the
 2031 m_{T2} distribution and how it distinguishes the WW background.

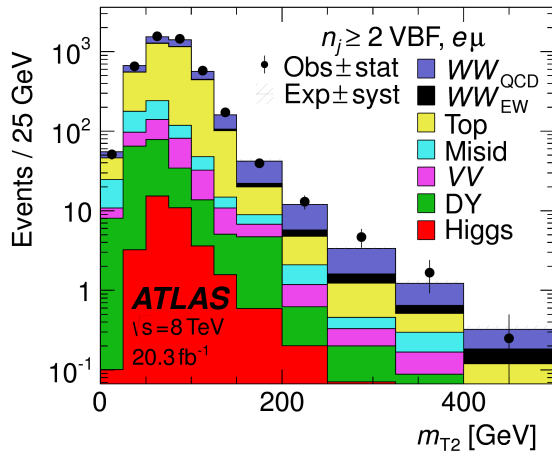


Figure 5.11: Distribution of m_{T2} in the WW validation region of the VBF analysis [74].

2032 **5.5.6 HIGGS PRODUCTION VIA GLUON-GLUON FUSION**

2033 Because this analysis is dedicated to measuring the VBF contribution to Higgs production, the compo-
 2034 nent of Higgs production from gluon-gluon fusion is treated as a background. The shape is taken directly
 2035 from simulation, using the generators described in table 5.4. In the final combined fit of all different signal
 2036 regions, the normalization is controlled by either a combined signal strength parameter μ , which controls
 2037 the normalization of both ggF and VBF production, or a separate parameter μ_{ggF} depending on the in-

2038 interpretation being presented in the final results.

2039 5.5.7 BACKGROUNDS WITH MISIDENTIFIED LEPTONS

2040 As discussed previously, the W +jets and QCD multijet backgrounds are derived with fully data-driven
2041 methods. These backgrounds do not make a large contribution to the final VBF signal region but their
2042 estimation methods are discussed briefly here.

2043 W +JETS BACKGROUND

2044 The W +jets background enters the signal region by having one of the jets mis-reconstructed as a lepton.
2045 The background is estimated by constructing a control sample with two leptons, where one lepton passes
2046 the usual lepton quality requirements but the second lepton fails one of those requirements (also known
2047 as the “anti-identified” lepton). This control region is rich in the W +jets contribution because if a second
2048 lepton is reconstructed in a W +jets event it is likely to be poor quality. The purity of this W +jets control
2049 sample is 85% to 90% depending on the exact configuration of leptons in the final state.

2050 The signal region estimate of W +jets is estimated by extrapolation from the control sample to the sig-
2051 nal region using extrapolation factors derived in a Z +jets control sample in data. The extrapolation factor
2052 is the ratio of the number of lepton candidates satisfying all quality criteria to the number of lepton can-
2053 didates anti-identified. This ratio is measured in bins of p_T and η . Thus, the final signal region estimate
2054 (binned as the extrapolation factor is binned) is simply the number of events in the anti-identified lepton
2055 control sample multiplied by the extrapolation factor derived from the Z +jets control sample. Figure 5.12
2056 shows the extrapolation factors derived for electrons and muons.

2057 QCD MULTIJET BACKGROUND

2058 The method for estimating the multijet background is very similar to the W +jets estimation method. The
2059 control sample in this case has two anti-identified leptons but otherwise satisfies all signal region require-
2060 ments. The extrapolation factor is estimated from a multijet sample and applied twice to the control sam-
2061 ple.

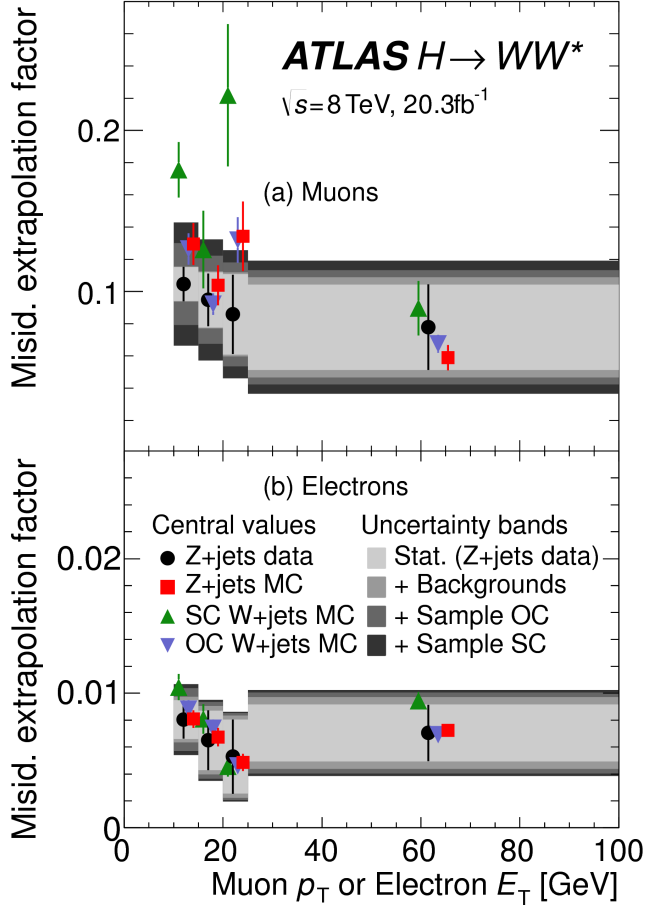


Figure 5.12: Extrapolation factors for the $W+jets$ estimate derived for muons (a) and electrons (b) as a function of lepton p_T [74].

5.5.8 BACKGROUND COMPOSITION IN SIGNAL REGION

After all of these estimation procedures, the signal region background composition can be calculated. The estimated yields are all shown in table 5.8. Figure 5.13 shows the relative percentages of the different background for the different flavor and same flavor final states. In $e\mu$, the leading backgrounds are top backgrounds, ggF Higgs, and SM WW production. In $ee/\mu\mu$, the leading background is Drell-Yan, followed by top and ggF Higgs.

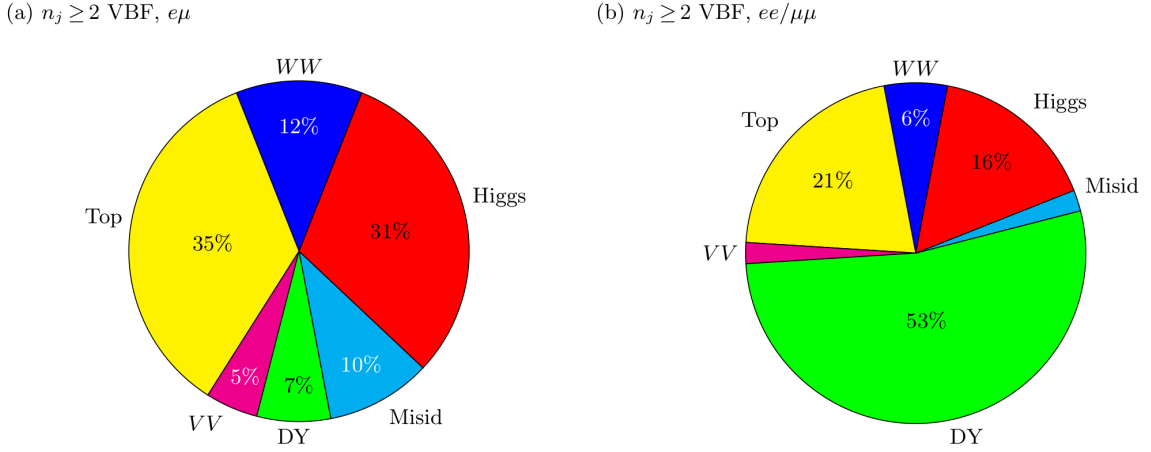


Figure 5.13: Background composition in final VBF signal region [74].

2068 5.6 SYSTEMATIC UNCERTAINTIES

2069 There are two main types of systematic uncertainties that are assessed for the analysis. First, theoretical
 2070 uncertainties associated with the signal and background yield estimates are discussed. Then, experimental
 2071 uncertainties due to detector effects are shown. Normalization uncertainties refer to uncertainties that
 2072 affect the cross section of the process in question in the signal region being probed. Shape uncertainties
 2073 refer to systematic uncertainties that affect the shape of the final discriminating variable (either m_T or
 2074 O_{BDT}).

2075 5.6.1 THEORETICAL UNCERTAINTIES

2076 There are four main components to theoretical uncertainties assigned to signal and background processes
 2077 taken from Monte Carlo. Each one is a different source of variation in the overall acceptance for that
 2078 process. The first involves variation of the QCD renormalization and factorization scales used in the cal-
 2079 culation. In this case, the two scales are varied both independently and simultaneously by factors of two
 2080 high or low. The resulting variation in normalization and shape for the process is taken as a systematic
 2081 uncertainty (referred to as scale uncertainty). This uncertainty approximates the level of the correction
 2082 to the cross section that would come from including the next order of the QCD calculation. Next, there
 2083 is an uncertainty associated with the PDF set used in generating the events. The uncertainty eigenvec-

2084 tors for the given PDF set are inspected, and the envelope of maximal variation is taken as an uncertainty
 2085 (referred to as PDF uncertainty). Finally, there are two uncertainties associated with the choice of MC
 2086 software. An uncertainty associated with the generator chosen for the hard scattering process is evaluated
 2087 by keeping the parton showering software constant but varying the matrix element generator and taking
 2088 the maximal variation as an uncertainty (referred to as the generator uncertainty). The converse variation
 2089 can also be done, where the matrix element generator remains constant and the generator used for the un-
 2090 derlying event/parton shower modeling is varied (referred to as the UE/PS uncertainty). In cases where
 2091 the background is normalized in a control region, the systematic uncertainty arises from variations of the
 2092 extrapolation factor α between the CR and the SR, which can affect the normalization of the background
 2093 in the SR.

2094 There are two additional uncertainties that are applied to the Higgs processes as well. First, there are
 2095 uncertainties assigned to the Higgs total production cross section. Then, there are uncertainties assigned
 2096 based on the fact that the analysis is done in exclusive jet bins and it is possible for signal events to migrate
 2097 from one bin to the next depending on the presence or absence of jets. These are assigned using the Jet Veto
 2098 Efficiency (JVE) procedure [18, 100] for ggF events and the Stewart-Tackmann (ST) method [101] for VBF
 2099 production. Table 5.13 shows the total theory uncertainties on the backgrounds in the cut-based analysis.
 2100 These are the sum in quadrature of the uncertainties from each of the variations described above.

Process	Theory syst. (%)
ggF H	48
Top	26
QCD WW	37
$Z/\gamma^* \rightarrow \tau\tau$	6.1

Table 5.13: Systematic uncertainties for various processes in the cut-based VBF analysis, given in units of % change
in yield. Values are given for the low m_{jj} signal region.

2101 Figures 5.14 and 5.15 show the variations in the extrapolation factor from the PDF and QCD uncertain-
 2102 ties on the top background estimate, binned in m_T , for the cut-based analysis. In both cases, there was
 2103 no significant shape uncertainty but normalization uncertainties were assigned according to the maximal
 2104 variation. These uncertainties enter into the 26% total uncertainty on top quark production quoted in
 2105 table 5.13

2106 While the estimate for the same-flavor $Z/\gamma^* \rightarrow \ell\ell$ background is data-driven, there is still a systematic
 2107 uncertainty taken for the non-closure of the method in Monte Carlo. This is taken as the maximum of the
 2108 deviation of the non-closure factor f_{corr} from unity and its uncertainty, or $\max(|1 - f_{\text{corr}}|, \delta f_{\text{corr}})$. For
 2109 the cut-based analysis this non-closure uncertainty 23%, while for the BDT analysis it is 17%.

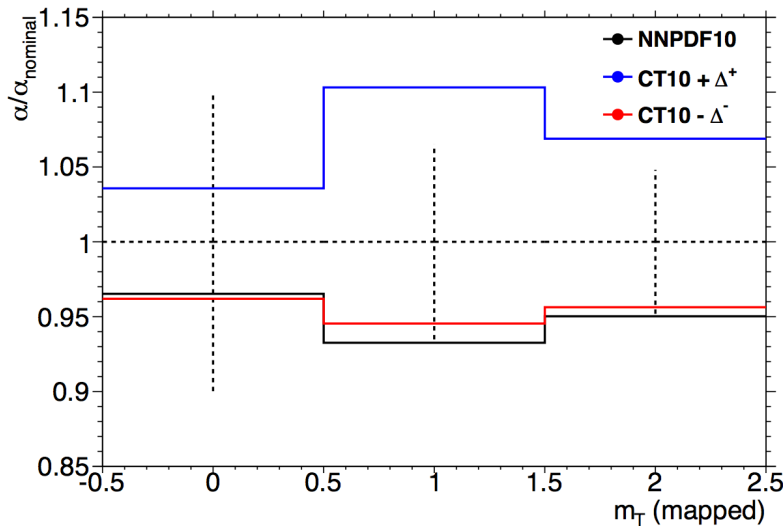


Figure 5.14: Variations in the top background extrapolation factor in the cut-based analysis due to PDF uncertainties. The uncertainties are shown in the three bins of m_T used in the final cut-based statistical fit. Variations from the eigenvector of the nominal PDF, CT10, as well as the result from an alternate PDF (NNPDF10), are compared.

2110 5.6.2 EXPERIMENTAL UNCERTAINTIES

2111 In this analysis, the theoretical uncertainties are the most dominant after statistical, but there are some ex-
 2112 perimental uncertainties that make a contribution as well. The first is the uncertainty on the measured in-
 2113 tegrated luminosity, which affects backgrounds whose normalizations are taken from MC and is measured
 2114 to be 2.8% in the 8 TeV dataset [102]. The dominant sources of uncertainty overall are uncertainties on the
 2115 jet energy scale and resolution and the b -tagging efficiency. Additional sources include lepton uncertain-
 2116 ties on identification, resolution, and trigger efficiency, as well as uncertainties on the missing transverse
 2117 momentum.

2118 The jet energy scale uncertainty is split into several independent components, including jet-flavor de-
 2119 pendingent calorimeter response uncertainties, uncertainties on modeling of pile-up interactions, uncertain-

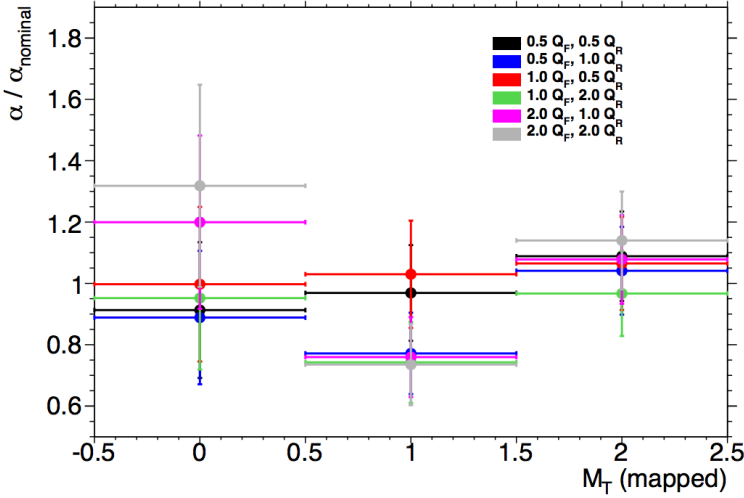


Figure 5.15: Variations in the top background extrapolation factor in the cut-based analysis due to QCD scale uncertainties. The uncertainties are shown in the three bins of m_T used in the final cut-based statistical fit. Q_F is the QCD factorization scale, while Q_R is the QCD renormalization scale.

ties on extrapolation from the central to forward detector regions, and MC non-closure [103]. The uncertainty on energy scale for jets used in this analysis ranges from 1% to 7% depending on the jet p_T and η . The jet energy resolution varies from 5% to 20%, with uncertainties ranging from 2% to 40% (the largest uncertainties occurring at the selection threshold).

The b-tagging efficiency is independently measured in data samples enriched in dileptonic decays of $t\bar{t}$ events or in events where a muon is reconstructed in the vicinity of a jet [104, 105]. The efficiencies and their uncertainties are binned in p_T and decomposed into uncorrelated components using an eigenvector method [106]. Uncertainties on the efficiency range from 1% to 7.8%. The uncertainty on the rate of misidentification of c -jets as b -jets ranges from 6-14%, while the uncertainty on the rate of light jet mistagging ranges from 9-19% depending on p_T and η .

The total experimental uncertainties on different signal and background components are summarized in table 5.14. They are compared to the level of other statistical and systematic uncertainties as well. Overall, the experimental uncertainties are sub-dominant compared to the statistical and theoretical uncertainties.

Sample	Total error	Stat. error	Expt. syst. err.	Theo. syst. err.
$n_j \geq 2$ VBF-enriched				
N_{sig}	13	—	6.8	12
N_{bkg}	9.2	4.7	6.4	4.5
N_{WW}	32	—	14	28
N_{top}	15	9.6	7.6	8.5
N_{misid}	22	—	12	19
N_{VV}	20	—	12	15
$N_{\tau\tau}$ (DY)	40	25	31	2.9
$N_{ee/\mu\mu}$ (DY)	19	11	15	—

Table 5.14: Composition of the post-fit uncertainties (in %) on the total signal (N_{sig}), total background (N_{bkg}), and individual background yields in the VBF analysis [74].

2133 5.7 RESULTS

2134 While the combined results of all the $H \rightarrow WW^*$ sub-analyses will be discussed in the next chapter, this
 2135 section presents the results of the VBF specific analysis and interpretations. As table 5.7 shows, the final
 2136 cut-based signal region contains 20 events in data with $m_T < 150$ GeV, 14 coming from the $e\mu$ channel
 2137 and 6 coming from the $ee + \mu\mu$ channel. The BDT analysis has many more candidates due to its looser
 2138 selection, and the yields in each bin of O_{BDT} are shown in table 5.15.

2139 Figure 5.16(a) shows the final distribution of data candidates compared to the expected m_T distribution
 2140 for signal and background. The data are very consistent with a VBF Higgs hypothesis. Figure 5.16(b) shows
 2141 where the data candidates fall in the two-dimensional binning of m_T and m_{jj} used in the fit for the cut-
 2142 based analysis. Figure 5.17 shows the distributions of O_{BDT} and m_T in the VBF BDT analysis. Again the
 2143 data are quite consistent with a VBF Higgs hypothesis.

2144 Because the cut-based result is used as a validation for the BDT analysis and the two signal regions are
 2145 not fully orthogonal, it is interesting to explore which events overlap between the two analyses. Of the
 2146 twenty events in the cut-based signal region, only seven were not selected by the BDT analysis, while the
 2147 other thirteen also enter the BDT signal region. Figure 5.18 shows where the different analysis candidates
 2148 lie in the m_{jj} - m_T plane. This shows clearly that the advantage of the BDT analysis is that it can extract
 2149 signal candidates from the lower m_{jj} region due to its ability to recognize correlations with other variables.

(a) Before the BDT classification

Selection	Summary						Composition of N_{bkg}									
	$N_{\text{obs}}/N_{\text{bkg}}$	N_{obs}	N_{bkg}	N_{signal}			N_{WW}^{QCD}	N_{WW}^{EW}	$N_{t\bar{t}}$	N_t	N_{Wj}	N_{jj}	N_{VV}	$N_{\text{Drell-Yan}}$	$N_{ee/\mu\mu}^{\text{QCD}}$	$N_{\tau\tau}^{\text{EW}}$
				N_{ggF}	N_{VBF}	N_{VH}										
$e\mu$ sample	1.04 ± 0.04	718	689	13	15	2.0	90	11	327	42	29	23	31	2.2	130	2
$ee/\mu\mu$ sample	1.18 ± 0.08	469	397	6.0	7.7	0.9	37	3	132	17	5.2	1.2	10.1	168	23	1

(b) Bins in O_{BDT}

$e\mu$ sample																
Bin 0 (not used)	1.02 ± 0.04	661	650	8.8	3.0	1.9	83	9	313	40	26	21	28	2.2	126	1
Bin 1	0.99 ± 0.16	37	37	3.0	4.2	0.1	5.0	1.0	17	3.1	3.3	1.8	2.6	—	4.0	0.2
Bin 2	2.26 ± 0.63	14	6.2	1.2	4.2	—	1.5	0.5	1.8	0.3	0.4	0.3	0.8	—	0.3	0.3
Bin 3	5.41 ± 2.32	6	1.1	0.4	3.1	—	0.3	0.2	0.3	0.1	—	—	0.1	—	0.1	0.1
$ee/\mu\mu$ sample																
Bin 0 (not used)	1.91 ± 0.08	396	345	3.8	1.3	0.8	33	2	123	16	4.1	1.1	8.8	137	20.5	0.5
Bin 1	0.82 ± 0.14	53	45	1.5	2.2	0.1	3.0	0.5	10.4	1.8	0.8	0.2	0.9	26	1.7	0.1
Bin 2	1.77 ± 0.49	14	7.9	0.6	2.5	—	0.8	0.3	1.1	0.2	0.2	—	0.3	4.4	0.3	0.1
Bin 3	6.52 ± 2.87	6	0.9	0.2	1.7	—	0.1	0.2	0.2	—	—	—	0.7	—	—	—

Table 5.15: Event selection for the VBF BDT analysis. The event yields in (a) are shown after the pre-selection and the additional requirements applied before the BDT classification (see text). The event yields in (b) are given in bins in O_{BDT} after the classification [74].

While the context of these results in the broader $H \rightarrow WW^*$ statistical analysis will be presented in the next chapter, the statistical significance of the VBF Higgs result is shown here. In the BDT analysis, the expected signal significance was 2.7σ , while the observed significance was 3.1σ . In the cut-based analysis, the expected significance was 2.1σ and the observed significance was 3.0σ . The compatibility between these two results can be evaluated by computing the probability of observing a larger difference in Z_0 values than the one measured. Using toy Monte Carlo with the ggF signal strength fixed to unity and considering only statistical uncertainties, this probability is computed to be 79%, indicating good agreement between the analyses. This result represents the first evidence of the vector boson fusion production of a Higgs boson.

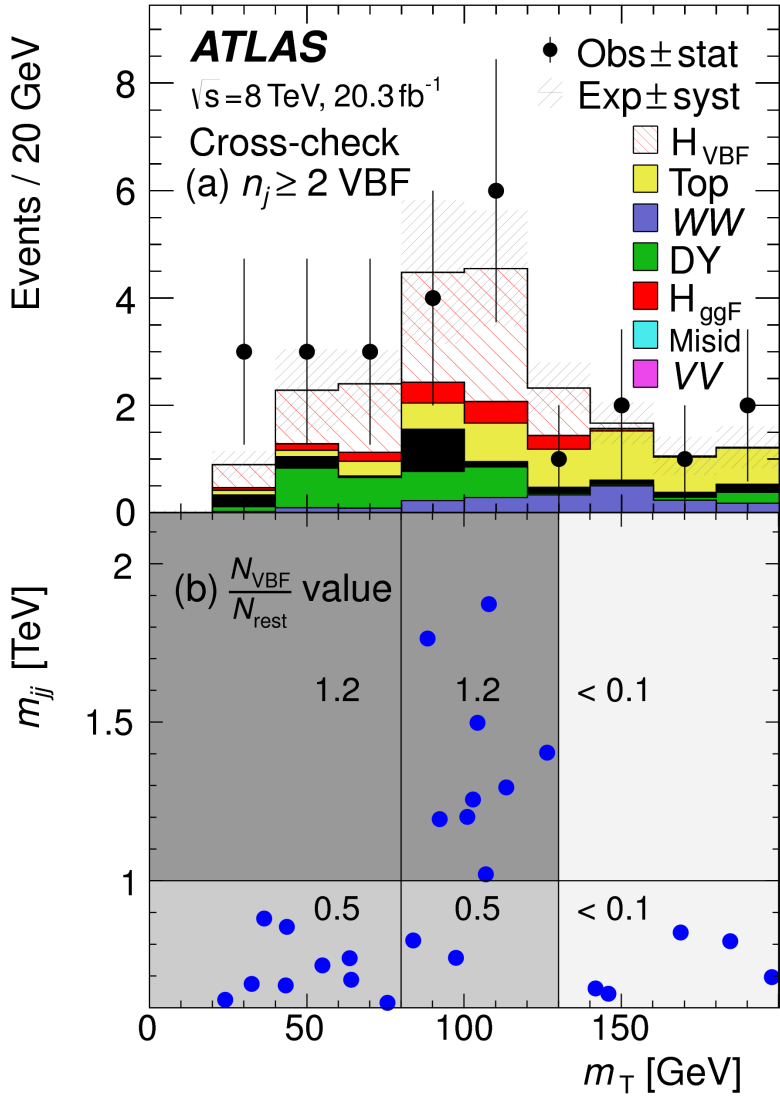


Figure 5.16: Post-fit distributions in the cut-based VBF analysis. Panel (a) shows the one-dimensional m_T distribution, while (b) shows the data candidates split into the bins of m_T and m_{jj} used in the final fit [74].

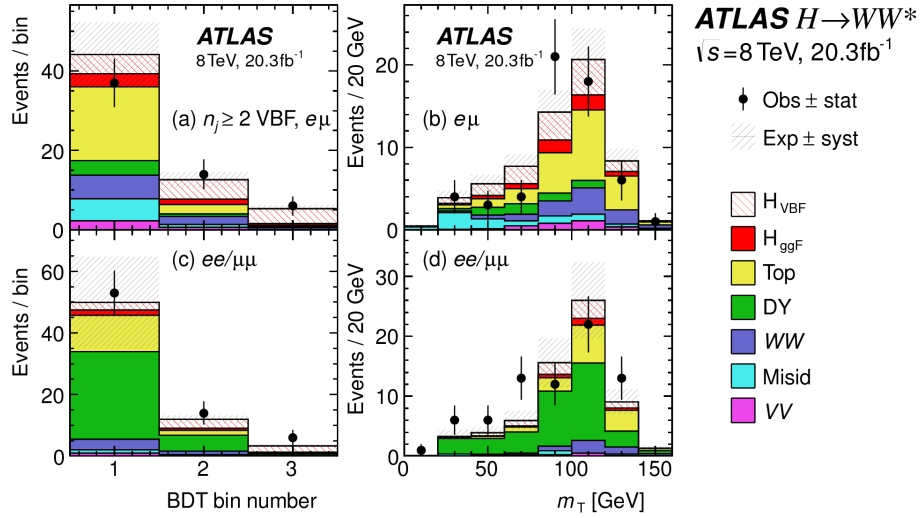


Figure 5.17: Postfit distributions in the BDT VBF analysis [74].

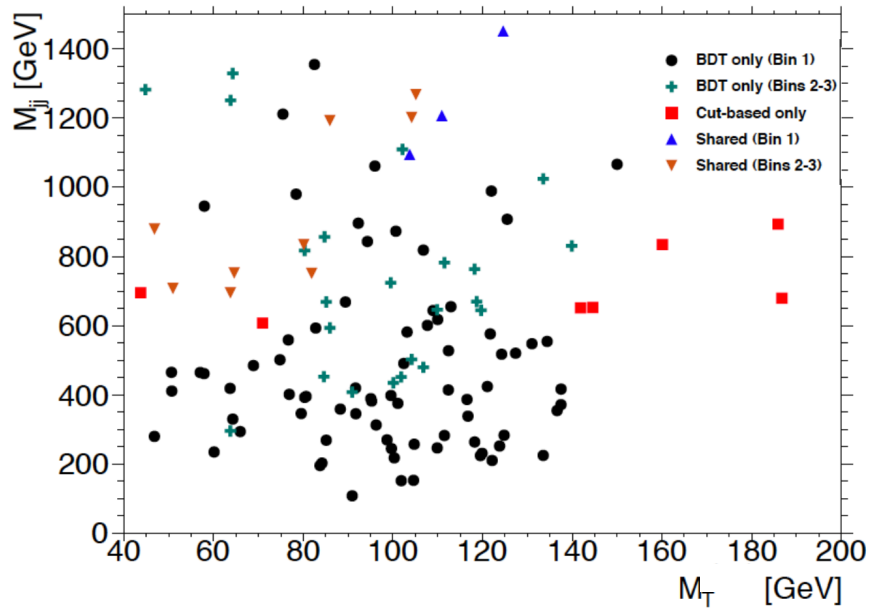


Figure 5.18: Overlap between cut-based and BDT VBF signal region candidates in the m_{jj} - m_T plane.

*The feeling is less like an ending than just another starting
point.*

Chuck Palahniuk

6

2159

2160

Combined Run I $H \rightarrow WW^* \rightarrow \ell\nu\ell\nu$

2161

results

2162 6.1 INTRODUCTION

2163 In the final statistical analysis of $H \rightarrow WW^* \rightarrow \ell\nu\ell\nu$, the dedicated gluon-gluon fusion and vector
2164 boson fusion sensitive signal regions are all combined into a single fit to determine the main parameters of
2165 interest, the Higgs signal strength μ and mass m_H . Therefore, while the specific requirements applied for
2166 the VBF sensitive analysis are discussed in chapter 5, the final measurement of these parameters can only be
2167 discussed in combination with the results of the ggF dedicated analysis. For example, because ggF Higgs
2168 production is considered a background in the VBF analysis, the ggF dedicated signal regions can actually
2169 constrain the normalization of this background in the VBF dedicated region.

2170 This chapter presents the combined interpretation of results in the $H \rightarrow WW^* \rightarrow \ell\nu\ell\nu$ analysis

2171 for gluon fusion and vector boson fusion Higgs production. First, the results of the dedicated gluon fu-
 2172 sion search are presented. Then, a comparison of the individual production mode signal strengths (μ_{ggF}
 2173 and μ_{VBF}) and a measurement of the combined signal strength (μ) are shown. Subsequently, the mea-
 2174 sured values of the Higgs couplings to fermions and vector bosons is presented. Finally, the cross section
 2175 measurement for ggF and VBF production are shown.

2176 6.2 RESULTS OF DEDICATION GLUON FUSION $H \rightarrow WW^* \rightarrow \ell\nu\ell\nu$ ANALYSIS

2177 The details of the dedicated gluon fusion $H \rightarrow WW^* \rightarrow \ell\nu\ell\nu$ analysis are not discussed in this thesis
 2178 and instead left to more comprehensive sources [74]. However, a brief summary of the results is essen-
 2179 tial for describing the measurements of Higgs properties and interpreting the the dedicated VBF Higgs
 2180 production search in a broader context. Additionally, the final Run 1 results on gluon fusion production
 2181 make use of the dedicated variables for same flavor final states developed in section 3.5. The results in the
 2182 same flavor final states will be shown here as well.

2183 6.2.1 RESULTS IN SAME FLAVOR ($ee/\mu\mu$) FINAL STATES

2184 Final states of the $H \rightarrow WW^* \rightarrow \ell\nu\ell\nu$ channel where both leptons have the same flavor ($ee/\mu\mu$)
 2185 were not included in the discovery result due to increased pileup conditions in the $\sqrt{s} = 8$ TeV data.
 2186 Dedicated techniques for background reduction in the same flavor final states were developed, as described
 2187 in section 3.5. The results shown in this section are the first published results using the same flavor channels
 2188 in the $H \rightarrow WW^*$ analysis.

2189 Table 6.1 shows the background estimate, expected signal yield, and event count in data for the same
 2190 flavor channels in the $n_j \leq 1$ signal regions. The dedicated same flavor background reduction techniques
 2191 allow this channel to preserve a signal to background ratio similar to that of the different flavor channels.

	N_{obs}	N_{bkg}	N_{ggF}	N_{VBF}
$n_j = 0$	1108	1040 ± 40	77 ± 15	2.4 ± 1.7
$n_j = 1$	467	427 ± 21	22 ± 6	3.6 ± 1.8

Table 6.1: Post-fit yields in ggF dedicated signal regions for the $ee/\mu\mu$ final states [74].

2192 Figure 6.1 shows the final m_T distribution in data for the $n_j \leq 1$ same flavor channels. The data is very
 2193 consistent with the Higgs hypothesis and it can be seen that the same flavor channels are indeed sensitive
 2194 to gluon fusion production of the Higgs.

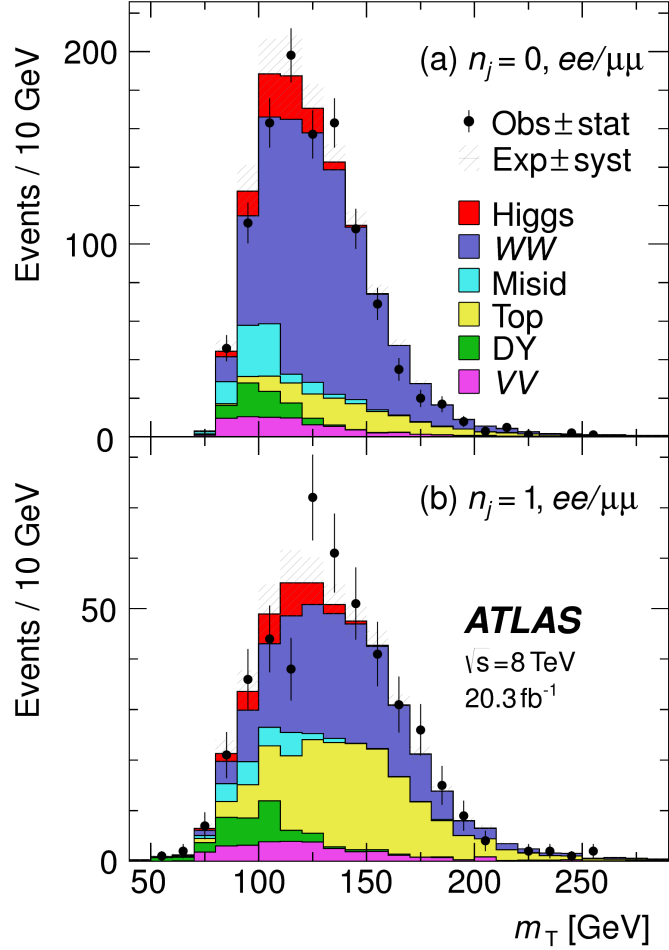


Figure 6.1: Post-fit m_T distribution in the $n_j \leq 1$ regions for the same flavor ($ee/\mu\mu$) final states [74].

2195 6.2.2 COMBINED GLUON FUSION RESULTS

2196 Table 6.2 shows the individual signal regions that were input into the final statistical fit. The ggF dedicated
 2197 bins use m_T as their discriminating variable and are separated into bins of p_T of the subleading lepton as
 2198 well. The VBF dedicated bin uses the O_{BDT} distribution as its final discriminant.

2199 Table 6.3 shows the yields in the various signal regions in both data and expected signal and back-
 2200 grounds. The yields for signal and background are all scaled according to the final normalizations cal-

SR category i				Fit var.	
n_j , flavor	$\otimes m_{\ell\ell}$	$\otimes p_T^{\ell 2}$	$\otimes \ell_2$		
$n_j = 0$	$e\mu$	$\otimes [10, 30, 55]$	$\otimes [10, 15, 20, \infty]$	$\otimes [e, \mu]$	m_T
	$ee/\mu\mu$	$\otimes [12, 55]$	$\otimes [10, \infty]$		m_T
$n_j = 1$	$e\mu$	$\otimes [10, 30, 55]$	$\otimes [10, 15, 20, \infty]$	$\otimes [e, \mu]$	m_T
	$ee/\mu\mu$	$\otimes [12, 55]$	$\otimes [10, \infty]$		m_T
$n_j \geq 2$ ggF	$e\mu$	$\otimes [10, 55]$	$\otimes [10, \infty]$		m_T
$n_j \geq 2$ VBF	$e\mu$	$\otimes [10, 50]$	$\otimes [10, \infty]$		O_{BDT}
	$ee/\mu\mu$	$\otimes [12, 50]$	$\otimes [10, \infty]$		O_{BDT}

Table 6.2: All signal regions definitions input into final statistical fit [74].

culated in the fit.

	N_{obs}	N_{bkg}	N_{ggF}	N_{VBF}
$n_j = 0$	3750	3430 ± 90	300 ± 50	8 ± 4
$n_j = 1$	1596	1470 ± 40	102 ± 26	17 ± 5
$n_j \geq 2$, ggF $e\mu$	1017	960 ± 40	37 ± 11	13 ± 1.4
$n_j \geq 2$, VBF	130	99 ± 9	7.7 ± 2.6	21 ± 3

Table 6.3: Post-fit yields in the both ggF and VBF dedicated signal regions with all lepton flavor final states combined [74].

Figure 6.2 shows the final post-fit m_T distribution in the $n_j \leq 1$ regions. The data are very consistent with the hypothesis of ggF Higgs production. These yields are used as input, along with the VBF results in chapter 5, for the physical interpretation of results presented in subsequent sections.

6.3 SIGNAL STRENGTH MEASUREMENTS IN GGF AND VBF PRODUCTION

When all of the signal regions are combined in the fit, there can be a combined measurement of the signal strength as well as the individual ggF and VBF signal strengths. The combined signal strength is the ratio of the measured cross section in the combined gluon fusion and VBF signal regions to the theory prediction

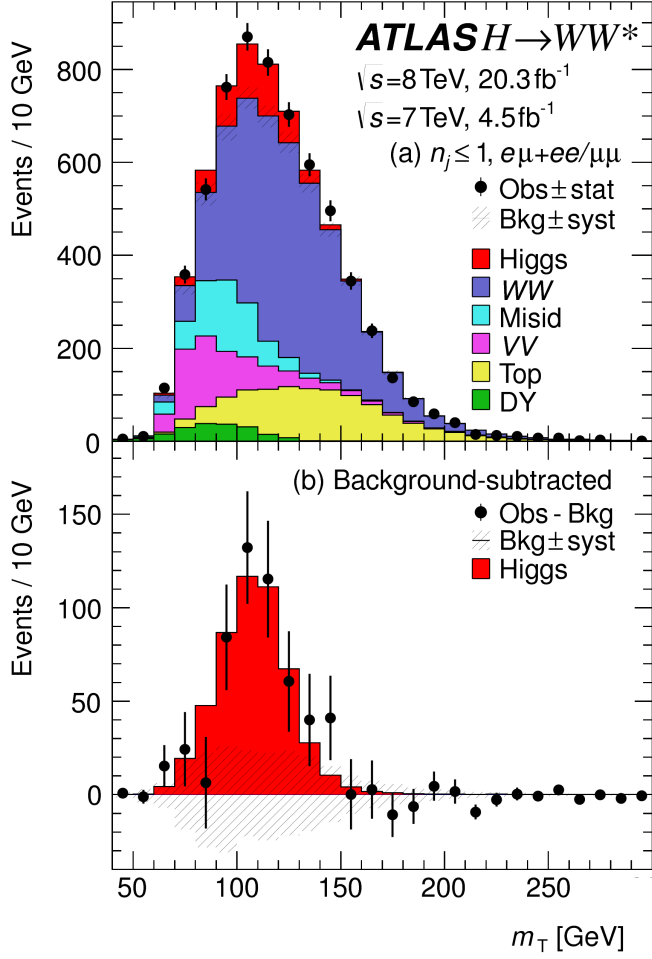


Figure 6.2: Post-fit m_T distribution in the $n_j \leq 1$ regions [74].

for the sum of of these two processes. It is a signal strength measurement for the total Higgs production cross section that this analysis is sensitive to. The final measured combined signal strength μ is measured shown in equation 6.1.

$$\begin{aligned}
 \mu &= 1.09 \quad {}^{+0.16}_{-0.15} (\text{stat.}) \quad {}^{+0.08}_{-0.07} \left(\frac{\text{expt}}{\text{syst}} \right) \quad {}^{+0.15}_{-0.12} \left(\frac{\text{theo}}{\text{syst}} \right) \quad \pm 0.03 \left(\frac{\text{lumi}}{\text{syst}} \right) \\
 &= 1.09 \quad {}^{+0.16}_{-0.15} (\text{stat}) \quad {}^{+0.17}_{-0.14} (\text{syst}) \\
 &= 1.09 \quad {}^{+0.23}_{-0.21}.
 \end{aligned} \tag{6.1}$$

2212 Figure 6.3 gives the best fit signal strength $\hat{\mu}$ as a function of the hypothesized Higgs mass. The value at
 2213 a mass of 125.36 GeV corresponds to the μ quoted in equation 6.1. This value of the Higgs mass is used
 2214 because it is the most precise mass measurement from ATLAS, a result of the combined $\gamma\gamma$ and ZZ mass
 2215 measurements [107].

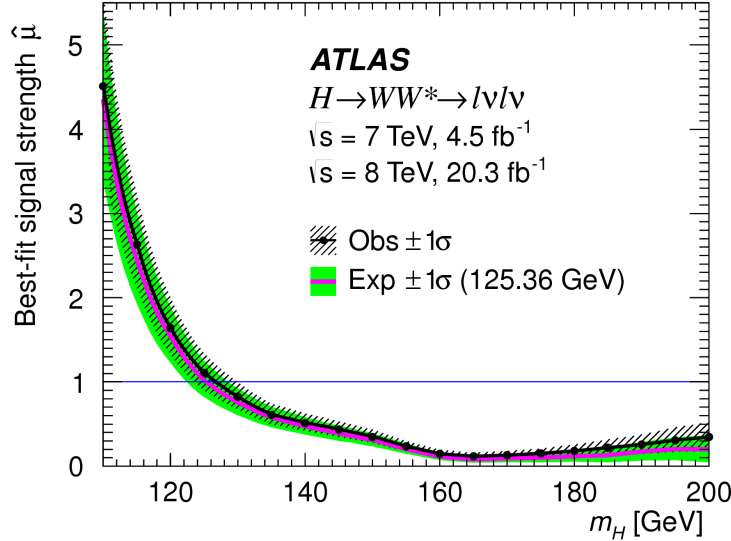


Figure 6.3: Best fit signal strength $\hat{\mu}$ as a function of hypothesized m_H [74].

2216 As explained in chapter 3, a probability p_0 can be computed using the test statistic q_0 to quantify the
 2217 probability that the background could fluctuate to produce an excess at least as large as the one observed
 2218 in the data. The local p_0 value is shown in figure 6.4 as a function of m_H . The minimum p_0 value is at
 2219 $m_H = 130$ GeV and corresponds to a significance of 6.1σ . The curve is relatively flat and the significance
 2220 is the same at 125.36 GeV within the quoted precision. The expected significance for a signal with strength
 2221 $\mu = 1.0$ is 5.8σ . This represents the first discovery level observation of Higgs production using only the
 2222 $H \rightarrow WW^* \rightarrow \ell\nu\ell\nu$ analysis.

2223 All the results presented so far in this section have been for the combined gluon fusion and VBF pro-
 2224 duction modes. However, each signal strength can be calculated separately in the likelihood as well. There
 2225 are two ways to do this. First, the likelihood can be parameterized in terms of a single parameter, the ratio
 2226 of the VBF and gluon fusion signal strengths. With this method, the statistical significance of the VBF
 2227 Higgs result can be evaluated. Figure 6.5 shows the likelihood as a function of the ratio $\mu_{\text{VBF}}/\mu_{\text{ggF}}$.

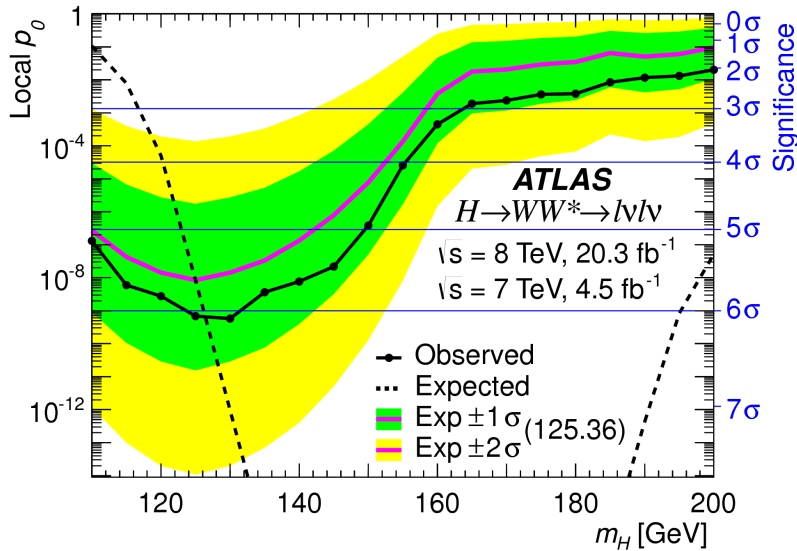


Figure 6.4: Local p_0 as a function of m_H [74].

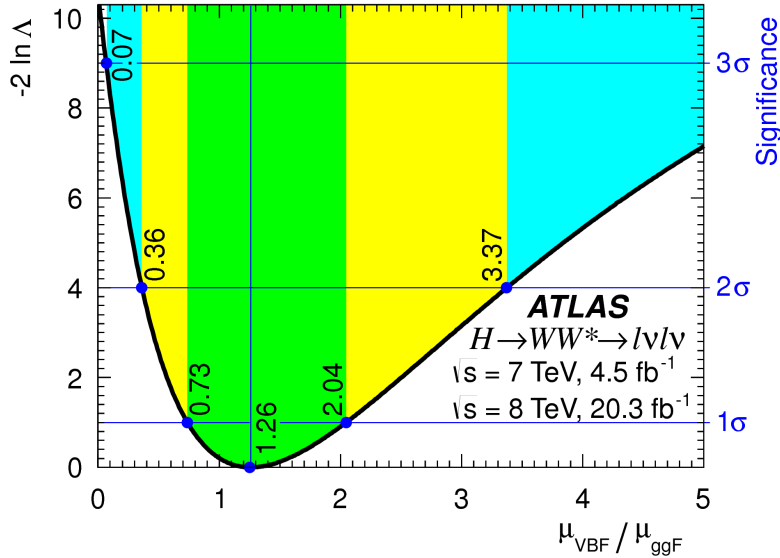


Figure 6.5: Likelihood as a function of $\mu_{\text{VBF}} / \mu_{\text{ggF}}$ [74].

2228 The best fit value of the ratio of signal strengths is shown in equation 6.2. Within the quoted uncer-
2229 tainties, it is consistent with a ratio of unity.

$$\frac{\mu_{\text{VBF}}}{\mu_{\text{ggF}}} = 1.26^{+0.61} (\text{stat.})^{+0.50} (\text{syst.}) = 1.26^{+0.79}_{-0.53} \quad (6.2)$$

2230 The null hypothesis for VBF production corresponds to a ratio of $\mu_{\text{VBF}}/\mu_{\text{ggF}} = 0$. The likelihood in
 2231 figure 6.5 gives a significance of 3.2σ at $\mu_{\text{VBF}}/\mu_{\text{ggF}} = 0$, as quoted in chapter 5.

2232 In addition to the ratio of signal strengths, each signal strength can be varied independently in the like-
 2233 lihood as well. Figure 6.6 shows the two dimensional likelihood scan in the $\mu_{\text{ggF}}-\mu_{\text{VBF}}$ plane. The best fit
 2234 values of the two signal strengths are shown in equation 6.3. Both are consistent with unity within their
 2235 uncertainties.

$$\begin{aligned} \mu_{\text{ggF}} &= 1.02 \pm 0.19^{+0.22}_{-0.18} = 1.02^{+0.29}_{-0.26} \\ \mu_{\text{VBF}} &= 1.27^{+0.44}_{-0.40}^{+0.29}_{-0.21} = 1.27^{+0.53}_{-0.45} \end{aligned} \quad (6.3)$$

(stat.) (syst.)

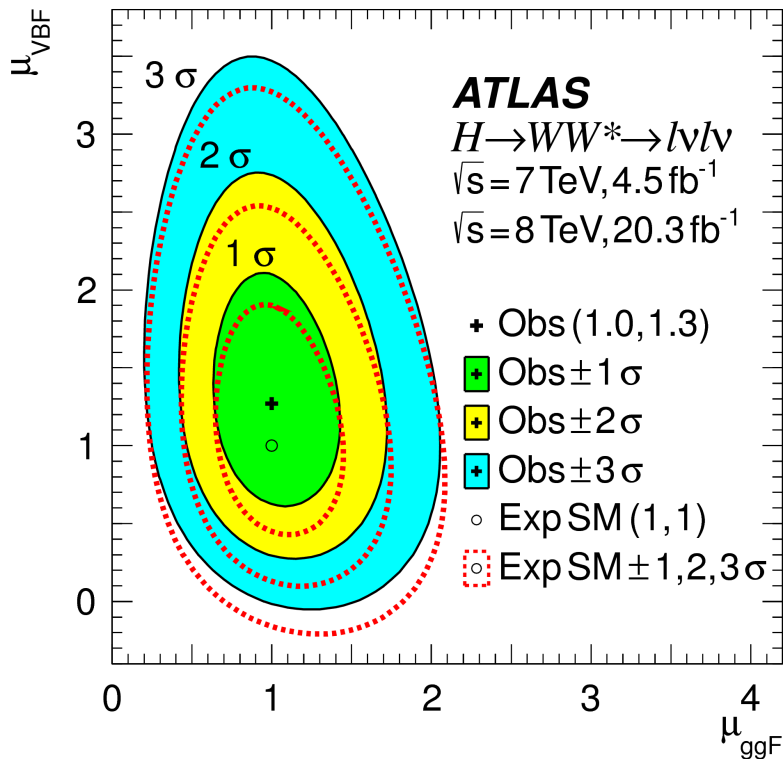


Figure 6.6: Two dimensional likelihood scan as a function of μ_{VBF} and μ_{ggF} [74].

2236 6.4 MEASUREMENT OF HIGGS COUPLINGS TO VECTOR BOSONS AND FERMIONS

2237 Similar to the parameterization of signal strength, the couplings of the Higgs to fermions and bosons can
 2238 also be parameterized. The parameter of interest in this case is κ , or the ratio of the measured coupling to
 2239 the Standard Model expectation. Both the fermion and boson couplings have these so-called scale factors,
 2240 κ_F for fermions and κ_V for bosons. Gluon fusion production is sensitive to the fermion couplings through
 2241 the top quark loops in its production, while VBF production is sensitive to the vector boson couplings in
 2242 its production. Both modes are sensitive to the vector boson couplings in their decays. The signal strengths
 2243 will have dependence on the coupling scale factors as described in equation 6.4 [18].

$$\begin{aligned}\mu_{\text{ggF}} &\propto \frac{\kappa_F^2 \cdot \kappa_V^2}{(\mathcal{B}_{H \rightarrow f\bar{f}} + \mathcal{B}_{H \rightarrow gg}) \kappa_F^2 + (\mathcal{B}_{H \rightarrow VV}) \kappa_V^2} \\ \mu_{\text{VBF}} &\propto \frac{\kappa_V^4}{(\mathcal{B}_{H \rightarrow f\bar{f}} + \mathcal{B}_{H \rightarrow gg}) \kappa_F^2 + (\mathcal{B}_{H \rightarrow VV}) \kappa_V^2}.\end{aligned}\quad (6.4)$$

2244 Figure 6.7 shows the two-dimensional likelihood scan of κ_F and κ_V . The best-fit values are given in equa-
 2245 tion 6.5. The best-fit values are consistent with unity within their uncertainties.

$$\begin{aligned}\kappa_F &= 0.93 & {}^{+0.24}_{-0.18} & {}^{+0.21}_{-0.14} & = 0.93 & {}^{+0.32}_{-0.23} \\ \kappa_V &= 1.04 & {}^{+0.07}_{-0.08} & {}^{+0.07}_{-0.08} & = 1.04 & \pm 0.11.\end{aligned}\quad (6.5)$$

(stat.) (syst.)

2246

2247 6.5 HIGGS PRODUCTION CROSS SECTION MEASUREMENT

2248 Another measurement that comes naturally from the signal strength measurements quoted earlier is the
 2249 production cross section and 7 and 8 TeV for both gluon fusion and VBF production. The general equa-

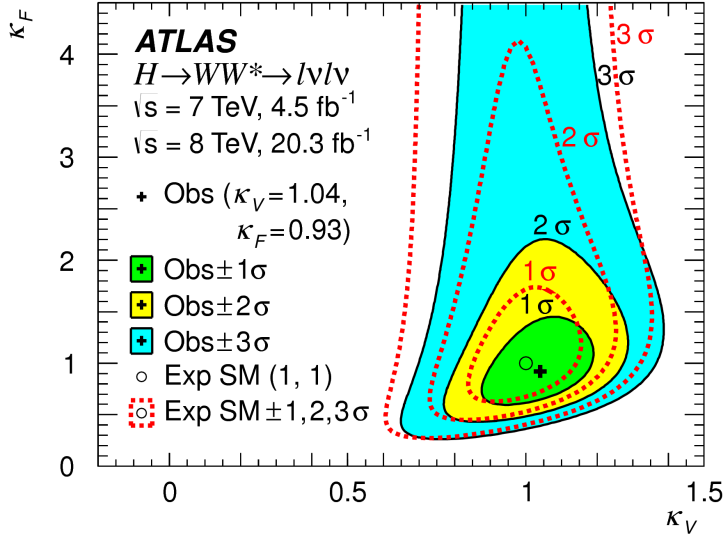


Figure 6.7: Likelihood scan as a function of κ_F and κ_V , the Higgs coupling scale factors [74].

tion for calculating the cross section is given in equation 6.6.

$$\begin{aligned}
 (\sigma \cdot \mathcal{B}_{H \rightarrow WW^*})_{\text{obs}} &= \frac{(N_{\text{sig}})_{\text{obs}}}{\mathcal{A} \cdot \mathcal{C} \cdot \mathcal{B}_{WW \rightarrow l\nu l\nu}} \cdot \frac{1}{\int L dt} \\
 &= \hat{\mu} \cdot (\sigma \cdot \mathcal{B}_{H \rightarrow WW^*})_{\text{exp}}
 \end{aligned} \tag{6.6}$$

$(N_{\text{sig}})_{\text{obs}}$ is the number of events observed in data. \mathcal{A} is the geometric and kinematic acceptance of the detector, while \mathcal{C} is the efficiency of the signal region selection for events that are reconstructed in the detector. The branching ratio of a WW system to leptons must also be divided out. The production cross section depends on the center of mass energy and the production mode desired (gluon fusion or VBF), and so three separate cross section measurements are quoted in equation 6.7.

$$\begin{aligned}
 \sigma_{\text{ggf}}^{7\text{TeV}} \cdot \mathcal{B}_{H \rightarrow WW^*} &= 2.0 \pm 1.7 \quad {}^{+1.2}_{-1.1} = 2.0 \quad {}^{+2.1}_{-2.0} \text{ pb} \\
 \sigma_{\text{ggf}}^{8\text{TeV}} \cdot \mathcal{B}_{H \rightarrow WW^*} &= 4.6 \pm 0.9 \quad {}^{+0.8}_{-0.7} = 4.6 \quad {}^{+1.2}_{-1.1} \text{ pb} \\
 \sigma_{\text{VBF}}^{8\text{TeV}} \cdot \mathcal{B}_{H \rightarrow WW^*} &= 0.51 \quad {}^{+0.17}_{-0.15} \quad {}^{+0.13}_{-0.08} = 0.51 \quad {}^{+0.22}_{-0.17} \text{ pb.}
 \end{aligned} \tag{6.7}$$

(stat.) (syst.)

2256 The predicted cross section values (including the branching ratio of $H \rightarrow WW^*$) for gluon fusion are
2257 3.3 ± 0.4 pb at 7 TeV and 4.2 ± 0.5 pb at 8 TeV, consistent with the measured values within their uncer-
2258 tainties. For vector boson fusion, the predicted cross section is 0.35 ± 0.02 pb, again consistent with the
2259 measured value.

2260 **6.6 CONCLUSION**

2261 The combined analysis of the gluon fusion and vector boson fusion processes in $H \rightarrow WW^* \rightarrow \ell\nu\ell\nu$ in
2262 the 7 and 8 TeV datasets has yielded the first discovery level significance for Higgs production in this decay
2263 channel. Additionally, precise measurements of the couplings to vector bosons and fermions are given.
2264 Finally, signal strengths and cross sections for each production mode are measured. Figure 6.8 shows the
2265 $H \rightarrow WW^* \rightarrow \ell\nu\ell\nu$ measurements in comparison with other Higgs decay channels in ATLAS. The
2266 measurement of signal strength from this channel remains the most sensitive in both the gluon fusion and
2267 VBF production modes for the Run 1 dataset.

ATLAS

Individual analysis

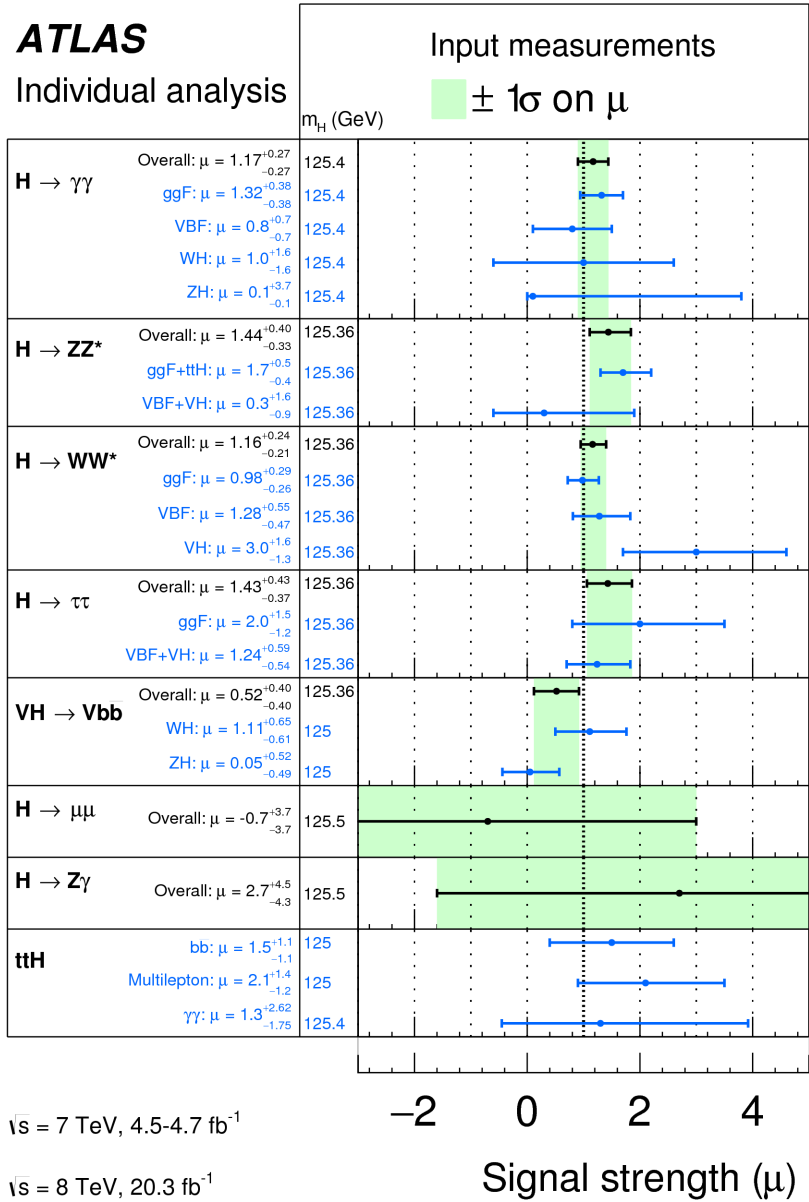


Figure 6.8: Comparison of signal strength measurements in different Higgs decay channels on ATLAS [io8].

2268

Part III

2269

Search for Higgs pair production in the

2270

$HH \rightarrow b\bar{b}b\bar{b}$ channel in LHC Run 2 at $\sqrt{s} =$

2271

13 TeV

Passion is in all great searches and is necessary to all creative endeavors.

W. Eugene Smith

7

2272

2273 Search for Higgs pair production in boosted 2274 $b\bar{b}b\bar{b}$ final states

2275 7.1 INTRODUCTION

2276 This chapter presents a search for resonant production of a Higgs pair in the $X \rightarrow HH \rightarrow b\bar{b}b\bar{b}$ final
2277 state in 3.2 fb^{-1} of data collected at $\sqrt{s} = 13 \text{ TeV}$. In particular, this chapter focuses on a search for this
2278 final state in the regime where m_X is large ($\gtrsim 1 \text{ TeV}$) and the Higgs bosons in the decay are significantly
2279 boosted. A tailored selection for this boosted selection, using novel techniques in jet substructure and b -
2280 tagging, is discussed. Then, the data-driven background estimate is presented. Finally, the results of the
2281 search are shown. The signal models used as benchmarks are a spin-2 Randall Sundrum graviton (RSG)
2282 and a narrow width spin zero resonance. These models are described in more detail in Chapter 1. Limits
2283 on signal models are reserved for the next chapter where the results of this chapter are combined with the

2284 results of a separate selection dedicated to the lower m_X regime.

2285 **7.2 MOTIVATION**

2286 With the center of mass energy increase from $\sqrt{s} = 8 \text{ TeV}$ to $\sqrt{s} = 13 \text{ TeV}$, the LHC and ATLAS are
2287 able to probe new resonances at higher mass scales than previously accessible in Run 1. This is a powerful
2288 motivator for searching for a new resonance in the early 13 TeV data. Figure 7.1 shows the ratios of parton
2289 luminosities between 8 and 13 TeV for different resonance masses. For a resonance of $M_X = 2 \text{ TeV}$, the
2290 cross section at $\sqrt{s} = 13 \text{ TeV}$ is roughly a factor of 10 larger than at $\sqrt{s} = 8 \text{ TeV}$.

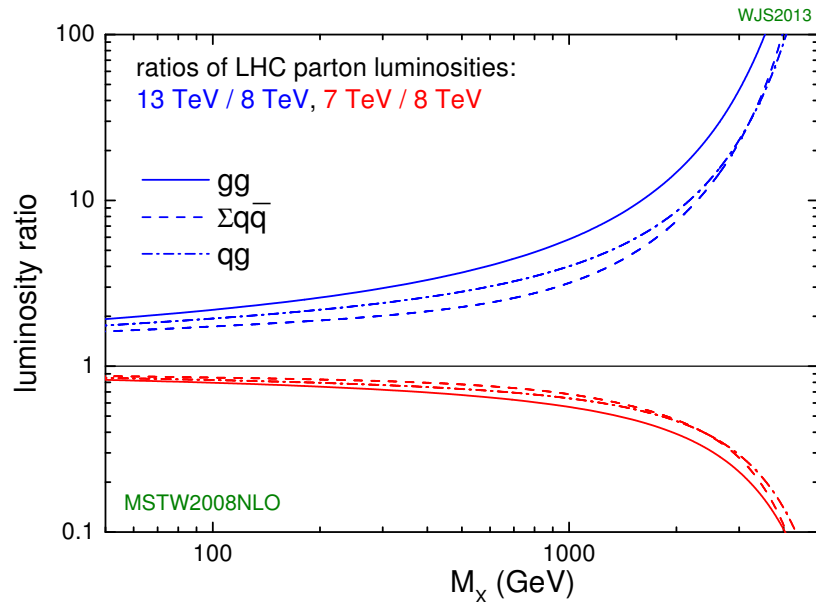


Figure 7.1: Parton luminosity ratios as a function of resonance mass M_X for 13/8 TeV and 7/8 TeV [109].

2291 Higgs pair production offers a vast array of unprobed regions of phase space where searches for BSM
2292 physics can be made. Chapter 1 discusses some possibilities for both resonant and non-resonant enhance-
2293 ment of the di-Higgs production cross section. Given the increased mass reach of the LHC in Run 2, it is
2294 particularly important to focus on resonant searches at high m_X . When conducting a search in the HH
2295 final state, the different possible decay modes of each Higgs must be considered. Figure 7.2 shows the
2296 branching ratio of the HH final state for different combinations of decays of each individual Higgs. As

2297 the largest branching ratio for the 125 GeV Higgs is $H \rightarrow b\bar{b}$, the $HH \rightarrow b\bar{b}b\bar{b}$ branching ratio is also the
2298 largest at 33%.

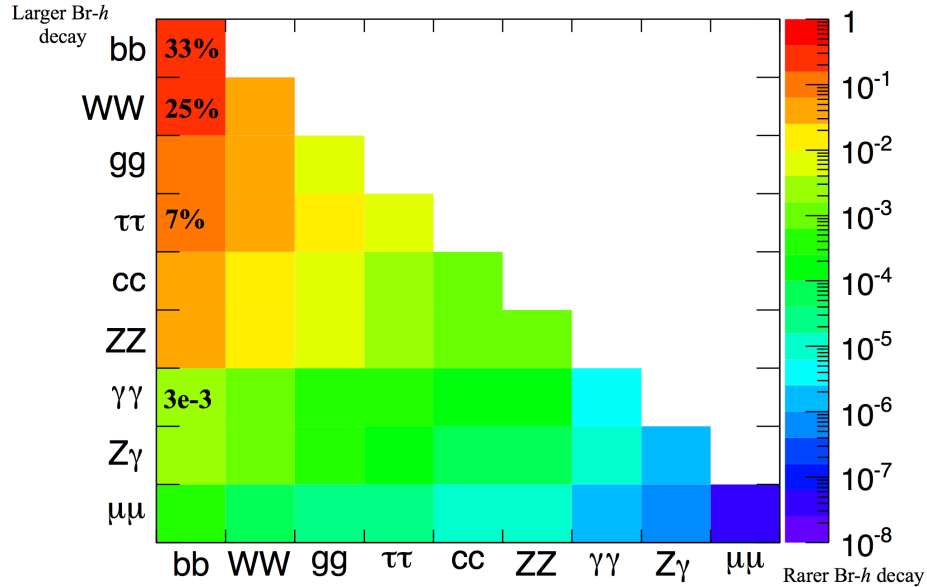


Figure 7.2: Summary of HH branching ratios [110].

2299 At high m_X , the Higgs bosons resulting from the decay of a heavy resonance will have large p_T ¹. The
2300 angular separation between the decay products of the Higgs, $\Delta R \equiv \sqrt{(\Delta\eta)^2 + (\Delta\phi)^2}$, is inversely
2301 proportional to the Higgs p_T , as shown in equation 7.1.

$$\Delta R \approx \frac{2m}{p_T} \quad (7.1)$$

2302 Figure 7.3 shows the minimum ΔR between truth level B decay vertices in simulation samples for Randall-
2303 Sundrum gravitons of different masses. The figure shows that as the mass of the graviton increases, the ΔR
2304 distribution between the b quarks in the Higgs decay tends to shift to lower values. Because of this effect,
2305 it is necessary to tailor a selection to target these merged b -jets.

¹In the limit that the resonance mass is much larger than the Higgs mass, the Higgs p_T is roughly $m_X/2$.

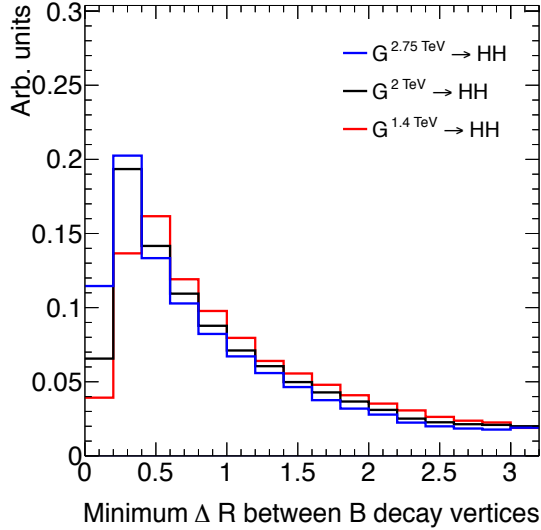


Figure 7.3: Minimum ΔR between B decay vertices for different RSG masses in a $G_{KK}^* \rightarrow HH \rightarrow 4b$ sample with $c = 1$.

2306 7.3 DATA AND SIMULATION SAMPLES

2307 7.3.1 SIGNAL MODELS

2308 While the resonance search is by its nature generic (as it is a simple search for a peak in the $4b$ invariant mass
 2309 spectrum), there are two signal models that the selection requirements have been optimized for. The first
 2310 is Randall-Sundrum (RSG) model, where a tower of massive spin-2 Kaluza-Klein gravitons is predicted.
 2311 The second is a heavy narrow scalar resonance, the so-called “heavy Higgs”. This type of resonance arises,
 2312 for example, in the two Higgs doublet model (2HDM). More details about the physics of these models
 2313 and their motivation is given in chapter 1.

2314 Signal graviton (G_{KK}^*) events are generated at leading order (LO) with **MADGRAPH5 v2.2.2** [ii]. The
 2315 PDF set used is the **NNPDF2.3 LO** set [ii]. For modeling parton shower and hadronization in jets, **PYTHIA**
 2316 8.186 is used with the A14 tune [90, ii]. The free parameters in the RSG model are the graviton mass
 2317 and the coupling constant $c \equiv k/\bar{M}_{\text{Pl}}^2$. Both the production cross section and width of the graviton are
 2318 proportional to c^2 . Samples are generated at both $c = 1$ and $c = 2$ for a variety of mass points between

² k is the curvature constant for the warped extra dimension and \bar{M}_{Pl} is the Planck mass divided by 8π

2319 300 GeV and 3 TeV.

2320 The second signal sample is a heavy spin-0 resonance H with a fixed width of $\Gamma_H = 1 \text{ GeV}$. This
2321 is generated with **MADGRAPH5** and uses the **CT10** PDF set [93]. The parton shower and hadronization
2322 are handled by **HERWIG ++** with the **CTEQ6L1** PDF set and the **UEEE5** event tune [94, 114, 115]. Because
2323 the width and branching ratios depend on 2HDM parameters, each mass point generated with this fixed
2324 width corresponds to a different point in the 2HDM parameter phase space. Mass points are generated
2325 between 300 GeV and 1 TeV as with the RSG signal samples.

2326 **7.3.2 BACKGROUND SAMPLES**

2327 While the dominant **QCD** multijet background is estimated with a fully data-driven method, the sub-
2328 dominant backgrounds $t\bar{t}$ and $Z+\text{jets}$ are modeled with some input from simulation.

2329 $t\bar{t}$ events are simulated at next-to-leading order (NLO) with the **POWHEG-BOX** version 1 generator us-
2330 ing the **CT10** PDF set [116]. The parton shower, hadronization, and underlying event are simulated with
2331 **PYTHIA 6.428** with the **CTEQ6L1** PDF set [89]. The Perugia 2012 tune is used [117]. NNLO **QCD** correc-
2332 tions to the cross sections are computed in **Top++ 2.0** [118]. The top quark mass is set to 172.5 GeV. The
2333 shapes of distributions in $t\bar{t}$ are taken from MC while the normalization is taken from data.

2334 Finally, the $Z+\text{jets}$ background is simulated with **PYTHIA 8.186** and the **NNPDF2.3** LO PDF set. This
2335 background is negligible compared to the others and is taken fully from MC.

2336 **7.3.3 DATA SAMPLE AND TRIGGER**

2337 This analysis is done on 3.2 fb^{-1} of data taken in 2015 at $\sqrt{s} = 13 \text{ TeV}$. The details of the machine
2338 conditions during this time can be found in Chapter 2. Only data which was taken during stable beam
2339 conditions with all detectors functioning is used. Events must pass a trigger which requires a single large
2340 radius ($R = 1.0$) jet with $p_T > 360 \text{ GeV}$ to be reconstructed in the HLT. Figure 7.4 shows the trigger
2341 efficiency for various trigger options as a function of graviton mass. Above $m_{G_{KK}^*} > 1 \text{ TeV}$, the single
2342 large radius jet trigger is 99% efficient for events passing the signal selection.

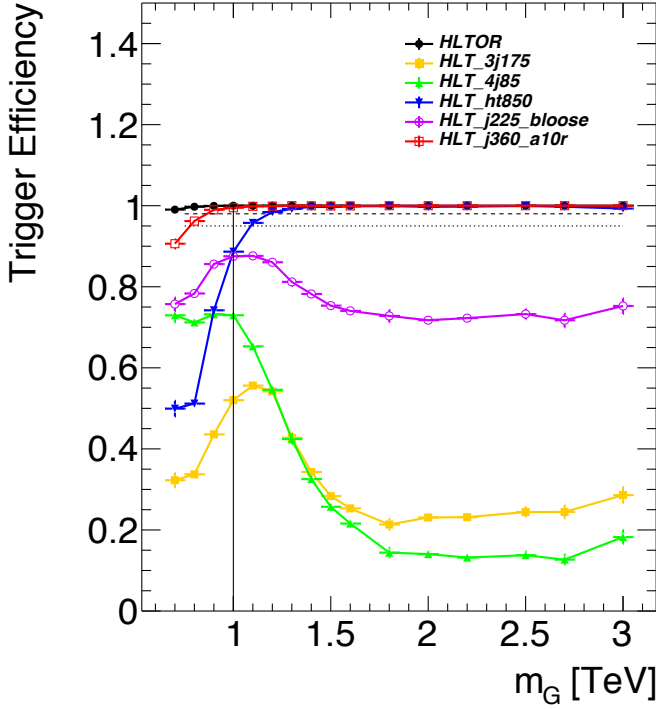


Figure 7.4: Trigger efficiency for events passing all signal region selections as a function of mass in $G_{KK}^* \rightarrow HH \rightarrow 4b$ samples with $c = 1$ [119]. In the trigger names, “j” refers to a jet or jets. “ht” refers to H_T , the scalar sum of transverse momenta in the event. “bloose” refers to a loose b -tagging requirement applied to the jet. “a10r” refers to anti- k_T jets with $R = 1.0$. The numbers at the end of each trigger name are the thresholds on the given quantity in GeV.

2343 7.4 EVENT RECONSTRUCTION AND OBJECT SELECTION

2344 The boosted selection first begins by defining a unique set of objects that can be exploited to increase signal
 2345 efficiency in the kinematic regime where the final state b -jets are very merged.

2346 7.4.1 LARGE RADIUS ($R = 1.0$) JETS

2347 The first step towards reconstructing the final state is to define objects that can be used to measure the
 2348 kinematics of the Higgs bosons. In the boosted selection anti- k_T jets with a radius parameter of 1.0 are
 2349 used. These jets are much larger in angular size than the typical $R = 0.4$ jets and are intended to encompass
 2350 all of the products of the Higgs decay³. The jets are built from clusters in the calorimeter calibrated with

³This is in contrast to the resolved selection, which uses two $R = 0.4$ anti- k_T jets for each Higgs.

local calibration weighting [69].

Because of the large extent of these jets, great care must be taken to remove potential contributions of calorimeter clusters from pile-up. This is done using a technique called jet trimming [120]. With trimming, the constituents of the large radius jet are re-clustered with a smaller radius using the k_T algorithm. Then, these so-called subjets are removed from the larger jet if $p_T^{\text{subjett}} / p_T^{\text{jet}} < f_{\text{cut}}$. In this analysis, the subjet radius is $R = 0.2$ and $f_{\text{cut}} = 0.05$. Trimming has been shown to improve the mass resolution of large radius jets. Figure 7.5 shows the effect of trimming on the large radius jet mass (M_J). Because the large radius jet fully contains the Higgs decay products, its invariant mass should correspond to the 125 GeV mass of the Higgs. The trimming algorithm brings the jet mass much closer to the expected Higgs mass and improves the mass resolution.

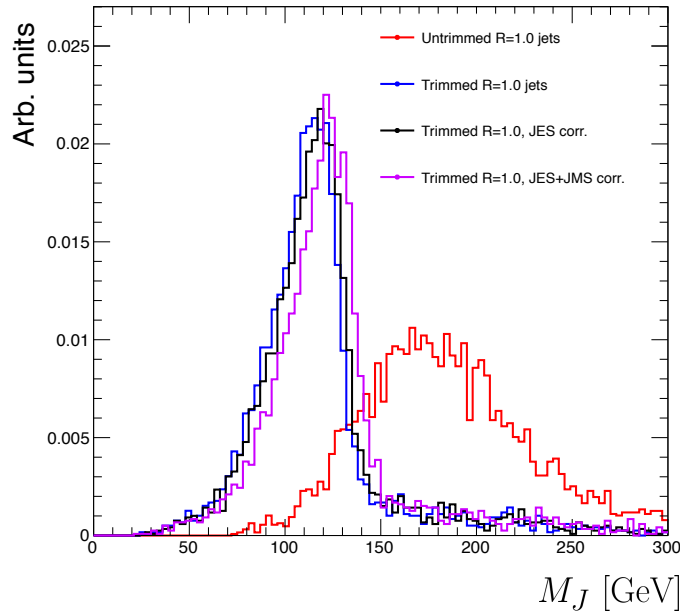


Figure 7.5: Comparison of untrimmed and trimmed jet masses for large radius jets in a RSG sample with $m_{G_{\text{KK}}^*} = 1 \text{ TeV}$. JES (JMS) refers to the standard jet energy (mass) scale calibration for ATLAS [69].

The large radius jets are required to satisfy $250 < p_T < 1500 \text{ GeV}$. They must also be within $|\eta| < 2.0$ in order to ensure that the full jet is within the inner detector tracking volume. Finally, they are required to have $M_J > 50 \text{ GeV}$. The upper p_T cut and lower threshold on mass are applied to correspond to the kinematic range where uncertainties are available in ATLAS calibrations [121, 122].

2365 7.4.2 TRACK JETS AND b -TAGGING

2366 Because the b -jets from boosted Higgs decays are so close together (as illustrated in figure 7.3), narrow radius
2367 jets are required to fully resolve both b -jets. The minimum radius feasible for jets based on calorimeter
2368 deposits is determined by the calorimeter granularity. However, because b -tagging relies on information
2369 from the inner detector, it is possible to define another type of jet that can have a smaller radius and better
2370 b -tagging resolution. These jets are called “track jets” [122, 123].

2371 Track jets are formed by applying the usual anti- k_T clustering algorithm to tracks that are required to be
2372 consistent with the primary vertex. After the jet axis has been determined using these tracks, a second step
2373 of track association is also performed to add tracks that can be useful for b -tagging [123]. In this analysis,
2374 the tracks are clustered with a radius parameter of $R = 0.2$. This radius has been shown to give good
2375 performance in boosted Higgs tagging [122, 123]. Figure 7.6 shows a comparison among different track jet
2376 radii of the efficiency for reconstructing two b -jets from each Higgs in a RSG sample as a function of mass.
Track jets with radius of 0.2 give the best performance, especially at high mass. In this analysis, track jets

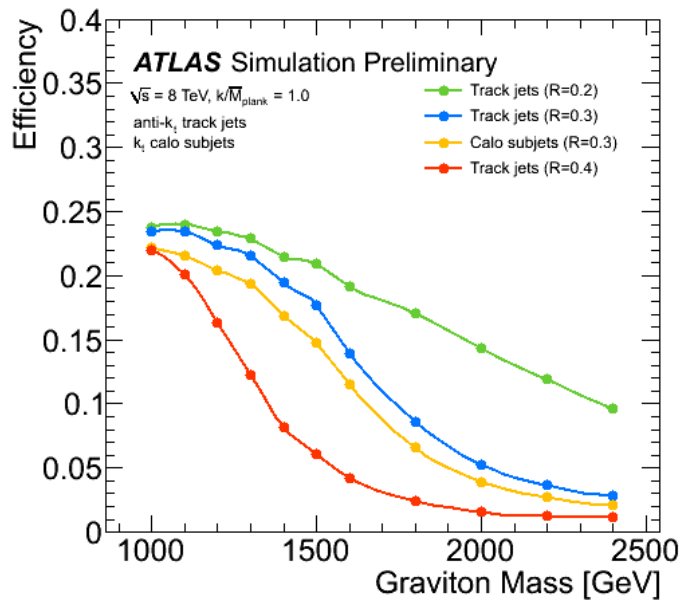


Figure 7.6: Efficiency of finding two b -jets from each Higgs in an RSG event using calorimeter jets with $R = 0.3$ and track jet radii of $R = [0.2, 0.3, 0.4]$ [123].

2377

2378 are required to have $p_T > 10$ GeV and $|\eta| < 2.5$. They must also have at least two tracks.

2379 **7.4.3 MUONS**

2380 Muons are used in this study to correct the four-momenta of calorimeter jets by accounting for semi-
2381 leptonic b decays. The muons used are combined ID and MS muons which must satisfy tight identification
2382 requirements [65]. The muons must have $p_T > 4 \text{ GeV}$ and $|\eta| < 2.5$. Table 7.1 summarizes the object
2383 requirements described in this section.

	R	p_T	$ \eta $	M
Calorimeter jets	1.0	$250 < p_T < 1500 \text{ GeV}$	< 2.0	$> 50 \text{ GeV}$
Track jets	0.2	$> 10 \text{ GeV}$	< 2.5	-
Muons	-	4 GeV	< 2.5	-

Table 7.1: Summary of requirements on objects used in the $X \rightarrow HH \rightarrow b\bar{b}b\bar{b}$ search

2384 **7.5 EVENT SELECTION**

2385 The first requirement in the boosted event selection is for ≥ 2 large radius jets satisfying the selections
2386 outlined above. The two highest momentum large-R jets in the event are referred to as “Higgs candidates”.
2387 The leading jet is required to have $p_T > 350 \text{ GeV}$.

2388 Track jets satisfying the object selections are matched to Higgs candidate jets via ghost association [124].
2389 Each Higgs candidate must have at least 2 track jets associated with it. These basic requirements are illus-
2390 trated graphically in figure 7.7.

2391 The QCD multijet background produces less central jets than high mass resonances, so there is an ad-
2392 dditional requirement that the two Higgs candidates be close together in η . The large-R jets are required to
2393 satisfy $|\Delta\eta(JJ)| < 1.7$.

2394 **7.5.1 MASS REQUIREMENTS**

2395 The final set of requirements ensures that the Higgs candidates are consistent with expected properties of
2396 the 125.0 GeV Higgs. First, a variable (X_{hh}) is defined to measure the consistency of both of the Higgs

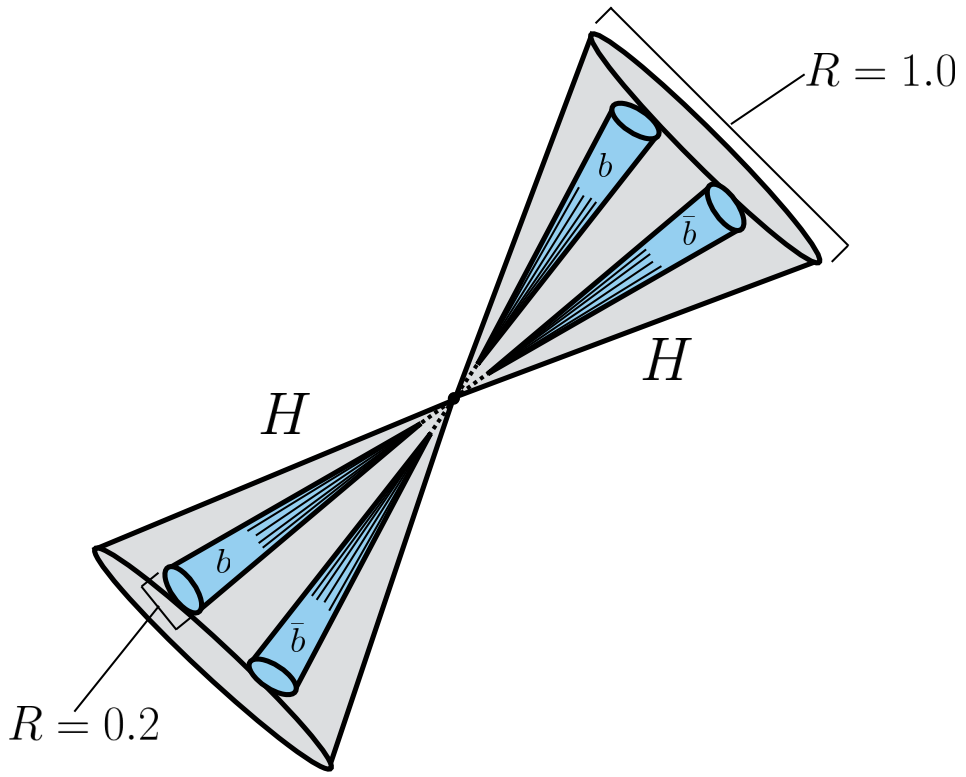


Figure 7.7: Illustration of the boosted selection requirements on Higgs candidates. Each large-radius calorimeter jet (Higgs candidate) must contain two track jets.

²³⁹⁷ candidate jets with the SM Higgs mass. This is shown in equation 7.2.

$$X_{hh} = \sqrt{\left(\frac{M_J^{\text{lead}} - 124 \text{ GeV}}{0.1 M_J^{\text{lead}}}\right)^2 + \left(\frac{M_J^{\text{sublead}} - 115 \text{ GeV}}{0.1 M_J^{\text{sublead}}}\right)^2} \quad (7.2)$$

²³⁹⁸ The mass values in the X_{hh} formula are optimized to maximize signal efficiency. The sub-leading jet typ-
²³⁹⁹ ically has a lower mass due to semi-leptonic b decays and final state radiation. X_{hh} effectively acts as a χ^2
²⁴⁰⁰ measurement of the consistency of the two Higgs candidate masses with the signal hypothesis. The de-
²⁴⁰¹ nominators of each term ($0.1 M$) give the uncertainty on the mass measurement for the large radius jets.
²⁴⁰² Events are required to satisfy $X_{hh} < 1.6$.

²⁴⁰³ Before making the requirement on X_{hh} , the masses of the Higgs candidates are corrected for semi-
²⁴⁰⁴ leptonic b decays using muons with the criteria outlined in the previous section. Any muons within a
²⁴⁰⁵ $\Delta R < 0.2$ of a b -tagged track jet (as described in the next section) have their four-momenta added to the

2406 four-momentum of the Higgs candidate. This correction does not affect the pre-selection requirements
2407 but does affect the X_{hh} requirement and the final invariant mass discriminant.

2408 **7.5.2 b-TAGGING REQUIREMENTS**

2409 The last requirement applied is on the number of b -tagged track jets. There are two signal regions defined.
2410 The first requires exactly four b -tagged track jets, two in each Higgs candidate (known as the $4b$ signal re-
2411 gion). At high resonance masses, this requirement is inefficient, so an additional signal region requiring
2412 only three b -tagged track jets is also defined (known as the $3b$ signal region). While this has a larger back-
2413 ground it is also more efficient for high resonance masses. For both signal regions, the MV2c20 algorithm,
2414 where the training sample for the algorithm has 20% charm events is used. More details for this algorithm
2415 can be found in Chapter 2.

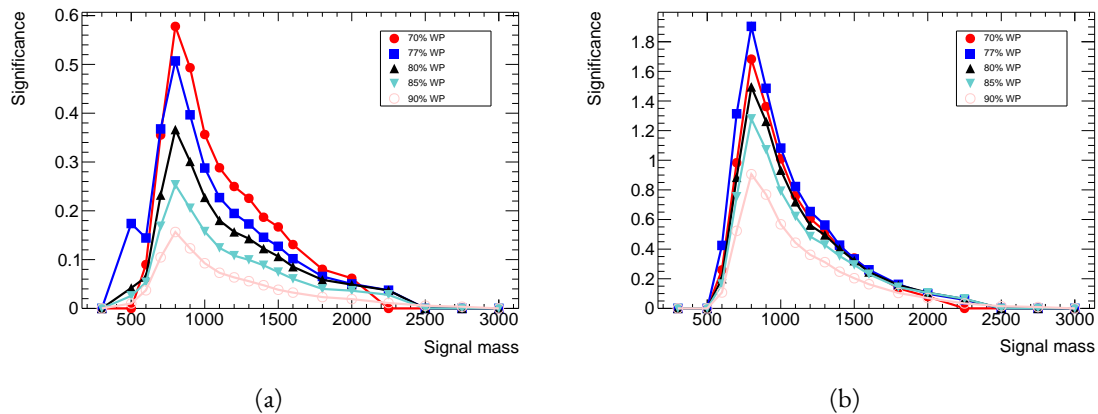


Figure 7.8: Estimated significance as a function of signal mass for RSG $c = 1$ models in the $3b$ (a) and $4b$ (b) regions for different b -tagging efficiency working points

2416 Once the algorithm is selected, an efficiency working point must also be chosen. This working point
2417 defines the efficiency with which true b -jets are tagged and also fixes the overall background rejection of the
2418 algorithm. Higher efficiency working points accept more true b -jets but also allow for more background.
2419 Five different working points (70%, 77%, 80%, 85%, 90%) are tested. With each working point, the
2420 full data driven background estimation method is run to quantify the amount of background that will be
2421 present in the final signal region. The significance is quantified using the median discovery significance for

²⁴²² signal and background with Poisson errors, given in equation 7.3 [125].

$$Z = \sqrt{2 \left((s + b) \ln \left(1 + \frac{s}{b} \right) - s \right)} \quad (7.3)$$

²⁴²³ Here, s is the expected number of signal events and b is the expected number of background events. This
²⁴²⁴ formula is derived using Poisson statistics with errors on both the signal and background. It is used because
²⁴²⁵ it is valid in the regime where s and b are of the same order. Note that in the limit where s is much smaller
²⁴²⁶ than b , this equation reduces to the more well known s/\sqrt{b} . Figure 7.8 shows the estimated significance as
²⁴²⁷ a function of signal mass in RSG $c = 1$ models for the $3b$ and $4b$ signal regions. The 77% working point
²⁴²⁸ gives the best performance over a wide range of masses in the $4b$ signal region. As this is the region which
²⁴²⁹ contributes the most to the total discovery significance, the 77% efficiency working point is chosen for the
²⁴³⁰ analysis.

²⁴³¹ 7.5.3 SELECTION EFFICIENCY

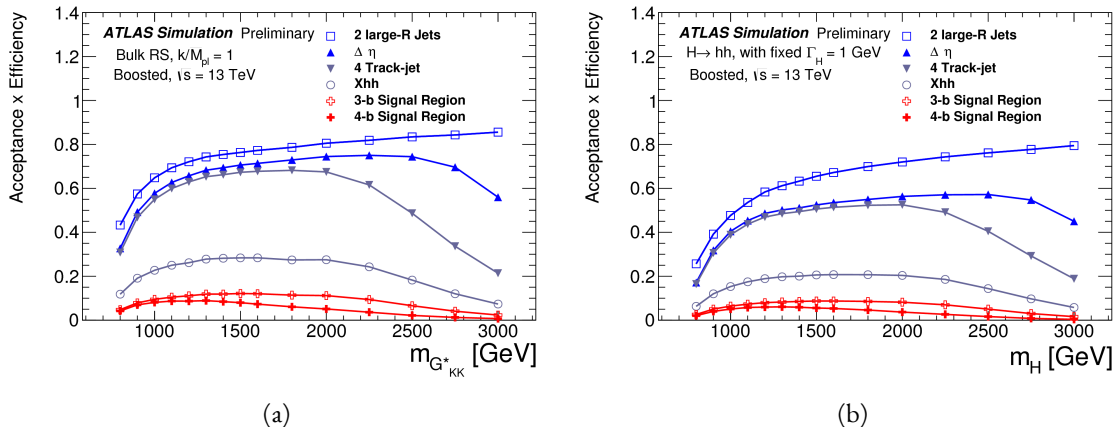


Figure 7.9: Acceptance × efficiency as a function of mass for (a) RSG and (b) narrow heavy scalar signal models [126].

²⁴³² Figure 7.9 shows the product of acceptance and efficiency as a function of mass for both the RSG and
²⁴³³ narrow heavy scalar resonance signal models. After $m_X > 1$ TeV, the efficiency of the $4b$ requirement
²⁴³⁴ begins to decline. After $m_X > 2$ TeV, the efficiency of requiring two track jets in each Higgs candidate
²⁴³⁵ begins to decline as well. Both of these behaviors illustrate the difficulty of resolving the merged decay

2436 products at high mass. Figure 7.10 shows a more detailed comparison of the signal efficiency in the $3b$ vs
 2437 $4b$ signal regions for the RSG model. The efficiencies shown here are relative to all prior selection require-
 2438 ments. It can be seen there that at high masses the $3b$ signal region is more efficient for signal.

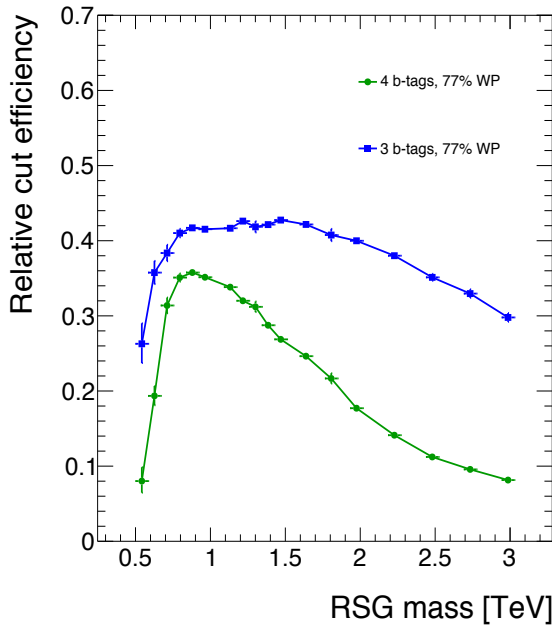


Figure 7.10: Efficiency of requiring 3 or 4 b -tagged track jets vs. RSG mass. The efficiency quoted is relative to the previous selection requirements (rather than an absolute efficiency).

2439 To investigate the degradation of b -tagging efficiency at high p_T , the individual jet tagging efficiencies can
 2440 be compared as a function of signal mass. This is shown in figure 7.11. The figure shows that the leading jet
 2441 tagging efficiency in both calorimeter jets degrades heavily, while the sub-lead jet tagging efficiency remains
 2442 relatively constant. More details on the cause of this degradation are shown in appendix A.

2443 The final discriminating variable used in the boosted analysis is M_{2J} , the invariant mass of the two
 2444 Higgs candidates. In order to improve the mass resolution, the four-momenta of each Higgs candidate
 2445 are scaled by m_h/M_J . The effect of this correction is small in the boosted analysis but is done for consis-
 2446 tency with the resolved selection. Table 7.2 shows the effect of the selection requirements on signal and
 2447 background simulations as well as data.

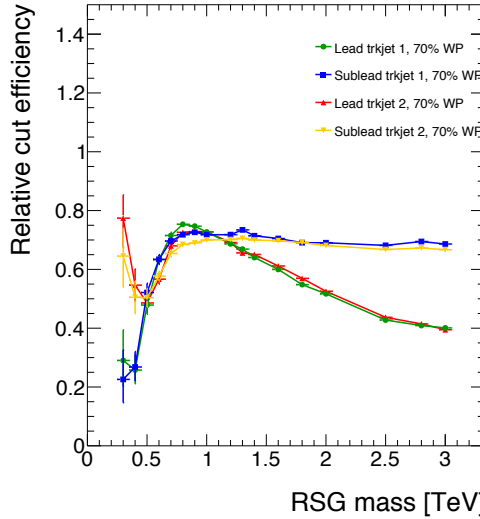


Figure 7.11: MV2c20 b -tagging efficiency for each of the four track jets in the boosted $4b$ selection as a function of RSG mass for $c = 1$ models.

Selection	Data	$m_{G_{KK}^*} = 1\text{TeV}$	$m_{G_{KK}^*} = 2\text{TeV}$	$t\bar{t}$	$Z + \text{jets}$
$N(\text{fiducial large-R jets}) \geq 2$	2202396	23.3	0.48	32345.2	4255.7
leading large-R jet $p_T > 350\text{ GeV}$	1873741	22.9	0.48	26511.7	3649.9
Both large-R jet $m > 50\text{ GeV}$	1854625	21.2	0.47	24369.8	3575.8
Both large-R jet $p_T < 1500\text{ GeV}$	1853601	21.2	0.46	24346.5	3572.9
$ \Delta\eta(JJ) < 1.7$	1435273	20.8	0.44	20751.0	3265.8
≥ 2 track-jets per large-R jet	1224727	19.8	0.40	18234.5	2692.6
3 b -tags, $X_{hh} < 1.6$	316	3.4	0.067	46.7	2.0
4 b -tags, $X_{hh} < 1.6$	20	2.9	0.030	1.4	0.0

Table 7.2: Effect of boosted selection on data, RSG signal models, $t\bar{t}$, and $Z + \text{jets}$. The numbers from simulation are normalized with the MC generator cross section and do not take into account the data driven estimates described in section 7.6 [127].

2448 7.6 DATA-DRIVEN BACKGROUND ESTIMATION

2449 The largest background to the $X \rightarrow HH \rightarrow b\bar{b}b\bar{b}$ final state is QCD multijet production, constitut-
 2450 ing 80-90% of the total background. Because of the difficulties in modeling higher order QCD processes,
 2451 this background is estimated with a fully data-driven method. The only other non-negligible background
 2452 is $t\bar{t}$, constituting the other 10-20%. Due to the presence of $t\bar{t}$ in the sideband region where the QCD

⁴The $Z + \text{jets}$ background is a sub-percent level contribution

2453 background will be estimated, the normalization of the QCD and $t\bar{t}$ backgrounds are simultaneously es-
2454 timated.

2455 **7.6.1 MASS REGION DEFINITIONS**

2456 The first step in the data-driven background estimate is to define a sideband mass region where the back-
2457 ground normalization can be derived. Additionally, a control region is defined where the background
2458 estimate can be validated. The control (CR) and sideband (SB) regions are defined using a radial distance
2459 in the two-dimensional large-R jet mass plane, R_{hh} , which is defined in equation 7.4.

$$R_{hh} = \sqrt{(M_J^{\text{lead}} - 124 \text{ GeV})^2 + (M_J^{\text{sublead}} - 115 \text{ GeV})^2} \quad (7.4)$$

2460 Events in the control region are required to fail the signal region $X_{hh} < 1.6$ requirement and have
2461 $R_{hh} < 35.8 \text{ GeV}$. The sideband region consists of those events which are not in the signal or control
regions. Figure 7.12 shows the definition of the signal, control, and sideband mass regions. Table 7.3 sum-

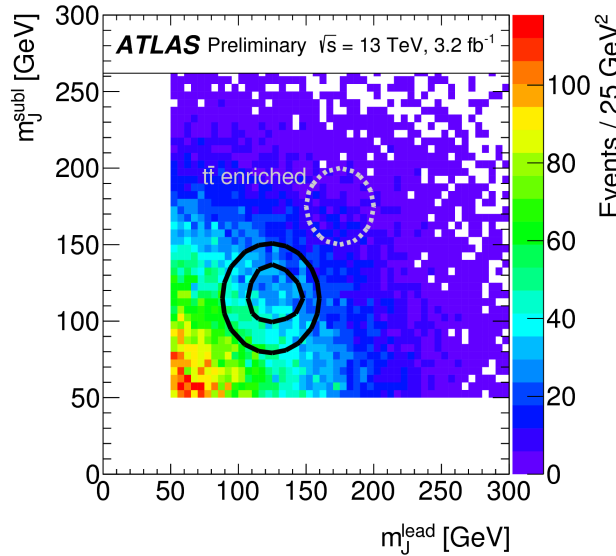


Figure 7.12: M_J^{sublead} vs. M_J^{lead} in a 2 b -tag data sample. The signal region is defined by the inner black contour ($X_{hh} < 1.6$) and the sideband region is defined by the outer contour ($R_{hh} > 35.8 \text{ GeV}$). The region between the black contours is the control region. The mass region which is enriched in $t\bar{t}$ background is also shown for illustration [[126](#)].

2462 marizes the mass region selections for the three different regions used in the analysis.
2463

Region	Requirement	Notes
Signal Region (SR)	$X_{hh} < 1.6$	-
Control Region (CR)	$R_{hh} < 35.8 \text{ GeV}$ and $X_{hh} > 1.6$	Used for validation of background estimates
Sideband Region (SB)	$R_{hh} > 35.8 \text{ GeV}$	Used to derive background normalization

Table 7.3: Mass region definitions used for background estimation.

2464 7.6.2 BACKGROUND ESTIMATION

2465 The method for estimating the background in this analysis is similar to the ABCD method presented in
 2466 Chapter 5. In this case, the two handles used to define different regions for the estimate are the number
 2467 of b -tagged track jets and the mass requirements. A region requiring exactly two b -tagged track jets in one
 2468 large-R jet (referred to as the 2-tag or $2b$ region) is defined for use in the background estimate. The number
 2469 of expected background events in the $3b$ and $4b$ signal regions is then given by equation 7.5.

$$N_{\text{bkg}}^{3(4)-\text{tag},\text{SR}} = \mu_{\text{Multijet}} N_{\text{Multijet}}^{2-\text{tag},\text{SR}} + \beta_{t\bar{t}} N_{t\bar{t}}^{3(4)-\text{tag},\text{SR}} + N_{Z+\text{jets}}^{3(4)-\text{tag},\text{SR}} \quad (7.5)$$

2470 In this equation, $N_{\text{bkg}}^{3(4)-\text{tag}}$ is the expected number of background events in the $3b$ or $4b$ signal regions.
 2471 $N_{\text{Multijet}}^{2-\text{tag}}$ is the number of multijet events in the 2-tag region. $N_{t\bar{t}}^{3(4)-\text{tag}}$ is the number of $t\bar{t}$ events pre-
 2472 dicted in the MC for the $3b$ or $4b$ signal region, and the variable is similarly defined for the $Z+\text{jets}$ back-
 2473 ground. The $\beta_{t\bar{t}}$ parameter is a scale factor used to correct the normalization of the $t\bar{t}$ estimate in the signal
 2474 region. μ_{Multijet} is an extrapolation factor that is derived in the sideband region and used to estimate the
 2475 ratio of 2-tag events to 3(4)-tag events in the signal region. It is defined in equation 7.6.

$$\mu_{\text{Multijet}} = \frac{N_{\text{Multijet}}^{3(4)-\text{tag},\text{SB}}}{N_{\text{Multijet}}^{2-\text{tag},\text{SB}}} = \frac{N_{\text{data}}^{3(4)-\text{tag},\text{SB}} - \beta_{t\bar{t}} N_{t\bar{t}}^{3(4)-\text{tag},\text{SB}} - N_{Z+\text{jets}}^{3(4)-\text{tag},\text{SB}}}{N_{\text{data}}^{2-\text{tag},\text{SB}} - \beta_{t\bar{t}} N_{t\bar{t}}^{2-\text{tag},\text{SB}} - N_{Z+\text{jets}}^{2-\text{tag},\text{SB}}} \quad (7.6)$$

2476 The $t\bar{t}$ scale factor ($\beta_{t\bar{t}}$) and the QCD multijet extrapolation factor (μ_{Multijet}) are estimated together in
 2477 a simultaneous fit in the sideband region. Then, the number of events in the 2-tag signal region is used,
 2478 along with the $t\bar{t}$ estimate in the $3b$ and $4b$ signal regions and μ_{Multijet} , to estimate the total number
 2479 of background events in the two final signal regions. The shape of the final discriminant M_{2J} is also

²⁴⁸⁰ taken from the 2-tag signal region where there are more events. This method is illustrated graphically in figure 7.13. In the 3 b region, the fit yields values of $\mu_{\text{Multijet}} = 0.160 \pm 0.03$ and $\beta_{t\bar{t}} = 1.02 \pm 0.09$.

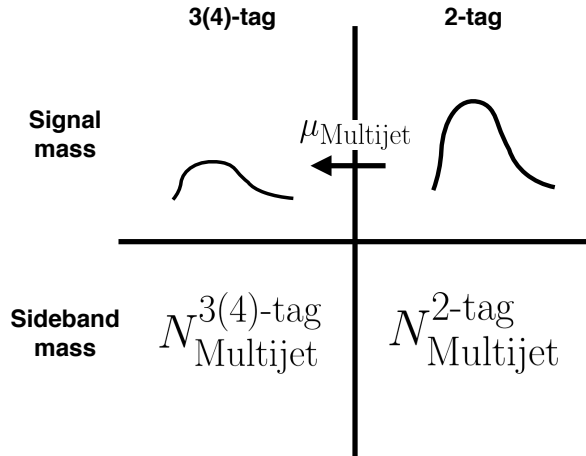


Figure 7.13: An illustration of the data-driven background estimation technique for the boosted analysis

²⁴⁸¹

²⁴⁸² In the 4 b region, the fit gives $\mu_{\text{Multijet}} = 0.0091 \pm 0.0007$ and $\beta_{t\bar{t}} = 0.82 \pm 0.39$. The uncertainties
²⁴⁸³ quoted are statistical only. The larger uncertainties in the 4 b values indicate the lower statistics available in
²⁴⁸⁴ that region.

²⁴⁸⁵ Figure 7.14 shows the distributions of data and background estimates in the 3 b and 4 b sideband regions
²⁴⁸⁶ after the background fit has been done. The normalizations are constrained from the fit to match that of
²⁴⁸⁷ the data, but good modeling of the shape of the mass of the leading large-R jet is seen as well. The shapes
²⁴⁸⁸ of the kinematic distributions for the $t\bar{t}$ background in the 4 b region are taken from the 3 b region due to
²⁴⁸⁹ the better MC statistics in that region.

²⁴⁹⁰ 7.6.3 BACKGROUND SHAPE FIT

²⁴⁹¹ As mentioned in the previous section, the background shape in the 3-tag and 4-tag signal regions is taken
²⁴⁹² from the 2-tag signal mass region. Due to the limited statistics available, the background shapes are addi-
²⁴⁹³ tionally smoothed after being extrapolated to the 3-tag and 4-tag signal regions. Only the data in the range
²⁴⁹⁴ $900 < M_{2J} < 2000$ GeV is included in the shape fit due to the limited statistics available above 2 TeV.
²⁴⁹⁵ Both the $t\bar{t}$ and QCD multijet background are independently fit with an exponential shape, $y = e^{ax+b}$.

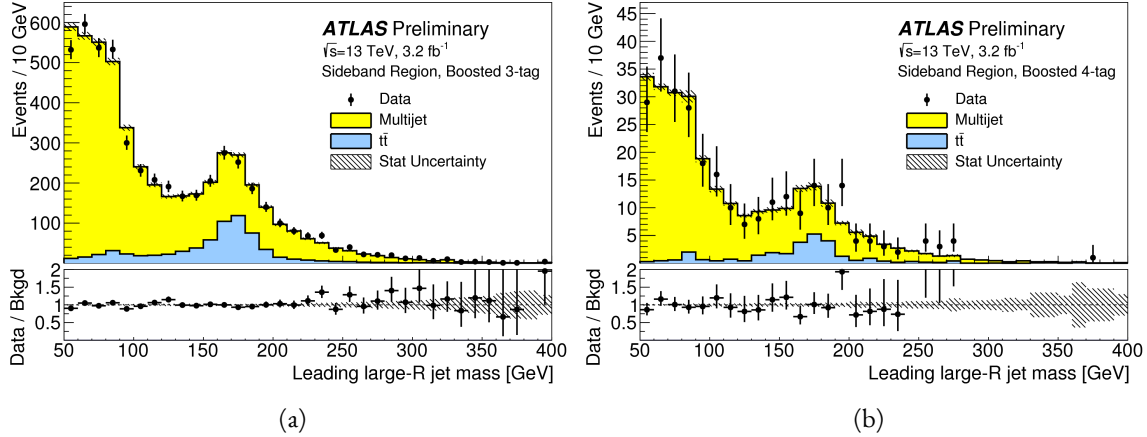


Figure 7.14: Leading large-R jet mass in the 3b (a) and 4b (b) sideband regions. The multijet and $t\bar{t}$ backgrounds are estimated using the data-driven methods described above. Because their normalizations are derived in the sideband region, the total background normalization is constrained by default to match the normalization of the data [126].

2496 Other shapes are considered and used for the systematic uncertainties. Table 7.4 shows the fit values for
 2497 the parameters. Because both the 3b and 4b QCD shapes come from the 2-tag region, the slopes derived
 2498 are very similar.

	a	b
QCD (4b)	0.00545 ± 0.00021	5.44 ± 0.24
$t\bar{t}$ (4b)	0.00746 ± 0.00021	4.88 ± 0.36
QCD (3b)	0.00545 ± 0.00021	8.30 ± 0.24
$t\bar{t}$ (3b)	0.00746 ± 0.00021	8.58 ± 0.36

Table 7.4: Parameters derived for exponential fit to background M_{2J} shape in the 3b and 4b signal regions [127].

2499 7.6.4 VALIDATION OF BACKGROUND ESTIMATE

2500 The background estimate can be validated by using the method to estimate the number of events in the
 2501 control mass region rather than the signal mass region. Figure 7.15 shows the M_{2J} distribution in the 3b
 2502 and 4b control regions, comparing data and background estimates. In both cases, both the background
 2503 shape and normalization are consistent with the data, indicating good agreement. The ratio of data to the
 2504 background estimates is also fit to a line in the figure to test for any shape difference. The slope of the
 2505 line is within 1σ (from the fit uncertainties) of flat, further indicating that the data is consistent with the
 2506 background estimate in the control region.

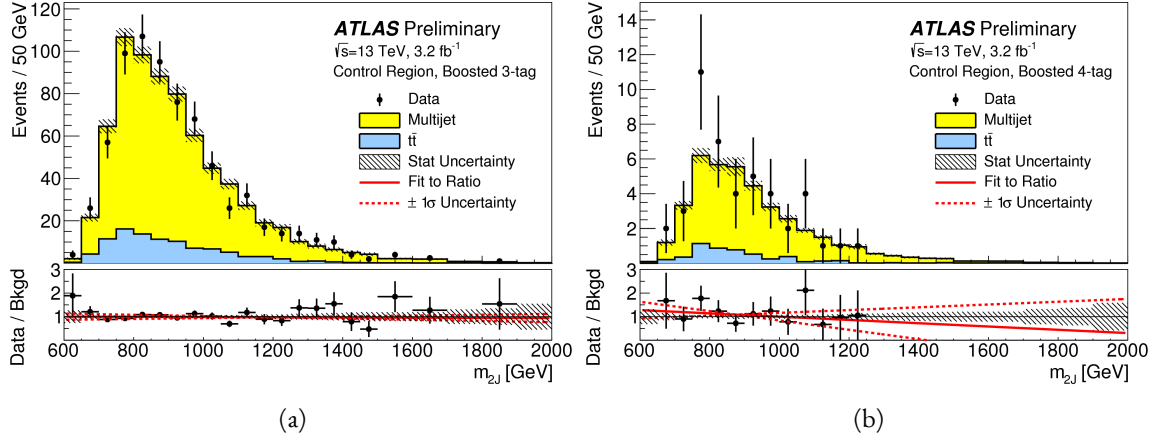


Figure 7.15: Di-jet invariant mass (M_{2J}) in the 3b (a) and 4b (b) control regions. The multijet and $t\bar{t}$ backgrounds are estimated using the data-driven methods described above [126].

Table 7.5 shows the yields in data and background estimates in the 3-tag and 4-tag sideband and control regions. Again, here, it can be seen that the total number of predicted background events from the data driven method is consistent with the number of data events in the region.

Sample (3-tag)	Sideband Region	Control Region
Multijet	4328 ± 27	607 ± 10
$t\bar{t}$	683.5 ± 8.1	99.6 ± 3.1
Z+jets	31.8 ± 3.7	7.7 ± 1.8
Total	5043 ± 28	715 ± 11
Data	5043	724
Sample (4-tag)	Sideband Region	Control Region
Multijet	247.4 ± 1.5	34.7 ± 0.6
$t\bar{t}$	28.4 ± 1.5	5.1 ± 0.7
Z+jets	3.4 ± 1.2	0.6 ± 0.5
Total	279.2 ± 2.5	40.3 ± 1.0
Data	279	45

Table 7.5: The number of events in data and predicted background events in the boosted 3-tag and 4-tag sideband and control regions [126]. The uncertainties shown are statistical only.

2510 7.7 SYSTEMATIC UNCERTAINTIES

2511 The systematic uncertainties in this analysis can be divided into two broad categories. The first type is
2512 uncertainties associated with the modeling of the signal processes. The second type of uncertainty is asso-
2513 ciated with both the shape and normalization of the background prediction.

2514 7.7.1 SIGNAL MODELING UNCERTAINTIES

2515 The signal modeling uncertainty has three main components: theoretical uncertainty on the acceptance,
2516 experimental uncertainties on the large-R jets, and experimental uncertainties on the track jets related to
2517 b -tagging. In this analysis the experimental uncertainties are the most significant.

2518 The first uncertainty on signal modeling is the theoretical uncertainty on the acceptance. As explained
2519 in section 5.6.1, there are four components to this uncertainty. The first is related to missing higher order
2520 terms from the matrix element calculations which is estimated by varying the QCD renormalization and
2521 factorization scales. The second is uncertainty due to the PDF set used. The third is a generator uncer-
2522 tainty which is estimated by modifying the generator used to model the underlying event and hadroniza-
2523 tion. Finally, there is an uncertainty associated with the modeling of the initial state and final state radia-
2524 tion (ISR/FSR). The total theoretical uncertainty on the signal yield is 3%, and this is dominated by the
2525 ISR/FSR modeling.

2526 There are uncertainties on the large-R jets in both the jet energy scale (JES) and jet energy resolution
2527 (JER) as well as the jet mass scale (JMS) and jet mass resolution (JMR). These are evaluated using $\sqrt{s} =$
2528 8 TeV data from Run 1 of ATLAS and extrapolated to the Run 2 beam and detector conditions using
2529 MC⁵. The details of these uncertainties can be found in reference [128].

2530 Uncertainties on the track jets are related to the b -tagging efficiency. The total uncertainty on the signal
2531 yield due to b -tagging is evaluated by propagating variations of the b -tagging efficiency through the boosted
2532 selection requirements. The uncertainties are calculated jet-by-jet and parameterized as a function of b -jet
2533 p_T and η [106]. For high p_T b -jets (with $p_T > 300$ GeV), the uncertainties are extrapolated using MC
2534 simulation from the lower p_T b -jets [129].

⁵The uncertainties are correspondingly larger due to the uncertainty of this extrapolation.

2535 Table 7.6 shows the systematic uncertainties on the signal normalization for models with $m_{G_{\text{KK}}^*} =$
 2536 1.5 TeV and both $c = 1$ and $c = 2$ as well as a narrow width heavy scalar. The dominant uncertainty
 2537 comes from b -tagging and this uncertainty is larger in the 4-tag region than the 3-tag region.

Source	Background		G_{KK}^*	H
	$c = 1$	$c = 2$		
Luminosity	-	5.0	5.0	5.0
3-tag				
JER	< 1	< 1	< 1	< 1
JES	2	< 1	< 1	< 1
JMR	1	12	12	11
JMS	5	14	13	17
b -tagging	1	23	22	23
Theoretical	-	3	3	3
Multijet Normalization	3	-	-	-
Statistical	2	1	1	1
Total	7	31	30	33
4-tag				
JER	< 1	< 1	< 1	< 1
JES	< 1	< 1	< 1	< 1
JMR	4	12	13	13
JMS	5	13	13	14
b -tagging	2	36	36	36
Theoretical	-	3	3	3
Multijet Normalization	14	-	-	-
Statistical	3	1	1	1
Total	15	42	42	43

Table 7.6: Summary of systematic uncertainties in the total background and signal event yields (expressed in %) in the boosted 3-tag and 4-tag signal regions. Systematic uncertainties on the signal normalization are shown for models with $m_{G_{\text{KK}}^*} = 1.5$ TeV and both $c = 1$ and $c = 2$ as well as a narrow width heavy scalar.

2538 **7.7.2 BACKGROUND UNCERTAINTIES**

2539 Uncertainties on the QCD multijet background normalization and shape are estimated using the con-
 2540 trol mass region. As shown previously, the background predictions in the control region match with the

2541 data yields within the statistical uncertainty in both the 3-tag and 4-tag control regions. As an additional
 2542 protection, the statistical uncertainty on the background prediction in the control region is assigned as a
 2543 systematic uncertainty on the normalization of the QCD background.

2544 Additional robustness tests are done by varying the definition of the control mass region and the b -
 2545 tagging requirements used to define the 2-tag sample. In all cases, the effect of the variations is found to be
 2546 within the statistical uncertainties on the background normalization in the control region.

2547 Shape uncertainties on the background are evaluated using two techniques. First, as shown in fig-
 2548 ure 7.15, the ratio between the data and background prediction is fit with a linear function. The uncer-
 2549 tainties on the slope of this fit are assigned as shape uncertainties. An additional uncertainty is assigned by
 2550 using alternate power law fit functions for the smoothing of the background shape. Table 7.7 shows the
 2551 alternate shapes used. The largest difference between the nominal fit function and the alternates, taking
 2552 into account the 1σ uncertainty band on each fit as well, is taken as a shape uncertainty.

Functional Form
$f_1(x) = p_0(1 - x)^{p_1}x^{p_2}$
$f_2(x) = p_0(1 - x)^{p_1}e^{p_2 x^2}$
$f_3(x) = p_0(1 - x)^{p_1}x^{p_2}x$
$f_4(x) = p_0(1 - x)^{p_1}x^{p_2} \ln x$
$f_5(x) = p_0(1 - x)^{p_1}(1 + x)^{p_2}x$
$f_6(x) = p_0(1 - x)^{p_1}(1 + x)^{p_2} \ln x$
$f_7(x) = \frac{p_0}{x}(1 - x)^{p_1-p_2} \ln x$
$f_8(x) = \frac{p_0}{x^2}(1 - x)^{p_1-p_2} \ln x$

Table 7.7: Alternate fit functions used to model the M_{2J} distribution in the QCD multijet background. In the equations, $x = M_{2J}/\sqrt{s}$.

2553 The uncertainties on the $t\bar{t}$ background are obtained by propagating the various experimental variations
 2554 (JES, JER, JMS, JMR, b -tagging) through the analysis selection requirements. Table 7.6 summarizes the
 2555 background uncertainties in the 3-tag and 4-tag regions.

2556 7.8 RESULTS

2557 Table 7.8 shows the observed yields in the 3-tag and 4-tag signal regions for the boosted analysis compared
 2558 to the predicted number of background events. In the 3-tag region, 316 events are observed with a pre-
 2559 dicted background of 285 ± 19 . In the 4-tag region, 20 events are observed with a predicted background
 2560 of 14.6 ± 2.4 . Figure 7.16 shows the M_{2J} distribution in the 3-tag and 4-tag regions. There are some
 2561 small excesses in the data, in particular in the 3-tag region around $M_{2J} \approx 900$ GeV and in the region of
 2562 $1.6 < M_{2J} < 2.0$ TeV. The significance of these excesses will be evaluated in the next chapter in the
 2563 statistical combination with the resolved results.

Sample	Signal Region (3-tag)	Signal Region (4-tag)
Multijet	235 ± 14	13.5 ± 2.4
$t\bar{t}$	48 ± 22	1.2 ± 1.0
$Z + \text{jets}$	2.0 ± 2.2	-
Total	285 ± 19	14.6 ± 2.4
Data	316	20
G_{KK}^* (1000 GeV), $c = 1$	3.4 ± 0.9	2.9 ± 1.1

Table 7.8: Observed yields in the 3-tag and 4-tag signal regions for the boosted analysis compared to the predicted number of background events Errors correspond to the total uncertainties in the predicted event yields. The yields for a graviton with $m_{G_{\text{KK}}^*} = 1$ TeV and $c = 1$ are also shown [126].

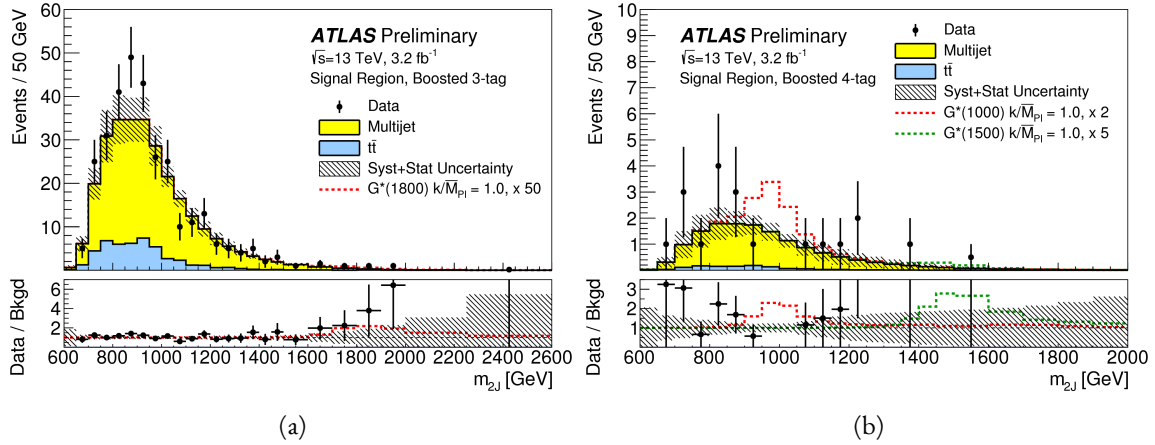


Figure 7.16: Di-jet invariant mass (M_{2J}) in the 3b (a) and 4b (b) signal regions. The multijet and $t\bar{t}$ backgrounds are estimated using the data-driven methods described above. In the 3b region, a graviton signal with $m_{G_{KK}^*} = 1.8$ TeV and $c = 1$ is overlaid, with the cross section multiplied by a factor of 50 so that the signal is visible. In the 4b region, signals with $m_{G_{KK}^*} = 1.0$ TeV and $m_{G_{KK}^*} = 1.5$ TeV are overlaid, both with $c = 1$ and the yields multiplied by factors of 2 and 5 respectively [126].

*There is no real ending. It's just the place where you stop
the story.*

Frank Herbert

8

2564

2565

Combined limits from boosted and resolved searches

2566

2567

8.1 INTRODUCTION

2568 In order to cover the full mass range of possible resonances decaying to di-Higgs final states, two distinct
2569 tailored selections were produced. The resolved selection is more sensitive in the mass range of $400 < m_X <$
2570 1100 GeV while the boosted selection is more sensitive to masses in the range $1100 < m_X <$
2571 3000 GeV . Chapter 7 presents the details of the boosted selection and results. In setting limits on spin-2
2572 Randall-Sundrum graviton (RSG) and narrow width heavy scalar (H) models, the results of the boosted
2573 selection are combined with the results of the resolved selection to cover the full mass range.

2574 This chapter presents limits on signal models resulting from the $X \rightarrow HH \rightarrow b\bar{b}b\bar{b}$ search in both
2575 the resolved and boosted selections. It first presents a brief overview of the resolved results that go into

2576 the limit setting. Then, an overview of the statistical methods used for the search and limit setting is given.
2577 Finally, limits on the RSG and heavy scalar models are presented.

2578 **8.2 RESOLVED RESULTS**

2579 The details of the resolved selection will not be presented here and can be found in reference [126]. In
2580 basic terms, the selection searches for four $R = 0.4$ b-tagged calorimeter jets (where each pair of jets is
2581 one Higgs candidate). This is distinct from the boosted methodology which searches for merged decay
2582 products. The backgrounds to the resolved selection are the same as those presented in Chapter 7 for the
2583 boosted analysis.

2584 Table 8.1 shows the results for data yields and expected background in the resolved signal region. Fig-
2585 ure 8.1 shows the M_{2J} distribution in the resolved signal region. The total number of events is consistent
2586 with the prediction and no significant excess is seen. One event in the boosted 4-tag signal is shared with
2587 the resolved signal region and has a mass of 852 GeV.

Sample	Signal Region Yield
Multijet	43.3 ± 2.3
$t\bar{t}$	4.3 ± 3.0
$Z + \text{jets}$	-
Total	47.6 ± 3.8
Data	46
SM hh	0.25 ± 0.07
$G_{\text{KK}}^*(800 \text{ GeV}), c = 1$	5.7 ± 1.5

Table 8.1: Observed yields in the resolved selection 4-tag signal region compared to the predicted number of background events Errors correspond to the total uncertainties in the predicted event yields. The yields for a graviton with $m_{G_{\text{KK}}^*} = 800$ GeV and $c = 1$ are also shown [126].

2588 **8.3 SEARCH TECHNIQUE AND RESULTS**

2589 The statistical technique used for the search in this analysis is the same as that used in the $H \rightarrow WW^*$
2590 analysis presented in section 3.6.2. The test statistic q_0 is used to define the p -values which measure the

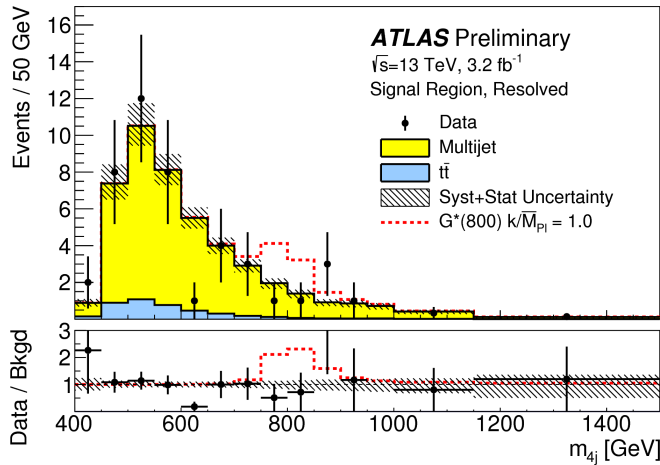


Figure 8.1: Di-jet invariant mass (M_{2J}) in the resolved signal region. A graviton signal with $m_{G_{KK}^*} = 800$ GeV and $c = 1$ is overlaid. [126].

compatibility of the data with the background-only hypothesis corresponding to a signal strength $\mu = 0$.

Local p_0 values are computed to quantify the probability that the background could produce a fluctuation greater than or equal to the one observed in the data. In the resolved analysis, no significant excesses are observed. The largest discrepancy with respect to the background only hypothesis occurs near a resonance mass of 900 GeV and is found to be less than 2σ in significance.

In the boosted selection, the largest local excess is a broad excess in the $3b$ signal region that begins near $M_{2J} \approx 1.7$ GeV. Assuming a G_{KK}^* with this mass and $c = 1.0$, the local significance of this excess is 2.0σ .

8.4 LIMIT SETTING

In the absence of any significant excess observed in the data, limits on different signal models can be set. This section describes the limit setting procedure and presents combined results of the resolved and boosted analyses.

8.4.1 LIMIT SETTING PROCEDURE

The procedure used for setting exclusion limits in this analysis is the CL_s method [130]. The first step in setting the limits is to define a test statistic which will be used. For limit setting, the test statistic is shown

2606 in equation 8.1.

$$\tilde{q}_\mu = \begin{cases} -2 \ln \frac{L(\mu, \hat{\theta}(\mu))}{L(0, \hat{\theta}(0))} & \hat{\mu} < 0 \\ -2 \ln \frac{L(\mu, \hat{\theta}(\mu))}{L(\hat{\mu}, \hat{\theta})} & 0 \leq \hat{\mu} < \mu \\ 0 & \hat{\mu} > \mu \end{cases} \quad (8.1)$$

2607 In the above equation, μ is the value of the signal strength under test, $\hat{\mu}$ is the best fit μ , $\hat{\theta}$ is the best fit
2608 value of the nuisance parameters, $\hat{\theta}$ is the best fit value of the nuisance parameters under the fixed μ value,
2609 and L is the Poisson likelihood of the data (as described in section 3.6.2).

2610 The test statistic \tilde{q}_μ is constructed to protect against two interesting corner cases when setting the upper
2611 limit on the cross section. First, it protects against negative signal strengths μ which are unphysical. Second,
2612 it does not count excesses in the data larger than those expected by a signal strength μ as evidence against
2613 the μ hypothesis.

2614 The CL_s statistic is constructed by taking a ratio of two probabilities. CL_{s+b} is the probability that the
2615 signal+background hypothesis would produce a value of the test statistic that is less than or equal to the
2616 observed value¹. CL_b is the probability that the background only hypothesis will produce a value
2617 of the test statistic less than or equal to the observed. The CL_s statistic is the ratio CL_{s+b}/CL_b . A 95%
2618 upper limit on the cross section is set at the value of μ that makes the CL_s statistic less than 5%. In practice,
2619 the limits are computed numerically within an asymptotic approximation for the distribution of the test
2620 statistic \tilde{q}_μ . The details of this approximation can be found in reference [76].

2621 The resolved and boosted analyses are combined using a very simple procedure rather than a full statis-
2622 tical combination. For each mass point tested, the limit which gives the most stringent constraint is used.
2623 This means that for mass points below 1.1 TeV the resolved signal region is used, while at and above this
2624 point the combination of the orthogonal 3b and 4b boosted signal regions is used.

2625 8.4.2 LIMIT SETTING RESULTS

2626 Figure 8.2 shows the combined 95% upper bounds as a function of mass for three different models: G_{KK}^*
2627 with $c = 1$, G_{KK}^* with $c = 2$, and a narrow heavy scalar H .

¹Lower values of \tilde{q}_μ mean better compatibility.

2628 The cross section of $\sigma(pp \rightarrow G_{\text{KK}}^* \rightarrow hh \rightarrow b\bar{b}b\bar{b})$ with $c = 1$ is constrained to be less than 70 fb
2629 for masses in the range $600 < m_{G_{\text{KK}}^*} < 3000$ GeV. For the RSG model with $c = 2$, cross sections limits
2630 between 40 fb and 200 fb are set for the mass range of $500 < m_{G_{\text{KK}}^*} < 3000$ GeV. Masses in the range
2631 of $475 < m_{G_{\text{KK}}^*} < 785$ GeV are excluded with $c = 1$ (with an exclusion of the range 465 to 745 GeV
2632 expected). Masses less than 980 GeV are excluded with $c = 2$ (with an exclusion for masses less than
2633 1 TeV expected).

2634 In the heavy Higgs model, the cross section upper limits for $\sigma(pp \rightarrow H \rightarrow hh \rightarrow b\bar{b}b\bar{b})$ ranges from
2635 30 to 300 fb in the mass range of $500 < m_H < 3000$ GeV. The resolved analysis can also set an upper
2636 limit on the Standard Model di-Higgs production cross section discussed in chapter 3. The upper limit on
2637 $\sigma(pp \rightarrow hh \rightarrow b\bar{b}b\bar{b})$ in the Standard Model is constrained to be less than 1.22 pb.

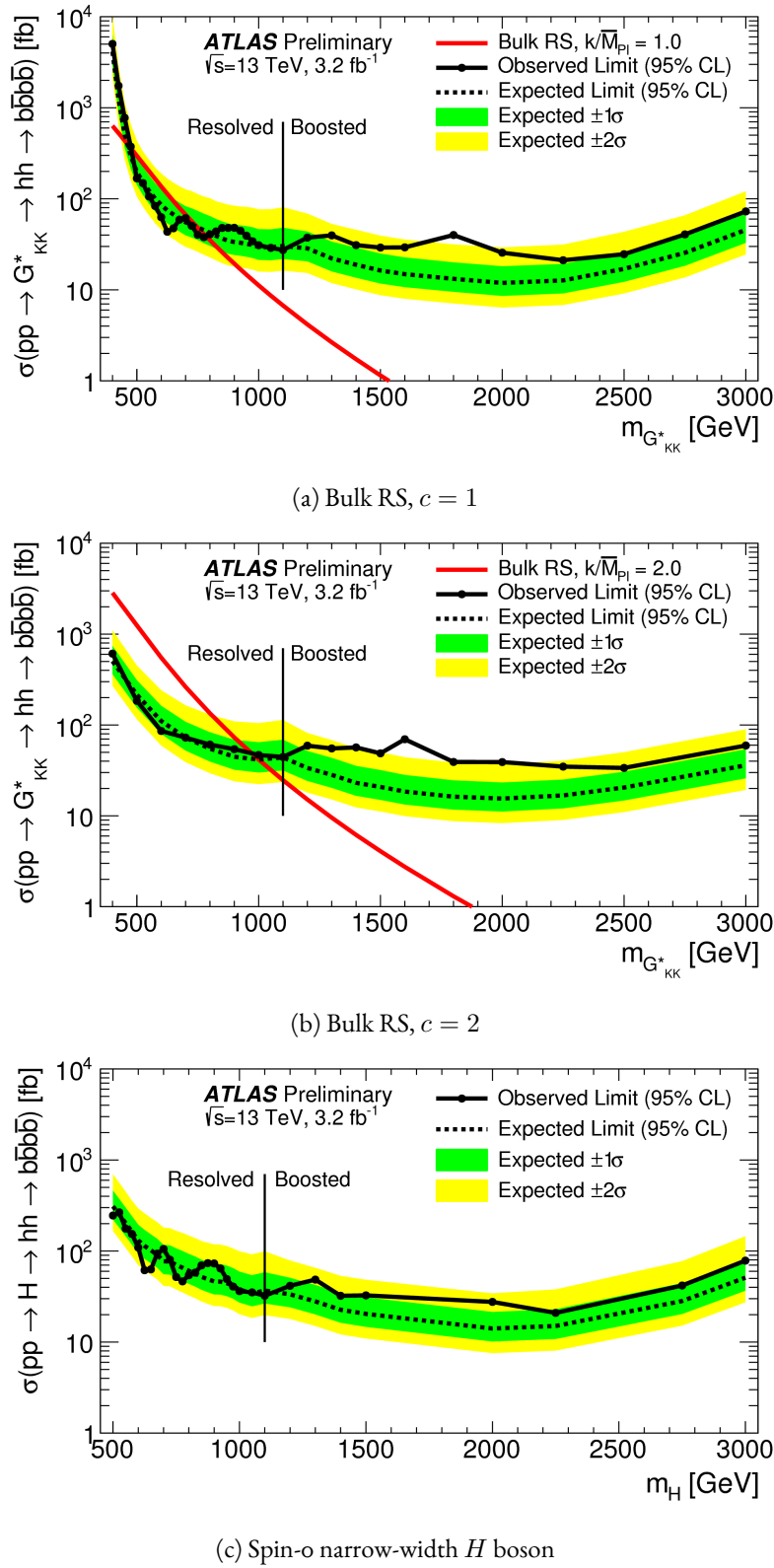


Figure 8.2: Expected and observed upper limit as a function of mass for G^*_{KK} in the RSG model with (a) $c = 1$ and (b) $c = 2$, as well as (c) H with fixed $\Gamma_H = 1$ GeV, at the 95% confidence level in the CL_s method [126].

2638

Part IV

2639

Looking ahead

9

2640

Conclusion

2641

2642 After being sought for many years at different collider experiments, the Higgs boson was discovered by
2643 the ATLAS and CMS experiments in 2012, confirming the leading theory for the source of electroweak
2644 symmetry breaking and filling in the last missing piece of the Standard Model. After its discovery, mea-
2645 surements of the particle's detailed properties and searches for new particles decaying to Higgs final states
2646 were both extremely important in constraining physics beyond the Standard Model. This dissertation
2647 presented this evolution through two results: the observation and measurement of the Higgs boson in the
2648 $H \rightarrow WW^* \rightarrow \ell\nu\ell\nu$ channel at $\sqrt{s} = 7$ TeV and $\sqrt{s} = 8$ TeV and a search for Higgs pair production
2649 in the $HH \rightarrow b\bar{b}b\bar{b}$ channel at $\sqrt{s} = 13$ TeV with the ATLAS detector in pp collisions at the Large
2650 Hadron Collider.

2651 In the $H \rightarrow WW^* \rightarrow \ell\nu\ell\nu$, results from both the discovery of the Higgs boson and the full ATLAS
2652 Run 1 dataset were presented. The Higgs boson was discovered with a 5.9σ significance in a combination
2653 of the $H \rightarrow \gamma\gamma$, $H \rightarrow ZZ \rightarrow 4\ell$, $H \rightarrow WW^* \rightarrow \ell\nu\ell\nu$ with 4.2 fb^{-1} at $\sqrt{s} = 7$ TeV and 5.2 fb^{-1} at

2654 $\sqrt{s} = 8$ TeV. With the full 20.3 fb^{-1} at $\sqrt{s} = 8$ TeV and 4.2 fb^{-1} at $\sqrt{s} = 7$ TeV, ATLAS achieved dis-
2655covery level significance in the $H \rightarrow WW^*$ channel alone and obtained the first evidence of vector boson
2656fusion production in that channel. The combined signal strength was measured to be $\mu = 1.09^{+0.23}_{-0.21}$. The
2657total observed significance of the $H \rightarrow WW^*$ process was observed to be 6.1σ (with 5.8σ expected). Ad-
2658vanced methods for background reduction and estimation, particularly in same-flavor lepton final states,
2659were shown. The VBF signal strength was measured to be $\mu_{\text{VBF}} = 1.27^{+0.53}_{-0.45}$ with an observed signifi-
2660cance of 3.2σ (with 2.7σ expected).

2661 These results required many novel innovations. The increase of pileup interactions in the higher in-
2662stantaneous luminosity LHC conditions of 2012 led to a degradation of missing transverse momentum
2663resolution. As a result, the prominent $Z/\gamma^* + \text{jets}$ background of the same flavor $H \rightarrow WW^* \rightarrow \ell\nu\ell\nu$
2664final states increased greatly. New variables, including a track-based missing transverse momentum and a
2665measurement of the balance between the dilepton system and recoiling jets, allowed for significant reduc-
2666tion of this background. In the VBF channel, selections were optimized to exploit the unique VBF final
2667state topology. Incorporating these variables into a boosted decision tree technique allowed the analysis
2668to exceed the 3σ statistical significance threshold.

2669 After the end of Run 1, the results of Higgs measurements from ATLAS were combined with those
2670from CMS to produce the most precise measurements of the Higgs boson so far [131]. Figure 9.1 shows the
2671combination of ATLAS and CMS data for the Higgs signal strength in and coupling measurements. In the
2672signal strength measurements of gluon fusion and vector boson fusion, the $H \rightarrow WW^*$ channel provides
2673the tightest constraints. Additionally, the Higgs coupling to W bosons is the most precisely measured with
2674a relative uncertainty of 10%.

2675 With the discovery of the Higgs firmly established and its properties measured, a natural next step was
2676to search for new physics with Higgs final states. At $\sqrt{s} = 13$ TeV, a search for Higgs pair production
2677in the $b\bar{b}b\bar{b}$ final state with 3.2 fb^{-1} was conducted. A signal region optimized for the boosted final states
2678arising from high mass resonances was constructed. This signal region utilized large-radius calorimeter jets
2679and b -tagging with small radius track jets to maximize the signal acceptance. No significant excesses were
2680observed, and upper limits on cross sections are placed for spin-2 Randall Sundrum gravitons (RSG) and

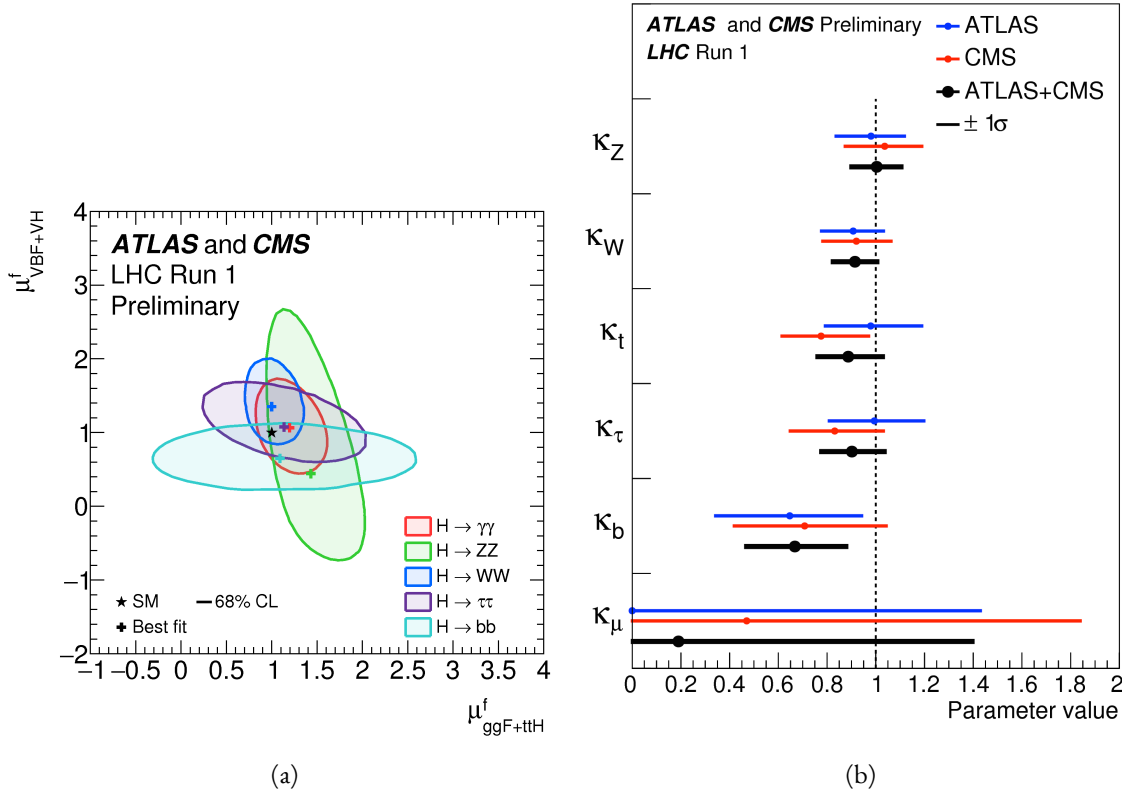


Figure 9.1: Combined ATLAS and CMS measurements in Run 1 for (a) Higgs signal strength in gluon fusion and VBF and (b) Higgs couplings normalized to their SM predictions

heavy narrow scalar resonances. The increase in center of mass energy in Run 2 allowed this analysis to quote upper cross section up to masses 3 TeV, while previous results from ATLAS in Run 1 only quote limits up to 2 TeV. The cross section of $\sigma(pp \rightarrow G_{\text{KK}}^* \rightarrow hh \rightarrow b\bar{b}b\bar{b})$ with $k/\bar{M}_{\text{Pl}} = 1$ was constrained to be less than 70 fb for masses in the range $600 < m_{G_{\text{KK}}^*} < 3000$ GeV. For the RSG model with $k/\bar{M}_{\text{Pl}} = 2$, cross sections limits between 40 fb and 200 fb are set for the mass range of $500 < m_{G_{\text{KK}}^*} < 3000$ GeV. The cross section upper limits for $\sigma(pp \rightarrow H \rightarrow hh \rightarrow b\bar{b}b\bar{b})$ ranges from 30 to 300 fb in the mass range of $500 < m_H < 3000$ GeV.

While there has been a rigorous program of measurements and searches involving the Higgs, there is still much room for improvement at the High Luminosity LHC (HL-LHC) and beyond. The measured signal strength for VBF production in $H \rightarrow WW^*$ still has a relative error at the level of 40%, largely dominated by statistical uncertainty. Projections for the HL-LHC show that the uncertainty on the VBF signal strength can be reduced to approximately 15% with 3000 fb^{-1} [132, 133]. This projection also assumes

2693 that theoretical uncertainties on the signal, which would be the largest contribution in the future dataset,
 2694 remain as they are now. Improvements in the theoretical understanding of the Higgs signal would also
 2695 reduce the signal strength uncertainty dramatically. Such precision results allow for measurements of the
 2696 Higgs coupling to vector bosons precise to the few percent level, therefore giving much power to constrain
 2697 or discover new physics.

2698 The prospects for detection of beyond the Standard Model resonant di-Higgs production at the HL-
 2699 LHC are also quite promising. Figure 9.2 shows projections for the discovery significance of RSG signals at
 2700 the HL-LHC in the $X \rightarrow HH \rightarrow b\bar{b}b\bar{b}$ search [133]. In all detector budget scenarios, a 1.5 TeV resonance
 is above or near 5σ significance, while a 2 TeV resonance is between $4-5\sigma$ except for the lowest budget.

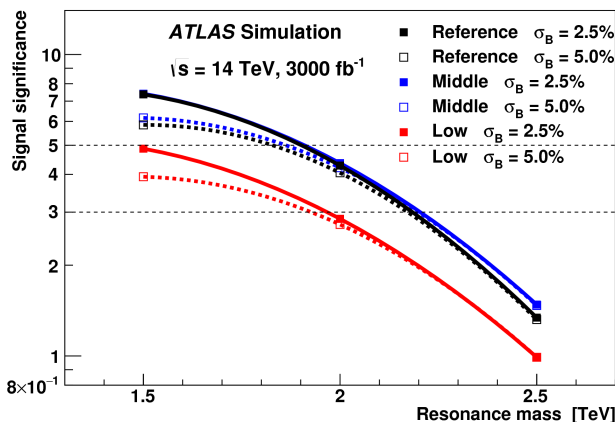


Figure 9.2: Discovery significance for RSG models at the HL-LHC in three different budget scenarios [133].
 Systematic uncertainties on the background prediction (σ_B) of 2.5% and 5.0% are both tested.

2701
 2702 The Higgs will continue to be an incredibly powerful tool in the understanding of nature at the HL-
 2703 LHC and beyond. Through both precision measurements and searches, the nature of electroweak symme-
 2704 try breaking will be better understood and the potential for the discovery of physics beyond the Standard
 2705 Model has never been greater.

A

2706

2707

b-tagging performance at high p_T

2708 One of the limiting factors of the signal acceptance in the $X \rightarrow HH \rightarrow b\bar{b}b\bar{b}$ search at high resonance
2709 masses is the degradation of the *b*-tagging efficiency for high p_T jets. This appendix presents a study of the
2710 underlying causes of this degradation.

2711 A.I CHANGES IN MV₂ SCORE AT HIGH p_T

2712 The degradation of *b*-tagging at high p_T was studied in particular in the context of RSG models at high
2713 mass. Figure A.I shows the p_T of the leading track jet inside of the leading calorimeter jet in RSG events.
2714 At high $m_{G_{KK}^*}$, the p_T spectrum of track jets is much harder than at lower masses due to the increased
2715 Higgs p_T .

2716 Figure A.2 shows the MV_{2c2o} algorithm score for the leading and subleading track jets inside of the
2717 leading calorimeter jet. In both cases, it can be seen that at higher RSG masses the MV₂ score shifts towards
2718 more background like (negative) values. Additionally, this effect is more pronounced in the leading track

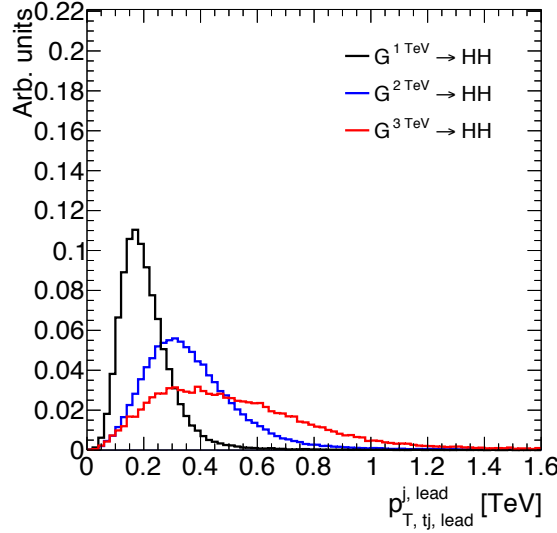


Figure A.1: p_T of the leading track jet in the leading calorimeter jet for different signal masses in RSG $c = 1$ models

²⁷¹⁹ jet than the subleading.

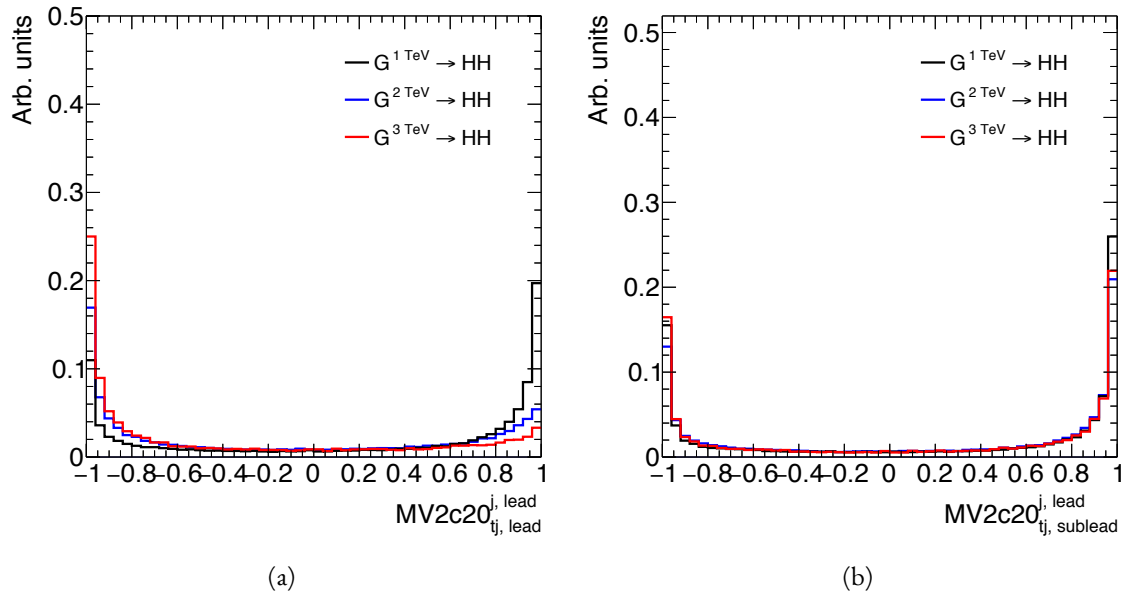


Figure A.2: MV2c20 score for the leading track jet (a) and subleading track jet (b) of the leading calorimeter jet for different signal masses in RSG $c = 1$ models

²⁷²⁰ To understand what is causing this change in the MV2c20 score, the same comparisons can be made for
²⁷²¹ the input variables of MV2c20. The focus in these comparisons will be on the leading track jet as this is the
²⁷²² one seen to have the largest difference in MV2 score. Figure A.3 shows the log likelihood ratio $\log(p_b/p_u)$

from the IP₃D (three dimensional impact parameter) algorithm. At higher masses, the IP₃D likelihood ratio distribution does become more background-like.

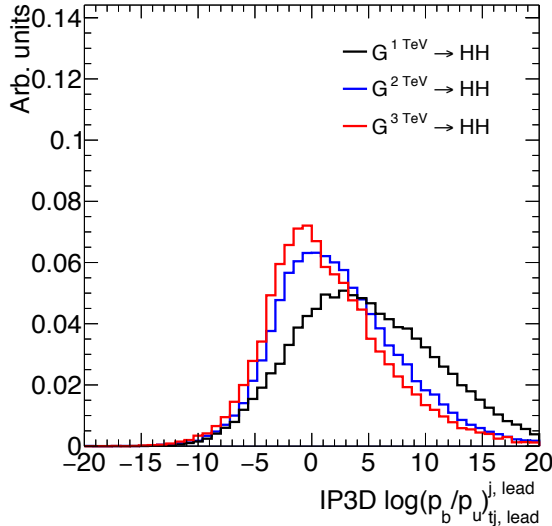


Figure A.3: IP₃D log-likelihood ratio ($\log(p_b/p_u)$) of the leading track jet in the leading calorimeter jet for different signal masses in RSG $c = 1$ models

Figure A.4 shows the mass and number of tracks at the secondary vertex computed by the SV1 algorithm. When there is no secondary vertex found, the algorithm assigns a default negative value for these quantities. Both of these distributions show that there is a significantly larger fraction of jets where no secondary vertex is found in the high mass samples compared to the $m_{G_{KK}^*} = 1$ TeV sample. The SV1 algorithm's inability to find a secondary vertex could be an important factor in the overall MV₂ score shift, as this eliminates eight of the input variables that would normally contribute information to the algorithm.

Figure A.5 shows the same quantities for the JetFitter algorithm. In this case, there is also a change in the fraction of jets which have their secondary vertices successfully reconstructed, but this change is not as drastic as that seen in SV1. There is also an increase in the number of jets which have high values of mass.

A.2 EFFECT OF MULTIPLE b -QUARKS INSIDE ONE JET

One hypothesis for why the efficiency of b -tagging the leading track jet degrades is that at high masses, the b quarks get close enough together that both of them are inside of the leading track jet. Because MV₂ is not

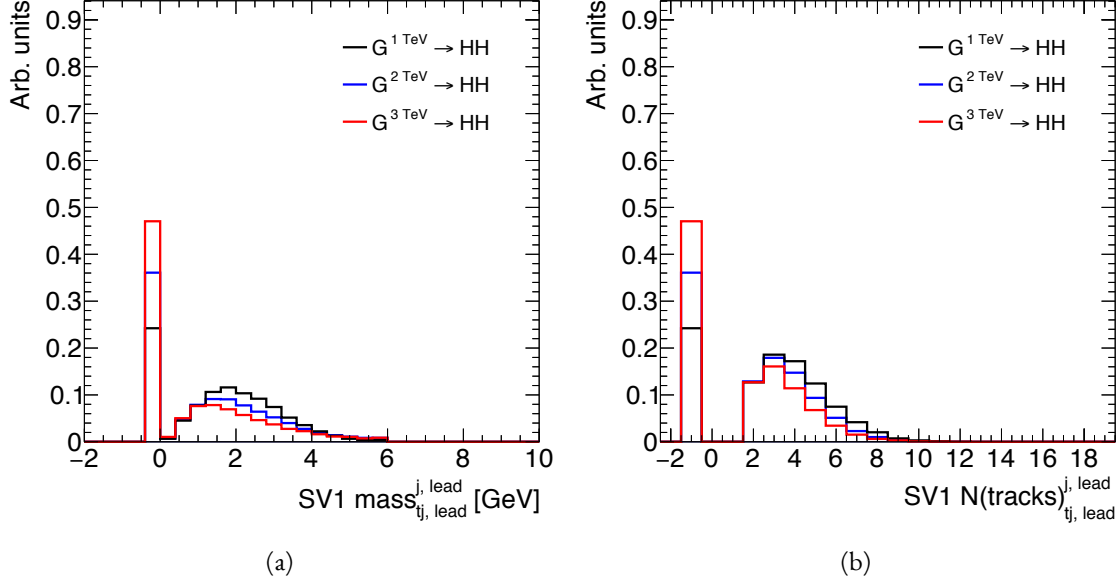


Figure A.4: Mass (a) and number of tracks (b) for the secondary vertices computed with the SV1 algorithm. When no secondary vertex is found, the quantities are assigned to default negative values.

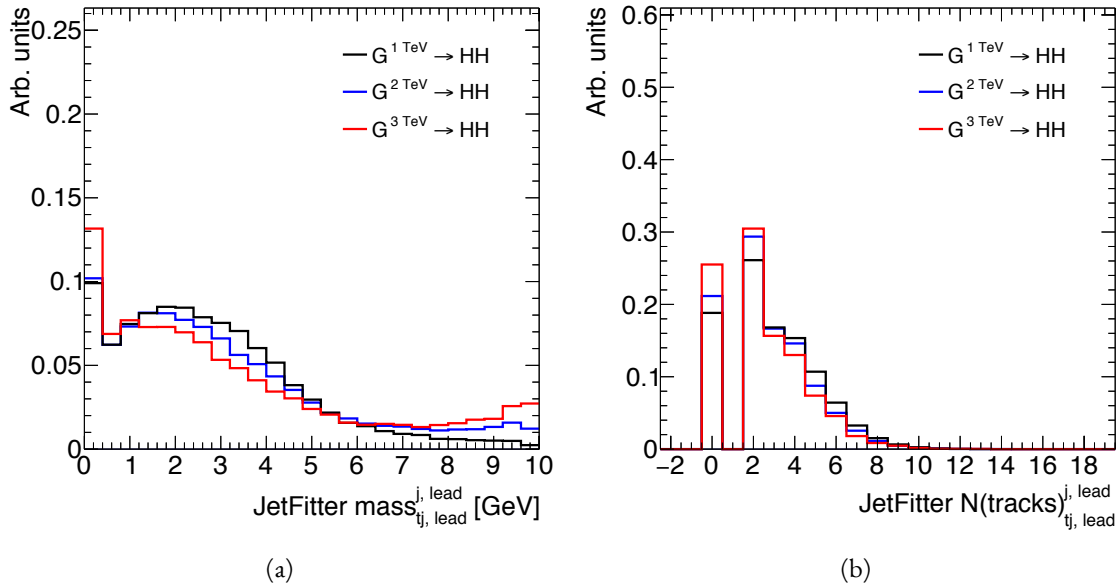


Figure A.5: Mass (a) and number of tracks (b) for vertices computed with the JetFitter algorithm. When no vertices are found, the quantities are assigned to default negative values.

2737 tuned for tagging multiple b quarks inside one jet, the tagging efficiency could degrade. Figure A.6 shows
 2738 MV2 scores and SV1 mass for cases where there are two b quarks at truth level within the radius of the

leading track jet compared to cases where there is only one true b^{l} . This figure suggests that the presence

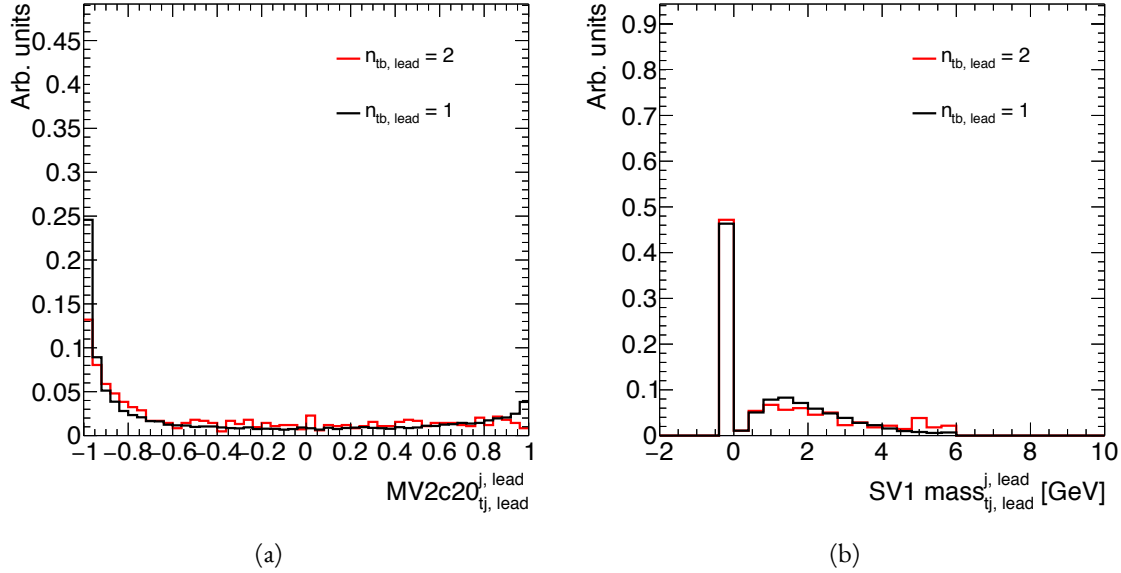


Figure A.6: MV₂c20 score (a) and SV1 mass (b) for leading track jets with two truth b quarks ($n_{\text{tb, lead}} = 2$) compared to those with only one truth b ($n_{\text{tb, lead}} = 1$).

of two b -quarks inside the leading jet is not the cause of the degradation in efficiency. There is a change in the shape of the MV₂ score distribution, but it is not nearly as pronounced as that seen in A.2 at higher masses. Additionally, the fraction of jets with no secondary vertex found is nearly identical in the track jets with two truth b -quarks.

A.3 CHANGES IN TRACK QUALITY AT HIGH p_{T}

Another hypothesis for the degradation of the b -tagging efficiency is a decrease in track quality for high p_{T} b jets. One way to check the overall quality of the tracking inside the jet is to investigate quantities related to the leading track inside of the track jet. Figure A.7 shows the fit χ^2/n_{DOF} and number of hits in the pixel detector for the leading track of the leading track jet. In both cases, the figure shows that in higher mass samples, the quality of the leading track inside of the track jet degrades substantially. The fit quality is lessened and the tracks have less hits in the pixel detector. This is likely due to the fact that at higher p_{T} ,

¹When two truth b quarks are required in the leading jet, the subleading jet is required to have zero. When one is required for the leading, one is also required for the subleading.

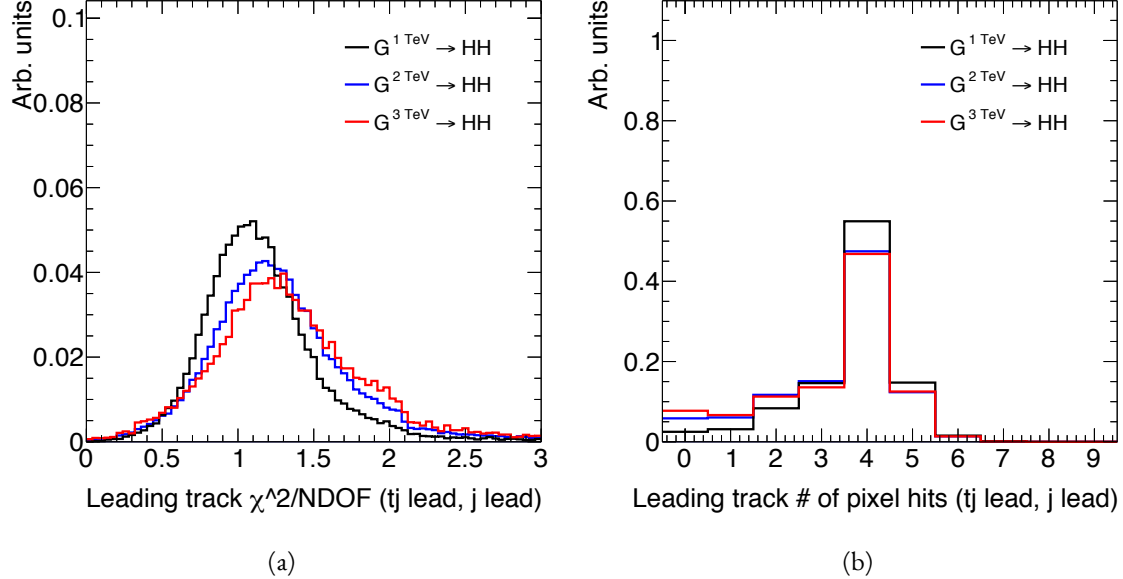


Figure A.7: Track fit χ^2/nDOF (a) and number of pixel detector hits (b) for the leading track of the leading track jet in different mass RSG $c = 1$ samples

the B -hadron will sometimes live long enough to miss the IBL and first pixel layer, thus decreasing the number of hits on the track.

To check whether this is the cause for the shift in the MV_2 score and the higher difficulty in reconstructing secondary vertices, jets whose leading track have at least four pixel hits are compared with those whose tracks have less than four pixel hits. The results for the MV_2 score and SV_1 mass are shown in figure A.8. Track jets where the leading track does not have at least four pixel hits are more likely to not have a secondary vertex reconstructed. Additionally, their MV_{2c2o} score is shifted more significantly to background-like values. This seems to confirm the hypothesis that degrading track quality is responsible for the lowered b -tagging efficiency at high p_T .

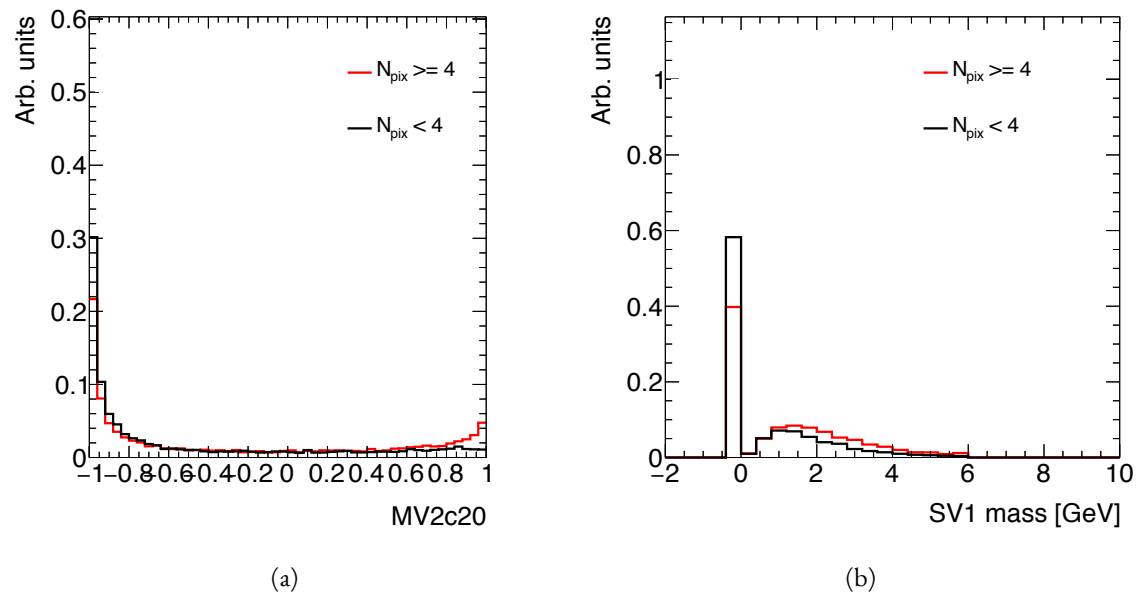


Figure A.8: MV₂c₂₀ score (a) and SV₁ mass (b) for leading track jets whose leading track jet has at least four pixel hits ($N_{\text{pix}} \geq 4$) compared to those which do not ($N_{\text{pix}} < 4$).

References

2760

- 2761 [1] Georges Aad et al. Observation of a new particle in the search for the Standard Model Higgs boson
2762 with the ATLAS detector at the LHC. *Phys. Lett.*, B716:1–29, 2012. doi: 10.1016/j.physletb.2012.
2763 08.020.
- 2764 [2] Serguei Chatrchyan et al. Observation of a new boson at a mass of 125 GeV with the CMS experi-
2765 ment at the LHC. *Phys. Lett.*, B716:30–61, 2012. doi: 10.1016/j.physletb.2012.08.021.
- 2766 [3] David Griffiths. *Introduction to elementary particles*. 2008.
- 2767 [4] F. Halzen and Alan D. Martin. *QUARKS AND LEPTONS: AN INTRODUCTORY COURSE
2768 IN MODERN PARTICLE PHYSICS*. 1984. ISBN 0471887412, 9780471887416.
- 2769 [5] Christopher G. Tully. *Elementary particle physics in a nutshell*. 2011.
- 2770 [6] K. A. Olive et al. Review of Particle Physics. *Chin. Phys.*, C38:090001, 2014. doi: 10.1088/1674-1137/
2771 38/9/090001.
- 2772 [7] Matthew D. Schwartz. *Quantum Field Theory and the Standard Model*. Cambridge University
2773 Press, 2014. ISBN 1107034736, 9781107034730. URL <http://www.cambridge.org/us/academic/subjects/physics/theoretical-physics-and-mathematical-physics/quantum-field-theory-and-standard-model>.
- 2776 [8] S. Dawson. Introduction to electroweak symmetry breaking. In *High energy physics and cosmology.
2777 Proceedings, Summer School, Trieste, Italy, June 29-July 17, 1998*, pages 1–83, 1998. URL <http://alice.cern.ch/format/showfull?sysnb=0301862>.
- 2779 [9] S. L. Glashow. Partial Symmetries of Weak Interactions. *Nucl. Phys.*, 22:579–588, 1961. doi: 10.
2780 1016/0029-5582(61)90469-2.
- 2781 [10] Steven Weinberg. A Model of Leptons. *Phys. Rev. Lett.*, 19:1264–1266, 1967. doi: 10.1103/
2782 PhysRevLett.19.1264.
- 2783 [11] A. Salam. *Elementary Particle Theory*. Almqvist and Wiksell, Stockholm, 1968.
- 2784 [12] J. Iliopoulos S.L. Glashow and L. Maiani. *D2:1285*, 1970.
- 2785 [13] R. Keith Ellis, W. James Stirling, and B. R. Webber. *QCD and collider physics*. *Camb. Monogr.
2786 Part. Phys. Nucl. Phys. Cosmol.*, 8:1–435, 1996.

- 2787 [14] P. W. Higgs. Broken symmetries and the masses of gauge bosons. *13*:508, 1964.
- 2788 [15] P. W. Higgs. Spontaneous symmetry breakdown without massless bosons. *145*:1156, 1966.
- 2789 [16] F. Englert and R. Brout. Broken symmetry and the mass of gauge vector mesons. *13*:321, 1964.
- 2790 [17] G. S. Guralnik, C. R. Hagen, and T. W. .B. Kibble. Global conservation laws and massless particles.
Phys. Rev. Lett., *13*:585, 1964. doi: [10.1103/PhysRevLett.13.585](https://doi.org/10.1103/PhysRevLett.13.585).
- 2792 [18] LHC Higgs Cross Section Working Group, S. Heinemeyer, C. Mariotti, G. Passarino, and
 2793 R. Tanaka (Eds.). Handbook of LHC Higgs Cross Sections: 3. Higgs Properties. 2013.
- 2794 [19] Charalampos Anastasiou and Kirill Melnikov. Higgs boson production at hadron colliders in
 2795 NNLO QCD. *Nucl. Phys.*, *B* **646**:220, 2002. doi: [10.1016/S0550-3213\(02\)00837-4](https://doi.org/10.1016/S0550-3213(02)00837-4).
- 2796 [20] M. Spira, A. Djouadi, D. Graudenz, and P. M. Zerwas. Higgs boson production at the LHC. *Nucl.*
 2797 *Phys.*, *B* **453**:17, 1995. doi: [10.1016/0550-3213\(95\)00379-7](https://doi.org/10.1016/0550-3213(95)00379-7).
- 2798 [21] Giuseppe Degrassi and Fabio Maltoni. Two-loop electroweak corrections to Higgs production at
 2799 hadron colliders. *Phys. Lett.*, *B* **600**:255, 2004.
- 2800 [22] U. Aglietti, R. Bonciani, G. Degrassi, and A. Vicini. Master integrals for the two-loop light fermion
 2801 contributions to $gg \rightarrow H$ and $H \rightarrow \gamma\gamma$. *600*:57, 2004. doi: [10.1016/j.physletb.2004.09.001](https://doi.org/10.1016/j.physletb.2004.09.001).
- 2803 [23] D. de Florian and M. Grazzini. Higgs production at the LHC: updated cross sections at $\sqrt{s} =$
 2804 8 TeV. *Phys. Lett.*, *B* **718**:117, 2012.
- 2805 [24] P. Bolzoni, F. Maltoni, S.-O. Moch, and M. Zaro. Higgs production via vector-boson fusion at
 2806 NNLO in QCD. *105*:011801, 2010. doi: [10.1103/PhysRevLett.105.011801](https://doi.org/10.1103/PhysRevLett.105.011801).
- 2807 [25] Tao Han, G. Valencia, and S. Willenbrock. Structure function approach to vector boson scattering
 2808 in $p p$ collisions. *Phys. Rev. Lett.*, *69*:3274–3277, 1992. doi: [10.1103/PhysRevLett.69.3274](https://doi.org/10.1103/PhysRevLett.69.3274).
- 2809 [26] Mariano Ciccolini, Ansgar Denner, and Stefan Dittmaier. Electroweak and QCD corrections to
 2810 Higgs production via vector-boson fusion at the LHC. *Phys. Rev.*, *D* **77**:013002, 2008. doi: [10.1103/PhysRevD.77.013002](https://doi.org/10.1103/PhysRevD.77.013002).
- 2812 [27] S. Catani, D. de Florian, M. Grazzini, and P. Nason. Soft-gluon re-summation for Higgs boson
 2813 production at hadron colliders. *JHEP*, *0307*:028, 2003. doi: [10.1088/1126-6708/2003/07/028](https://doi.org/10.1088/1126-6708/2003/07/028).
- 2814 [28] Abdelhak Djouadi. The Anatomy of electro-weak symmetry breaking. I: The Higgs boson in the
 2815 standard model. *Phys. Rept.*, *457*:1–216, 2008. doi: [10.1016/j.physrep.2007.10.004](https://doi.org/10.1016/j.physrep.2007.10.004).

- 2816 [29] J. Baglio, A. Djouadi, R. Gröber, M. M. Mühlleitner, J. Quevillon, and M. Spira. The mea-
 2817 surement of the Higgs self-coupling at the LHC: theoretical status. *JHEP*, 04:151, 2013. doi:
 2818 10.1007/JHEP04(2013)151.
- 2819 [30] Matthew J. Dolan, Christoph Englert, and Michael Spannowsky. New Physics in LHC Higgs boson
 2820 pair production. *Phys. Rev.*, D87(5):055002, 2013. doi: 10.1103/PhysRevD.87.055002.
- 2821 [31] Roberto Contino, Margherita Ghezzi, Mauro Moretti, Giuliano Panico, Fulvio Piccinini, and An-
 2822 drea Wulzer. Anomalous Couplings in Double Higgs Production. *JHEP*, 08:154, 2012. doi:
 2823 10.1007/JHEP08(2012)154.
- 2824 [32] R. Grober and M. Mühlleitner. Composite Higgs Boson Pair Production at the LHC. *JHEP*, 06:
 2825 020, 2011. doi: 10.1007/JHEP06(2011)020.
- 2826 [33] Lisa Randall and Raman Sundrum. A Large mass hierarchy from a small extra dimension. *Phys.*
 2827 *Rev. Lett.*, 83:3370–3373, 1999. doi: 10.1103/PhysRevLett.83.3370.
- 2828 [34] Kaustubh Agashe, Hooman Davoudiasl, Gilad Perez, and Amarjit Soni. Warped Gravitons at the
 2829 LHC and Beyond. *Phys. Rev.*, D76:036006, 2007. doi: 10.1103/PhysRevD.76.036006.
- 2830 [35] A. Liam Fitzpatrick, Jared Kaplan, Lisa Randall, and Lian-Tao Wang. Searching for the Kaluza-
 2831 Klein Graviton in Bulk RS Models. *JHEP*, 09:013, 2007. doi: 10.1088/1126-6708/2007/09/013.
- 2832 [36] Julien Baglio, Otto Eberhardt, Ulrich Nierste, and Martin Wiebusch. Benchmarks for Higgs Pair
 2833 Production and Heavy Higgs boson Searches in the Two-Higgs-Doublet Model of Type II. *Phys.*
 2834 *Rev.*, D90(1):015008, 2014. doi: 10.1103/PhysRevD.90.015008.
- 2835 [37] G. C. Branco, P. M. Ferreira, L. Lavoura, M. N. Rebelo, Marc Sher, and Joao P. Silva. Theory and
 2836 phenomenology of two-Higgs-doublet models. *Phys. Rept.*, 516:1–102, 2012. doi: 10.1016/j.physrep.
 2837 2012.02.002.
- 2838 [38] Howard E. Haber and Oscar Stål. New LHC benchmarks for the \mathcal{CP} -conserving two-Higgs-
 2839 doublet model. *Eur. Phys. J.*, C75(10):491, 2015. doi: 10.1140/epjc/s10052-015-3697-x.
- 2840 [39] Jose M. No and Michael Ramsey-Musolf. Probing the Higgs Portal at the LHC Through Resonant
 2841 di-Higgs Production. *Phys. Rev.*, D89(9):095031, 2014. doi: 10.1103/PhysRevD.89.095031.
- 2842 [40] Johan Alwall, Michel Herquet, Fabio Maltoni, Olivier Mattelaer, and Tim Stelzer. MadGraph
 2843 5:Going Beyond. *JHEP*, 1106:128, 2011. doi: 10.1007/JHEP06(2011)128.
- 2844 [41] Oleg Antipin, Tuomas Hapola. CP3 Origins implementation of Randall-Sundrum model. 2013,
 2845 URL <http://cp3-origins.dk/research/units/ed-tools>.

- 2846 [42] Georges Aad et al. Constraints on new phenomena via Higgs boson couplings and invisible decays
2847 with the ATLAS detector. *JHEP*, 11:206, 2015. doi: 10.1007/JHEP11(2015)206.
- 2848 [43] Lyndon R Evans and Philip Bryant. LHC Machine. *J. Instrum.*, 3:S08001, 164 p, 2008. URL
2849 <https://cds.cern.ch/record/1129806>. This report is an abridged version of the LHC De-
2850 sign Report (CERN-2004-003).
- 2851 [44] ATLAS Collaboration. The ATLAS experiment at the CERN Large Hadron Collider. *JINST*, 3:
2852 S08003, 2008. doi: 10.1088/1748-0221/3/08/S08003.
- 2853 [45] CMS Collaboration. The cms experiment at the cern lhc. *Journal of Instrumentation*, 3(08):S08004,
2854 2008. URL <http://stacks.iop.org/1748-0221/3/i=08/a=S08004>.
- 2855 [46] LHCb Collaoration. The LHCb Detector at the LHC. *JINST*, 3:S08005, 2008. doi: 10.1088/
2856 1748-0221/3/08/S08005.
- 2857 [47] ALICE Collaboration. The alice experiment at the cern lhc. *Journal of Instrumentation*, 3(08):
2858 S08002, 2008. URL <http://stacks.iop.org/1748-0221/3/i=08/a=S08002>.
- 2859 [48] Lyndon Evans. The Large Hadron Collider. In Holstein, BR and Haxton, WC and Jawah-
2860 ery, A, editor, *ANNUAL REVIEW OF NUCLEAR AND PARTICLE SCIENCE, VOL*
2861 *61*, volume 61 of *Annual Review of Nuclear and Particle Science*, pages 435–466. 2011. doi:
2862 {10.1146/annurev-nucl-102010-130438}.
- 2863 [49] ATLAS Collaboration. Luminosity Determination in pp Collisions at $\sqrt{s} = 7$ TeV Using the
2864 ATLAS Detector at the LHC. *Eur. Phys. J.*, C 71:1630, 2011. doi: 10.1140/epjc/s10052-011-1630-5.
- 2865 [50] Mike Lamont for the LHC team. The First Years of LHC Operation for Luminosity Production.
2866 International Particle Accelerator Conference, 2013. URL <https://accelconf.web.cern.ch/>
2867 accelconf/IPAC2013/talks/moyab101_talk.pdf.
- 2868 [51] Paul Collier for the LHC team. LHC Machine Status. CERN Resource Review Board, 2015. URL
2869 <https://cds.cern.ch/record/2063924/files/CERN-RRB-2015-119.PDF>.
- 2870 [52] Track Reconstruction Performance of the ATLAS Inner Detector at $\sqrt{s} = 13$ TeV. Technical
2871 Report ATL-PHYS-PUB-2015-018, CERN, Geneva, Jul 2015. URL <http://cds.cern.ch/>
2872 [record/2037683](https://cds.cern.ch/record/2037683).
- 2873 [53] M Capeans, G Darbo, K Einsweiller, M Elsing, T Flick, M Garcia-Sciveres, C Gemme, H Perneg-
2874 ger, O Rohne, and R Vuillermet. ATLAS Insertable B-Layer Technical Design Report. Technical
2875 Report CERN-LHCC-2010-013, ATLAS-TDR-19, CERN, Geneva, Sep 2010. URL <https://cds.cern.ch/>
2876 [record/1291633](https://cds.cern.ch/record/1291633).

- 2877 [54] ATLAS Collaboration. ATLAS Trigger Operations Public Results. 2015. URL <https://twiki.cern.ch/twiki/bin/view/AtlasPublic/TriggerOperationPublicResults>.
- 2878
- 2879 [55] ATLAS Collaboration. ATLAS Luminosity Public Results, Run 1. 2012. URL <https://twiki.cern.ch/twiki/bin/view/AtlasPublic/LuminosityPublicResults>.
- 2880
- 2881 [56] ATLAS Collaboration. ATLAS Luminosity Public Results, Run 2. 2015. URL <https://twiki.cern.ch/twiki/bin/view/AtlasPublic/LuminosityPublicResultsRun2>.
- 2882
- 2883 [57] T Kawamoto, S Vlachos, L Pontecorvo, J Dubbert, G Mikenberg, P Iengo, C Dallapiccola, C Amelung, L Levinson, R Richter, and D Lellouch. New Small Wheel Technical Design Report. Technical Report CERN-LHCC-2013-006. ATLAS-TDR-020, CERN, Geneva, Jun 2013.
- 2884 URL <https://cds.cern.ch/record/1552862>. ATLAS New Small Wheel Technical Design
- 2885 Report.
- 2886
- 2887
- 2888 [58] Y. Giomataris, Ph. Rebours, J.P. Robert, and G. Charpak. Micromegas: a high-granularity position-sensitive gaseous detector for high particle-flux environments. *Nuclear Instruments and Methods in Physics Research Section A: Accelerators, Spectrometers, Detectors and Associated Equipment*, 376(1):29 – 35, 1996. ISSN 0168-9002. doi: [http://dx.doi.org/10.1016/0168-9002\(96\)00175-1](http://dx.doi.org/10.1016/0168-9002(96)00175-1). URL <http://www.sciencedirect.com/science/article/pii/0168900296001751>.
- 2889
- 2890
- 2891
- 2892
- 2893
- 2894 [59] T. Alexopoulos, J. Burnens, R. de Oliveira, G. Glonti, O. Pizzirussi, V. Polychronakos, G. Sekhniadze, G. Tsipolitis, and J. Wotschack. A spark-resistant bulk-micromegas chamber for high-rate applications. *Nuclear Instruments and Methods in Physics Research Section A: Accelerators, Spectrometers, Detectors and Associated Equipment*, 640(1):110 – 118, 2011. ISSN 0168-9002.
- 2895 doi: <http://dx.doi.org/10.1016/j.nima.2011.03.025>. URL <http://www.sciencedirect.com/science/article/pii/S0168900211005869>.
- 2896
- 2897
- 2898
- 2899
- 2900 [60] Joao Pequenao and Paul Schaffner. An computer generated image representing how ATLAS detects particles. Jan 2013. URL <https://cds.cern.ch/record/1505342>.
- 2901
- 2902
- 2903 [61] Improved electron reconstruction in ATLAS using the Gaussian Sum Filter-based model for bremsstrahlung. Technical Report ATLAS-CONF-2012-047, CERN, Geneva, May 2012. URL
- 2904 <https://cds.cern.ch/record/1449796>.
- 2905
- 2906
- 2907 [62] Electron efficiency measurements with the ATLAS detector using the 2012 LHC proton-proton collision data. Technical Report ATLAS-CONF-2014-032, CERN, Geneva, Jun 2014. URL
- 2908 <https://cds.cern.ch/record/1706245>.
- 2909
- 2910 [63] Georges Aad et al. Electron and photon energy calibration with the ATLAS detector using LHC Run 1 data. *Eur. Phys. J.*, C74(10):3071, 2014. doi: 10.1140/epjc/s10052-014-3071-4.

- 2910 [64] Georges Aad et al. Measurement of the muon reconstruction performance of the ATLAS detector
 2911 using 2011 and 2012 LHC proton–proton collision data. *Eur. Phys. J.*, C74(11):3130, 2014. doi:
 2912 10.1140/epjc/s10052-014-3130-x.
- 2913 [65] Georges Aad et al. Muon reconstruction performance of the ATLAS detector in proton–proton
 2914 collision data at $\sqrt{s}=13$ TeV. 2016.
- 2915 [66] W Lampl, S Laplace, D Lelas, P Loch, H Ma, S Menke, S Rajagopalan, D Rousseau, S Snyder,
 2916 and G Unal. Calorimeter Clustering Algorithms: Description and Performance. Technical Re-
 2917 port ATL-LARG-PUB-2008-002. ATL-COM-LARG-2008-003, CERN, Geneva, Apr 2008. URL
 2918 <https://cds.cern.ch/record/1099735>.
- 2919 [67] Georges Aad et al. Topological cell clustering in the ATLAS calorimeters and its performance in
 2920 LHC Run 1. 2016.
- 2921 [68] Matteo Cacciari, Gavin P. Salam, and Gregory Soyez. The Anti- $k(t)$ jet clustering algorithm. *JHEP*,
 2922 04:063, 2008. doi: 10.1088/1126-6708/2008/04/063.
- 2923 [69] Monte Carlo Calibration and Combination of In-situ Measurements of Jet Energy Scale, Jet Energy
 2924 Resolution and Jet Mass in ATLAS. Technical Report ATLAS-CONF-2015-037, CERN, Geneva,
 2925 Aug 2015. URL <http://cds.cern.ch/record/2044941>.
- 2926 [70] Georges Aad et al. Performance of b -Jet Identification in the ATLAS Experiment. 2015.
- 2927 [71] Expected performance of the ATLAS b -tagging algorithms in Run-2. Technical Report
 2928 ATL-PHYS-PUB-2015-022, CERN, Geneva, Jul 2015. URL <http://cds.cern.ch/record/2037697>.
- 2929 [72] Georges Aad et al. Performance of Missing Transverse Momentum Reconstruction in Proton-
 2930 Proton Collisions at 7 TeV with ATLAS. *Eur. Phys. J.*, C72:1844, 2012. doi: 10.1140/epjc/
 2931 s10052-012-1844-6.
- 2932 [73] Performance of Missing Transverse Momentum Reconstruction in ATLAS studied in Proton-
 2933 Proton Collisions recorded in 2012 at 8 TeV. Technical Report ATLAS-CONF-2013-082, CERN,
 2934 Geneva, Aug 2013. URL <http://cds.cern.ch/record/1570993>.
- 2935 [74] ATLAS Collaboration. Observation and measurement of Higgs boson decays to WW^* with the
 2936 ATLAS detector. *Phys. Rev. D*, 92(012006), 2015.
- 2937 [75] Aaron James Armbruster. Discovery of a Higgs Boson with the ATLAS detector. 2013. CERN-
 2938 THESIS-2013-047.
- 2939 [76] G. Cowan, K. Cranmer, E. Gross, and O. Vitells. Asymptotic formulae for likelihood-based tests
 2940 of new physics. *Eur. Phys. J.*, C71:1554, 2011. doi: 10.1140/epjc/s10052-011-1554-0.

- 2942 [77] R.K. Ellis, I. Hinchliffe, M. Soldate, and J.J. Van Der Bij. Higgs decay to $\tau+\tau$ –a possible signature
 2943 of intermediate mass higgs bosons at high energy hadron colliders. *Nuclear Physics B*, 297(2):221
 2944 – 243, 1988. ISSN 0550-3213. doi: [http://dx.doi.org/10.1016/0550-3213\(88\)90019-3](http://dx.doi.org/10.1016/0550-3213(88)90019-3). URL <http://www.sciencedirect.com/science/article/pii/0550321388900193>.
- 2946 [78] ATLAS Collaboration. Limits on the production of the Standard Model Higgs Boson in pp
 2947 collisions at $\sqrt{s} = 7$ TeV with the ATLAS detector. *Eur. Phys. J.*, C 71:1728, 2011. doi:
 2948 [10.1140/epjc/s10052-011-1728-9](https://doi.org/10.1140/epjc/s10052-011-1728-9).
- 2949 [79] Leo Breiman, Jerome Friedman, Charles J Stone, and Richard A Olshen. *Classification and regres-*
 2950 *sion trees*. CRC press, 1984.
- 2951 [80] Yoav Freund and Robert E Schapire. A decision-theoretic generalization of on-line learning and an
 2952 application to boosting. *Journal of Computer and System Sciences*, 55(1):119 – 139, 1997. ISSN 0022-
 2953 0000. doi: <http://dx.doi.org/10.1006/jcss.1997.1504>. URL <http://www.sciencedirect.com/science/article/pii/S002200009791504X>.
- 2955 [81] Jerome H. Friedman. Stochastic gradient boosting. *Computational Statistics and Data Analysis*, 38
 2956 (4):367 – 378, 2002. ISSN 0167-9473. doi: [http://dx.doi.org/10.1016/S0167-9473\(01\)00065-2](http://dx.doi.org/10.1016/S0167-9473(01)00065-2). URL <http://www.sciencedirect.com/science/article/pii/S0167947301000652>. Non-
 2957 linear Methods and Data Mining.
- 2959 [82] ATLAS Collaboration. Performance of the ATLAS muon trigger in pp collisions at $\sqrt{s} = 8$ TeV.
 2960 *Eur. Phys. J. C*, (arXiv:1408.3179. CERN-PH-EP-2014-154):75, 19 p, Aug 2014. URL <https://cds.cern.ch/record/1749694>.
- 2962 [83] ATLAS collaboration. Electron trigger performance in 2012 ATLAS data, 2015. ATLAS-COM-
 2963 DAQ-2015-091.
- 2964 [84] Paolo Nason. A new method for combining NLO QCD with shower Monte Carlo algorithms.
 2965 *JHEP*, 11:040, 2004.
- 2966 [85] B. P. Kersevan and E. Richter-Was. The Monte Carlo event generator AcerMC version 2.0 with
 2967 interfaces to PYTHIA 6.2 and HERWIG 6.5. 2004.
- 2968 [86] Nikolas Kauer and Giampiero Passarino. Inadequacy of zero-width approximation for a light Higgs
 2969 boson signal. 2012.
- 2970 [87] T. Gleisberg, Stefan Hoeche, F. Krauss, M. Schonherr, S. Schumann, et al. Event generation with
 2971 SHERPA 1.1. *JHEP*, 0902:007, 2009. doi: <10.1088/1126-6708/2009/02/007>.
- 2972 [88] Michelangelo L. Mangano et al. ALPGEN, a generator for hard multiparton processes in hadronic
 2973 collisions. *JHEP*, 0307:001, 2003. doi: <10.1088/1126-6708/2003/07/001>.

- 2974 [89] Torbjorn Sjostrand, Stephen Mrenna, and Peter Z. Skands. PYTHIA 6.4 Physics and Manual.
 2975 *JHEP*, 0605:026, 2006. doi: [10.1088/1126-6708/2006/05/026](https://doi.org/10.1088/1126-6708/2006/05/026).
- 2976 [90] Torbjorn Sjostrand, Stephen Mrenna, and Peter Z. Skands. A Brief Introduction to PYTHIA 8.1.
 2977 *Comput.Phys.Commun.*, 178:852–867, 2008. doi: [10.1016/j.cpc.2008.01.036](https://doi.org/10.1016/j.cpc.2008.01.036).
- 2978 [91] G. Corcella et al. HERWIG 6: An event generator for hadron emission reactions with interfering
 2979 gluons (including super-symmetric processes). *JHEP*, 01:010, 2001. doi: [10.1088/1126-6708/2001/01/010](https://doi.org/10.1088/1126-6708/2001/01/010).
- 2980 [92] J. M. Butterworth, Jeffrey R. Forshaw, and M. H. Seymour. Multiparton interactions in photo-
 2981 production at HERA. *Z. Phys.*, C 72:637, 1996. doi: [10.1007/s002880050286](https://doi.org/10.1007/s002880050286).
- 2982 [93] Jun Gao, Marco Guzzi, Joey Huston, Hung-Liang Lai, Zhao Li, et al. The CT10 NNLO Global
 2983 Analysis of QCD. *Phys.Rev.*, D89:033009, 2014. doi: [10.1103/PhysRevD.89.033009](https://doi.org/10.1103/PhysRevD.89.033009).
- 2984 [94] P. M. Nadolsky. Implications of CTEQ global analysis for collider observables. *Phys. Rev.*, D 78:
 2985 013004, 2008. doi: [10.1103/PhysRevD.78.013004](https://doi.org/10.1103/PhysRevD.78.013004).
- 2986 [95] A. Sherstnev and R. S. Thorne. Parton distributions for the LHC. *Eur. Phys. J.*, C 55:553, 2009. doi:
 2987 [10.1140/epjc/s10052-008-0610-x](https://doi.org/10.1140/epjc/s10052-008-0610-x).
- 2988 [96] A. Bredenstein, Ansgar Denner, S. Dittmaier, and M. M. Weber. Precise predictions for the Higgs-
 2989 boson decay $H \rightarrow WW/ZZ \rightarrow 4$ leptons. *Phys. Rev.*, D74:013004, 2006.
- 2990 [97] A. Djouadi, J. Kalinowski, and M. Spira. HDECAY: A program for Higgs boson decays in the
 2991 standard model and its supersymmetric extension. *Comput. Phys. Commun.*, 108:56, 1998. doi:
 2992 [10.1016/S0010-4655\(97\)00123-9](https://doi.org/10.1016/S0010-4655(97)00123-9).
- 2993 [98] S. Agostinelli et al. GEANT4, a simulation toolkit. *Nucl. Instrum. Meth.*, A 506:250, 2003. doi:
 2994 [10.1016/S0168-9002\(03\)01368-8](https://doi.org/10.1016/S0168-9002(03)01368-8).
- 2995 [99] Eilam Gross and Ofer Vitells. Transverse mass observables for charged Higgs boson searches at
 2996 hadron colliders. *Phys. Rev.*, D81:055010, 2010. doi: [10.1103/PhysRevD.81.055010](https://doi.org/10.1103/PhysRevD.81.055010).
- 2997 [100] J. R. Andersen et al. Les Houches 2013: Physics at TeV Colliders: Standard Model Working Group
 2998 Report. 2014.
- 2999 [101] I. Stewart and F. Tackmann. Theory uncertainties for Higgs mass and other searches using jet bins.
 3000 *Phys. Rev.*, D 85:034011, 2012. doi: [10.1103/PhysRevD.85.034011](https://doi.org/10.1103/PhysRevD.85.034011).
- 3001 [102] ATLAS Collaboration. Luminosity Determination in pp Collisions at $\sqrt{s} = 7$ TeV Using the
 3002 ATLAS Detector at the LHC. *Eur. Phys. J.*, C 71:1630, 2011. doi: [10.1140/epjc/s10052-011-1630-5](https://doi.org/10.1140/epjc/s10052-011-1630-5).

- 3004 [103] Jet energy scale and its systematic uncertainty in proton-proton collisions at $\sqrt{s} = 7$ tev with atlas
 3005 data. *ATLAS-CONF-2013-004*, 2013.
- 3006 [104] Calibrating the b -tag efficiency and mistag rate in 35 pb^{-1} of data with the atlas detector. *ATLAS-*
 3007 *CONF-2011-089*, 2011.
- 3008 [105] ATLAS Collaboration. Measurement of the b -tag Efficiency in a Sample of Jets Containing Muons
 3009 with 5 fb^{-1} of Data from the ATLAS Detector. *ATLAS-CONF-2012-043*, 2012. URL <http://cdsweb.cern.ch/record/1435197>.
- 3010 [106] ATLAS Collaboration. Calibration of b -tagging using dileptonic top pair events in a combinatorial
 3011 likelihood approach with the ATLAS experiment. (ATLAS-CONF-2014-004), 2014. URL <http://cds.cern.ch/record/1664335>.
- 3012 [107] Georges Aad et al. Measurement of the Higgs boson mass from the $H \rightarrow \gamma\gamma$ and $H \rightarrow ZZ^* \rightarrow$
 3013 4ℓ channels with the ATLAS detector using 25 fb^{-1} of pp collision data. *Phys. Rev.*, D90(5):052004,
 3014 2014. doi: 10.1103/PhysRevD.90.052004.
- 3015 [108] Georges Aad et al. Measurements of the Higgs boson production and decay rates and coupling
 3016 strengths using pp collision data at $\sqrt{s} = 7$ and 8 TeV in the ATLAS experiment. *Eur. Phys. J.*,
 3017 C76(1):6, 2016. doi: 10.1140/epjc/s10052-015-3769-y.
- 3018 [109] W.J. Stirling. $7/8$ and $13/8$ TeV LHC luminosity ratios. 2013. URL http://www.hep.ph.ic.ac.uk/~wstirlin/plots/lhclumi7813_2013_v0.pdf.
- 3019 [110] J Alison. Experimental Studies of hh. Oct 2014. URL <http://cds.cern.ch/record/1952581>.
- 3020 [111] J. Alwall et al. The automated computation of tree-level and next-to-leading order differential cross
 3021 sections, and their matching to parton shower simulations. *JHEP*, 07:079, 2014.
- 3022 [112] Richard D. Ball et al. Parton distributions with LHC data. *Nucl. Phys. B*, 867:244, 2013.
- 3023 [113] ATLAS Collaboration. ATLAS Run 1 Pythia8 tunes. (ATL-PHYS-PUB-2014-021), Nov 2014.
 3024 URL <https://cds.cern.ch/record/1966419>.
- 3025 [114] M. Bahr et al. Herwig++ Physics and Manual. *Eur. Phys. J. C*, 58:639–707, 2008. doi: 10.1140/
 3026 epjc/s10052-008-0798-9.
- 3027 [115] Stefan Gieseke, Christian Rohr, and Andrzej Siódmiok. Colour reconnections in Herwig++. *Eur.*
 3028 *Phys. J. C*, 72:2225, 2012. doi: 10.1140/epjc/s10052-012-2225-5.
- 3029 [116] Simone Alioli, Paolo Nason, Carlo Oleari, and Emanuele Re. A general framework for implement-
 3030 ing NLO calculations in shower Monte Carlo programs: the POWHEG BOX. *JHEP*, 06:043,
 3031 2010.
- 3032

- 3035 [117] Peter Zeiler Skands. Tuning Monte Carlo Generators: The Perugia Tunes. *Phys. Rev. D*, 82:074018,
 3036 2010. doi: 10.1103/PhysRevD.82.074018.
- 3037 [118] Michal Czakon and Alexander Mitov. Top++: A Program for the Calculation of the Top-Pair
 3038 Cross-Section at Hadron Colliders. 2011.
- 3039 [119] Baojia (Tony) Tong. Private communication.
- 3040 [120] D. Krohn, J. Thaler, and L.-T. Wang. Jet Trimming. *JHEP*, 02:084, 2010. doi: 10.1007/
 3041 JHEP02(2010)084.
- 3042 [121] ATLAS Collaboration. Identification of Boosted, Hadronically Decaying W Bosons and Compar-
 3043 isons with ATLAS Data Taken at $\sqrt{s} = 8$ TeV. 2015.
- 3044 [122] Expected Performance of Boosted Higgs ($\rightarrow b\bar{b}$) Boson Identification with the ATLAS Detector
 3045 at $\sqrt{s} = 13$ TeV. Technical Report ATL-PHYS-PUB-2015-035, CERN, Geneva, Aug 2015. URL
 3046 <https://cds.cern.ch/record/2042155>.
- 3047 [123] Flavor Tagging with Track Jets in Boosted Topologies with the ATLAS Detector. Technical Report
 3048 ATL-PHYS-PUB-2014-013, CERN, Geneva, Aug 2014. URL <https://cds.cern.ch/record/1750681>.
- 3049 [124] Matteo Cacciari and Gavin P. Salam. Pileup subtraction using jet areas. *Phys. Lett. B*, 659:119, 2008.
 doi: 10.1016/j.physletb.2007.09.077.
- 3050 [125] Glen Cowan, Eilam Gross. Discovery significance with statistical uncertainty in the background
 3051 estimate. 2008. URL <http://www.pp.rhul.ac.uk/~cowan/stat/notes/SigCalcNote.pdf>.
- 3052 [126] Search for pair production of Higgs bosons in the $b\bar{b}b\bar{b}$ final state using proton-proton collisions
 3053 at $\sqrt{s} = 13$ TeV with the ATLAS detector. Technical Report ATLAS-CONF-2016-017, CERN,
 3054 Geneva, Mar 2016. URL <https://cds.cern.ch/record/2141006>.
- 3055 [127] Qi Zeng. Private communication.
- 3056 [128] ATLAS Collaboration. Identification of boosted, hadronically-decaying W and Z bosons in
 3057 $\sqrt{s} = 13$ TeV Monte Carlo Simulations for ATLAS. (ATL-PHYS-PUB-2015-033), Aug 2015. URL
 3058 <https://cds.cern.ch/record/2041461>.
- 3059 [129] ATLAS Collaboration. Performance of b -Jet Identification in the ATLAS Experiment. 2015.
- 3060 [130] Alexander L. Read. Presentation of search results: The $CL(s)$ technique. *J. Phys. G*, 28:2693, 2002.
 3061 doi: 10.1088/0954-3899/28/10/313.

- 3065 [131] Measurements of the Higgs boson production and decay rates and constraints on its couplings
3066 from a combined ATLAS and CMS analysis of the LHC pp collision data at $\sqrt{s} = 7$ and 8 TeV.
3067 Technical Report ATLAS-CONF-2015-044, CERN, Geneva, Sep 2015. URL <http://cds.cern.ch/record/2052552>.
3068
- 3069 [132] Projections for measurements of Higgs boson signal strengths and coupling parameters with the
3070 ATLAS detector at a HL-LHC. Technical Report ATL-PHYS-PUB-2014-016, CERN, Geneva,
3071 Oct 2014. URL <http://cds.cern.ch/record/1956710>.
- 3072 [133] ATLAS Phase-II Upgrade Scoping Document. Technical Report CERN-LHCC-2015-020. LHCC-
3073 G-166, CERN, Geneva, Sep 2015. URL <http://cds.cern.ch/record/2055248>.



3074

THIS THESIS WAS TYPESET using \LaTeX , originally developed by Leslie Lamport and based on Donald Knuth's \TeX . The body text is set in 11 point Egenolff-Berner Garamond, a revival of Claude Garamont's humanist typeface. The above illustration, *Science Experiment 02*, was created by Ben Schlitter and released under [CC BY-NC-ND 3.0](#). A template that can be used to format a PhD dissertation with this look & feel has been released under the permissive [AGPL](#) license, and can be found online at github.com/asm-products/Dissertate or from its lead author, Jordan Suchow, at suchow@post.harvard.edu.